Developing Selective Immunomodulatory Solutions for Cardiovascular Devices

Angus James Grant

A thesis submitted in fulfilment of the requirements for the degree of

Doctor of Philosophy

Faculty of Medicine and Health

The University of Sydney

2026

Statement of Originality

I certify that the intellectual content of this thesis is entirely the product of my own work, except where stated otherwise. All assistance received in preparing this thesis and sources used have been acknowledged. This thesis has not been submitted for any other degree or purpose.

Angus James Grant

Artificial Intelligence Statement

During the preparation of the thesis, I have used ChatGPT for the purposes of text enhancement including sentence structure and grammar. I confirm that where text was modified by generative AI, the content was reviewed for possible errors, inaccuracies, and bias. I take full responsibility for the submitted thesis and ensure the work is my own and have used generative AI within the parameters of use outlined by the University of Sydney generative AI guide for researchers.

Australian Government Support Statement

This research was supported by an Australian Government Research Training (RTP) stipend Scholarship.

Acknowledgements

A PhD may begin with curiosity, but it is only completed through the generosity and support of others. The following work reflects not just my efforts, but the kindness and brilliance of those who have guided me throughout.

To my supervisors Professor Steven Wise and Dr Richard Tan. Steve, thank you for guiding me through my science journey, instilling in me that a science is not just about collecting data, but about using data to tell a story. And to Rich, thank you for teaching me the ways of "beast mode". I entered this lab naively thinking I knew what hard work was, but to see you in action when the going got tough inspired me to unlock my own inner beast mode both in and out of the lab, and for that I am forever thankful.

To my other colleagues, past and present, Chien, Alex, Kieran, Tim, Shereen, Joy, Monica, Miguel and Eric. I am deeply grateful for the daily support, advice and camaraderie you have all provided over the years. Chien, thank you for the patience and care you showed in teaching me animal surgeries and countless other lab skills. Your passion and expertise proved that with the right teacher, anyone can learn even the most challenging techniques. Alex, since joining this group you have given me a fresh light in the lab. Embodying the "power of friendship" model, you were always willing to lend a hand when I needed it. In the words of Isaac Newton, "If I have seen further, it is by standing on the shoulders of Giants". You are that Giant.

To the staff at Sydney microscopy, in particular Dr Ying Ying Su and Dr Errin Johnson. I would be a mere mortal with macroscopic vision if it wasn't for the training, support and expertise you have both provided me. The beautiful images in this thesis would not exist without your help.

Finally, to my family. I am forever grateful for your continuous support and always encouraging me to pursue what I love. Thank you for coming on this journey with me.

Author Attribution Statement

The following publication resulted directly from work conducted during my Doctoral candidature. Chapter 3 of this thesis includes verbatim the text of the publication. I designed the study, acquired and analysed the data, and wrote the drafts of the manuscript.

> **Grant AJ**, Yang N, Moore MJ, Lam YT, Michael PL, Chan AH, Santos M, Rnjak-Kovacina J, Tan RP, Wise SG, Selective NLRP3 Inflammasome Inhibitor MCC950 Suppresses Inflammation and Facilitates Healing in Vascular Materials. *Advanced Science.* 2023, 10, 2300521.

The following manuscripts resulting directly from work conducted during my Doctoral candidature are currently under review. These correspond to chapters 2 and 5, respectively. In both cases, I designed the study, acquired and analysed the data, and wrote the drafts of the manuscript.

> **Grant AJ,** Tan RP, Wise SG, Engineering Anti-inflammatory Drug Strategies for Cardiovascular Devices. *Trends in Biotechnology.* Submitted.

> **Grant AJ**, Chan AH, Xu Xs, Kieran Lau, Mitchell TC, Giaretta JE, Naficy S, Ng MKC, Wise SG and Tan RP, Plasma Polymerised Nanoparticle Coatings for Simple Biofunctional Drug Presentation on Bioprosthetic Heart Valves. *Advanced Functional Materials.* Submitted.

The following publications resulted from collaborative work conducted throughout my Doctoral candidature, but the contents are not included in this thesis:

> Michael PL, Lam YT, Mitchel TC, Santos M, Chan HP, Liu X, **Grant AJ**, Moore MJ, Fletcher DF, Tan RP, Wise SG. Harnessing Physiological Shear Stress in a Perfusion

Bioreactor for Enhanced Endothelialization of Small-Diameter Vascular Grafts. *Advanced NanoBiomed Research.* 2025, 5, 2500025

Chan HP, Xu XS, Chin IL, **Grant AJ**, Lau K, Hu Y, Michael PL, Lam YT, Wise SG, Tan RP, Dapansutrile OLT1177 suppresses foreign body response inflammation while preserving vascularisation of implanted materials. *Journal of Materials Chemistry B.* 2024, 12, 7334-7347.

Chan AH, Moore MJ, **Grant AJ**, Lam YT, Darnell MV, Michael PL, Wise SG, Tan RP, Selective Immunosuppression Targeting the NLRP3 Inflammasome Mitigates the Foreign Body Response to Implanted Biomaterials While Preserving Angiogenesis. *Advanced Healthcare Materials.* 2023, 12, 2301571.

Tan RP, Hung JC, Chan HP, **Grant AJ**, Moore MJ, Lam YT, Michael PL, Wise SG, Highly reproducible rat arterial injury model of neointimal hyperplasia. *PLoS ONE.* 2023, 18(8): e0290342.

Lee BSL, Yang N, Santos M, Moore MJ, **Grant AJ**, Jang J-H, et al. Truncated vascular endothelial cadherin enhances rapid endothelialization of small diameter synthetic vascular grafts. Materials Today Advances (2022) 14, 100222.

The following provisional patent application directly relates to intellectual property developed in chapter 5 of this thesis:

Tan RP, Wise SG, **Grant AJ**, “Plasma nanoparticle functionalisation of biomedical implants.” Application PRV/AU2025/511254. 1 June 2025

As per the authorship attribution statements above, this thesis only contains published material where I hold substantial authorship.

Angus J. Grant

As supervisor for the candidature upon which this thesis is based, I can confirm that the authorship attribution statements above are correct.

Professor Steven G. Wise

Conference presentations

I presented the contents of this thesis at the following conference presentations:

Grant AJ, Tan RP, Wise SG. Using the selective anti-inflammatory MCC950 for drug-eluting devices in vascular disease. ASBTE Annual Conference, Christchurch, New Zealand, April 13, 2023.

Grant AJ, Chan HP, Tan RP, Wise SG. Selective inhibition of the NLRP3 inflammasome suppresses inflammation and facilitates healing in vascular materials. World biomaterials conference, Daegu, Korea, May 30, 2024.

Abstract

Cardiovascular devices such as stents, balloons and artificial heart valves are foundational in the treatment of cardiovascular diseases, yet their long-term performance is limited by local inflammatory responses. Depending on the device and its location within the vasculature, these responses can manifest in distinct forms of maladaptive tissue remodelling including fibrosis, neointimal hyperplasia, and calcification. Contemporary devices mitigate downstream consequences of this response by eluting anti-proliferative or cytotoxic drugs, but they do not address the underlying inflammation nor actively promote healing around the device, resulting in poor durability. Although inflammation has long been considered a central driver of device failure, it has remained a challenging therapeutic target due to off-target risks associated with systemic immunosuppression. This thesis explored strategies to overcome this challenge by combining selective immunomodulation as a new drug strategy with advanced localised delivery platforms to enhance cardiovascular device longevity.

The first component of this thesis evaluated MCC950, a selective NLRP3 inflammasome inhibitor, as an alternative drug-elution agent for vascular materials. *In vitro* studies demonstrated its ability to reduce inflammatory cytokine secretion without cytotoxic effects, while also reducing clot weight and fibrin deposition through inhibition of platelet-driven inflammation. *In vivo*, MCC950 promoted functional endothelialisation and sustained suppression of neointimal hyperplasia, outperforming current commercial agents and highlighting that selective inhibition of inflammation can both reduce restenosis and promote vascular healing. These findings provide the first evidence for MCC950 as a targeted anti-inflammatory drug-elution strategy for vascular devices.

The second component focused on developing a delivery platform to translate these benefits to other vascular settings. Plasma polymerised nanoparticles (PPN) were characterised as a novel nanocarrier, showing predictable biodistribution, clearance through normal physiological

routes, and no off-target accumulation. PPN enabled simple, one-step conjugation of diverse anti-inflammatory agents, preserving the activity of both MCC950 and IL-10. *In vivo*, PPN improved arterial retention of cargo leading to enhanced therapeutic effects of MCC950 and IL10, reducing neointimal hyperplasia and promoting endothelial repair. These results highlight the potential of PPN to extend the therapeutic potential of selective immunomodulation beyond conventional drug-eluting devices.

Finally, this thesis applied PPN technology to bioprosthetic heart valves through a novel coating strategy. A cysteine pre-treatment enabled PPN binding to glutaraldehyde-fixed pericardium while reducing residual aldehydes and enhancing cell compatibility with no impairment of mechanical properties. PPN coatings enabled rapid immobilisation of diverse therapeutics including apixaban, MCC950, and phytic acid, each addressing key pathways of valve failure including thrombosis, inflammation, and calcification, respectively. Importantly, PPN coatings preserved the hydrodynamic performance of a commercial bioprosthetic valve, supporting their scalability and clinical feasibility. Together, these findings establish PPN coatings as a new platform for actively engaging with the biology surrounding bioprosthetic valves to improve their long-term durability.

Collectively, this work demonstrates that pairing selective immunomodulatory drugs with versatile PPN-based delivery may offer new pathways to reduce inflammation-driven failure and pave the way toward more durable cardiovascular devices.

Table of Contents

List of Figures

List of Abbreviations

ANOVA	Analysis of Variance
APX	Apixaban
AS	Aortic stenosis
ATP	Adenosine triphosphate
BBB	Blood brain barrier
BMS	Bare-metal stent
BSA	Bovine serum albumin
CAD	Coronary artery disease
CLTI	Critical limb threatening ischemia
CT	Compute tomography
CVD	Cardiovascular disease
DCB	Drug-coated balloon
DES	Drug-eluting stent
DFO	Desferrioxamine
DTPA	Diethylenetriaminepentaacetic acid
EC	Endothelial cell
ECM	Extracellular matrix
EDC	N-(3-dimethylaminopropyl)-N′-ethylcarbodiimide
EDS	Energy dispersive X-ray spectroscopy
EV	Extracellular vesicle
FDA	U.S. Food and Drug Administration
FTIR	Fourier transform infra-red spectroscopy
HAC	Hydroxyapatite crystal
HEPES	4-(2-hydroxyethyl)-1-piperazineethanesulfonic acid

H&E	Haematoxylin and eosin
ICAM-1	Intracellular cell adhesion molecule 1
ICAM-2	Intracellular cell adhesion molecule 2
IL-1β	Interleukin-1β
IL-6	Interleukin-6
IL-18	Interleukin-18
iTLC	Instant thin-layer chromatography
IVIS	*In vivo* imaging system
LbL	Layer-by-layer
LDL-C	Low-density lipoprotein cholesterol
LPS	Lipopolysaccharide
MMP	Matrix metalloproteinase
mTOR	Mammalian target of rapamycin
NFW	Nuclease free water
NHS	N-hydroxysuccinimide
NO	Nitric oxide
PAD	Peripheral artery disease
PB	Phosphate buffer
PBMS	Poly(butyl methacrylate)
PBS	Phosphate buffer saline
PEG	Poly(ethylene glycol)
PET	Positron Emission Tomography
PEVA	Polyethylene-vinyl acetate
PLGA	Poly(lactic-co-glycolic acid)
PLLA	Poly-l-lactic acid

PMA	Phorbol 12-myristate 13-acetate
PTA	Percutaneous transluminal angioplasty
ROS	Reactive oxygen species
rpm	Revolutions per minute
SAVR	Surgical aortic valve replacement
SEM	Scanning electron microscopy
SIBS	Poly(styrene-isobutylene-styrene)
SMC	Smooth muscle cell
SVD	Structural valve degeneration
TAC	Time activity curve
TAVR	Transcatheter aortic valve replacement
TEM	Transmission electron microscopy
TGF-β1	Transforming growth factor-beta-1
TNF-α	Tumour necrosis factor alpha
VCAM-1	Vascular cell adhesion molecule 1
VEGF	Vascular endothelial growth factor
VOI	3D region of interest
VSMC	Vascular smooth muscle cell
vWF	von Willebrand Factor

Chapter 1

General Introduction

1. General introduction

1.1. The cardiovascular system

1.1.1. Arteries

Arteries are blood vessels that transport blood away from the heart to tissues and organs. Arteries are responsible for the transportation of oxygen (excluding the pulmonary artery), nutrients, waste products, electrolytes and hormones to maintain cellular homeostasis [1]. They have specific structures and properties that allow them to withstand the pressure produced by the heart and to ensure constant blood flow around the body. Specifically, arteries comprise of three distinct layers arranged concentrically: the tunica intima (innermost layer), tunica media (middle layer), and tunica adventitia (outermost layer) (Figure 1.1) [2]. It should be noted that the described structures in this chapter are those found in homo sapiens and not other primates.

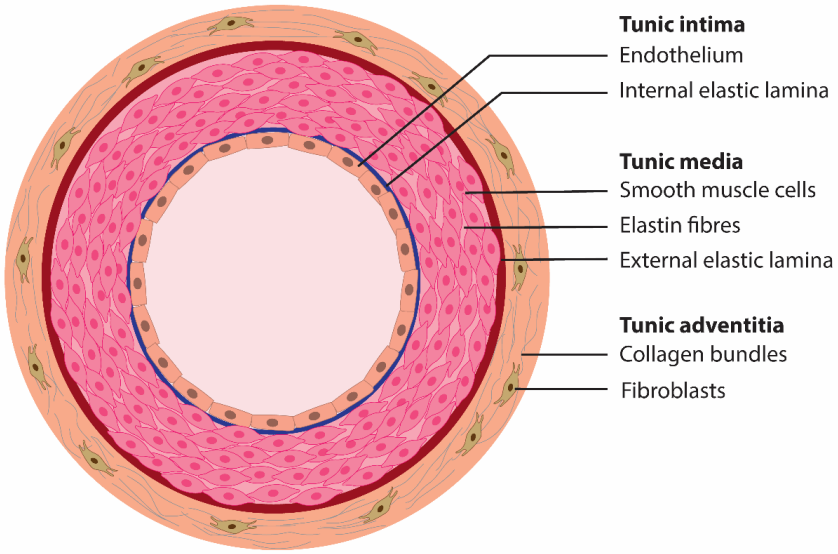

Figure 1.1: Anatomy of an artery
Schematic showing that arteries comprise of three distinct layers including the tunica intima, tunica media, and tunica adventitia. The tunica intima consists of the endothelium and the internal elastic lamina. The tunica media largely consists of smooth muscle cells, elastin fibres and the external elastic lamina. The tunica adventitia consists of collagen networks and resident fibroblasts.

The tunica intima consists of a monolayer of endothelial cells (EC) anchored to a continuous basal membrane, and the internal elastic lamina which separates the tunica intima from the tunica media. The endothelium consists of the ECs and the basal membrane and acts as a cellular barrier between the blood passing through the lumen and the underlying tissues [3]. The ECs which make up the endothelium are tightly connected via tight junctions and adherens junctions to form an aligned monolayer. This aligned monolayer prevents the adherence and aggregation of platelets, creating a non-thrombogenic surface for the blood to flow over. ECs additionally prevent blood coagulation by expressing anti-thrombotic molecules such as thrombomodulin and prostacyclin [4]. Thrombomodulin is a glycoprotein that binds to thrombin and inhibits its procoagulant functions, whereas prostacyclin is a prostaglandin which inhibits platelet aggregation. These molecules are major components of the endothelial glycocalyx, a network of various membrane bound proteoglycans, glycosaminoglycans, and glycoproteins that present on the luminal side of the endothelium [5]. By producing and secreting other signalling molecules, ECs are also capable of regulating vascular homeostasis and inflammation. For instance, ECs can regulate local blood pressure and vascular tone by secreting vasoactive factors including nitric oxide (vasodilator) and endothelin-1 (vasoconstrictor), which relax or constrict the smooth muscle cells (SMCs) in the tunic media, respectively [3]. In regards to inflammation, ECs can control the adhesion and transmigration of immune cells circulating in the blood into the underlying tissue by expressing adhesion molecules including intramolecular cell adhesion molecule 1 and 2 (ICAM-1, 2) and vascular cell adhesion molecule 1 (VCAM-1) in response to inflammatory stimulus [3].

The tunica media consists of smooth muscle cells layered throughout a collagen and elastin rich extracellular matrix (ECM). As mentioned above, SMCs respond to the molecular signals produced by endothelial cells, causing them to either relax or contract, resulting in vasodilation

or vasoconstriction, respectively . Elastin is an ECM protein that is organised into elastic fibres and gives arteries their ability to expand and recoil as blood pressure oscillates [6].

The tunica adventitia plays a crucial role in maintaining structural integrity of arteries. Similar to the tunica media, it mainly consists of collagen and elastin. However, the tunica adventitia has a significantly higher collagen content [7]. This collagen is organised into thick, dense bundles which provide the artery with most of its strength. The adventitia also has an active role in arterial healing and inflammation, owing to the various types of cells residing in this layer including fibroblasts, adipocytes, leukocytes, and a number of progenitor cells [8].

1.1.2. The heart

The heart is a muscular pump which receives and displaces blood throughout the vasculature [9]. It is located in the thoracic cavity enclosed in a protective sac called the pericardium [10]. The heart is divided into four main champers: the right atrium (upper right section), left atrium (upper left section), right ventricle (lower right section), and the left ventricle (lower left section). Deoxygenated blood from the body flows into the right atrium and then into the right ventricle through the tricuspid valves [11]. Valves are an essential component of the heart as they ensure unidirectional flow of blood, preventing backflow during ventricular contractions [9]. When the right ventricle contracts, it sends blood into the pulmonary artery (through the pulmonary valve) and into the lungs where carbon dioxide in the blood is exchanged or oxygen. The now oxygenated blood returns to the left atrium via the pulmonary veins and flows into the left ventricle through the mitral valve. Here, the left ventricle contracts, pumping oxygenated blood into the aorta through the aortic valve and to the rest of the body.

1.1.3. The aortic valve

The aortic valve acts as a one-way doorway that regulates blood flow from the left ventricle into systemic circulation. It is considered clinically the most important valve due to its pivotal role in maintaining unidirectional blood flow, preventing regurgitation and ensuring efficient cardiac output [12]. The aortic valve is a tricuspid valve composed of three semilunar leaflet cusps which attach to the aortic root. This site of attachment is known as the annulus ring and gives structural support to the valve. The space directly behind each leaflet, between the leaflets and the aortic wall, is called the Sinus of Valsalva and plays a critical role in facilitating smooth valve closure by creating swirling blood flow, helping the leaflets close evenly without excessive stress [12]. Each leaflet is comprised of three distinct layers: fibrosa which faces the aorta; spongiosa which is the middle layer; and the ventricularis which faces the ventricle (Figure 1.2). The fibrosa is rich in type 1 collagen arranged circumferentially in parallel bundles giving the leaflets their tensile strength. The spongiosa is primarily made up of glycosaminoglycans that act as shock absorbers, providing the flexibility and deformability function of the leaflets. The ventricularis contains mostly elastin fibres arranged along the radial direction which facilitates leaflet motion and recoil during the cardiac cycle [13].

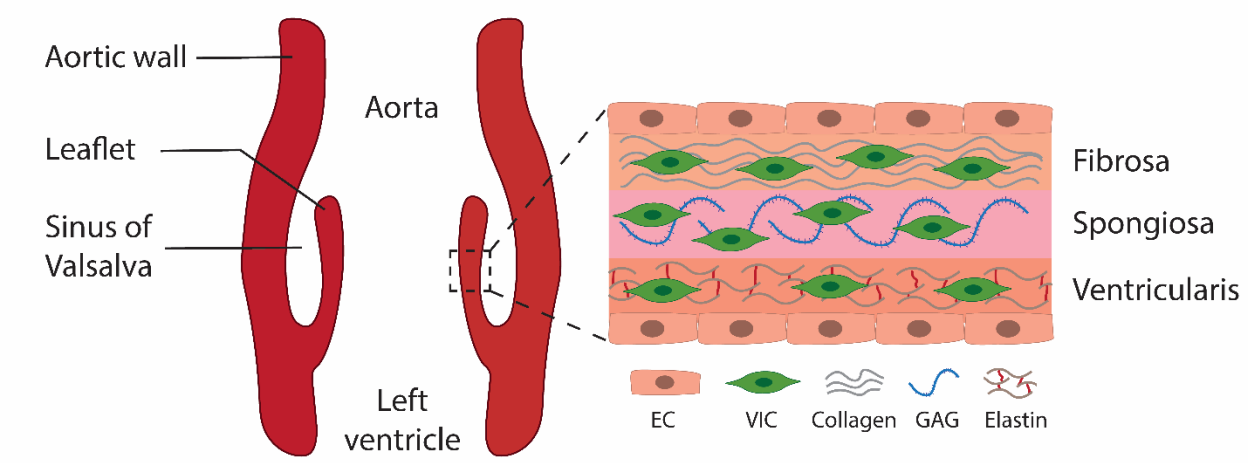

Figure 1.2: Aortic valve anatomy and cellular composition
Schematic showing how the aortic valve forms the doorway between the left ventricle and the aorta. Each leaflet consists of three main layers: the fibrosa (aortic side), spongiosa (middle) and ventricularis (ventricular side). Endothelial cells (EC) line the leaflets. Valvular interstitial cells (VIC) are found in each layer of the valve. Collagen is predominately found in the fibrosa layer, glycosaminoglycans (GAG) are found in the spongiosa, and elastin fibres make up the ventricularis.

The cellular composition of the aortic valve is essential to its functionality. It consists of two primary cell types: ECs and valve interstitial cells. ECs line the leaflets along the fibrosa and ventricularis. They perform the same function as discussed previously for arteries, regulating immune responses, preventing thrombosis and maintaining homeostasis. However, they show some genetic differences to arterial ECs, most important of which is their higher propensity to undergo endothelial to mesenchymal transition, making them a more dynamic population [14]. Valve interstitial cells make up the majority of the valve and are responsible for producing and regulating the ECM, providing mechanical strength to the valve [15]. Even more so than valve ECs, they exist in a dynamic state, capable of different phenotypes depending on environmental conditions, particularly hemodynamic factors and mechanical stresses. This makes valve interstitial cells a key factor in pathologies related to the aortic valve.

The aortic valve operates in a complex hemodynamic environment, opening and closing with each cardiac cycle in response to pressure differentials between the left ventricle and the aorta.

During systole, when ventricular pressure exceeds aortic pressure, the valve opens fully to allow rapid ejection of blood into the aorta. This phase is characterised by high-velocity, laminar flow through the valve, with peak velocities ranging between 1.0 to 1.7 m/s in normal physiological conditions [16]. Peak velocities are reached when the leaflets are fully open. When this occurs, the pressure between the ventricle and the aorta is minimal. As the heart relaxes, the pressure in the ventricle drops, lowering to diastolic pressure of the aorta causing the valves to close [17]. Due to the high-pressure gradient and the anatomic design of the leaflet cusps, the valve closes efficiently and rapidly, with very little retrograde blood flow.

1.2. Cardiovascular diseases

1.2.1. Vascular disease

Cardiovascular diseases (CVD) are disorders of the heart and circulatory system. They are the leading cause of death globally, claiming more lives annually than all forms of cancer and chronic lower respiratory disease combined, the second and third leading causes of death respectively [18]. One of the major hallmarks of CVD is atherosclerosis, the build-up of plaque inside arterial vessels [19]. This plaque is made up of mostly fatty substances, cholesterol and cellular waste products which initially develop in the vessel wall and underlying smooth muscle. Over time, the plaque grows along with the build-up of fibrous tissues and the proliferation of surrounding smooth muscle, creating an obstruction inside the arteries that reduces blood flow to the organs (known as vessel occlusion) [20]. This can eventually lead to plaque rupture and clotting, resulting in complete obstruction of blood flow causing severe vascular complications including death.

Depending on where plaque develops, atherosclerosis can manifest as different types of CVD. Coronary artery disease (CAD) arises from plaque development in the coronary arteries and can cause heart failure. CAD is the leading cause of death globally. In 2022, there were 315 million prevalent cases of CAD globally [21]. In Australia alone, CAD was the underlying cause of 18,600 deaths, attributing to 9.8% of all deaths [22]. Alternatively, peripheral artery disease (PAD) is caused by atherosclerotic development in the lower limbs which can lead to claudication (leg pain when walking), numbness, and in severe cases, limb amputation [23]. In Australia, PAD was the cause of 1,900 deaths in 2022, equating to 1% of all deaths [22]. In the U.S., critical limb threatening ischemia (CLTI), the most severe presentation of PAD, leads to approximately 200,000 limb amputations each year, significantly impacting patient quality of life [24].

For over 50 years, high levels of low-density lipoprotein cholesterol (LDL-C) in arterial vessels has been considered the major cause of atherosclerosis. These lipoproteins are able to migrate across the endothelium into the tunic intima where they accumulate and become oxidised, initiating a pro-inflammatory cascade. However, substantial evidence suggests that factors other than lipoproteins can also initiate this pro-inflammatory vascular environment and drive atherogenesis [25]. Inflammatory biomarkers including high-sensitivity C-reactive protein and interleukin-6 (IL-6) have a strong association with increased risks of atherosclerosis, independent of cholesterol levels [26]. Hence, despite being once considered “a bland lipid storage disease”, atherosclerosis is now understood to be fundamentally an inflammatory disease.

The atherosclerotic inflammatory cascade is initiated by endothelial injury caused by cardiovascular risk factors including hypertension, smoking and diabetes. These conditions can produce free radicals that disrupt the balance of nitric oxide (NO) within the vasculature, damaging the endothelium [27]. Loss of biological activity and NO production in the endothelium leaves it overly permeable, allowing toxins to pass into the vascular wall leading to increased expression of proinflammatory cytokines and chemotactic factors [28]. A prominent cytokine with growing clinical importance is interleukin-1β (IL-1β). Its significance is evident in several population studies which showed genetic polymorphisms in IL-1β to be associated with premature onset of atherosclerosis and acute myocardial infarction [29]. IL-1β is a pro-inflammatory mediator which, upon activation, amplifies the inflammatory response characterised by increased SMC proliferation, increased cytokine and chemokine production in leukocytes, and recruitment of monocytes and lymphocytes into the vascular wall through the upregulation of cell adhesion molecules including ICAM-1 and VCAM-1 [30]. Of these adhesion molecules, VCAM-1 is most notable as it binds monocytes to the endothelium. Once adherent to the endothelial layer, chemoattractant cytokines (chemokines) cause monocyte migration between intact endothelial cells into the arterial intima where they subsequently differentiate into macrophages. This accumulation of inflammatory cells in arterial vessels and their invasion into the intima is a key step in nascent atherosclerotic plaque formation [31].

Macrophages are key effector cells in inflammation [32]. They ingest excess LDL-C deposited in the intima leading to foam cell formation, large constituents of atherosclerotic plaques and the major component of the first grossly visible atherosclerotic lesion known as fatty streaks [33]. These lipid-laded macrophages release more proinflammatory cytokines, propagating a vicious cycle of inflammation in the lesion site resulting in plaque growth. SMCs also play a key role in plaque progression [34]. For instance, cytokines (including IL-1β) increase SMC

proliferation and migration from the tunica media into the intima. SMCs in turn enhance the rate of ECM synthesis which can entrap lipoproteins and promote further lipid accumulation at the lesion site. During repeated cycles of inflammation, macrophages and SMCs begin to die and contribute to the formation of an advanced complicated stable atherosclerotic lesion characterised by a fibrous cap of SMCs overlaying a necrotic core, mostly containing dead macrophages [35]. As the lesion increases in size, it intrudes into the lumen and restricts blood flow to the organs. If unabated, the plaque becomes unstable and ruptures, resulting in severe clinical manifestations including thrombosis, heart attack, stroke or aneurysm [20].

1.2.2. Valvular disease

Valvular heart disease is another leading cause of CVD morbidity and mortality worldwide. It involves dysfunction of the valves which otherwise ensure unidirectional flow of blood through the heart. Stenosis is the primary driver of valvular disease, characterised by valve leaflet thickening and narrowing. In healthy individuals, there is a perfect match between valve leaflet thickness and the force the heart generates to open them. However, as stenosis develops, the leaflets thickens and the valve narrows, reducing blood flow. To compensate, the heart must work harder to supply blood to necessary organs around the body. Overtime, the heart can tire, leading to heart failure.

While stenosis of all heart valves can occur, aortic stenosis is the most common [36]. Aortic stenosis (AS) can arise from congenital abnormalities, rheumatic heart disease, and/or can develop due to calcification over time. With prevalence dramatically increasing in an aging population, approximately 7% of individuals over 65 suffer from AS, which is expected to increase by 25% by 2027. In Australia alone, there is an estimated minimum of 97,000

Australians living with severe AS [37]. Furthermore, the burden of moderate to severe AS is projected to impact 266,000 Australians in 2051 [38]. In severe cases, AS boasts a 30%-50% mortality rate at only 12 months after symptom onset [39]. These symptoms may include feelings of fatigue, chest pain and shortness of breath, particularly during exercise.

While rheumatic fever is a serious condition that can lead to AS and is largely considered the most common cause in developing countries, inflammation is becoming increasingly implicated in the pathogenesis of AS [40]. Increased systemic C-reactive protein concentrations as well as inflammatory macrophage activity has been shown to correlate with AS severity [41, 42]. As such, the pathogenesis of AS has many similarities to that of atherosclerosis. EC damage for example is believed to be the initiating event which begins the inflammatory cascade leading to AS [43]. Endothelial damage is most commonly caused by increased mechanical stress on the valve and changes to shear stress. This leads to early lesion development, characterised by subendothelial thickening on the aortic side of the leaflets [44]. It has been shown that these lesions primarily develop at the base of the leaflet (the flexion area of the cusps near their attachment to the aortic root) where ECs are under oscillatory shear and high mechanical stress during systole, and high pressure during diastole [45]. Interestingly, the more extreme mechanical forces experienced in patients born with a bicuspid aortic valve correlates with a significantly higher incidence and, on average, 20 years earlier development of AS compared to patients with tricuspid valves [46]. This illustrates the significant role mechanical forces play in the pathogenesis of AS.

Damage to endothelial cells reduces their ability to control the infiltration of proteins and cells into the underlying fibrosa. In particular, lipoproteins including low-density lipoprotein and

lipoprotein(a) migrate across the endothelium and accumulate in the subendothelial layer where they undergo oxidative modification [47]. Again, similar to that of atherogenesis, this propagates an intense inflammatory cascade, initially characterised by infiltration of T lymphocytes and monocytes into the subendothelial space. Here, the monocytes differentiate into macrophages which exacerbate the inflammatory progression by secreting pro-inflammatory and pro-fibrotic cytokines including transforming growth factor-beta-1 (TGF-β1), tumour necrosis factor alpha (TNF-α), and IL-1β [44]. Circulating pro-inflammatory and pro-fibrotic cytokines additionally drive the differentiation of valve interstitial cells (the majority of which are fibroblasts) into myofibroblast- and osteoblast-like cells. Myofibroblasts secrete large amounts of collagen, matric metalloproteinases (MMPs), fibronectin and laminin, all of which help to form a disorganised layering of ECM on the valve surface. This accumulation of fibrous tissue (known as fibrosis) leads to thickening of the leaflets and increased stiffness, thereby disrupting the proper mechanical function of the valve, further contributing to the vicious cycle. One study reported that under pathological conditions, the percentage of myofibroblasts in valve leaflets increases from 5% (percentage under normal conditions) to 30%, and was closely associated with loss of valve structural integrity [48].

As the vicious cycle of inflammation and fibrosis continues over many years, calcification begins to occur. As the degree of valvular calcification increases, so does the severity of valve stenosis and likelihood of adverse events. In the early stages of disease progression, ECs and valve interstitial cells undergo cell apoptosis in response to high mechanical stress, inflammation and/or oxidative damage, releasing apoptotic bodies and promoting release of extracellular vesicles (EVs) from macrophages [49]. These structures serve as nucleation sites for calcium phosphate deposition, leading to hydroxyapatite crystal formation. This process is amplified over time by inflammatory signalling which promotes the differentiation of valve

interstitial cells into osteoblast-like cells, key drivers of mineralisation. Despite not being real osteoblasts, these osteoblast-like cells display similar mineral resorption capabilities and begin to coordinate calcification within the leaflets, a process similar to that of new bone formation [49]. This progression leads to increased valve stiffness and functional impairment, contributing to the pathophysiology of aortic stenosis.

1.3. Endovascular intervention: Overview of existing technologies

Endovascular intervention refers to a minimally invasive procedure that is performed within the vasculature without the need for open surgery. It has become the gold standard for the majority of occlusive cardiovascular diseases due to its minimal invasiveness translating to more favourable patient outcomes including faster recovery times, decreased risk of major surgical complications and often better disease treatment compared to traditional open surgical procedures [50, 51]. Endovascular intervention has revolutionised treatment for many cardiovascular related diseases, originating first for treatment of vascular disease and later expanding to valves. The two mainstay endovascular treatment options for arterial disease are currently percutaneous transluminal angioplasty (PTA) and stenting. Despite the advancements in the devices used during these procedures, the fundamental percutaneous transluminal nature of the operation has stayed consistent since it was first performed in 1977 [52]. For other, more complicated cardiovascular diseases such as valvular disease, it wasn't until this century before endovascular intervention started to be performed as a treatment option. Dr Alain Cribier performed the first transcatheter aortic valve replacement (TAVR) in 2002, establishing a new frontier in the treatment of valvular disease [53].

1.3.1. Percutaneous transluminal angioplasty

PTA, also known as balloon angioplasty, revolutionised the treatment of vascular disease by providing a minimally invasive alternative to surgical revascularisation (Figure 1.3). Before its introduction by Andreas Grüntzig in the late 1977, patients with symptomatic arterial disease often required open surgical procedures such as endarterectomy or bypass grafting, both associated with prolonged hospitalisation and limited applicability in high-risk populations. PTA dramatically changed this landscape by enabling revascularisation through a percutaneous approach, reducing procedural risk, recovery time, and expanding the pool of patients eligible for intervention [54].

In contrast to open surgery techniques which require general anaesthesia, PTA is generally performed under local anaesthesia with or without mild sedation. Access to the vasculature is provided by a small incision often in the femoral or radial artery. A thin flexible guidewire is inserted through the access site and navigated through to the lesion site under fluoroscopic guidance. The balloon catheter is then advanced over the guidewire to the site of blockage. Balloons are available in a wide range of diameters, and it is generally considered that the diameter of the inflated balloon should approximate or only slightly exceed the diameter of the normal arterial segment [55]. Correct sizing of the balloon is a critical component of the procedure. Oversizing of the balloon risks vessel rupture or dissection, while under sizing can result in residual stenosis [55].

Once positioned, the balloon is inflated to high pressures, often between 8-12 atm for coronary applications and up to 20 atm for calcified or peripheral lesions, using a radiopaque contrast solution to assist with visibility. Inflation times are usually short, ranging from 30-60 seconds per inflation cycle [56]. Longer inflation times greater than 60 seconds have been associated with lower risk of residual stenosis and reduced need for adjunctive procedures in both

coronary and peripheral vessels, however long-term data is heterogeneous and inconsistently reported, and remains an option only for heavily calcified or resistant lesions [57]. The balloon compresses atherosclerotic plaque against the arterial wall and stretches the vessel, thereby enlarging the lumen and restoring blood flow. Multiple inflation-deflation cycles are often required depending on the lesion type [58].

A major advantage of PTA compared with open surgical approaches is the reduced invasiveness of the procedure. Because it is performed percutaneously, patients generally require only short periods of monitoring, with many discharged within 24-48 hours. Same-day discharge is also possible for some low-risk patients, having been shown to have no increased risk of major adverse events compared to overnight stay [59]. Complications such as access site bleeding, vessel dissection, or acute thrombosis can occur, but advances in catheter and procedural design have markedly reduced rates of major adverse events. Recovery is rapid, with most patients able to return to normal activities within a week [60]. This is in contrast to bypass grafting which requires 6-12 weeks of recovery before exercise is recommended [61].

In summary, PTA transformed vascular intervention by offering a safe, effective, and minimally invasive treatment for occlusive vascular disease. The technical refinements in balloon design, sizing strategies, and inflation protocols, coupled with shorter recovery times and avoidance of general anaesthesia, highlight why PTA remains the fundamental procedure on which subsequent innovations such as stent implantation and TAVR have been built. However, plain balloon angioplasty on its own is now rarely practiced, as high rates of restenosis and elastic recoil limited its long-term durability and frequently led to acute vessel failure. These

shortcomings ultimately drove the development of metallic scaffolds, ushering in the stent era and establishing a new standard for percutaneous vascular intervention.

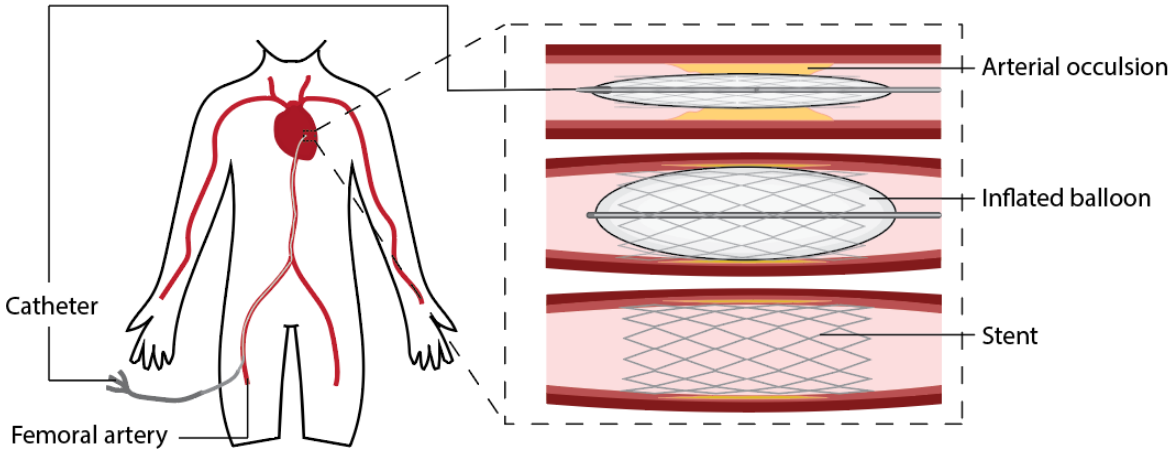

Figure 1.3 Endovascular intervention
Schematic showing how a balloon catheter, with or without a crimped stent depending on the procedure, is inserted through a small incision in the femoral artery (common access site) and fed through the vasculature to the site of occlusion. Here, the balloon is inflated, compressing the plaque against the arterial wall and reopening the artery to blood flow. If the procedure involves stenting, a stent is deployed after balloon inflation and remains in position post-surgery.

1.3.2. Stenting

After the initial work done by Grüntzig in PTA, it was apparent that angioplasty by itself was unable to maintain luminal patency in the long-term. One major contributing factor to this was elastic recoil in the artery. As outlined in section 1.1.1 of this thesis, arteries contain a layer of elastic tissue known as the elastic lamina which helps them accommodate the high pressure of blood flow through the body. Immediately after angioplasty, the artery therefore can recoil inwards, leading to a rebound occlusion of the artery [62]. This led to the invention of the stent, a metallic tubular scaffold that can be implanted into the artery and kept in position, thereby maintaining constant outward pressure on the vascular wall, preventing elastic recoil and reducing likelihood of vessel re-narrowing. The first reported coronary stent implantation in a human coronary artery was performed by Sigwart and Puel in 1986, however its clinical utility

was limited due to its poor delivery system and was withdrawn from market in 1991 [63]. It was the Palmaz-Schatz stent (Johnson & Johnson), developed in 1987, the first balloon-expandable, stainless steel stent that began the transition away from balloon angioplasty to stenting throughout the 1990s and into the early 2000s [64].

There are currently two main types of stents, balloon expandable (like the Palmaz-Schatz) or self-expanding. Both stent types are implanted at the site of blockage in a surgery identical to PTA. In the case of balloon-expandable stents, these stents are crimped over the deflated angioplasty balloon inside the catheter and then, upon balloon inflation, deployed. They are primarily made of stainless steel or cobalt-chromium and because they are being expanded at high pressure assisted by the balloon, provide greater radial pressure to the vascular wall [65]. As such, balloon-expandable stents are the preferred choice for CAD, where all clinically used stents are balloon-expandable, and in other large or heavily calcified vessels [66, 67]. However, due to the rigidity of the alloys they use, they are more susceptible to permanent deformation under external forces, making them less suitable for locations subject to repetitive movement or compression. In contrast, self-expanding stents are made from shape-memory alloys, such as nitinol (nickel-titanium), which allow them to expand automatically upon deployment without the need of an angioplasty balloon. These stents are compressed within a delivery sheath and expand to their predetermined diameter once released. Their flexibility and ability to conform to vessel movement make them ideal for treating PAD, particularly in the femoropopliteal arteries located in the leg, where vessels are subject to extensive motion, bending, and external compression [68]. One study showed that between balloon-expandable and self-expanding stents, only self-expanding stents were associated with significant improvements in patency rates out to two years in patients with PAD of the femoral arteries [68]. Self-expanding stents can also recover from mild deformation, making them resistant to

fractures in high-mobility areas. However, they generally exert lower radial force compared to balloon-expandable stents, which make them less suitable for heavily calcified lesions [67].

1.3.3. Transcatheter aortic valve replacement

Transcatheter aortic valve replacement (TAVR) is the current gold standard treatment option for patients over the age of 65 with severe AS. It involves minimally invasively replacing a diseased aortic valve with a bioprosthetic valve [69]. Before TAVR, surgical aortic valve replacement (SAVR) was the standard of care for these patients. SAVR requires open-heart surgery, traditionally performed through a median sternotomy characterised by a vertical midline incision and sternal division with a saw, followed by cardiopulmonary bypass and valve excision. Although effective, SAVR is highly invasive and associated with considerable perioperative morbidity, rendering it unsuitable for high-risk patients [70].

To overcome this, Alain Cribier developed the first catheter-based treatment approach for AS in 1985 which involved balloon inflation within the diseased valve to break-up calcified regions, known as balloon aortic valvuloplasty [71]. While this technique provided symptomatic benefit, it demonstrated poor long-term efficacy. This limitation led to the hypothesis that a permanent intravalvular scaffold could achieve more sustained outcomes, echoing the earlier trajectory of vascular stent development for treatment of vascular disease. In 1989, Henning Rud Andersen tested this concept by suturing porcine aortic valves into metal stents and implanting them into the native aortic valves of pigs using a balloon catheter [72]. Although promising, this prototype never reached first-in-human trials.

Building upon this foundation, Cribier subsequently refined the concept by mounting three bovine pericardial leaflets within a stainless-steel balloon-expandable stent. In 2002, he performed the first successful human TAVR procedure using this design, termed the percutaneous heart valve [53]. Despite subsequent refinements in stent architecture, delivery systems, and procedural techniques, the essential principle of a stented frame supporting animal-derived pericardial leaflets still forms the basis of TAVR valves used today.

Similar to balloon angioplasty and stenting, TAVR involves inserting a catheter through the femoral artery (most common access point) and guiding the bioprosthetic replacement valve via the arterial system to the aortic valve. Depending on the valve type, either an angioplasty balloon is inflated to expand the valve into place (balloon-expandable), or the valve will expand on its own when released from the catheter (self-expanding). The replacement bioprosthetic valve pushes aside the native valve leaflets, anchoring itself securely in the aortic annulus (Figure 1.4).

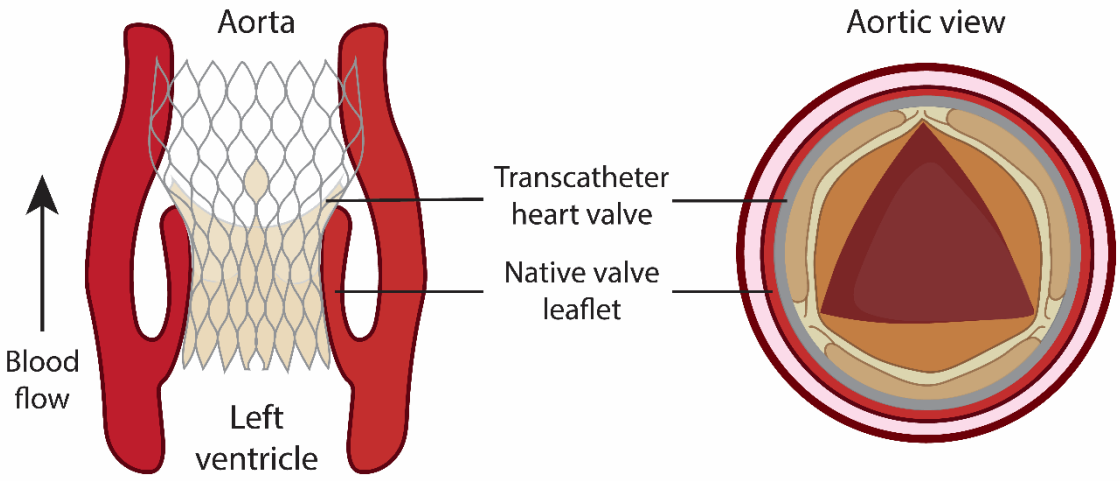

Figure 1.4: Transcatheter aortic valve replacement
Schematic showing how the bioprosthetic transcatheter aortic valve pushes aside the native valve when implanted. Blood flows from the left ventricle to the aorta through the new bioprosthetic valve which contains three flexible leaflets directionally aligned similar to the native valve leaflets. This is a self-expandable transcatheter aortic valve.

Since its introduction in 2002, TAVR has increasingly become the preferred treatment option for AS patients over the age of 65, and in particular those over the age of 80 who are deemed too high risk for SAVR [73]. This can largely be attributed to the minimally invasive nature of the procedure. Patients undergoing SAVR typically spend around 3-4 days in the intensive care unit, with full recovery in 8-12 weeks [74]. This is compared to TAVR where patients are frequently discharged within 24 hours and full recovery occurs within 1-2 weeks [74, 75]. For this reason, TAVR has clear benefits over SAVR. Over the last two decades, clinical trials have progressively evaluated TAVR against SAVR in different patient populations, initially beginning with patients at high surgical risk to most recently evaluating TAVR in low-risk patients.

The CoreValve High-Risk Study was a landmark trial which evaluated TAVR versus SAVR in patients with severe aortic stenosis and who were at increased surgical risk [76]. It showed that TAVR was associated with a significantly higher rate of survival at 1 year compared to SAVR. The authors largely attributed this improvement to the less-invasive nature of TAVR and the more rapid mobilisation and recovery that occurs with this approach. Other studies have shown comparable results between TAVR and SAVR in the short term. For instance, the PARTNER Cohort A study compared TAVR and SAVR in high operative risk patients and showed similar rates of survival after 1-year [77]. These studies led to an update in the 2017 American College of Cardiology/The Society of Thoracic Surgeons (ACC/STS) guidelines which included a recommendation for TAVR for symptomatic patients with severe AS at prohibitive and/or high risk for SAVR [78].

Subsequent trials, including the PARTNER 2 and Surgical Replacement and Transcatheter Aortic Valve Implantation (SURTAVI) trials, assessed the long-term outcomes of TAVR as compared with SAVR in patients with severe aortic stenosis and intermediate surgical risk. These studies concluded that there were no significant differences in major clinical outcomes including the incidence of death or disabling stroke, at 5 years across the two groups [79, 80]. Patients randomised to TAVR in the PARTNER 2 trial received the SAPIEN XT (Edwards Lifescience) valve, a second-generation balloon-expandable valve approved by the FDA to treat severe AS in 2014 [79]. Conversely, SURTAVI randomised patients to TAVR with the self-expandable CoreValve system, receiving either the CoreValve or Evolut R (Medtronic) [80]. In this way, these trials demonstrated the non-inferiority of both types of TAVR valves to SAVR, leading to both the European and Unites States guidelines granting a TAVR recommendation for use in intermediate-risk patients [81].

Following on from these landmark studies, clinical trials including PARTNER 3 and EVOLUT Low Risk evaluated TAVR against SAVR in patients with low surgical risk. These trials both included the use of third generation valves for patients randomised to TAVR. At the 5-year follow-up for both trials, there were no significant differences in death, stroke or rehospitalisation between TAVR and SAVR [82, 83]. The average ages in these trials were also significantly lower than earlier studies discussed above, with the mean age in the PARTNER 3 trial being 73 years and the mean age in the EVOLUT Low Risk trial being 74 years. Taken together, these pivotal studies have led to the most recent ACC/STS guidelines recommending SAVR for patients <65 years of age and with life expectancy of 20 years, SAVR or TAVR for patients 65 to 80 years, and TAVR for those >80 years of age [84]. As a result, new clinical

trials are beginning to be drawn out that evaluate the newest-generation TAVR valves in younger patients, preferably under 65. In this use case, valve durability is a major factor which needs to be considered due to the extended life-expectancy and more-exercise filled lifestyles seen for younger patients.

1.4. Role of inflammation in endovascular device failure

1.4.1. Restenosis

Despite the incorporation of drug-elution technology for stents and balloons, restenosis remains the primary cause of failure for these endovascular interventions [85]. Inflammation plays a central role in the pathophysiology of restenosis [86]. This underlying inflammatory cascade is triggered by balloon dilation (barotrauma) and/or stent placement during endovascular intervention, causing mechanical injury to the vascular wall and damaging the endothelial layer [87]. In a similar manner to atherogenesis, damaged ECs undergo oxidative stress, producing reactive oxygen species (ROS) which upregulate endothelial adhesion molecules, facilitating leukocyte recruitment into the vessel wall. Monocytes and neutrophils can also infiltrate into the tunic intima from the vasa vasorum, a network of blood vessels which run through the tunic adventitia and tunic media. Monocytes can then differentiate into macrophages which release various growth factors and pro-inflammatory cytokines including IL-1β, interleukin-18 (IL-18) and IL-6 which drive further inflammatory cell recruitment and activation, creating a vicious cycle.

The primary cause of the vessel narrowing characteristic to restenosis is the over proliferation of SMCs in the lumen, a phenomenon known as neointima hyperplasia [86]. Under

physiological conditions, contractile SMCs reside in the tunica media with minimal proliferation. However, following vascular injury and secretion of pro-inflammatory cytokines and reduced endothelium-derived inhibitory factors (nitric oxide), SMCs transition into a synthetic phenotype, characterised by increased migration, proliferation, and ECM secretion. In the early stages of restenosis, the synthetic SMCs proliferate mainly within the tunica media. However, resident adventitial macrophages are eventually signalled to migrate into the sub-intimal space where they release MMPs that degrade the existing ECM, facilitating SMC migration past the internal elastic lamina into the tunica intima [88]. Once in the sub-endothelial space, SMCs continue to hyper proliferate and are able to pass through the damaged endothelium into the lumen where they again secrete ECM, forming a stable neointima. As the SMCs continue to proliferate and secrete ECM, the neointima increases in size, narrowing the vessel lumen and ultimately leading to restenosis (Figure 1.5) [86].

Resident adventitial fibroblasts also respond to ROS-mediated oxidative stress and inflammatory cytokines by differentiating into myofibroblasts. These cells contribute to restenosis through increased proliferation, migration, and collagen synthesis [89]. Myofibroblasts play a dual role in restenosis by participating in both neointimal formation and negative remodelling. In the neointima, myofibroblasts deposit ECM and contribute to lesion stability, while in the adventitia, they promote vascular stiffening and chronic constriction. The excessive ECM deposition in the adventitia results in fibrotic thickening, which reduces vessel compliance and luminal diameter, a process known as negative remodelling. Unlike acute elastic recoil, which occurs within minutes, negative remodelling develops gradually over weeks to months and is a key contributor to restenosis following PTA [90]. The contractile properties of myofibroblasts further exacerbate vessel constriction by generating sustained tension within the adventitia, effectively reducing vessel patency over time. Additionally,

crosstalk between myofibroblasts, macrophages, and ECs perpetuates a chronic inflammatory state, further driving maladaptive remodelling and restenosis [91].

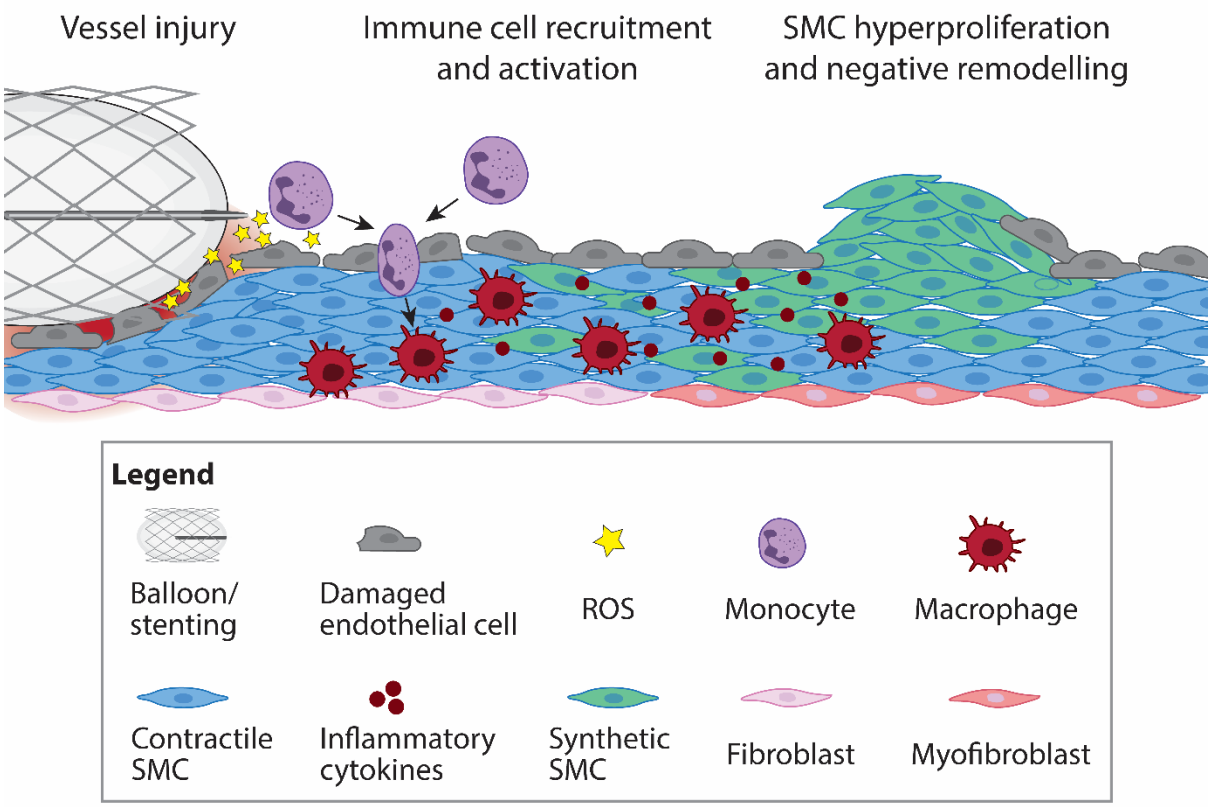

Figure 1.5: Restenosis pathophysiology
Schematic depicting how vessel injury results from balloon angioplasty and/or stent deployment, damaging the endothelium and releasing reactive oxygen species (ROS). This promotes monocyte and other immune cell recruitment and eventual migration into the tunica media where they differentiate into macrophages. Macrophages secrete pro-inflammatory cytokines, causing contractile smooth muscle cells (SMC) to differentiate into synthetic SMC which hyperproliferate and migrate across the damaged endothelium and into the vessel lumen. The inflammatory environment also causes the phenotypic switch of tunica adventitia resident fibroblasts into myofibroblasts, resulting in negative remodelling.

1.4.2. Structural valve degeneration

Key clinical trials have shown the advantages of TAVR up to five years post-implantation. However, due to the only recent introduction of this technology, there are currently very few long-term follow up studies that look at TAVR performance up to and past 10 years. Of these few studies, the majority point to increasing cases of valve failure over time. The Nordic Aortic

Valve Intervention (NOTION) trial, which evaluated TAVR and SAVR performance across a broad range of surgical risk patients with severe AS showed that while risk of major clinical outcomes was comparable to SAVR group, bioprosthetic valve failure occurred in 9.7% of TAVR patients after 10 years, an increase from 0.01% at 3 years [92]. The primary driver of TAVR valve failure, and bioprosthetic valve failure more generally, is a biological response known as structural valve degeneration (SVD) which develops around and within the prosthesis over time [93]. SVD limits the durability of bioprosthetic valves, ultimately leading to valve failure and/or redo valve replacement, a major surgical intervention. The NOTION trial showed that 15.4% of TAVR patients had moderate to severe SVD at 10 years compared to only 0.02% at 6 years, highlighting that SVD is a gradual process which develops over time [92].

SVD is fundamentally an inflammation-driven process that manifests through leaflet thrombosis, fibrosis, and calcification (Figure 1.6). Following implantation, bioprosthetic heart valves, including both surgical transcatheter valves, trigger the foreign body response, a highly inflammatory reaction characterised by the adsorption of serum proteins onto the valve surface, leukocyte adhesion, and immune cell activation [94]. Dysfunctional ECs populate the leaflet surface as early as day 1, potentially impairing their ability to prevent thrombosis formation [95]. As the inflammatory response progresses, fibroblasts and myofibroblasts secrete ECM components on the leaflet surface, leading to stiffening and restricted leaflet mobility, ultimately contributing to stenosis [96]. In the later stages, build-up of calcium deposition across the leaflet exacerbates leaflet stiffening and loss of physiological function [97]. Studies have shown that the chronic inflammatory environment established by persistent thrombus and excessive fibrosis likely fosters conditions that accelerate calcium deposition, culminating in irreversible leaflet dysfunction [95, 98].

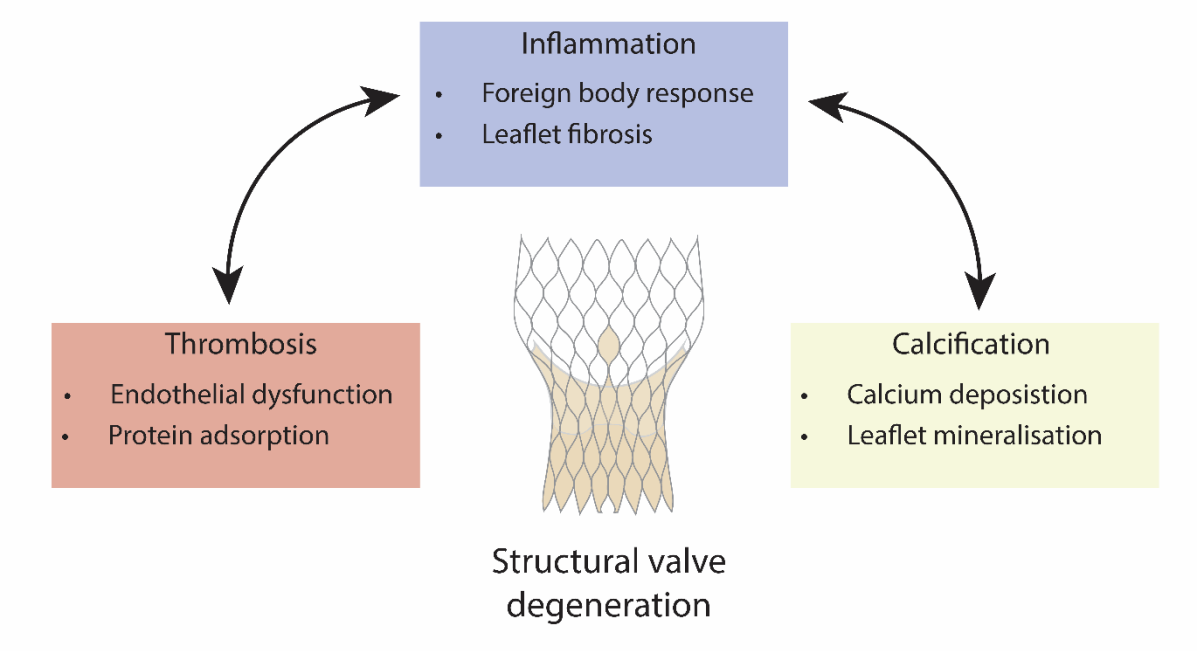

Figure 1.6: Determinants of structural valve degeneration
Structural valve degeneration generally comprises of three interconnected biological processes including thrombosis, inflammation, and calcification. Inflammation acts as the intermediary between thrombosis and calcification, both exacerbating these two modes of failure and forming the underlying link between them.

Chapter 2

Opinion review

2. Chapter 2 - Opinion review

2.1 The need for longer lasting cardiovascular devices

Cardiovascular disease (CVD) remains the leading cause of death globally and is projected to almost double in prevalence over the next 25–30 years [99]. In advanced cases such as arterial occlusion, structural heart disease, and heart failure, where mortality risks are highest, cardiovascular devices are playing an increasingly prominent role, complementing and/or taking precedence over drug therapies. Devices such as vascular stents, balloons, grafts, and bioprosthetic heart valves are now frontline treatments, offering immediate and often life-saving intervention. The added benefit of these devices being deliverable through minimally invasive procedures has further accelerated their use across broader patient populations, reinforcing their role in modern cardiovascular care [100].

While these devices are effective at restoring acute cardiovascular function, there is currently no cardiovascular implant that guarantees permanent, lifelong function without risk. Implantation of all cardiovascular devices triggers local injury responses driven by chronic inflammation which commonly manifests as excessive tissue growth around the implant/deployment site, leading to device failure [101]. Efforts to overcome these inflammatory and tissue responses have increasingly come to rely on drug-eluting technologies, which remain the most effective solution for extending device longevity [102]. However, vascular inflammation is difficult to suppress indefinitely, and current drugs used to modulate it either influence tissue remodelling in ways that ultimately limit long-term device performance and/or place patients at elevated risks from systemic off-target effects. This reliance on drugs has also shifted focus away from the translation of novel vascular materials, which remain largely unchanged despite decades of research. Most implants are still made from

the same metals and polymers first introduced in the 1950s and efforts to deviate from these have been hindered by challenges in scalability, reproducibility and regulatory approval of promising new materials. As life-expectancy continues to rise, the field increasingly seeks cardiovascular devices with high durability and low risk. This review proposes an emerging paradigm in cardiovascular biomaterials, in which actively modulating inflammation to promote tissue healing may serve as the main driver of long-term device performance and safety. Recent advances in drug selectivity and delivery platforms point toward next-generation cardiovascular technologies that engage, rather than evade, vascular inflammation.

2.2 Transition from anti-proliferative to anti-inflammatory drug strategies

Drug-eluting approaches have traditionally relied on non-specific anti-proliferative agents that, while effective at preventing short-term device failure, also hinder tissue remodelling/healing essential for long-term durability [103, 104]. Advances in the field's understanding of vascular inflammation have prompted a shift toward selective anti-inflammatory strategies that more precisely target pathological pathways while supporting tissue repair.

2.2.1 Current clinical approach

Since the early 2000s, sirolimus and paclitaxel have been the cornerstone drugs used in drug-eluting stents and balloons [105-108]. Sirolimus, a mammalian target of rapamycin (mTOR) inhibitor, and paclitaxel, a microtubule stabilizer with cytotoxic effects, were initially selected for their potent ability to suppress smooth muscle cell proliferation and reduce neointimal hyperplasia after device implantation. Early trials investigating their benefits highlighted a dramatic 40-70% decrease in restenosis rates in coronary lesions compared to uncoated/non-

eluting devices, and their success helped solidify drug-eluting platforms as the clinical standard [106, 108, 109]. These anti-proliferative agents, along with several other -limus family drugs, remain the gold standard clinical choice today. However, there is growing recognition of their inherent biological trade-offs including off-target effects and poor implant integration.

Both sirolimus and paclitaxel are non-selective inhibitors of cell proliferation, suppressing pathological smooth muscle cell proliferation and also impairing endothelial repair. Delayed re-endothelialisation drives late thrombosis and restenosis, while persistent inflammation creates a pro-thrombotic and pro-fibrotic environment that these drugs fail to address. Despite improving short-term durability, anti-proliferative drugs still fail to prevent long-term device failure, reflecting a focus on immediate outcomes rather than the ultimate goal of implants that remain functional in the body forever (Figure 2.1A). For instance, over 40% of patients required repeat vascular intervention within 5-year post-treatment for PAD with a paclitaxel-coated balloon [110].

Safety concerns of anti-proliferative drugs, particularly with paclitaxel, also remain a major issue since Katsanos et al., first reported links to increased mortality and major amputation [111, 112]. This is especially concerning for devices in direct contact with the circulatory system, where the drugs can enter systemic circulation and cause off-target effects. Although several follow-up studies have now cast uncertainty over these findings, the lingering ambiguity has drawn increased regulatory scrutiny from the FDA, prompting the field to seek safter alternatives. Most recently, the Swedish Drug-Elution Trial in Peripheral Arterial Disease 2 (SWEDEPAD2) associated paclitaxel-coated devices with significantly higher mortality rates over 5 years in patients undergoing infrainguinal endovascular revascularisation, reigniting the

fields concerns with non-specific anti-proliferative solutions [113]. These collective limitations underscore the need to explore inflammation, the primary driver of device failure, as a potentially more specific target for achieving long-term efficacy, while still acknowledging systemic safety risks.

2.2.2 Non-specific anti-inflammatories

Corticosteroids such as dexamethasone (DEX) and prednisone were amongst the first explored anti-inflammatory approaches, owing to their broad immunosuppressive activity and established pharmacologic profiles [114]. However, despite their conceptual appeal, they largely underperformed and were deemed unsafe. Early pre-clinical and clinical studies showed that DEX coated stents failed to reduce restenosis compared to non-coated controls, and in some models compromised vessel wall integrity and impaired endothelialisation [115, 116]. These results were in fact inferior to those achieved with anti-proliferative agents, underscoring that broad suppression of inflammation is inherently non-specific. Since inflammation regulates a wide spectrum of vascular processes beyond cell proliferation, non-targeted inhibition can similarly impair critical tissue remodelling of endothelial repair and healing.

To overcome the safety and efficacy limitations of broad-spectrum anti-inflammatories, researchers have investigated naturally derived anti-inflammatory compounds with more favourable safety profiles. Incorporation of Quercetin, a flavonoid with antioxidant and anti-inflammatory properties, into bioprosthetic valve leaflets reduced macrophage activation and oxidative stress *in vivo* without systemic or local toxicity [117]. However, it failed to meaningfully enhance endothelialisation or immune-mediated tissue integration, demonstrating that its effects were largely passive and insufficient to reprogram the long-term

immune responses. Similarly, resveratrol-coated angioplasty balloons demonstrated no adverse effects in porcine vessel injury models, but failed to improve endothelialisation, underscoring the persistent challenge of translating short-term anti-inflammatory activity into tangible regenerative outcomes [118]. Bio-inspired strategies have also shared this limitation. Hu et al investigated exosome-eluting stents derived from mesenchymal stem cells in a rat abdominal aorta model [119]. These stents significantly suppressed inflammation and reduced restenosis compared to bare metal controls, while outperforming traditional anti-proliferative stents in endothelial coverage. However, they offered no improvement in endothelialisation relative to bare metal stents. This demonstrated that inflammation could be targeted to achieve restenosis suppression comparable to anti-proliferative drugs without the drawback of impaired healing. Importantly, it also underscored the need for the next generation of eluting agents that are capable of not only passively avoiding harm to endothelialisation, but actively driving regenerative repair.

Collectively, these findings highlight progress in moving beyond anti-proliferative or broad immunosuppressive drugs toward safer functional agents. However, most current non-specific anti-inflammatory strategies remain passive, capable of halting pathological inflammation but unable to actively promote robust vascular regeneration. This unmet need has driven interest in more selective, targeted immunotherapies that can both suppress harmful immune responses and directly support long-term tissue repair.

2.2.3 Selective anti-inflammatories

Active immunomodulation strategies have either combined complementary agents in dual-drug systems or focused on single agents capable of simultaneously suppressing pathological inflammation while promoting/preserving vascular regeneration.

Recent advances in dual-elution platforms highlight the value of combining agents that act on distinct but complementary processes, incorporating one agent directed toward suppressing pathological inflammation, while the other supports endothelial repair and regeneration. Tu et al designed a co-delivery stent coating pairing vascular endothelial growth factor (VEGF) with copper-mediated nitric oxide (NO) generation [120]. VEGF drives endothelial migration and vessel coverage, while the promotion of endogenous NO generation facilitated vascular homeostasis, reducing smooth muscle hyperproliferation and inflammatory activation. Together, these functions achieved both rapid re-endothelialisation and sustained suppression of neointimal hyperplasia after 30-days in a rabbit iliac stenting model. Furthermore, bilayer vascular grafts designed to release both hydrogen sulfide, which has shown to promote inflammation resolution and inhibit smooth muscle cell proliferation, and exogenous NO, to stimulate endothelial regeneration and angiogenesis, have been extensively studied. Li et al demonstrated in a long-term rat abdominal replacement model that this approach promoted endothelialisation with 100% patency rates, while additionally highlighting no observable off-target inflammation or injury [121]. A similar dual approach has been employed in vascular grafts incorporating 4-octyl itaconate and the REDV peptide. Here, 4-octyl itaconate acted as the inflammation-focused component, suppressing M1 macrophage activation and limiting smooth muscle proliferation, while the REDV peptide functioned as the regenerative element, selectively promoting endothelial adhesion and coverage resulting in a 21% increase in patency after 1-month *in vivo* [122]. Collectively, these examples demonstrate how dual-elution strategies can suppress pathological inflammation and prevent downstream device failure

modes while providing cues that encourage vascular repair and integration. While promising, these approaches are limited to short-term benefits and scaling them for longer-term durability will be challenging due to the complexity of coordinating multiple drugs and the need to maintain precise release kinetics over extended periods. These challenges have motivated efforts to identify single molecules capable of achieving multifunctional effects, offering a streamlined path towards selective immunomodulation.

MCC950, a selective NLRP3 inflammasome inhibitor, has been shown in a mouse carotid grafting model to reduce neointimal hyperplasia while enhancing re-endothelialisation, outperforming paclitaxel and sirolimus and also achieving better endothelialisation than un-coated controls [123]. These benefits stem from its selectivity for targeting NLRP3-driven inflammation, which is implicated in restenosis but not in vascular healing/angiogenesis, enabling suppression of pathological inflammation while preserving, and potentially enhancing natural vascular repair. Targeting macrophage polarisation has also shown to selectively resolve inflammation while actively supporting tissue repair. Local delivery of IL-10 post-balloon inflation in a rat carotid injury model led to a three-fold increase in proportion of pro-reparative M2 phenotype macrophages within the vasculature, resulting in reduced neointimal thickening and enhanced endothelial coverage after 14 days compared to injury only control [124]. IL-4 coated grafts showed comparable effects, driving M2 polarisation and significantly reducing neointimal hyperplasia by 51%-69% compared to non-coated groups, depending on the section of the graft [125]. Together, these examples illustrate a new paradigm in drug approaches in which inflammation may be redirected into a driver of vascular repair and functional restoration (Figure 2.1B).

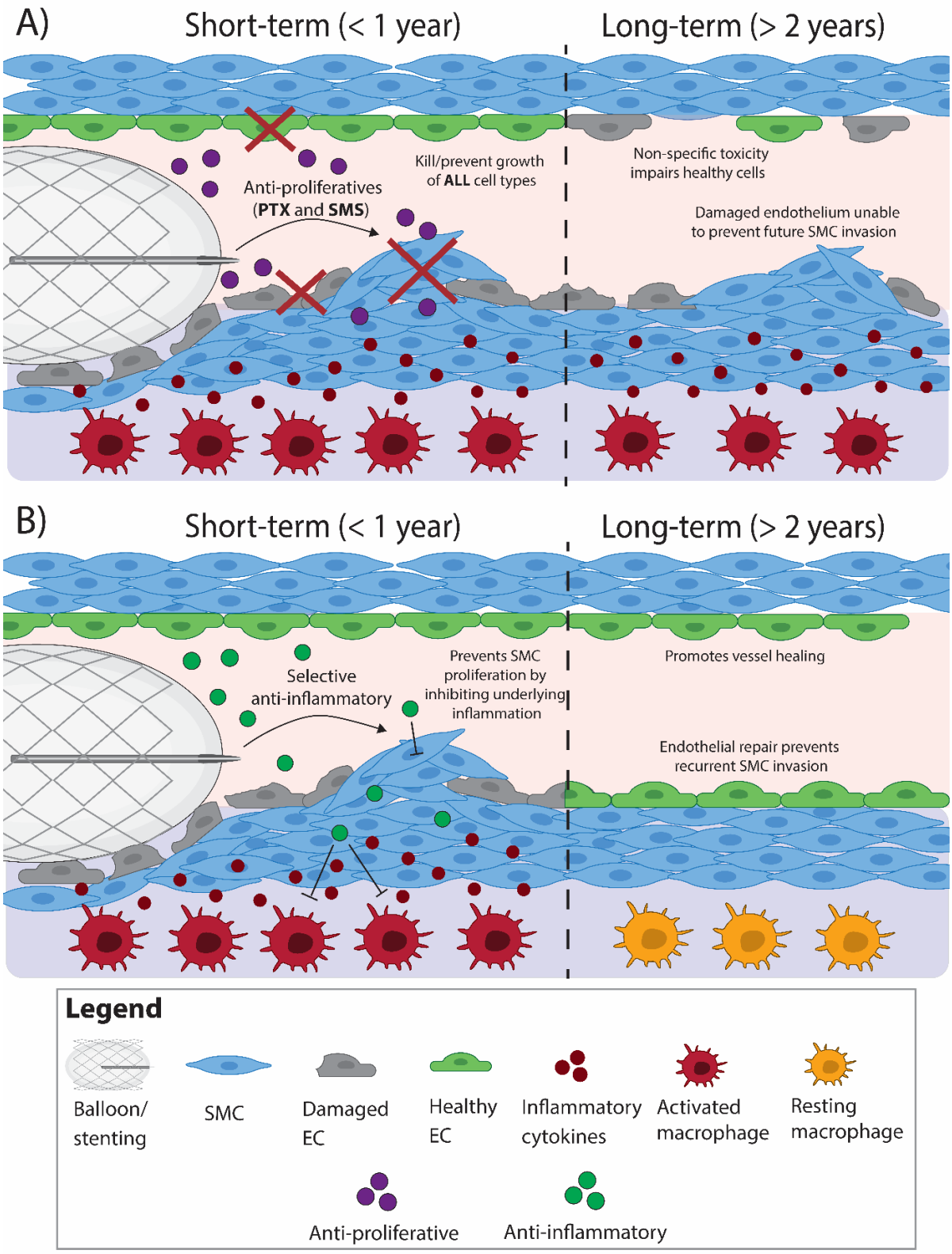

Figure 2.1: The benefits of a selective anti-inflammatory drug-elution approach
A) Anti-proliferative agents including paclitaxel (PTX) and sirolimus (SMS) are able to reduce smooth muscle cell (SMC) proliferation in the short-term, but damage endothelial cells (EC) and to not address the underlying inflammation, resulting in neointimal hyperplasia in the long term. B) Selective anti-inflammatories contrastingly are able to reduce vessel inflammation and promote vessel healing, resulting in improved long-term outcomes.

2.3 Drug delivery platforms

While drug selection is a critical determinant of device longevity, the choice of delivery platform is equally important. Effective platforms must offer controlled and durable drug release, be adaptable for different device use cases, and remain suitable for scalable manufacturing and off-the-shelf use. The most common delivery platforms being currently researched include polymeric coatings, hydrogel coatings and nanoparticle platforms.

2.3.1 Polymeric coatings

Polymer based coatings remain the most established platform for drug delivery in cardiovascular devices, with strategies such as dip-coating, layer-by-layer (LbL) assembly, and chemical linkage each offering distinct advantages. Their strongest contribution has been the ability to achieve sustained and precisely tailored drug release. Dip-coating, the most clinically adopted approach, can sustain release for over 12 months, aligning with the long-term progression of neointimal hyperplasia [126]. This durability has underpinned the clinical success of drug-eluting vascular devices. LbL assembly further extends control over release kinetics, enabling sequential or environmentally responsive delivery of multiple agents [127, 128]. Similarly, chemical linkage strategies tether biological agents directly to the device surface, preventing premature washout under flow conditions and enabling bioactivity to be preserved at the implantation site. For example, N-(3-dimethylaminopropyl)-N′-ethylcarbodiimide/ N-hydroxysuccinimide (EDC/NHS) coupling has been used to attach recombinant type III collagen or chemerin 15 peptides to stents for local inflammation resolution [129, 130], while ROS-responsive chemistries have enabled exosome-eluting stents that selectively release their cargo under oxidative stress [119]. Collectively, these features

position polymeric coatings as a highly effective platform for tailored drug functionalisation and release.

Despite these strengths, polymeric coatings show limited adaptability across cardiovascular device classes. Dip-coated films are inherently thick [131], a feature tolerated on rigid stent struts but problematic on delicate, dynamic substrates like bioprosthetic valve leaflets, where cracking and delamination may occur under repetitive strain as well as the potential to disrupt leaflet mechanics. LbL coatings would similarly add thickness to the coated device, a factor that is undesirable for valves as this can impair leaflet motion or other mechanical functions of moving tissues, limiting translation beyond relatively static surfaces. Chemical linkage strategies offer ultrathin, stable modification but require complex chemistries and precise control over surface functional groups, complicating use on bioprosthetic tissues. These limitations highlight why polymeric coatings, despite excelling in drug release for stenting, remain less suited for dynamic environments such as those experienced by bioprosthetic valves.

From a translational standpoint, polymeric coatings perform relatively well on manufacturability and off-the-shelf properties. Dip-coating is simple, scalable, and already embedded in clinically approved stents, supporting feasibility for mass production [132]. This maturity distinguishes polymeric coatings from other platforms, even if their broader application requires careful tailoring to the mechanical and biological constraints of specific devices. Overall, polymeric coatings represent a proven and effective strategy for stents and grafts, but their role in next-generation cardiovascular devices will depend on overcoming limitations in adaptability.

2.3.2 Hydrogel coatings

Hydrogels have emerged as a promising platform for cardiovascular device functionalisation because of their high water content, tissue-like mechanics, and inherent biocompatibility [133]. Their soft, elastic structure makes them particularly well-suited for coating delicate or dynamic substrates such as valve leaflets, where rigid polymer coatings would otherwise crack or delaminate [134, 135]. Hydrogels can encapsulate a wide range of therapeutics, and release profiles can be tuned by adjusting crosslinking density, degradability, or responsiveness to local cues such as pH, reactive oxygen species, or enzymatic activity [135-137]. These properties provide clear advantages for tailoring delivery to inflamed or injured vascular environments, and multifunctional hydrogels capable of sequential release show potential for addressing multiple failure modes simultaneously.

Nevertheless, hydrogel coatings provide only moderate control over drug release. Many formulations degrade relatively quickly within 6-months *in vivo*, which limits their ability to sustain delivery over long periods [138, 139]. This instability raises concerns in scenarios such as restenosis or chronic inflammation, where therapeutic benefit often requires drug release over 6-12 months. Burst release is also common due to their high-water content, particularly for hydrophobic molecules. These limitations suggest that, although hydrogels can be engineered for short- to medium-term delivery, they remain less effective than polymeric platforms at achieving prolonged elution.

Hydrogels offer better adaptability across cardiovascular devices compared with polymers, especially in contexts that demand flexibility or tissue-like compliance. However, their performance under high shear stress and pulsatile flow remains largely unexplored. The

hydrated, loosely crosslinked networks that give hydrogels their biocompatibility also make them prone to detachment in dynamic conditions. While preclinical studies have demonstrated local bioactivity in static or subcutaneous models, very few have examined hydrogel retention in pulse duplicators or accelerated fatigue systems that replicate the arterial or valvular environment [135]. Li et al have made headway into this space, evaluating their hydrogel coating in an abdominal aorta transplantation model, however there is still a significant gap for testing in physiological environments [140]. This lack of data raises unresolved questions about whether hydrogel coatings can maintain stability on devices exposed to repetitive strain or constant flow.

From a translational perspective, hydrogel systems perform poorly in terms of manufacturability and off-the-shelf readiness. Many rely on multi-component formulations, complex chemistries, or in situ polymerisation methods that hinder large-scale production and complicate regulatory pathways. Unlike polymeric coatings, which already have a long clinical precedent, hydrogel platforms lack established processing pipelines for integration into cardiovascular devices. As such, their path to translation will require simplification of chemistries, better demonstration of durability under clinically relevant conditions, and strategies to extend drug retention. Overall, hydrogels represent an adaptable and biologically appealing coating strategy, but their future in cardiovascular medicine depends on solving the challenges of mechanical stability and translational feasibility.

2.3.3 Nanoparticle platforms

Nanoparticles represent another promising drug delivery strategy for cardiovascular devices due to their ability to improve localisation, retention, and arterial uptake of drugs. By

encapsulating biological agents within nanoscale carriers, these systems can improve drug pharmacokinetic properties, a key determinant that has long limited the translation of many agents, especially in the case of drug-coated balloons. Their capacity to enhance tissue penetration and retention has enabled less lipophilic drugs, such as sirolimus, to achieve comparable clinical efficacy to paclitaxel in drug-eluting balloons [141]. Nanoparticles have also been shown to reduce required drug concentrations without compromising efficacy, thereby lowering systemic exposure and potentially improving safety. This principle is exemplified by the SirPlux Duo balloon, which co-encapsulates paclitaxel and sirolimus into biodegradable nanoparticles at significantly reduced drug doses while maintaining efficacy in pre-clinical models [142]. Beyond small molecules, nanoparticle carriers have been adapted for gene-based therapeutics such as CRISPR-Cas9, offering opportunities for highly selective modulation of pathological pathways and the potential for gene-editing therapies to be incorporated into drug-eluting cardiovascular devices [143]. Together, these findings demonstrate that nanoparticle systems are capable platforms for improving drug delivery in cardiovascular devices. See section 4.1.3 of this thesis for a more detailed review of current nanoparticle-based drug delivery strategies.

Their adaptability across device types, while promising, remains less established. Nanoparticles can be engineered for sustained or stimuli-responsive release, and surface modifications allow for selective targeting to inflamed or injured tissues. Designs such as microenvironment-responsive carriers coated onto vascular stents release anti-inflammatory drugs in response to MMP activity, reducing neointimal hyperplasia, highlighting the potential for pathology-linked delivery [144]. Furthermore, biomimetic formulations, including red blood cell-coated nanoparticles, have shown improved biocompatibility and reduced calcification when applied to bioprosthetic heart valves [145]. These examples underscore the

conceptual adaptability of nanocarriers to diverse cardiovascular settings. However, evaluation in physiologically relevant models is sparse. Like hydrogels, nanoparticle coatings have seldom been tested under conditions of high shear stress or pulsatile flow, raising questions about their stability on valve leaflets or within large arteries. Furthermore, their exposure to systemic circulation introduces additional concerns, including rapid clearance and unpredictable biodistribution, as well as the risk of accumulation or toxicity with non-degradable carriers [146, 147]. These uncertainties limit the confidence with which nanoparticles can be extended across all device classes.

From a translational perspective, nanoparticle coatings face considerable hurdles. Manufacturing complexity is a central challenge, particularly when multifunctional formulations or responsive chemistries are involved, and reproducibility across batches remains difficult to control. Scale-up has proven especially challenging in large-animal models of vascular inflammation, where macrophage-targeted nanotherapies highlighted the key considerations required to move towards clinical translation [148]. Unlike polymeric coatings, nanoparticles lack established pipelines for device integration, and off-the-shelf readiness is limited. Despite these drawbacks, their unique ability to improve drug localisation and retention makes nanoparticles a leading candidate for next-generation cardiovascular drug delivery, provided that future work addresses durability under flow, systemic clearance, and manufacturing standardisation.

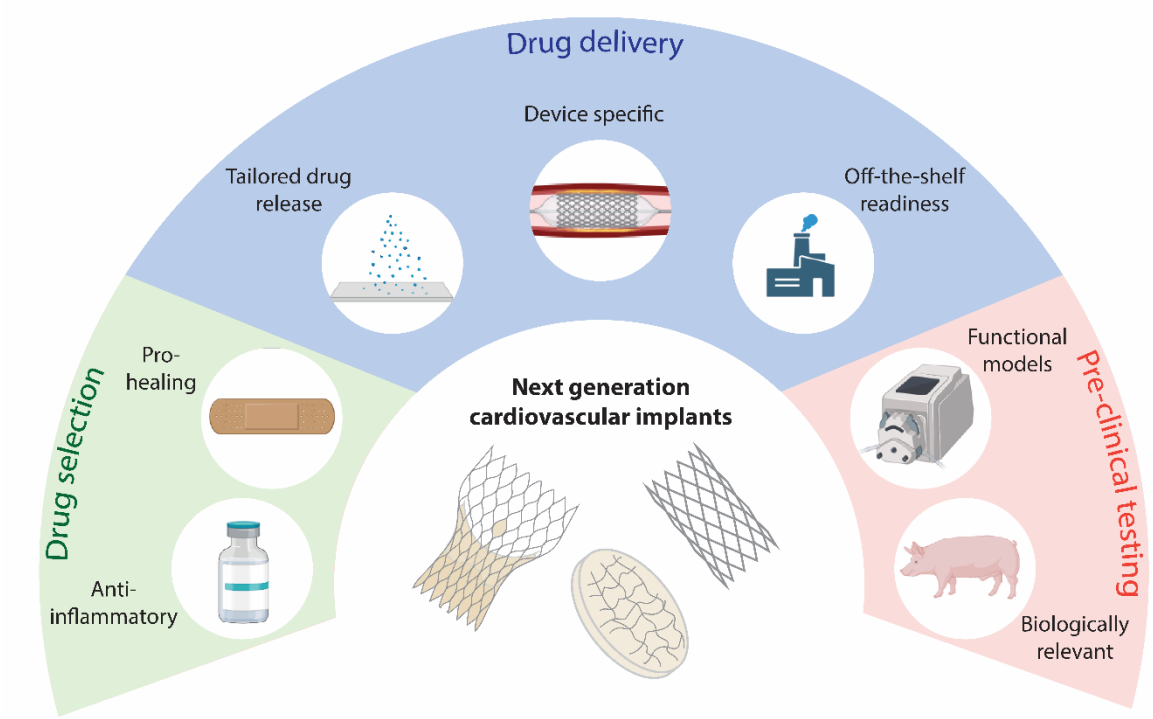

Figure 2.2: Engineering next generation cardiovascular devices

In order to achieve cardiovascular devices that last the entire lifespan of patients, devices can be coupled with selective anti-inflammatory drugs which prevent scar-like tissue growth around the implant whilst promoting healthy integration between the implant and the body. Drug delivery strategies should be tailored to the specific device type and environment that the device is subject to. Commercial viability and translatability of both the drug agent and the drug delivery platform should be taken into account. Finally, pre-clinical testing should be performed under dynamic conditions (e.g. under flow with pressure and shear stress) and in biologically relevant large animal studies.

2.4 Future directions and concluding remarks

The clinical translation of immunomodulatory cardiovascular devices requires careful consideration of practical requirements beyond experimental efficacy. Ensuring the safety of both the drug and delivery platform is essential, given that locally delivered agents are inevitably exposed to systemic circulation when applied to most cardiovascular devices. Equally important are feasibility and scalability. The most promising solutions will employ drugs with favourable safety profiles, cost-effectiveness, and regulatory familiarity, alongside coating or delivery methods that are reproducible and compatible with current manufacturing practices. For widespread adoption, platforms must also integrate seamlessly into surgical

workflows. Fundamentally, the field must prioritise aligning the right drug with the right delivery platform for the biomechanical and biological environment of the specific device.

Future development in the field hinges upon developing novel platforms and device strategies and translating them into the clinic. Over the last 50 years, the progress made in better understanding biological failure modes and device pathology has significantly outpaced the innovations made in cardiovascular device design. Drug-eluting strategies first described over two decades ago remain the gold-standard treatment for patients suffering from cardiovascular diseases [106, 108, 149]. To overcome this, a greater commitment to translation and commercial viability should be enforced in the early period of device development. Currently too many studies present promising therapeutic strategies and technologies that do not take translational capabilities into consideration, causing this build-up of platforms and literature in the basic science research phase of the translational pathway. By better understanding commercial requirements and interacting with clinicians early in the development stage, devices will more likely progress into pre-clinical and clinical studies, enhancing the potential for commercial viability [150]. Parallel to this, preclinical testing must advance from static, non-functional models toward large animal studies that better recapitulate the flow, stress, and scale of cardiovascular environments. Such models will be critical for assessing coating retention, drug release, and long-term integration under conditions that mimic clinical reality, and will help identify platforms with translational potential.

As progress approaches human studies, variability in immune responses across patients will represent one of the greatest hurdles. Differences in comorbidities, pharmacological backgrounds, and immune function may significantly impact therapeutic outcomes [151].

Addressing this challenge will require strategies for patient stratification, as well as adaptive platform designs that retain robustness across diverse populations. Equally, reproducibility of manufacturing, scalability of production, and ease of surgical uptake will determine which platforms advance to clinical use. Meeting these translational challenges will depend on coordinated efforts across disciplines, but doing so offers the opportunity to deliver a new generation of cardiovascular devices that not only restore function but actively guide healing and improve long-term durability.

2.5 Aims

This thesis is concerned with developing immunomodulatory solutions to improve the durability of cardiovascular devices. The specific aims are as follows:

1. To evaluate the potential of MCC950, a novel selective anti-inflammatory, as a drug-eluting agent for vascular materials.
2. To establish and validate plasma polymerised nanoparticles (PPN) as a localised drug delivery platform for the selective anti-inflammatory agents MCC950 and interleukin-10, in the context of vascular injury.
3. To develop a PPN-based coating for bioprosthetic heart valves that enables drug immobilisation to address key failure modes.

Chapter 3

Selective NLRP3 inflammasome inhibitor MCC950 suppresses inflammation and facilitates healing in vascular materials

3. Chapter 3 – Selective NLRP3 Inflammasome Inhibitor MCC950 Suppresses Inflammation and Facilitates Healing in Vascular Materials

ADVANCED SCIENCE Open Access
www.advancedscience.com

Selective NLRP3 Inflammasome Inhibitor MCC950 Suppresses Inflammation and Facilitates Healing in Vascular Materials

Angus J. Grant, Nianji Yang, Matthew J. Moore, Yuen Ting Lam, Praveesuda L. Michael, Alex H.P. Chan, Miguel Santos, Jelena Rnjak-Kovacina, Richard P. Tan, and Steven G. Wise**

Minimally invasive interventions using drug-eluting stents or balloons are a first-line treatment for certain occlusive cardiovascular diseases, but the major long-term cause of failure is neointimal hyperplasia (NIH). The drugs eluted from these devices are non-specific anti-proliferative drugs, such as paclitaxel (PTX) or sirolimus (SMS), which do not address the underlying inflammation. MCC950 is a selective inhibitor of the NLRP3-inflammasome, which drives sterile inflammation commonly observed in NIH. Additionally, in contrast to broad-spectrum anti-inflammatory drugs, MCC950 does not compromise global immune function due this selective activity. In this study, MCC950 is found to not impact the viability, integrity, or function of human coronary endothelial cells, in contrast to the non-specific anti-proliferative effects of PTX and SMS. Using an in vitro model of NLRP3-mediated inflammation in murine macrophages, MCC950 reduced IL-1β expression, which is a key driver of NIH. In an in vivo mouse model of NIH in vascular grafts, MCC950 significantly enhanced re-endothelialization and reduced NIH compared to PTX or SMS. These findings show the effectiveness of a targeted anti-inflammatory drug-elution strategy with significant implications for cardiovascular device intervention.

1. Introduction

Minimally-invasive endovascular intervention has become the preferred treatment for certain occlusive cardiovascular diseases, due to low incidences of in-hospital mortality and faster patient recovery times compared to open surgery.[1] These therapies rely on the deployment of balloons and/or stents within diseased blood vessels which push aside plaque deposits and restore blood flow. Despite their acute benefits, endovascular therapies commonly fail in the long-term due to post-operative vessel re-narrowing caused by smooth muscle cell (SMC) invasion of the vessel lumen, a pathological process known as neointimal hyperplasia (NIH).[2] Both balloon expansion and stent placement cause collateral damage to the endothelium and vessel wall, triggering a chronic inflammatory injury response.[2] Macrophages are the dominant responders to this injury, up-regulating the secretion of pro-inflammatory cytokines, namely interleukin-1β (IL-1β), which initiate the phenotypic switching of SMCs in the vessel wall toward a hyperproliferative "synthetic" phenotype.[3] Without an intact endothelial barrier, highly proliferative SMCs grow into the vessel lumen, driving NIH and vessel re-narrowing.[4] This has inspired the widespread use of drug-eluting technology which attempts to minimize NIH by inhibiting SMC growth and extend the acute beneficial outcomes of endovascular intervention.

The evolution of commercial drug-eluting stents (DES) and drug-eluting balloons has seen the development of device coatings with water-insoluble antiproliferative agents including paclitaxel (PTX), sirolimus (SMS), and more recently, SMS family derivatives.[5] PTX prevents cell proliferation by promoting the assembly of stable microtubules and inhibiting their depolymerization, leading to cell-cycle arrest and apoptosis.[6] Conversely, SMS inhibits the activation of mammalian target of rapamycin (mTOR), an essential kinase that regulates cell proliferation, arresting cells in the G1 phase of the cell cycle causing a cytostatic effect.[7] Although numerous clinical trials have now validated the efficiency of drug-elution technology in preventing NIH, it is

A. J. Grant, N. Yang, M. J. Moore, Y. T. Lam, P. L. Michael, A. H. Chan, M. Santos, R. P. Tan, S. G. Wise
School of Medical Sciences
Faculty of Health and Medicine
Charles Perkins Centre
University of Sydney
Sydney, NSW 2006, Australia
E-mail: richard.tan@sydney.edu.au; steven.wise@sydney.edu.au
J. Rnjak-Kovacina
Graduate School of Biomedical Engineering
University of New South Wales
Sydney, NSW 2006, Australia

The ORCID identification number(s) for the author(s) of this article can be found under https://doi.org/10.1002/advs.202300521

DOI: 10.1002/advs.202300521

also widely recognized that these drugs compromise the proliferation of many different cell types.[8] Drug-eluting devices fail to address the underlying causes of inflammation, inhibit endothelial cell recovery and healing, and have only limited elution times, ultimately resulting in NIH in the long-term.[9] Furthermore, safety concerns have emerged regarding the use of PTX in particular for drug-eluting devices, with studies showing an overall increased risk of all-cause mortality.[10] Despite the need for further studies to confirm these findings and determine the mechanisms underlying the increased risk, the non-specific, cytotoxic nature of these drugs is an important concern relating to safety and efficacy of drug-eluting approaches. PTX and SMS are also inherently limited as they target only end-stage vessel re-narrowing, rather than the early stages of inflammation triggered by the initial injury to the vessel wall.[2] The ideal drug would instead simultaneously inhibit SMC proliferation while allowing endothelial cell re-growth. Recent studies have indicated that drugs which target this initial inflammatory response hold significant promise for improving the long-term performance of vascular devices.

Despite the well characterized role inflammation plays in NIH and the recent therapeutic links identified between inflammation-targeting drugs and better cardiovascular outcomes, their use in drug-eluting devices has yet to be clinically established. An emerging target in vascular inflammation is the NLRP3 (NOD-, LRR-, and PYD-containing protein 3) inflammasome, a cytosolic signaling pathway of the innate immune system responsible for the proteolytic activation of IL-1β.[11] Driven by a growing number of studies implicating its role in the pathogenesis of cardiovascular disease and injury, antagonism of the NLRP3 inflammasome is an increasing focus in vascular medicine.[11b] MCC950 was the first developed small molecule inhibitor which covalently binds to and prevents NLRP3 oligomerization. In mouse models of atherosclerosis, intravenous MCC950 attenuates IL-1β, significantly reducing atherosclerotic plaque development.[12] Further studies in mouse models of myocardial infarction have shown that intraperitoneal injections of MCC950 reduces fibrosis and improves cardiac remodeling.[13] More importantly, in vascular healing studies, MCC950 causes no significant impairments to native angiogenesis, suggesting that the selective functions of MCC950 carry robust and targeted anti-inflammatory actions without the anti-angiogenic effects of antiproliferative drugs.[14] However, despite overlapping inflammatory mechanisms with atherosclerosis, evidence demonstrating the potential of MCC950 and NLRP3 inhibition in suppressing NIH has not yet been reported in the context of vascular devices/materials.

In this paper, we conduct a comparative study of MCC950 against the established agents PTX and SMS, as a potential alternative for long-term suppression of NIH. Functioning through an entirely distinct mechanism to PTX and SMS, we first show in vitro that MCC950 is non-toxic to vascular cells critical to vessel remodeling. MCC950 also selectively reduces expression of inflammatory factors from cultured macrophages which drive NIH while supporting endothelial integrity and function. Further evaluation of MCC950 in a 28 days in vivo vascular graft model of NIH demonstrated superior performance to PTX and SMS across a range of key metrics. MCC950 showed long-term reduction in vascular inflammation coupled with an early enhancement of endothelial coverage and function. These events were ultimately consistent with a significant and long-term reduction of NIH and reduced fibrin deposition. These findings collectively highlight MCC950 as a potentially more targeted, effective, and safer drug-eluting approach for vascular devices (**Figure 1**A).

2. Results

2.1. MCC950 Is Non-Toxic to Vascular Cells

The distinct modes of action for each drug were investigated by performing cytotoxicity assays in the three major cell types relevant to the pathophysiology of vessel injury and repair (macrophages, endothelial cells, and SMCs). A viability dosage response curve was generated for each cell type after 3 days of treatment with each drug. Across all cell types both PTX and SMS led to dose-dependent reductions in viability compared to control (**Figure 2**A). PTX showed the most significant decreases when dose matched against SMS. Immunostaining showed that when compared to control, PTX and SMS drastically reduced cell density in macrophages (Figure 2B), compromised junction formation in endothelial monolayers (Figure 2C), and impaired cytoskeleton spindles SMCs (Figure 2D). In contrast, MCC950 treated cells had no observable differences compared to control, highlighting that cytotoxicity was not its primary mechanism of action or an adverse side effect. Similar effects were observed in human THP-1–derived macrophages (Figure S1, Supporting Information).

2.2. MCC950 Immunosuppression Is Selective to the NLRP3 Inflammasome In Vitro

Validation of MCC950 function was conducted by establishing an in vitro model of NLPR3-mediated inflammation. Stimulated macrophages were treated with each drug for 24 h followed by quantification of IL-1β secretion and pyroptosis-mediated cell death, the major products of NLRP3 inflammasome activation (Figure S2, Supporting Information). TNF-α secretion was also quantified to serve as a control inflammatory cytokine non-specific to the NLRP3 pathway (TNF-α is collaterally secreted by the priming LPS stimulus as the first component of NLRP3 activation). PTX and SMS treatment showed broad suppression of inflammatory cytokine release, reducing both IL-1β and TNF-α (**Figure 3**A,B). However, neither drug was able to elevate levels of intracellular F-actin staining relative to stimulated groups, indicating an inability to rescue macrophages from pyroptosis (Figure 3C). In contrast, MCC950 showed markedly reduced levels of IL-1β relative to stimulated control and to a greater degree than both PTX and SMS (6.6 ± 0.76 vs 27.78 ± 3.08, 16.27 ± 2.02, and 17.91 ± 2.0 pg mL^{-1}, respectively). Additionally, MCC950 alone rescued stimulated macrophages from pyroptosis raising F-actin levels by 76% above stimulated controls ($90.5 \pm 1.98\%$ vs $21.77 \pm 1.13\%$). MCC950 had no effect on TNF-α secretion, highlighting that its anti-inflammatory functions were specific to the NLRP3 pathway. Similar observations, though with a higher degree of variability, were recorded in human THP-1–derived macrophages due to the non-adherent nature of this cell type,

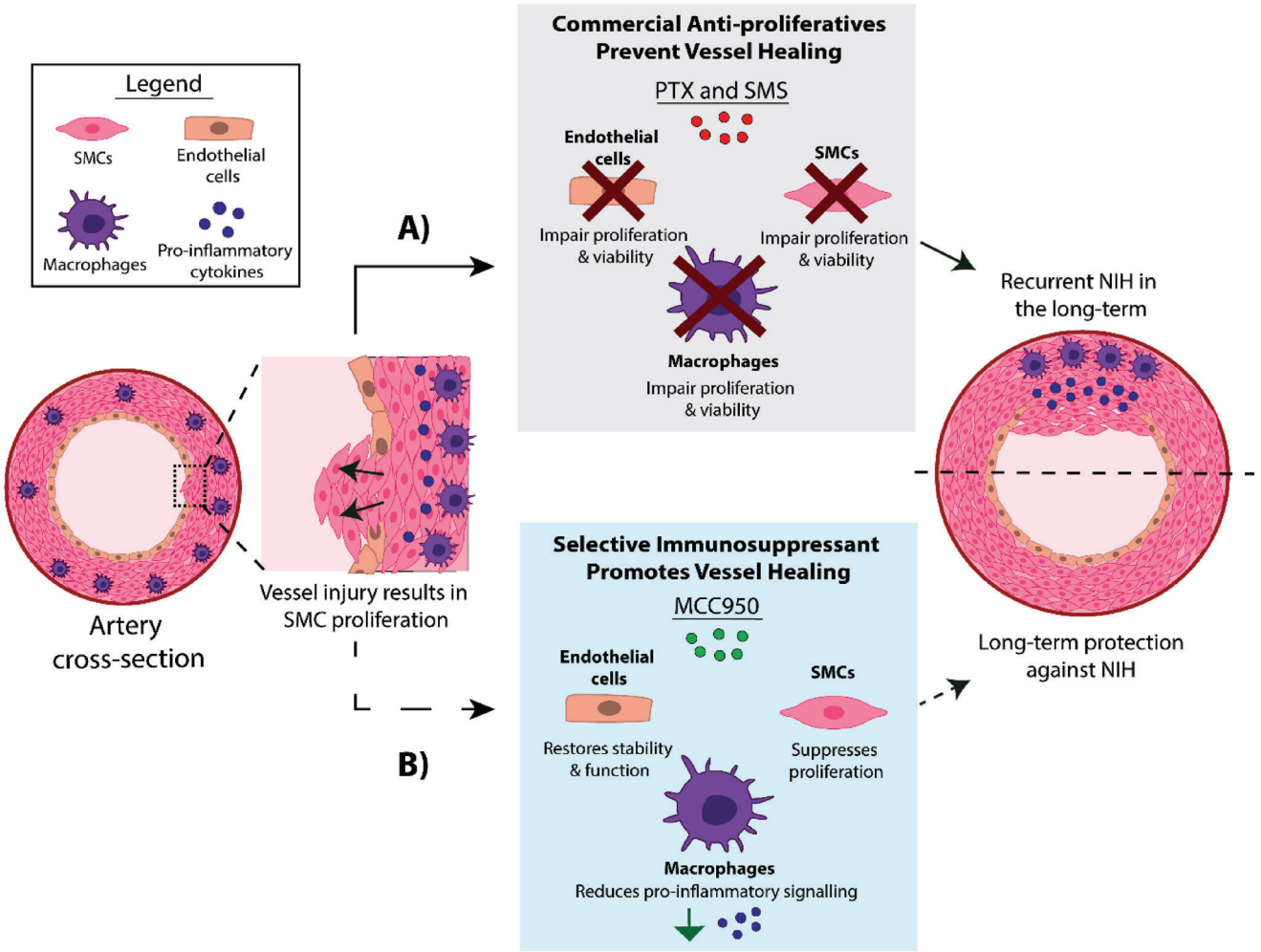

Figure 1. Schematic representation of A) current drug-eluting endovascular interventions using anti-proliferative drugs, paclitaxel (PTX) and sirolimus (SMS). Endovascular interventions cause injury to the vessel wall (black arrows), stimulating macrophage-driven immune responses that causes neointimal hyperplasia (NIH), an over-proliferation of smooth muscle cells (SMC) into the vessel lumen. Elution of non-specific anti-proliferative drugs PTX and SMS reduces NIH in the short-term, but also negatively impacts endothelial cells and macrophages, preventing vessel healing and leading to long-term outcomes of recurrent NIH. B) Targeting NLRP3-mediated inflammation, a potential underlying cause of NIH, using the selective inhibitor MCC950 may suppress NIH without adverse impacts on vessel healing which could ultimately lead to superior long-term suppression of NIH compared to PTX and SMS.

where MCC950 inhibited IL-1β secretion and rescued pyroptosis, with negligible effect on TNF-α (Figure S3, Supporting Information).

2.3. MCC950 Does Not Compromise Endothelial Cell Integrity or Function In Vitro

The major limitation of anti-proliferative drugs like PTX and SMS are their non-specific cytotoxic effects which compromise functional re-endothelialization and subsequent vessel healing. To determine any negative effects MCC950 may have directly on endothelial cells, levels of vascular endothelial-cadherin (VE-cadherin) and endothelial nitric oxide synthase (eNOS) were measured to assess endothelial integrity and regulatory function. Compared to untreated controls, VE-cadherin expression was reduced at junctions between neighboring endothelial cells after treatment with PTX or SMS by 55% and 61%, respectively (**Figure 4**A,B), an effect which appeared to be dose-dependent (Figure S4A, Supporting Information). MCC950 however showed strong VE-cadherin staining with no quantifiable differences in expression compared to control. Similarly, cells treated with PTX or SMS showed an 81% and 79% reduction in eNOS expression, respectively, in contrast to MCC950 which maintained levels of eNOS comparable to control groups (Figure 4C,D). The effects of PTX and SMS were also dose dependent (Figure S4B, Supporting Information). Additional analysis using real-time qPCR of typical endothelial phenotype and function genes cadherin 5 (CDH5), platelet endothelial cell adhesion molecule (PECAM), and eNOS further supported the compatibility of MCC950 by showing no downregulation of these genes (Figure S4C–E, Supporting Information). Collectively, this

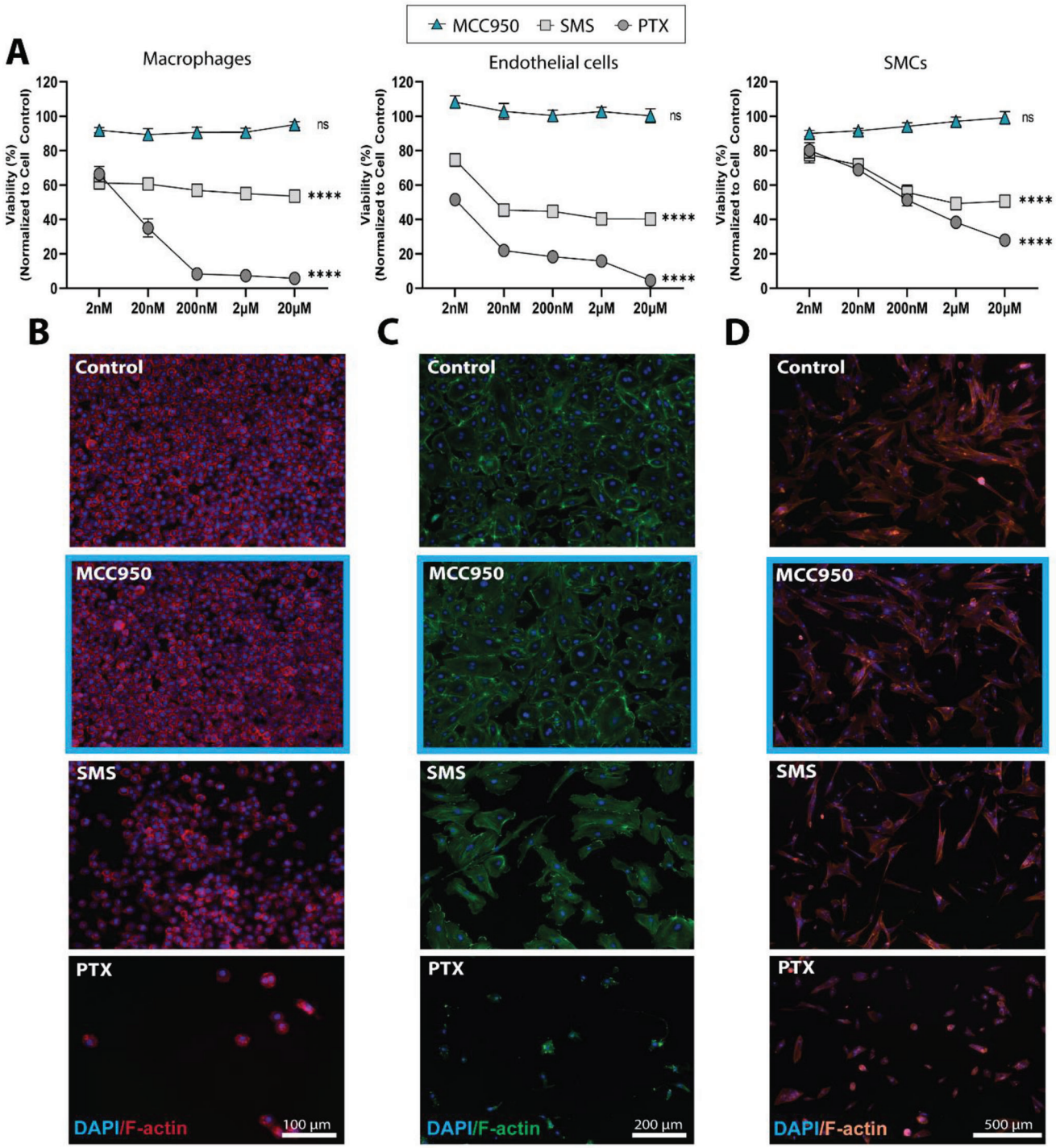

Figure 2. MCC950 is non-toxic to key vascular cells. A) Viability of J774a murine macrophages, human coronary artery endothelial cells, and smooth muscle cells (SMCs) 3 days after being treated with MCC950, sirolimus (SMS), or paclitaxel (PTX). Data represents mean ± SEM ($n = 4$). Statistical significance was determined using Dunnett's multiple comparison test ($^{****}p < 0.0001$). Representative images of B) macrophages, C) endothelial cells, and D) smooth muscle cells treated with highest dose (20 μM) MCC950, SMS, or PTX. DAPI stained in blue, F-actin stained in red, green, and light orange, respectively. Scale bars represent 100, 200, and 500 μm, respectively.

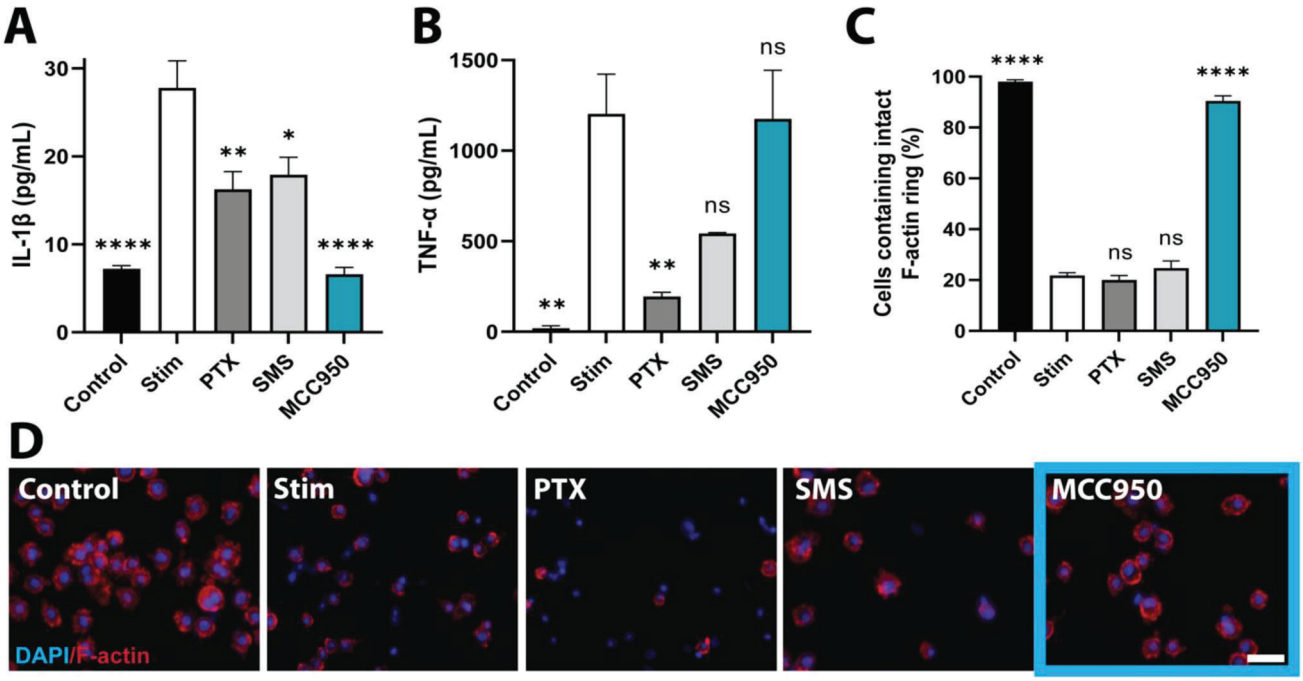

Figure 3. MCC950 selectively suppresses components of the NLRP3 inflammasome pathway in murine macrophages. The effect of high dose (20 μM) MCC950, paclitaxel (PTX), and sirolimus (SMS) on A) IL-1β, B) TNF-α and C) pyroptosis levels post-NLRP3 inflammasome stimulation with LPS (1 μg mL^{-1}) and ATP (2.5 mM) in J774a macrophages. Stim refers to stimulated only group. IL-1β and TNF-α levels measured by ELISA. Data represents mean ± SEM (n = 3–4). Statistical significance was determined using Dunnett's multiple comparison test relative to stimulated group ($^{*}p < 0.05$, $^{**}p < 0.01$, $^{***}p < 0.001$, $^{****}p < 0.0001$). D) Representative images of control, stimulated only, and stimulated and drug treated macrophages used for pyroptosis quantification. Cells stained with DAPI (blue) and rhodamine phalloidin (red) to visualize cell nucleus and F-actin, respectively. Scale bar represents 50 μm.

suggested that MCC950 had negligible adverse effects on endothelial cells.

To further investigate the effects of MCC950 on endothelial function over PTX and SMS, a HCAEC tube formation assay was performed (Figure 4E). Both PTX and SMS significantly impaired tubule formation, decreasing branching tube length, number of tube junctions, and number of tube meshes formed (Figure 4F). This contrasted with MCC950 which showed no significant reduction in any of these outcomes. This further highlighted that MCC950 does not compromise endothelial cell integrity or function, suggesting that it may not have the negative impacts on re-endothelialization in vivo known for PTX and SMS.

2.4. MCC950 Improves Hemocompatibility In Vitro

Drug hemocompatibility, a key feature of eluted agents used in vascular settings, was studied using an established in vitro human whole blood clotting assay. Fresh human blood was added to silk scaffolds and treated with PTX, SMS, or MCC950.[15] Scaffolds were then washed and their surface analyzed to determine the weight of clotting blood (**Figure 5**A). No significant differences in clot weight were observed after PTX or SMS treatment compared to control, whereas MCC950 significantly reduced clotting weight by 69% (Figure 5B). SEM imaging of these samples was conducted to qualitatively examine fibrin network formation, a critical precursor event to thrombus formation (Figure 5C). In these experiments, PTX and SMS again were indistinguishable from control whereas MCC950 showed a substantial decrease in fibrin networks. Taken together, these findings demonstrated the improved hemocompatibility of MCC950 over PTX and SMS.

2.5. MCC950 Suppresses Vascular Inflammation In Vivo

Drug evaluation was next performed in vivo by passively adsorbing each drug onto vascular grafts prior to implantation in a mouse carotid interposition model of graft healing and NIH for 28 days (**Figure 6**A). To test the anti-inflammatory effects of MCC950 in vivo, macrophage recruitment was quantified by CD68^{+} immunostaining to first determine changes to local vascular inflammation (Figure 6B). From day 7 to 28, macrophage recruitment was found to decrease across all groups (Figure 6C). Significant differences occurred at day 28 only in grafts treated with MCC950 which showed an average 57% decrease in total macrophages compared to control. The majority of these macrophages were observed on the exterior of the graft surface. The effects on vascular inflammation were further examined by analyzing IL-1β and TNF-α expression (Figure 6D,E and Figure S5, Supporting Information). By day 28, MCC950 had the largest significant reductions in IL-1β expression followed by PTX when compared to control (0.13 ± 0.01 and 0.41 ± 0.13 vs 0.96 ± 0.2 mm^2, respectively) (Figure 6D). For TNF-α, all drugs

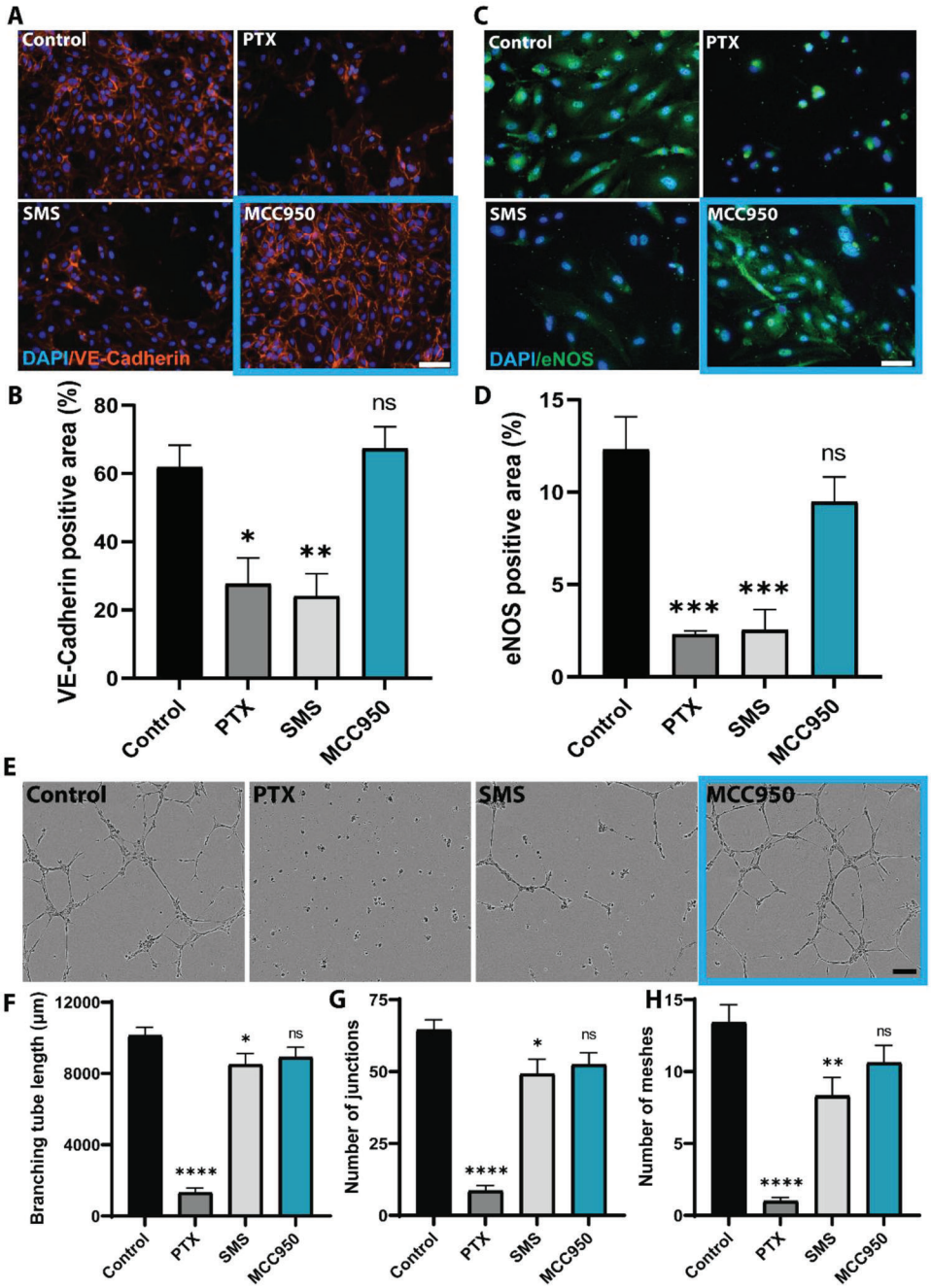

Figure 4. MCC950 does not impair endothelial functionality in vitro. A) Representative images of human coronary artery endothelial cells 3 days after treatment with high dose (20 μM) paclitaxel (PTX), sirolimus (SMS), or MCC950. DAPI stained in blue, vascular endothelial (VE)-Cadherin in orange. Scale bar represents 100 μm. B) Quantification of total VE-cadherin staining represented as a percentage of total area. C) Representative images of human coronary artery endothelial cells 3 days after treatment with paclitaxel (PTX), sirolimus (SMS), or MCC950. DAPI stained in blue, endothelial nitric oxide synthase (eNOS) in green. Scale bar represents 50 μm. D) Quantification of total eNOS staining represented as a percentage of total area. E) Representative images of HCAEC tubule formation assay following 6 h treatment with high concentration (20 μM) paclitaxel (PTX), sirolimus (SMS), or MCC950. Scale bar represents 150 μm. F–H) Quantitative analysis of tubule formation assay presented as G) branching tube length, H) number of tubule junctions formed, and I) number of tubule meshes formed. Data represents mean ± SEM ($n = 3$–4). Statistical significance was determined using Dunnett's multiple comparison test against control group ($^{*}p < 0.05$, $^{**}p < 0.01$, $^{***}p < 0.001$, $^{****}p < 0.0001$).

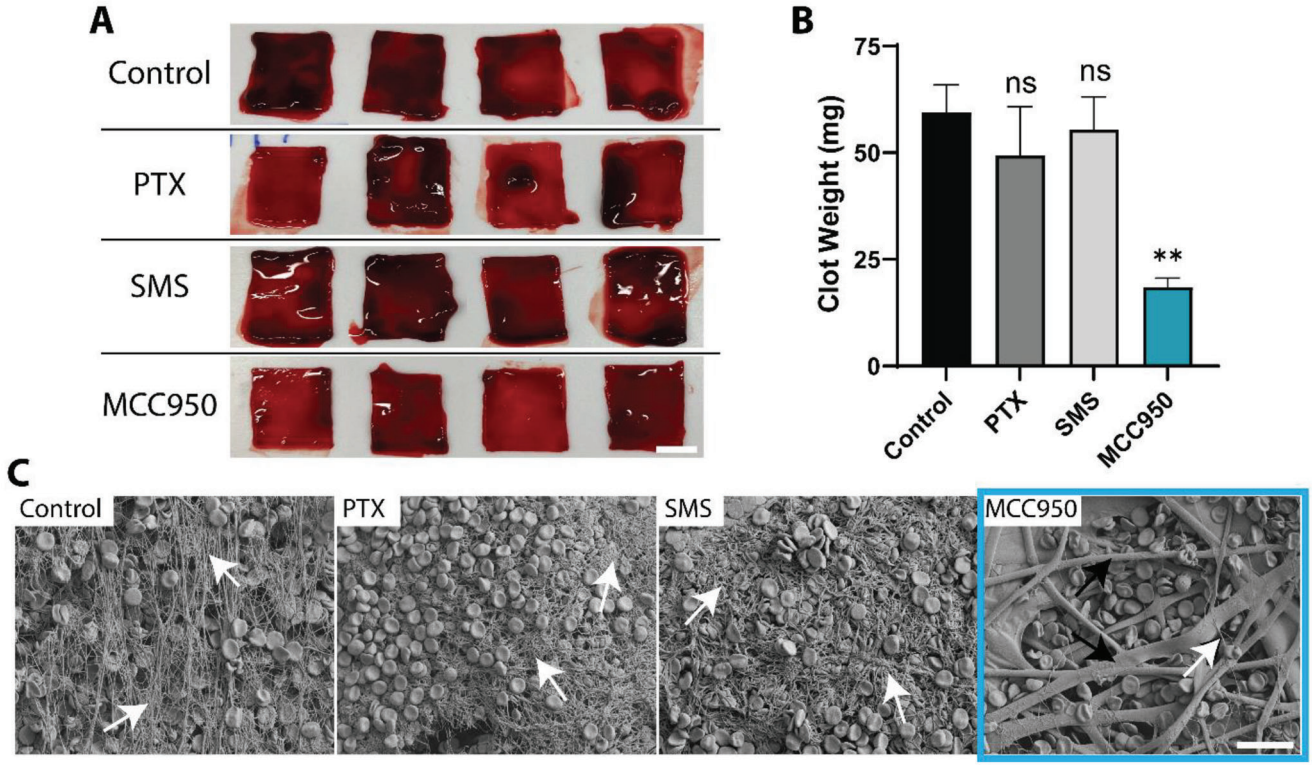

Figure 5. MCC950 shows greater hemocompatibility compared to commercial agents PTX and SMS. A) Representative images of human whole blood clotting assay using high porosity silk scaffolds treated with 30 μM paclitaxel (PTX), sirolimus (SMS), or MCC950 for 1 h. Scale bar = 0.5 cm. B) Quantitative analysis of blood clot weight following 1 h drug incubation. C) Representative scanning electron micrograph images of silk scaffolds following clotting assay. White arrows demonstrate fibrin networks and black arrows show the underlying silk scaffold fibers. Scale bar = 20 μm. Data represents mean ± SEM ($n = 2$–4). Statistical significance was determined using Dunnett's multiple comparison test against control group ($^{**}p < 0.01$, $^{***}p < 0.001$).

led to significant reductions compared to control (0.66 ± 0.18, 0.42 ± 0.12, and 0.35 ± 0.12 vs 1.98 ± 0.34 mm^2, respectively) with the most significant reductions occurring in the MCC950 groups (Figure 6E). Collectively, these results suggested MCC950 was more effective at achieving comprehensive suppression of local inflammation.

2.6. MCC950 Promotes Re-Endothelialization In Vivo

To determine the effects of each drug on functional endothelialization, grafts were immunostained for endothelial coverage (CD31) and function (eNOS), respectively. Endothelialization peaked at day 7 with no changes by day 28 in all grafts (**Figure 7**A). Control, PTX, and SMS treated grafts showed patchy and incomplete $CD31^+$ endothelial coverage of the graft lumen at day 7 when compared to the endothelial layer in MCC950 groups which appeared almost complete. This coverage was quantified at ≈97 ± 1.8% of the total graft lumen, a 25% increase compared to control (Figure 7C). Similarly, at day 7, low levels of $eNOS^+$ staining were evident across the luminal surface of control, PTX and SMS grafts compared to grafts with MCC950 which showed almost complete positive staining (Figure 7B). Over 28 days eNOS was found to increase in control grafts. Notable changes in $eNOS^+$ coverage was observed at day 7, where both PTX and MCC950 showed increased recovery of eNOS function compared to control, although to a significantly higher degree in MCC950 groups (50.49 ± 0.04% and 82 ± 3.14% vs 33.62 ± 3.65%, respectively) (Figure 7D). By day 28 these increases had largely resolved with both PTX and SMS showing decreased $eNOS^+$ coverage compared to control. In contrast, $eNOS^+$ coverage in MCC950 had returned to control levels. These findings suggest that MCC950 promotes more rapid and functional endothelialization.

2.7. MCC950 Suppresses Fibrotic Encapsulation and Neointimal Hyperplasia In Vivo

The ultimate functional outcomes of each drug were assessed by measuring the development of fibrotic encapsulation and NIH using haematoxylin and eosin (H&E) staining (**Figure 8**A,B). The area of the fibrotic capsule surrounding control grafts decreased marginally between day 7 and day 28 (Figure S6A, Supporting Information). Compared to controls, PTX showed a 51% reduction in capsule area at day 7 which was largely maintained by day 28 (1.38 ± 0.16 vs 2.8 ± 0.28 mm^2, Figure 8C). SMS had no effect on capsule area at day 7 but was found to decrease capsule area by 65% by day 28 (0.8 ± 0.14 vs 2.3 ± 0.76 mm^2). Similar to PTX groups, MMC950 showed increasing reductions across

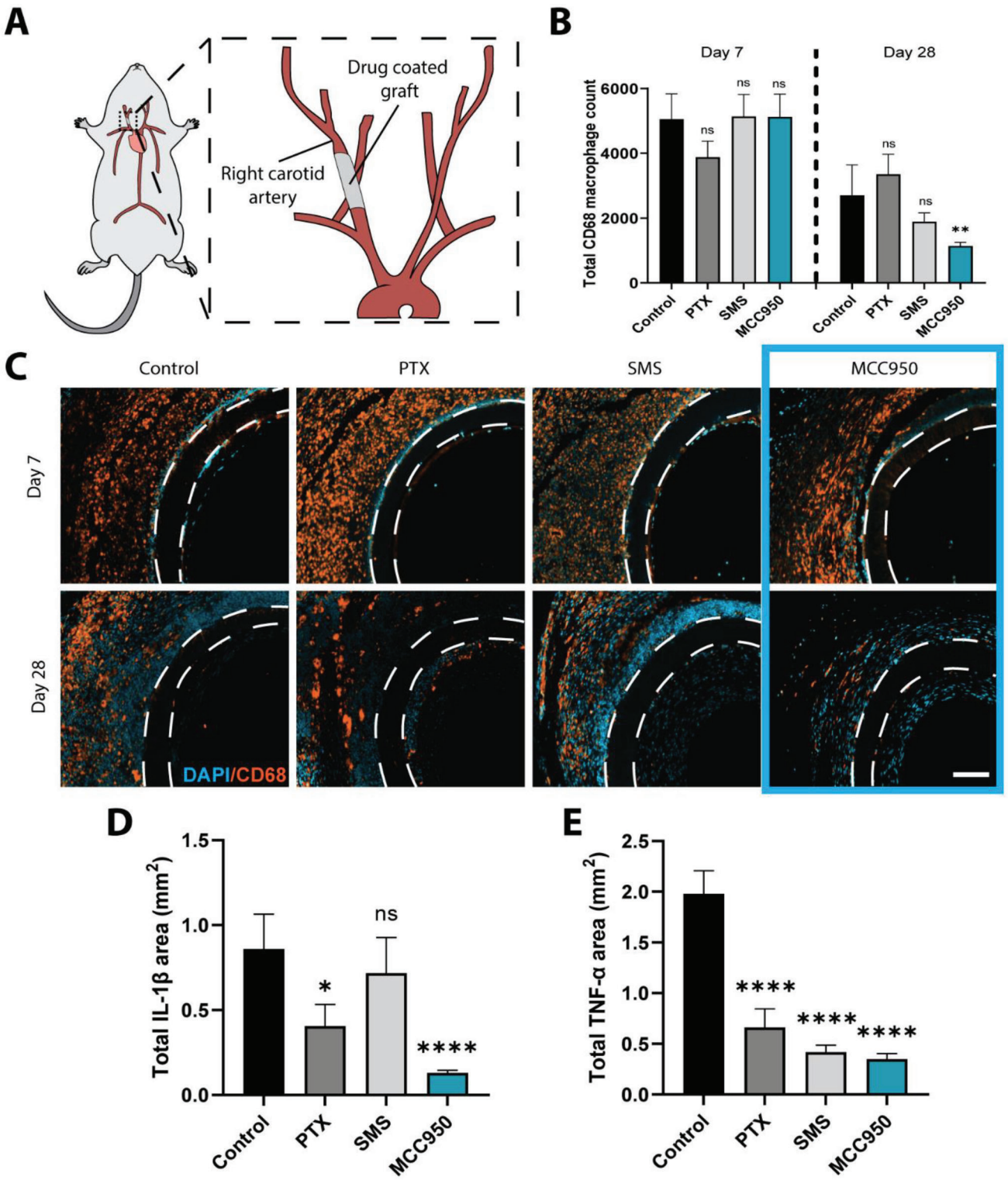

Figure 6. MCC950 strongly suppresses vascular inflammation. A) Schematic representation of the in vivo interposition vascular graft model used in this study. B) Quantification of total number of $CD68^+$ cells. C) Representative images of CD68 stain taken from middle region of explanted grafts. DAPI stained in blue, CD68 stained in orange. Scale bar represents 100 µm. D,E) Quantification of total IL-1β (D) and TNF-α (E) positively stained area at day 28. Data represents mean ± SEM (n = 3–4). Statistical significance was determined using Dunnett's multiple comparison test ($^{*}p < 0.05$, $^{**}p < 0.01$, $^{****}p < 0.0001$).

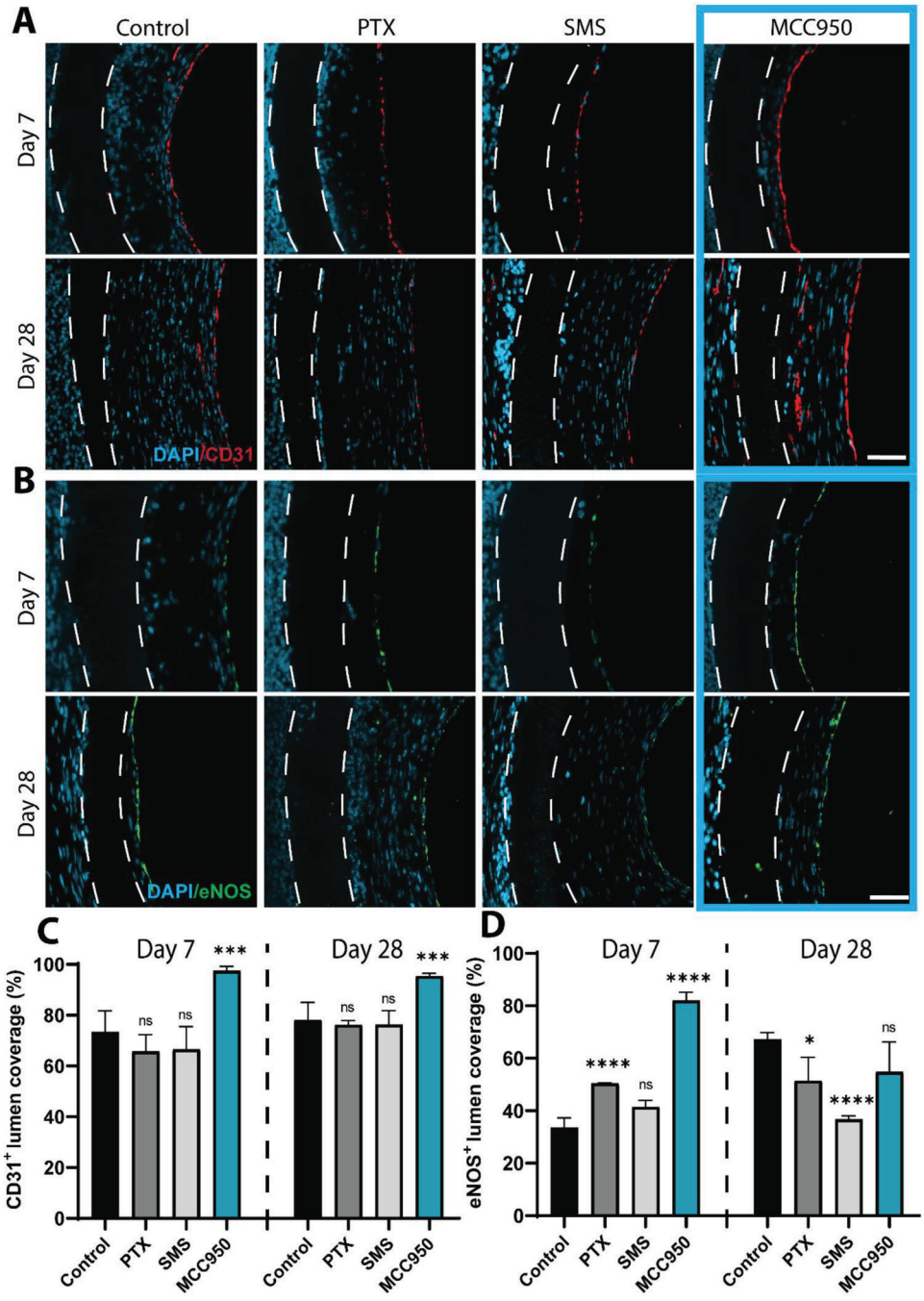

Figure 7. MCC950 promotes rapid re-endothelialization. A,B) Representative images of $CD31^+$ (A) stained sections in red and $eNOS^+$ (B) stained sections in green taken from middle portion of explanted grafts after 7 and 28 days. Scale bar represents 50 µm. C,D) Quantification of $CD31^+$ (C) and $eNOS^+$ (D) staining at day 7 and day 28. Data represents mean ± SEM (n = 2–3). Statistical significance was determined using Dunnett's multiple comparison test against control ($^{***}p < 0.001$, $^{****}p < 0.0001$).

both timepoints. However, despite a smaller a 27% reduction at day 7, MCC950 showed a much larger reduction of 81% at day 28.

Neointima occlusion in the graft lumen of control groups was also found to increase over 28 days (Figure S6B, Supporting Information). PTX treatment showed no significant difference to control groups at any timepoint while SMS showed a 33% increase in neointima occlusion compared to control at day 28 (75.84 ± 3.34% vs 50.88 ± 7.68% occlusion) (Figure 8D). Interestingly, at both days 7 and 28, treatment with MCC950 significantly reduced neointimal occlusion by 49% and 33%, respectively, compared to control (15.64 ± 0.9% vs 30.75 ± 6.29% and 34.13 ± 13.23% vs 50.88 ± 7.68% occlusion). Collectively, this suggested that by suppressing the inflammatory microenvironment surrounding the

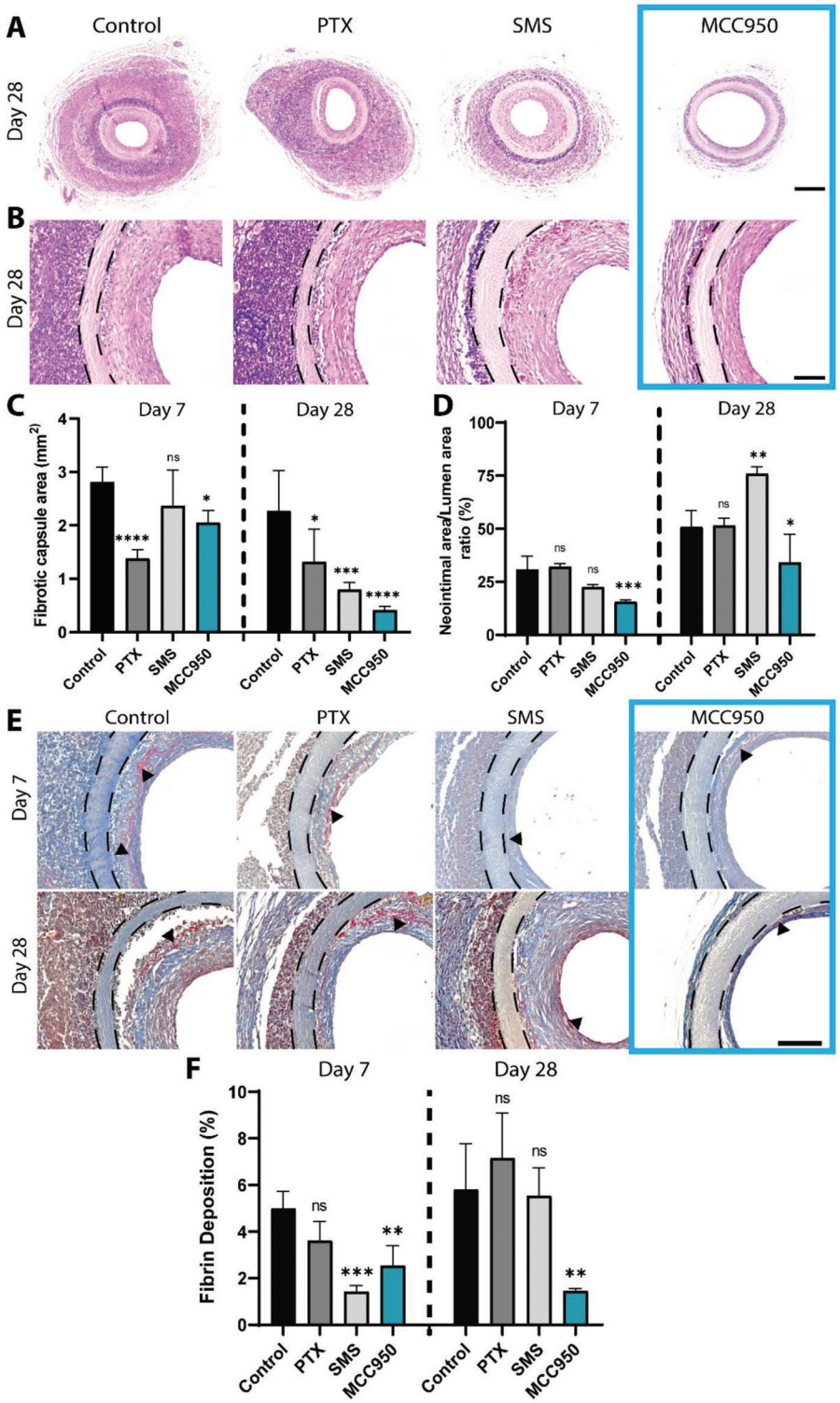

Figure 8. MCC950 reduces fibrotic encapsulation, neointimal hyperplasia, and fibrin deposition. A) Representative images of hematoxylin and eosin-stained grafts at day 28 showing fibrotic capsule surrounding the graft. Scale bar represents 300 µm. B) Representative images of hematoxylin and eosin-stained grafts at day 28 showing neointimal hyperplasia. Black dotted lines show graft outline. Scale bar represents 100 µm. C) Quantification of fibrotic capsule area surrounding graft. D) Quantification of neointimal area expressed as a percentage of total lumen area. E) Representative brightfield images of Martius Scarlet Blue stain. Mature fibrin is stained in red (demonstrated with black arrows), fresh fibrin in yellow, and collagen in blue. Scale bar = 100 µm. F) Quantification of mature fibrin (red) deposition within the neointima at days 7 and 28, represented as a percentage of the positive staining area versus total lumen area. Data represents mean ± SEM ($n = 2$–4). Statistical significance was determined using Dunnett's multiple comparison test against control ($^{*}p < 0.05$, $^{**}p < 0.01$, $^{***}p < 0.001$, $^{****}p < 0.0001$).

graft, MCC950 was able to achieve better long-term suppression of NIH.

Fibrin deposition within the graft lumen was also analyzed using Martius Scarlet Blue staining as an additional measure of hemocompatibility and indicator of potential thrombosis (Figure 8E). Over the 28 days, fibrin deposition increased across all groups except for grafts treated with MCC950, which showed a sustained reduction in fibrin (Figure 8F). Compared to control, MCC950 significantly decreased fibrin by 49% and 74% at day 7 and 28, respectively. Although SMS decreased fibrin deposition at day 7, it was unable to sustain this effect at day 28. PTX showed no significant reduction in fibrin levels at either time point compared to control.

3. Discussion

Current drug-eluting endovascular balloons and stents using anti-proliferative agents PTX and SMS largely fail to address the underlying inflammation which drives NIH. This leads to poor long-term patency and frequent re-intervention in areas of aggressive NIH, such as the legs.[9] Additionally, in the case of PTX use in peripheral applications, high doses and long elution times have led to increases in amputation rates and mortality, highlighting the need for a safer, more effective drug-eluting strategy with more durable benefits.[10] The NLRP3 inflammasome is a component of the innate immune system with growing evidence for its involvement in vascular inflammation specific to athero-occlusive cardiovascular diseases.[16] However, examination of the NLRP3-inflammasome as a potential drug-eluting target for endovascular devices and vascular injury has not yet been studied. Here, we evaluate antagonism of the NLRP3 inflammasome using the selective small molecule inhibitor MCC950, in comparison to commercial agents used in drug-eluting devices, PTX and SMS.

Driven by non-specific anti-proliferative functions acting broadly on all cells present within the vessel wall and lumen, PTX and SMS compromise long-term vessel inflammation and healing.[17] Consistent with these actions, these drugs caused a dose-dependent decrease in cell viability within macrophages, endothelial cells, and SMCs in vitro. In agreement with clinical observations, this effect was most notable in PTX. PTX action as a cytotoxic agent is strategically utilized to treat more aggressive cases of NIH occurring in settings such as peripheral arterial disease.[18] Additionally, PTX usage comes with a trade-off between effective suppression of NIH and patient safety. Its significant cytotoxic effects can be detrimental to organs downstream from the vasculature from where its delivered.[10] SMS showed similar reductions in cell viability but to a lesser extent. This was most likely due to its cytostatic rather than cytotoxic mechanism of action, which halt cell division rather than promoting cell death.[7] These features make SMS beneficial in regions such as the coronary arteries where NIH is less aggressive and allows clinicians to prioritize patient safety.[8b] However, these collective anti-proliferative effects are of greatest impact to endothelial cells, highlighting safety limitations in preventing short-term vessel healing and increased risk of thrombosis, demonstrated by the poor clinical performance of first-generation DES in coronary applications.[19] In contrast, MCC950 showed negligible cytotoxic effects on all tested cell lines. This is the first direct evidence to show biosafety of MCC950 on vascular endothelial cells, macrophages, and SMCs in direct comparison to PTX and SMS. Support of MCC950 cytocompatibility has increasingly been reported, previously shown to be non-toxic to human kidney HEK293 and liver HepG2 cell lines.[20] More broadly, these results also suggest that MCC950 functions through mechanisms distinct from blocking proliferation, representing a fundamental departure from PTX and SMS.

Further examination of MCC950 mechanism of action was performed in macrophages using an immune activation model that aims to model the NLRP3-inflammasome. LPS stimulation was used as a priming signal to activate TLR4 receptors, triggering the secretion of TNF-α and initiating the transcription of the NLRP3 protein. Secondary co-stimulation with ATP facilitated the oligomerization/activation of the NLRP3 inflammasome leading to the secretion of IL-1β and initiation of pyroptotic cell death. Quantification of TNF-α was used as a surrogate measure of systemic inflammation while IL-1β and rate of pyroptosis was measured as a specific output of NLRP3-mediated inflammation. In this model, both PTX and SMS decreased IL-1β and TNF-α, but showed no effect on pyroptosis. These results can be largely attributed to the broad effects these two drugs are known to have on inflammation. In an LPS-induced liver injury model in mice, PTX was shown to decrease levels of TNF-α, IL-1β and IL-6 by upregulating miR-27a, a known inhibitor of cell proliferation and systemic inflammation.[21] Similarly, SMS has been reported to down-regulate widely acting inflammatory cytokines including IL-6 and TNF-α in THP-1 macrophages treated with LPS.[22] Although the immunomodulatory effects of SMS are still poorly understood, some reports have indicated that the drug can increase sirtuin 1 which leads to decreased NF-κB activity, reducing pro-inflammatory cytokine production.[22,23] In contrast, MCC950 showed no effect on TNF-α secretion but instead reduced IL-1β secretion and prevented pyroptosis only. As exclusive products of NLRP3-inflammasome activation, this validated that MCC950 was highly selective for NLRP3-mediated inflammation. Previous studies have similarly validated inhibition of the NLRP3 inflammasome without affecting other elements of the innate immune system including activation of other inflammasomes such as AIM2, NLRC4, or NLRP1.[24] Our study evaluated both murine and human derived macrophages, and found the trends to be similar. However, consistent with previous studies, we observed that the murine derived cell line, being adherent and more responsive to stimuli, yielded less variability.[25] Collectively, our results demonstrate the targeted anti-inflammatory functions of MCC950 on NLRP3-mediated inflammation and further highlight its distinction from PTX and SMS.

Further evidence of the potential benefits of MCC950 as an alternative drug-eluting approach was observed in endothelial integrity and function assays. In response to vascular injury, locally derived endothelial cells and endothelial progenitor cells repair and repopulate the endothelium.[26] However, delayed re-endothelialization is common in the context of drug-eluting devices. In endothelial cells in vitro, PTX and SMS caused reductions in the expression of vascular endothelial cadherin (VE-cadherin) and eNOS, indicating impairment to critical aspects of endothelial recovery. VE-cadherin is an endothelial specific adhesion molecule essential to controlling the integrity and permeability of junctions within the healing vessel endothelium.[26] The

healing endothelium also requires functional eNOS to synthesize nitric oxide which plays numerous central roles from the regulation of vascular tone to injury recovery.[27] Reduced expression of both markers are key indicators of endothelial dysfunction. MCC950 alone preserved the expression of both VE-cadherin and eNOS, suggesting its improved suitability for endothelial recovery. This was supported with transcriptional analysis of CDH5, PECAM, and eNOS genes that showed MCC950 caused no significant reductions in their expression compared to control. Further analysis using the established Matrigel-based tubule formation assay[28] to examine endothelial function exemplified the negative effects of both PTX and SMS on endothelial recovery. Both drugs function mechanistically to disrupt cell growth and division, preventing neo-capillary formation. In contrast, MCC950 had no impact on tubule formation, demonstrating a clear distinction between its mechanism of action which had no adverse effects on endothelial cells and showcases its potential for improved re-endothelialization in vivo.

Hemocompatibility and the risk of thrombosis is a major concern for all vascular devices. Current devices that employ PTX or SMS can lead to high rates of late-stage thrombosis due to poor re-endothelialization and excessive fibrin accumulation in the vessel wall.[29] Drugs eluted from these devices should ideally have high hemocompatibility and can carry additional benefit by reducing the risk of thrombosis. In human whole blood clotting assays, MCC950 decreased clotting weight and fibrin accumulation. Previous studies have shown the NLRP3 inflammasome to be activated in platelets during thrombosis resulting in the secretion of both IL-1β and tissue factor (TF).[30] IL-1β along with other mediators are known to promote platelet activation and aggregation, while TF helps to initiate the coagulation cascade by increasing platelet production of fibrinogen, the precursor to fibrin.[31] Our study is in agreement with previous research suggesting a link between NLRP3 inhibition and reduced arterial thrombosis. However, our findings are the first to directly compare the efficacy of MCC950 with commercial drug standards PTX and SMS.

Extending these findings to the in vivo, drug evaluation was conducted using vascular grafts passively absorbed with each drug prior to implantation in an established mouse carotid interposition grafting model of NIH for 7 and 28 days.[32] Vascular inflammation was first assessed by quantifying macrophages. Macrophages resolved over the 28 days, however PTX and SMS showed no differences in macrophage levels compared to control. In contrast, MCC950 enhanced resolution of macrophages by day 28, indicative of strong anti-inflammatory effects. As the principal drivers of vascular inflammation, large populations of macrophages surrounding vascular lesions are associated with increased risk of NIH.[33] Surprisingly, this was not entirely associated with pro-inflammatory cytokine expression. Both PTX and SMS showed reductions in IL-1β and TNF-α despite no significant changes to macrophage content. This could potentially be explained by increased macrophage retention by PTX and SMS, compared to MCC950 which enhanced macrophage resolution. Previous studies have suggested that both PTX and SMS shift the balance of macrophage polarization toward the pro-inflammatory M1 phenotype directly via the TLR4 and mTOR pathways, respectively, independent of cytokine stimuli and/or cytokine production.[34] M1 macrophages are enriched within inflamed tissue until signaled to resolve by anti-inflammatory cytokines. Increased macrophage retention together with enhanced cellular dysfunction because of PTX and SMS treatment could also explain how cytokine levels were lowered. Compared to PTX and SMS, MCC950 showed even greater reductions of both IL-1β and TNF-α together with reduced macrophage levels. As the major product of NLRP3-mediated inflammation, IL-1β promotes the recruitment and retention of macrophages during inflammatory conditions.[35] In agreement with our observations, a previous study showed MCC950 decreased infiltrating $CD68^+$ macrophages in a mouse model of myocardial infarction and suggested IL-1β suppression was, at least in part, a driving factor.[13] However, contrary to previous in vitro findings, MCC950 also reduced TNF-α. This was suggestive of indirect anti-inflammatory effects that reflect a broader immunosuppressive effect. These outcomes demonstrate the widespread effects MCC950 had on the local inflammatory microenvironment surrounding the graft.

Re-endothelialization is a critical step in healing and reducing NIH in the long term.[36] Despite the short-term benefits PTX and SMS have on NIH, a limitation of these anti-proliferative agents is delayed re-endothelialization.[37] We chose the mouse grafting model to study this as it has been previously well characterized and demonstrated to be a highly reproducible model of re-endothelialization in a compressed 28-day time frame, making it ideal for comparative studies identifying promising new candidate molecules.[32] Here, endothelial coverage was found to occur prior to the re-establishment of endothelial function. PTX and SMS showed no differences from control at day 7 or 28, indicating that both drugs had only achieved baseline levels of re-endothelialization. This was also associated with reduced eNOS function in both groups by day 28, suggesting that both drugs were impairing the re-establishment of endothelial function. Contrary to these findings, MCC950 grafts not only had the highest levels of endothelial coverage, achieving near complete re-endothelialization by day 7, but also enhanced rates of early eNOS expression compared to control. Antagonism of NLRP3 has been previously linked to similar endothelial protective effects. NLRP3 inflammasome-mediated pyroptosis has been shown to closely associate with endothelial membrane rupture and cell lysis, releasing various cellular contents including pro-inflammatory cytokines and high-mobility group box 1 which further exacerbate endothelial dysfunction by increasing cell permeability and disrupting endothelial junctions.[38] These effects are likely to occur naturally in control implants potentially explaining the enhanced re-endothelialization of MCC950 grafts compared to control. These results are the first to show positive re-endothelialization effects due to MCC950 in the context of materials implanted directly into the vasculature. Interestingly, these enhanced rates of eNOS expression had resolved back down to control levels by day 28. This may suggest that these effects are dependent upon MCC950 acting directly upon endothelial cells, rather than indirectly through changes to macrophages and the local immune microenvironment.

Inflammatory processes drive fibrotic capsule formation and NIH, the main biological causes of endovascular device failure.[39] Minimizing fibrotic encapsulation is associated with a suppressed local inflammatory response and has been closely linked to end-stage tissue healing.[40] Following stent implantation, a fibrous capsule made up of mostly collagen fibers forms

around the implant and induces the progression of NIH.[41] Consistent with the benefits MCC950 showed in suppressing inflammatory conditions discussed above, we also demonstrated the striking reductions MCC950 had in fibrotic capsule development, further highlighting its ability to reduce the inflammatory microenvironment and promote healthy vascular remodeling. In addition, contrary to clinical observations, PTX and SMS showed no reductions in NIH in our model. Given that this carotid grafting model is an accelerated model of NIH, the dosage and rate of drug delivery may have been insufficient for both drugs, while their usual physiological mode of action is heavily dependent on absorption into the native vascular wall. In our context, SMS appeared to worsen hyperplasia development at day 28. However, the aggressive formation of NIH in this model did demonstrate the striking impact of NLRP3-antagonism and MCC950. In this model, MCC950 was comparatively stronger at suppressing hyperplasia, showing significant reductions as early as day 7 which persisted to day 28. Hemocompatibility is a critical factor that affects the long-term performance of vascular materials. When fibrin accumulates on the material surface, it increases the risk of thrombus formation which can obstruct blood flow and potentially lead to life-threatening conditions. PTX and SMS were unable to sustain a reduction in fibrin deposition within the neointima, while MCC950 significantly decreased fibrin levels at day 28. Fibrin deposition and re-endothelialization are closely related, as excessive deposition can impede the re-endothelialization process. Rapid endothelialization on the other hand is associated with a reduced risk of fibrin deposition. Achieving rapid re-endothelialization is a key strategy to improving the long-term performance of vascular materials and devices both in limiting NIH development, fibrin deposition, and thrombus formation.[42] Coupled with enhanced rates of re-endothelialization, these results showcase the potential long-term benefits of MCC950. Collectively, these in vivo findings represent crucial proof-of-concept data for the therapeutic benefit of a selective immunosuppressive MCC950 approach. This has important implications for stenting and balloon applications with this study justifying further testing and validation of our approach in established large animal models specific to these applications.

4. Conclusion

This study demonstrated the advantages of a selective anti-inflammatory approach using the NLRP3-inflammasome inhibitor MCC950 over the current clinical standards for reducing NIH employing anti-proliferative drugs. Compared to the non-specific function of PTX and SMS, MCC950 does not impair the viability or function of endothelial cells, allowing re-endothelialization and vessel healing to occur. By instead selectively targeting NLRP3-mediated inflammation, MCC950 exhibited a robust suppression of the inflammatory microenvironment surrounding implanted vascular grafts leading to sustained reductions of NIH. Our findings are the first to demonstrate the effectiveness of MCC950 as a drug-elution strategy for materials implanted in the vasculature. Further validation of this targeted anti-inflammatory approach in large animal models is now warranted.

5. Experimental Section

Cell Culture: Murine macrophages (J774a.1, passage 3–6, Sigma Aldrich, MA, USA), SMCs (CSC-C4357X, passage 4–6, Creative Bioarray, Shirley, NY, USA), human coronary artery endothelial cells (HCAECs, 300–05a, passage 4–6, Cell Applications, San Diego, CA, USA), and THP-1 (passage 3–6, Sigma Aldrich, MA, USA) were maintained at 37 °C in a 5% CO_2 humidified incubator. Macrophages were cultured in Dulbecco's Modified Eagle Medium (10 mL,) supplemented with Fetal Bovine Serum (10% v/v,) and 1% antibiotics (100 U mL^{-1} Penicillin and 100 µg mL^{-1} Streptomycin), SMCs in SMC medium (Merck, Darmstadt, Germany), HCAECs in Mesoendo medium (Merck, Kenilworth, NJ, USA), and THP-1s in RPMI-1640 medium (Merck, Kenilworth, NJ, USA). The cell culture media was replaced with fresh media every 2 – 3 days. Cells were subcultured after reaching ≥85% confluency by first aspirating the old medium, washing with Phosphate-Buffered Saline (10 mL, PBS), and adding fresh medium (10 mL). A cell scraper was used to mechanically detach macrophages from the flask while SMCs and HCEACs were trypsinized. THP-1s were aspirated from flask. Resulting cell suspension was transferred to a falcon tube for centrifugation (1200 rpm, 5 min). The supernatant was aspirated, and the pellet was resuspended in fresh medium (2–5 mL, depending on size). Cell concentration was determined by staining with Trypan Blue (1:1) and manually counting cells using a haemocytometer. The cell suspension was triturated before seeding the required volume onto a new T75 flask and adding fresh medium (10 mL).

Cell Viability Assay: Cells were seeded into 96-well plates at a density of 3×10^4 cells per well followed by immediate treatment with drug groups (200 µL medium in total with drug) at specified concentrations. For THP-1s, cells were treated with phorbol 12-myristate 13-acetate (PMA, 100 ng mL^{-1}) for 24 h before seeding. Cultures were left to incubate for 3 days. Cell viability was quantified using an Alamar Blue assay at a ratio of 1:10 with fresh cell culture media. Plates were incubated for 3 h and quantified using a microplate reader (Infinite M1000 PRO) for fluorescence analysis. Excitation and emission wavelengths were set at 560 and 590 nm, respectively. Complementary morphological analysis of treated cultures was conducted at 3 days post-seeding. Cells were rinsed twice with PBS prior to fixation with 10% formalin for 10 min and an additional two 5 min washes in PBS. Cells were then permeabilized using a Triton X-100 detergent (0.1% in PBS) for 10 min followed by two 5 min washes in PBS. Cell nuclei were fluorescently stained using NucBlue Fixed Cell ReadyProbes Reagent (DAPI, ThermoFisher Scientific, 1 drop per mL PBS) and F-actin with ActinRed 555 Reagent (Rhodamine phalloidin, ThermoFisher Scientific, 1 drop per mL PBS). Cells were visualized and imaged using Zen inverted fluorescent microscope.

NLRP3 Inflammasome Activation Assay: J774a.1 murine macrophages were seeded onto a 24-well plate at a density of 1.2×10^5 cells per well. Following pre-treatment with PMA (100 ng mL^{-1}) for 24 h, THP-1s were also seeded at the same density as murine macrophages. NLRP3 inflammasome activation was achieved in two steps. First, the inflammasome was primed by stimulating cells with lipopolysaccharide (1 µg mL^{-1}) for 3 h at 37 °C, inside the humidified incubator (5% CO_2). After 90 min, drugs were added at the specified range of doses. After an additional 90 min (3 h post-LPS stimulation), cells were stimulated with ATP (1.25 mM) to activate the inflammasome and left in the incubator overnight. Enzyme-linked immunosorbent assay (ELISA) kits for TNFα (Abcam, ab208348 and ab181421) and IL-1ß (Abcam, ab197742 and ab214025) were used to quantify cytokine levels in supernatants according to manufacturer's instructions. Pyroptosis was evaluated through measurement of F-actin degradation by co-staining cells with DAPI and Rhodamine Phalloidin, as described above. Percentage of cells undergoing pyroptosis was quantified by manually counting DAPI positive cell nuclei containing an intact F-actin ring and normalized against total amount of DAPI positive cell nuclei.

In Vitro Endothelial Integrity Assay: Endothelial cell integrity was assessed using immunohistochemistry. HCAECs were seeded as per cell viability protocols and on day 3 were similarly fixed and permeabilized as described above. Cells were then blocked with bovine serum albumin (BSA, 5% in PBS-Tween 20) for 1 h at room temperature. After blocking, cells were stained with primary antibodies against vascular endothelial

(VE)-cadherin (1:200, ab33168, Abcam) or endothelial nitric oxide synthase (eNOS) (1:100, ab76198, Abcam) for 48 h at 4 °C. Cells were then washed with PBST (2 × 10 min) and secondary antibody (1:500, ab150077, Abcam) was added for 1 h at room temperature. After a series of washes with PBST (2 × 10 min) and PBS (1 × 5 min), DAPI solution (ThermoFisher Scientific, 1 drop per mL PBS) was added. Cells were left to rest in the dark for 10 min before being visualized and imaged using Zen inverted fluorescent microscope. Using a constant threshold, amount of VE-cadherin and eNOS positive staining was measured as a percentage of total area.

qPCR: Quantitative PCR was performed using iQ SYBR-Green Supermix and the iCycler real-time PCR detection system (Bio-Rad). Angiogenesis-related gene expression was calculated using primers for eNOS (forward, 5′-CGGAGAATGGAGAGAGCTTTG-3′; reverse, 3′-TGCTGTTGAAGCGGATCTTA-5′), CDH5 (forward, 5′-CGCAATAGACAAGGACATAAC-3′; reverse, 3′-TATCGTGTGATTATCCGTGAGG-5′), PECAM1 (forward, 5′-AGATACTCTAGAACGGAAGG-3′; reverse, 3′-CAGAGGTCTTGAAATACAGG-5′), KDR (forward, 5′-GTACATAGTTGTCGTTGTAGG-3′; reverse, 3′-TCAATCCCACATTTAGTTC-5′), and 18S (forward, 5′-GTAACCCGTTGAACCCCATT-3′; reverse, 3′-CCATCCAATCGGTAGTAGGG-5′). 18s was used as a universal housekeeping gene and fold change calculated using the delta–delta CT method.

Endothelial Cell Tube Formation: Matrigel (Corning, 354 248)-coated 96-well plates were used to culture HCAECs at a concentration of 10 000 cells per well. Drugs were mixed with fresh HCAEC growth media to the listed final concentrations, and then added to the Matrigel cultures. The cells were monitored for 16 h and time-lapse images were captured using an IncuCyte Zoom live cell imager (Essen Bioscience). To analyze the capillary network, four representative images were selected at 5 h post-seeding from each condition with five replicate wells. The number of junctions, meshes, and segments were analyzed using the angiogenesis analyzer plugin in ImageJ.

Silk Graft Manufacture: *Bombyx mori* silk cocoons (Tajima Shoji Co., LTD., Yokohama, Japan) were purified as previously described.[43] Briefly, silk cacoons (5 g) were boiled in sodium carbonate (0.02 M, 2 L) for 30 min to remove sericin. Extracted silk fibers were washed in ultrapure water (Arium Pro, Sartorius, Göttingen, Germany) and dried overnight at room temperature before being dissolved in lithium bromide (9.3 M, LiBr) for 4 h at 60 °C to produce a 20% w/v solution. Dissolved silk–LiBr solution was transferred to SnakeSkin dialysis tubing (3500 kDa MWCO; Themo Fisher Scientific, Waltham, MA, USA) and dialyzed against 5 L of ultrapure water for 72 h. Water was changed three times a day to maintain diffusion gradient and ensure complete removal of LiBr. The solution was then centrifuged twice to remove impurities (12 000 g, 4 °C, 20 min). Silk solution was then lyophilized for 48 h and dissolved in hexafluoroisopropanol at 15% w/v.

This solution was electrospun using an IME Medical Electrospinner (IME Medical Electrospinning, Leiden, Netherlands) from a 0.6 mm diameter needle with an applied voltage of 16 kV onto a 0.5 mm stainless steel mandrel rotating at 500 rpm. Flow rate was 2 mL h^{-1}, controlled by a syringe pump (Elite 11, Harvard Apparatus), and distance between needle and grounded mandrel was 220 mm. Relative humidity was regulated within the chamber and maintained at 30 ± 5%. Immediately following electrospinning, silk grafts were crosslinked on the mandrel by water annealing for 18 h.[44] Residual HFP was removed by gently stirring grafts in 2 L ultrapure overnight, followed by drying at room temperature. Grafts were stored in a plastic container at room temperature with silica gel desiccant.

Mouse Carotid Graft: Study was approved by the University of Sydney Animal Ethics Committee (protocol number 2020/1785). Experiments were conducted in accordance with the Australian Code of Practice for the Care and Use of Animals for Scientific Purpose. C57BL/6 mice (male, 9–10 weeks old, 25 ± 2 g), purchased from Animal Resources Center (Canning Vale, WA, Australia), were used for this model. Silk grafts 10 mm in length and 0.5 mm in diameter were disinfected in 70% ethanol and exposed to ultraviolet light for 30 min. The drugs were loaded by submerging silk grafts in a high concentration solution of each drug (1 mg mL^{-1} in PBS) and incubated overnight at 4 °C to ensure complete drug saturation. Drug-coated grafts were implanted into the right common carotid artery as previously described.[32] Briefly, the midpoint of the right common carotid artery was double ligated and dissected between the ligations. Polyimide cuffs (Cole–Parmer North America, Vernon Hills, Illinois) were guided onto each end of the arteries and clamped. Overhanging ends of the arteries were everted over cuffs and secured using 8–0 sutures. Silk grafts were sleeved over each cuff and secured using 8–0 sutures. Clamps were released and blood flow was confirmed with pulsation, therefore indicating successful graft implantation. After 7 or 28 days, mice were perfused using heparinized saline (50 U mL^{-1}) and the grafted carotid artery was isolated and dissected proximal and distal to the graft.

Hemocompatibility Assay: Wells in a 24 well plate were coated with 3% BSA for 1 h. Plates were then washed 3× with PBS and left to dry overnight. High porosity silk scaffold sheets, electrospun using the same properties provided above were cut into 0.8 × 1.2 cm samples, pre-weighed and placed into individual wells. Fresh blood was collected and mixed with heparin (0.3 U mL^{-1}). Blood (750 µL per well) was added onto samples followed by treatment by MCC950 (30 µM), PTX (30 µM), or SMS (30 µM). Samples were left for 1 h on an orbital shaking incubator (65 rpm, 37 °C). Blood was removed and samples were washed 3× with PBS before being weighed. Clot weight was calculated by subtracting the weight of the scaffold post-blood incubation by initial scaffold weight.

Histology and Immunohistochemistry: Explanted grafts were fixed in paraformaldehyde (4%) overnight at room temperature. Samples were dehydrated through an ascending ethanol gradient, embedded in paraffin and sectioned transversely at 5 µm from proximal to distal anastomosis. For histology staining, five slides from equidistant points along the graft (proximal to distal) were deparaffinized, rehydrated, and stained with H&E staining and Martius Scarlet Blue staining. The same procedure was conducted for immunohistochemistry staining but stained with primary antibodies against CD68 (1:500, ab125212, Abcam), IL-1β (1:500, ab205924, Abcam), TNF-α (1:200, ab34674, Abcam), CD31 (1:100, ab182981, Abcam), and eNOS (1:50, ab300071, Abcam). Secondary antibodies against rabbit (1:250, ab150080, Abcam and 1:500, ab150077, Abcam) were used to detect primary antibodies. Sections were mounted and cover slipped with DAPI-containing mounting media (Sigma Fluoroshield with DAPI, F6057).

Quantitative Analysis: Analysis of histology and immunohistochemistry slides was done using ImageJ. For H&E staining, neointima was quantified as percentage of total lumen area defined by the inner graft wall. For Martius Scarlet Blue staining, fibrin deposition was quantified using the "Colour Threshold" function in ImageJ to calculate amount of positive red staining present within the neointima, which was then represented as a percentage of total lumen area. Fibrotic capsule was represented as total adventitial tissue area surrounding the graft. For CD68 staining, total $CD68^+$ cell count and $CD68^+$ cell count within the graft wall was quantified using a constant threshold intensity. Total IL-1β and TNF-α positive staining area was also measured. CD31 lumen coverage was quantified by first measuring the lumen circumference, followed by measuring the length of endothelium showing positive staining. Lumen coverage was then calculated as length of $CD31^+$ staining divided by lumen circumference. eNOS lumen coverage was quantified in the same way, represented as length of $eNOS^+$ staining divided by lumen circumference.

Statistical Analysis: Data are expressed as mean ± standard error of the mean. Analysis was performed in GraphPad Prism 9 (Graphpad Software, San Diego, California) and statistically significant differences were determined by *t*-test, or using one- or two-way analysis of variance followed by Dunnett's multiple comparisons test. For in vivo data, statistical analysis was performed on the grouped data comprising of all five graft regions. In vivo figures in this paper represent the respective averages of all regions for each graft. $P < 0.05$ was considered statistically significant. *, **, *** and **** display $P < 0.05$, $P < 0.01$, $P < 0.001$, and $P < 0.0001$ respectively.

Supporting Information

Supporting Information is available from the Wiley Online Library or from the author.

Acknowledgements

This work was supported by the National Health and Medical Research Council (APP1162969; S.G.W), funding from the Sydney Local Health District (S.G.W), and from NSW Health in the form of a NSW Cardiovascular Early-Mid Research Grant (S.G.W and R.P.T H21/174585). R.P.T. receives funding as a National Heart Foundation Postdoctoral Fellow. S.G.W receives funding as a National Heart Foundation Future Leader Fellow. J.R.K receives funding as an ARC Future Fellow (FT210100668). The authors acknowledge the facilities as well as scientific and technical assistance at the Australian Center for Microscopy and Microanalysis, The University of Sydney.

Open access publishing facilitated by The University of Sydney, as part of the Wiley - The University of Sydney agreement via the Council of Australian University Librarians.

Conflict of Interest

The authors declare no conflict of interest.

Data Availability Statement

The data that support the findings of this study are available from the corresponding author upon reasonable request.

Keywords

MCC950, neointimal hyperplasia, NLRP3, restenosis, vascular inflammation

Received: January 24, 2023
Revised: March 31, 2023
Published online: May 7, 2023

[1] A. K. Thukkani, S. Kinlay, *Circ. Res.* **2015**, *116*, 1599.
[2] M. Schillinger, E. Minar, *Vasc. Health Risk Manage.* **2005**, *1*, 73.
[3] R. P. Tan, I. Ryder, N. Yang, Y. T. Lam, M. Santos, P. L. Michael, D. A. Robinson, M. K. Ng, S. G. Wise, *JACC: Basic Transl. Sci.* **2021**, *6*, 693.
[4] S. O. Marx, H. Totary-Jain, A. R. Marks, *Circ.: Cardiovasc. Interventions* **2011**, *4*, 104.
[5] D.-H. Lee, J. de la Torre Hernandez, *Eur. Cardiol.* **2018**, *13*, 54.
[6] D. Zhang, Y. Ruhao, S. Wang, Z. Dong, *Drug Des., Dev. Ther.* **2014**, *8*, 279.
[7] S. N. Sehgal, *Transplant. Proc.* **2003**, *35*, S7.
[8] a) K. McKeage, D. Murdoch, K. L. Goa, *Am. J. Cardiovasc. Drugs* **2003**, *3*, 211; b) F.-J. Neumann, W. Desmet, E. Grube, J. Brachmann, P. Presbitero, P. Rubartelli, A. Mügge, F. D. Pede, D. Füllgraf, W. Aengevaeren, L. Spedicato, J. J. Popma, *Circulation* **2005**, *111*, 2107; c) J. Waugh, A. J. Wagstaff, *Am. J. Cardiovasc. Drugs* **2004**, *4*, 257; d) S. Müller-Hülsbeck, K. Keirse, T. Zeller, H. Schroë, J. Diaz-Cartelle, *J. Endovasc. Ther.* **2016**, *23*, 701.
[9] a) D. Siablis, D. Karnabatidis, K. Katsanos, A. Diamantopoulos, S. Spiliopoulos, G. C. Kagadis, J. Tsolakis, *J. Vasc. Interv. Radiol.* **2009**, *20*, 1141; b) S. Müller-Hülsbeck, K. Keirse, T. Zeller, H. Schroë, J. Diaz-Cartelle, *CardioVasc. Interventional Radiol.* **2017**, *40*, 1832; c) G. Tepe, T. Zeller, M. Moscovic, J.-M. Corpataux, J. K. Christensen, K. Keirse, G. Nano, H. Schroeder, C. A. Binkert, M. Brodmann, *CardioVasc. Interventional Radiol.* **2021**, *44*, 207.
[10] K. Katsanos, S. Spiliopoulos, P. Kitrou, M. Krokidis, D. Karnabatidis, *J. Am. Heart Assoc.* **2018**, *7*, e011245.
[11] a) M. Takahashi, *Cardiovasc. Res.* **2021**, *118*, 372; b) A. González-Moro, I. Valencia, L. Shamoon, C. F. Sánchez-Ferrer, C. Peiró, F. de la Cuesta, *Antioxidants* **2022**, *11*, 269.
[12] T. van der Heijden, E. Kritikou, W. Venema, J. van Duijn, P. J. van Santbrink, B. Slütter, A. C. Foks, I. Bot, J. Kuiper, *Arterioscler., Thromb., Vasc. Biol.* **2017**, *37*, 1457.
[13] R. Gao, H. Shi, S. Chang, Y. Gao, X. Li, C. Lv, H. Yang, H. Xiang, J. Yang, L. Xu, Y. Tang, *Int. Immunopharmacol.* **2019**, *74*, 105575.
[14] J. S. Lee, A. A. B. Robertson, M. A. Cooper, K. Khosrotehrani, *Int. J. Mol. Sci.* **2018**, *19*, 3289.
[15] M. Santos, E. C. Filipe, P. L. Michael, J. C. Hung, S. G. Wise, M. M. M. Bilek, *ACS Appl. Mater. Interfaces* **2016**, *8*, 9635.
[16] a) Y. Jin, J. Fu, *J. Am. Heart Assoc.* **2019**, *8*, e012219; b) A. Grebe, F. Hoss, E. Latz, *Circ. Res.* **2018**, *122*, 1722.
[17] R. D. Kenagy, in *Mechanisms of Vascular Disease: A Reference Book for Vascular Specialists* (Eds: R. Fitridge, M. Thompson), University of Adelaide Press, Adelaide, Australia **2011**, Ch.*7*.
[18] J. L. Mills, M. S. Conte, M. H. Murad, *J. Vasc. Surg.* **2019**, *70*, 3.
[19] M. Joner, A. V. Finn, A. Farb, E. K. Mont, F. D. Kolodgie, E. Ladich, R. Kutys, K. Skorija, H. K. Gold, R. Virmani, *J. Am. Coll. Cardiol.* **2006**, *48*, 193.
[20] M. Salla, M. S. Butler, R. Pelingon, G. Kaeslin, D. E. Croker, J. C. Reid, J. M. Baek, P. V. Bernhardt, E. M. J. Gillam, M. A. Cooper, A. A. B. Robertson, *ACS Med. Chem. Lett.* **2016**, *7*, 1034.
[21] Q. Yang, D. Zhang, Y. Li, Y. Li, Y. Li, *Biomed. Pharmacother.* **2018**, *97*, 1424.
[22] Z. Varghese, R. Fernando, J. F. Moorhead, S. H. Powis, X. Z. Ruan, *Am. J. Physiol.* **2005**, *289*, F43.
[23] Y. Liu, F. Yang, S. Zou, L. Qu, *Front. Pharmacol.* **2019**, *9*, 1520.
[24] R. C. Coll, A. A. B. Robertson, J. J. Chae, S. C. Higgins, R. Muñoz-Planillo, M. C. Inserra, I. Vetter, L. S. Dungan, B. G. Monks, A. Stutz, D. E. Croker, M. S. Butler, M. Haneklaus, C. E. Sutton, G. Núñez, E. Latz, D. L. Kastner, K. H. G. Mills, S. L. Masters, K. Schroder, M. A. Cooper, L. A. J. O'Neill, *Nat. Med.* **2015**, *21*, 248.
[25] W.-t. He, H. Wan, L. Hu, P. Chen, X. Wang, Z. Huang, Z.-H. Yang, C.-Q. Zhong, J. Han, *Cell Res.* **2015**, *25*, 1285.
[26] C. Evans, M. Iruela-Arispe, Y.-Y. Zhao, *Am. J. Pathol.* **2021**, *191*, 52.
[27] C. Heiss, A. Rodriguez-Mateos, M. Kelm, *Antioxid. Redox Signaling* **2015**, *22*, 1230.
[28] Y. T. Lam, C. J. Hsu, P. J. L. Simpson, L. L. Dunn, R. W. Chow, K. H. Chan, A. S. C. Yong, Y. Yu, D. P. Sieveking, L. Lecce, J. Yuan, D. S. Celermajer, S. G. Wise, M. K. C. Ng, *Endocrinology* **2020**, *161*, bqaa043.
[29] A. V. Finn, G. Nakazawa, M. Joner, F. D. Kolodgie, E. K. Mont, H. K. Gold, R. Virmani, *Arterioscler., Thromb., Vasc. Biol.* **2007**, *27*, 1500.
[30] Q. Jianlin, W. Xiaoqing, L. Qi, W. Guangyu, X. Mengdi, W. Yulu, L. Yun, L. Xiaoqian, Z. Jie, J. Wen, F. Lin, C. Chong, W. Qingyun, Z. Shengyun, Q. Kunming, L. Depeng, L. Zhenyu, K. A. Robert, Z. Lingyu, E. G. Elizabeth, X. Kailin, *Haematologica* **2018**, *103*, 1568.
[31] S. Chanchal, A. Mishra, M. Singh, M. Ashraf, *Front. Cell Dev. Biol.* **2020**, *8*, 73.
[32] A. H. P. Chan, R. P. Tan, P. L. Michael, B. S. L. Lee, L. Z. Vanags, M. K. C. Ng, C. A. Bursill, S. G. Wise, *PLoS One* **2017**, *12*, e0174773.
[33] P. R. Moreno, V. H. Bernardi, J. Lo´pez-Cue´llar, J. B. Newell, C. McMellon, H. K. Gold, I. F. Palacios, V. Fuster, J. T. Fallon, *Circulation* **1996**, *94*, 3098.
[34] a) J. Cullis, D. Siolas, A. Avanzi, S. Barui, A. Maitra, D. Bar-Sagi, *Cancer Immunol. Res.* **2017**, *5*, 182; b) A. Mercalli, I. Calavita, E. Dugnani, A. Citro, E. Cantarelli, R. Nano, R. Melzi, P. Maffi, A. Secchi, V. Sordi, L. Piemonti, *Immunology* **2013**, *140*, 179.
[35] P. Rider, Y. Carmi, O. Guttman, A. Braiman, I. Cohen, E. Voronov, M. R. White, C. A. Dinarello, R. N. Apte, *J. Immunol.* **2011**, *187*, 4835.
[36] N. Kipshidze, G. Dangas, M. Tsapenko, J. Moses, M. B. Leon, M. Kutryk, P. Serruys, *J. Am. Coll. Cardiol.* **2004**, *44*, 733.

[37] T. Inoue, K. Croce, T. Morooka, M. Sakuma, K. Node, D. I. Simon, *JACC: Cardiovasc. Interv.* **2011**, *4*, 1057.
[38] B. Bai, Y. Yang, Q. Wang, M. Li, C. Tian, Y. Liu, L. H. H. Aung, P.-f. Li, T. Yu, X.-m. Chu, *Cell Death Dis.* **2020**, *11*, 776.
[39] P. K. Shah, *Circulation* **2003**, *107*, 2175.
[40] J. J. Li, H. Zreiqat, in *Encyclopedia of Biomedical Engineering* (Ed: R. Narayan), Elsevier, New York **2019**, p. 270.
[41] I. Koniari, N. G. Kounis, G. Hahalis, *J. Thorac. Dis.* **2016**, *8*, 3056.
[42] A. V. Finn, M. Joner, G. Nakazawa, F. Kolodgie, J. Newell, M. C. John, H. K. Gold, R. Virmani, *Circulation* **2007**, *115*, 2435.
[43] D. N. Rockwood, R. C. Preda, T. Yücel, X. Wang, M. L. Lovett, D. L. Kaplan, *Nat. Protoc.* **2011**, *6*, 1612.
[44] X. Hu, K. Shmelev, L. Sun, E.-S. Gil, S.-H. Park, P. Cebe, D. L. Kaplan, *Biomacromolecules* **2011**, *12*, 1686.

Supporting Information

The selective NLRP3 inflammasome inhibitor MCC950 suppresses inflammation and facilitates healing in vascular materials

Angus J. Grant, Nianji Yang, Mathew J. Moore, Yuen Ting Lam, Praveesuda L. Michael, Miguel Santos, Jelena Rnjak-Kovacina, Richard P. Tan[*^], Steven G. Wise[*^]

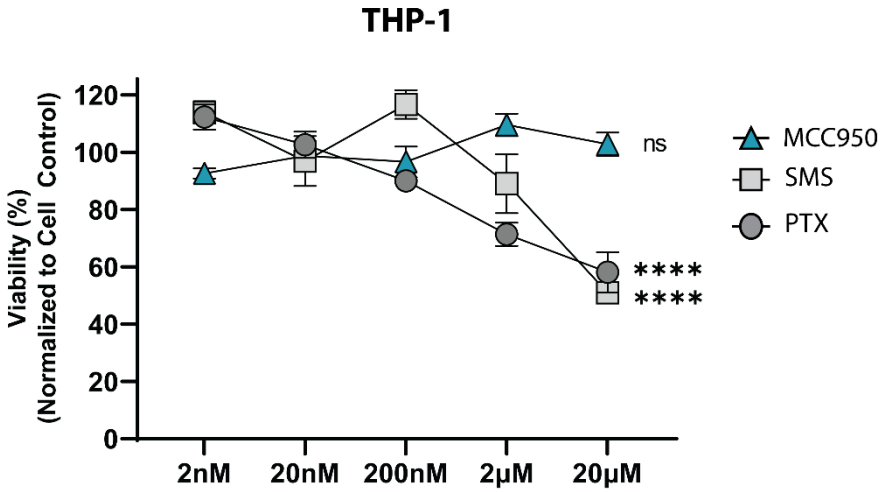

Figure S1: MCC950 is non-toxic to THP-1 derived macrophages. Viability of THP-1 derived macrophages 3 days after being treated with MCC950, Sirolimus (SMS), and Paclitaxel (PTX). Data represents mean ± SEM (n = 4). Statistical significance was determined using Dunnett's multiple comparison test ($^{****}p < 0.0001$)

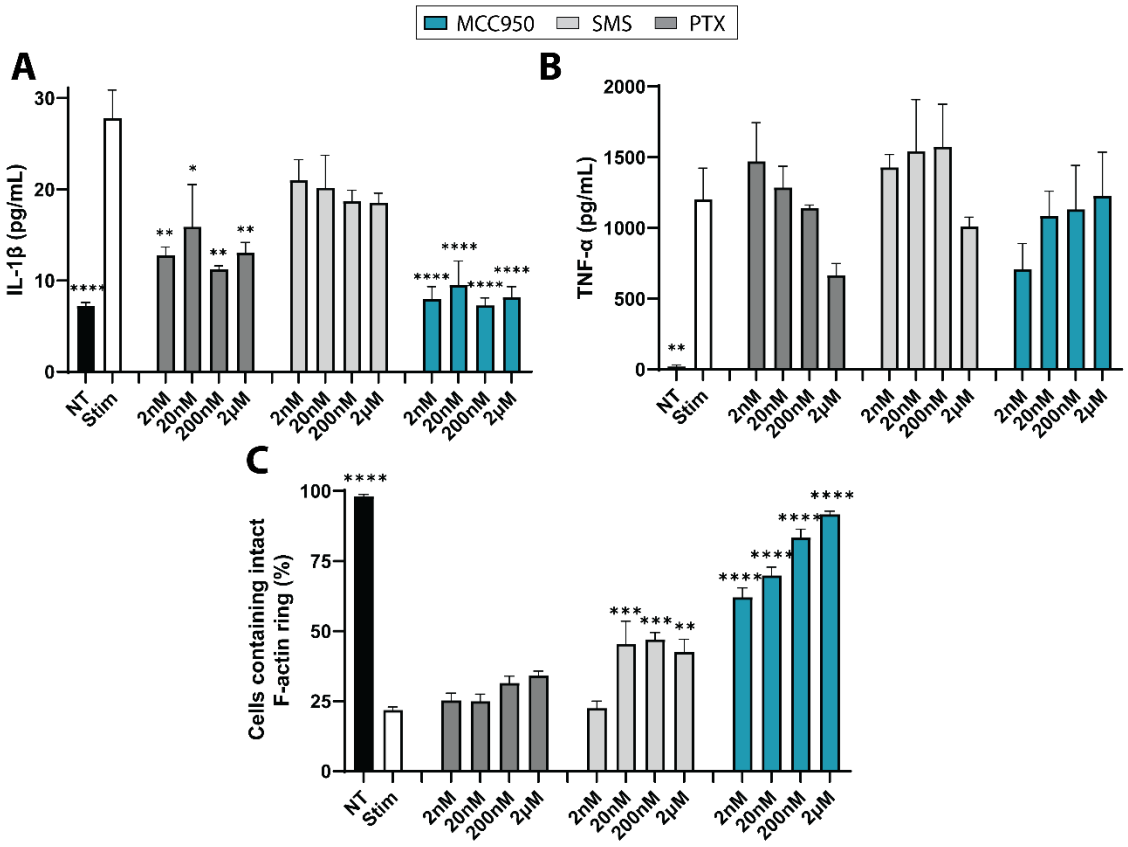

Figure S2: Inhibitory effects on products of the NLRP3 inflammasome pathway. The effect of MCC950, Paclitaxel (PTX) and Sirolimus (SMS) at doses between 2nM-2μM on IL-1β (A), TNF-α (B) and pyroptosis (C) levels post-NLRP3 inflammasome stimulation with LPS (1 μg/mL) and ATP (2.5 mM) in J774a macrophages. Stim refers to stimulated only group. IL-1β and TNF-α levels measured by ELISA. Data represents mean ± SEM (n = 3-4). Statistical significance was determined using Dunnett's multiple comparison test relative to stimulated group ($^{*}p < 0.05$, $^{**}p < 0.01$, $^{****}p < 0.0001$).

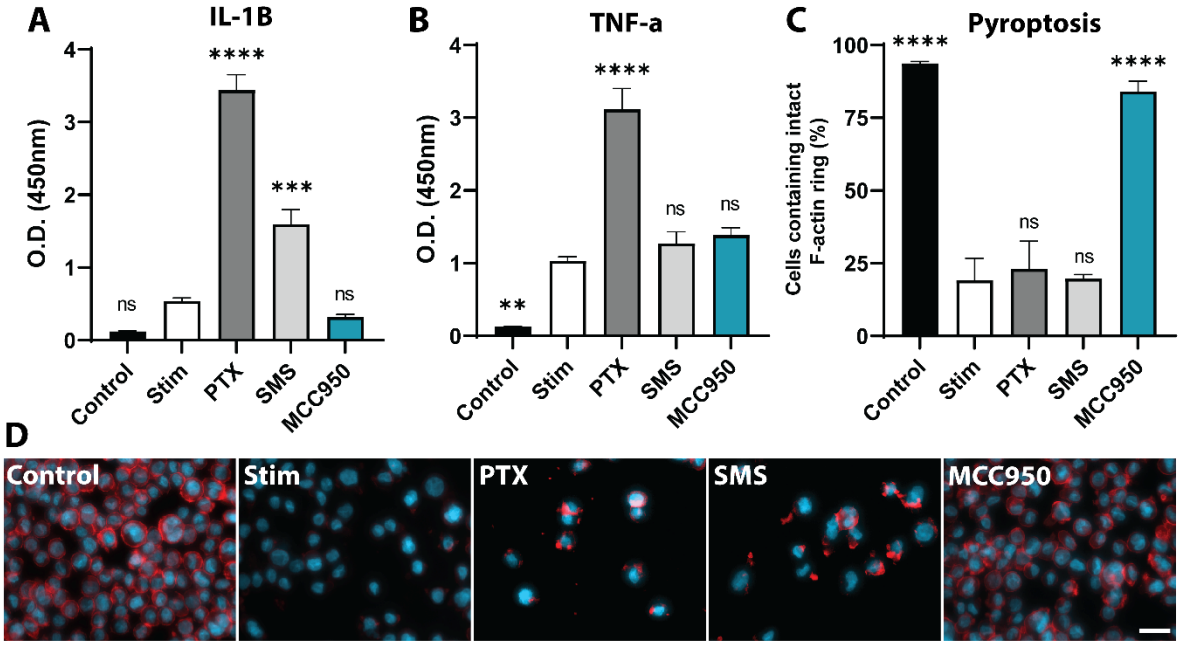

Figure S3: MCC950 is selective to the NLRP3 inflammasome pathway in THP-1 derived macrophages. The effect of high dose (20µM) MCC950, Paclitaxel (PTX) and Sirolimus (SMS) on IL-1β (A), TNF-α (B) and pyroptosis (C) levels post-NLRP3 inflammasome stimulation with LPS (1 µg/mL) and ATP (2.5 mM) in THP-1 derived macrophages. Stim refers to stimulated only group. IL-1β and TNF-α levels measured by ELISA. Data represents mean ± SEM (n = 3-4). Statistical significance was determined using Dunnett's multiple comparison test relative to stimulated group ($^{**}p < 0.01$, $^{***}p < 0.001$, $^{****}p < 0.0001$). D) Representative images of control, stimulated only, and stimulated and drug treated macrophages used for pyroptosis quantification. Cells stained with DAPI (blue) and rhodamine phalloidin (red) to visualize cell nucleus and F-actin respectively. Scale bar represents 50µm.

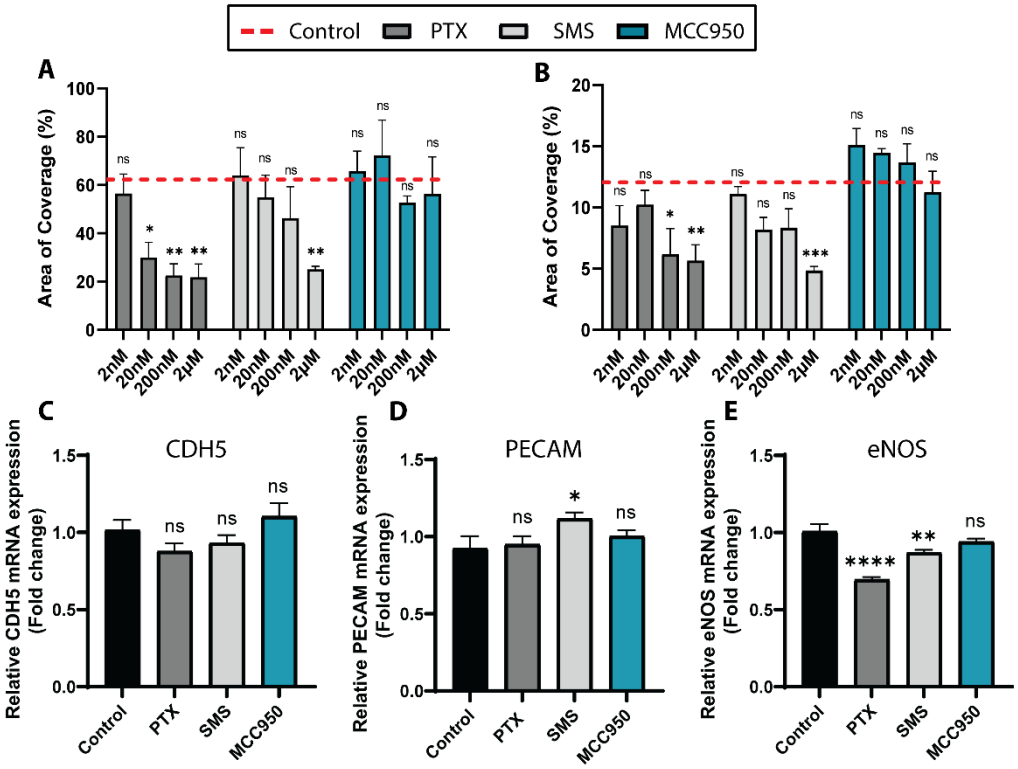

Figure S4: Endothelial functionality assay. Quantification of total HCEAEC expression of VE-Cadherin (A) and eNOS (B) 3 days after treatment with Paclitaxel (PTX), Sirolimus (SMS) or MCC950 at doses between 2nM-2µM. C, D, E) Quantitative RT-PCR detection of Cadherin 5 (CDH5) (C), platelet endothelial cell adhesion molecule (PECAM) (D), and eNOS (E) mRNA expression. Data represents mean ± SEM (n = 3-4). Statistical significance was determined using Dunnett's multiple comparison test relative to control ($^{*}p < 0.05$, $^{**}p < 0.01$, $^{***}p < 0.001$).

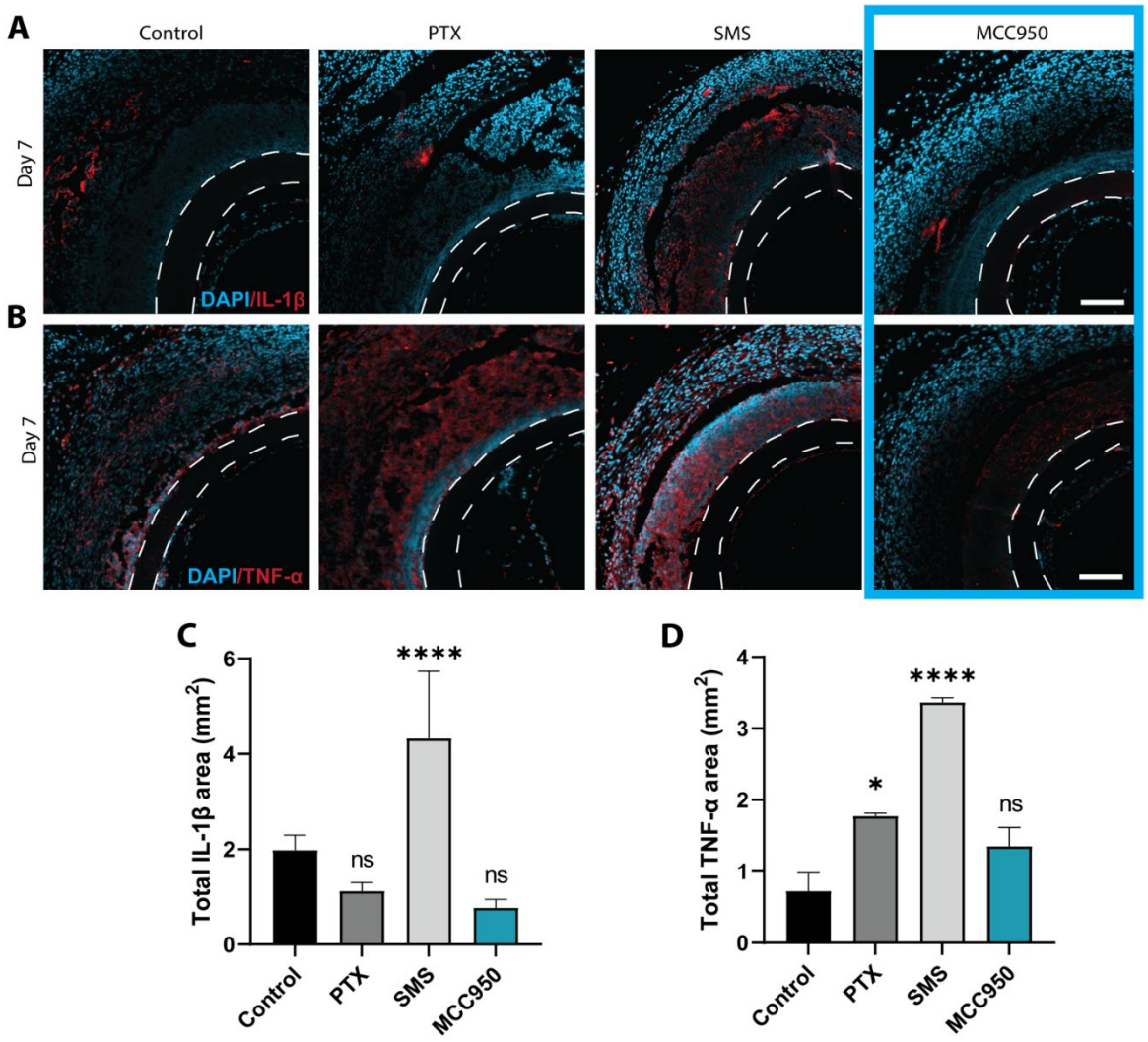

Figure S5: Treatment effect on cytokine production in vivo. A,B) Day 7 representative images of IL-1β (A) and TNF-α (B) stain taken from middle region of explanted grafts. DAPI stained in blue, IL-1β or TNF-α stained in red. Scale bar represents 100 µm. C, D) Quantification of total IL-1β (C) and TNF-α (D) positively stained area at day 7. Data represents mean ± SEM (n = 3-4). Statistical significance was determined using Dunnett's multiple comparison test ($^{*}p < 0.05$, $^{****}p < 0.0001$).

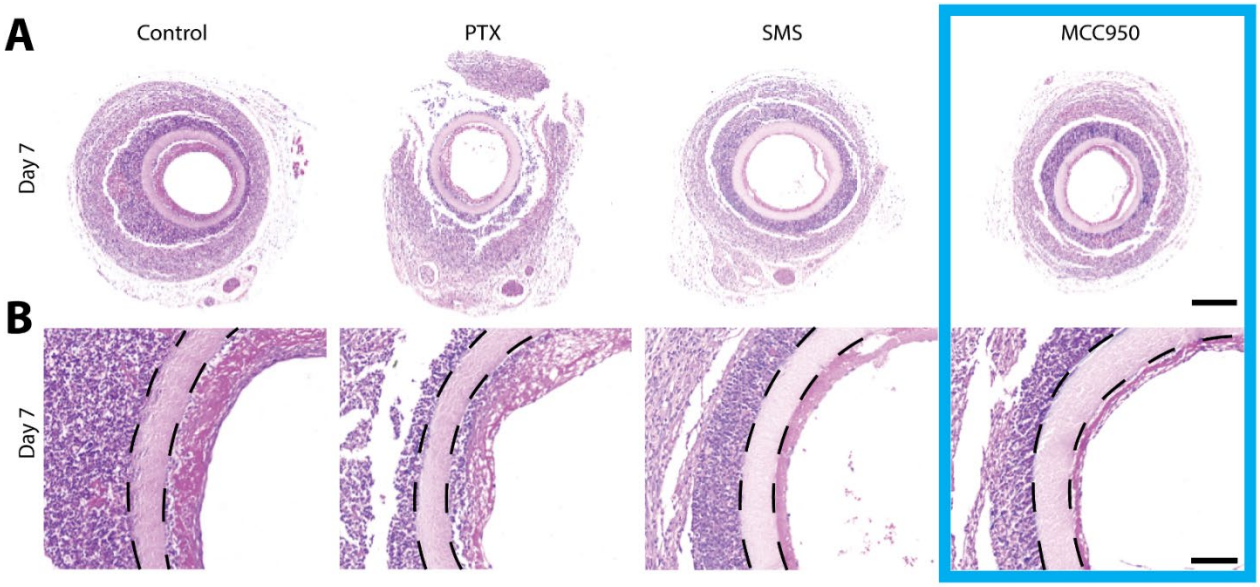

Figure S6: MCC950 reduces fibrotic capsule formation and neointimal hyperplasia. A) Representative images of hematoxylin and eosin-stained grafts after 7 days showing fibrotic capsule surrounding the graft. Images were taken from middle portion of each graft. Scale bar represents 300 µm. B) Representative images of hematoxylin and eosin-stained grafts after 7 days showing neointimal hyperplasia. Black dotted lines show graft outline. Scale bar represents 100 µm.

Chapter 4

Localised delivery of immunotherapies using plasma polymerised nanoparticles for cardiovascular applications

4. Chapter 4 – Localised delivery of immunotherapies using plasma polymerised nanoparticles for cardiovascular applications

4.1 Introduction

4.1.1 Need for localised drug delivery after vascular injury

Percutaneous endovascular interventions such as balloon angioplasty and stenting restore blood flow to obstructed vasculature by mechanically reopening the vessel lumen. For angioplasty in the coronaries, this usually requires pressures of 8-12 atm in order to effectively collapse the occlusive atherosclerotic plaque while peripheral angioplasty requires slightly higher pressures ranging from 15-20 atm [152, 153]. This pressure causes overexpansion of the blood vessel, resulting in significant injury to the vessel wall.

Vascular injury primarily involves damage to the endothelium, often exposing subendothelial collagen triggering platelet activation and the coagulation cascade [154]. In many cases, the internal elastic lamina is fractured, causing stretching, compression, or rupture of smooth muscle cells residing in the tunica media. These cells undergo necrosis or apoptosis, releasing intracellular contents that amplify local danger signals. Surviving medial smooth muscle cells undergo phenotypic modulation from a contractile to a synthetic state, re-entering the cell cycle, proliferating, and migrating into the intima where they deposit extracellular matrix proteins such as collagen and proteoglycans [86]. The net effect is the formation of a neointimal layer that progressively grows into the lumen.

Stent implantation following angioplasty compounds this injury. Stent struts penetrate into the vessel wall, crushing plaque into the media, further tearing the elastic lamina, and sometimes

extending injury into the adventitia [86]. At sites of malapposed struts, local turbulence and altered shear stress exacerbate the inflammatory response and hinder re-endothelialisation [155]. Intravascular imaging has confirmed that strut-associated regions often remain uncovered or poorly healed long after implantation, creating an avenue for hyperproliferating smooth muscle cells to migrate through into the lumen [156, 157].

This understanding is what drove the field to couple drugs with endovascular interventions. Mechanical structures are limited in their ability to control biological responses, whereas drugs are purpose built for this. The first generation of drug-eluting devices were introduced to directly suppress smooth muscle cell proliferation, attenuate neointimal hyperplasia, and maintain long-term vessel patency. While next generation drug strategies are targeting inflammation (as discussed in section 2.2.3 of this thesis), delivery of these agents becomes paramount.

The vascular injury is heterogeneous and layered, meaning that the drug must act precisely at the site of endothelial denudation, medial tearing, and strut penetration. Systemic therapies rarely achieve sufficient concentration within these microdomains without producing systemic effects [158, 159]. Local delivery ensures high drug levels where they are required, promoting more selective modulation of the vascular healing response leading to reduced restenosis.

4.1.2 Drug-eluting approaches for vascular injury

There are currently two prominent drug-eluting approaches in the vasculature: drug-eluting stents (DES) and drug-coated balloons (DCB). This section will go into detail regarding how

drug-eluting technology was introduced into these devices, and how this technology enables localised delivery of drugs to injury sites, highlighting their essential characteristics and how the devices have progressed towards a “leave nothing behind” approach.

4.1.2.1 Drug-eluting stents

Stents act as permanent reservoirs for local drug delivery, meaning DES do not rely on rapid arterial uptake in the way DCB do (see section 4.1.2.2 below). Instead, DES are coated in polymer platforms that slowly release the drug over time as chemical bonds break between the polymer and the drug. In this way, their success relies heavily on controlled and sustained drug release [160]. DES were developed to overcome the high rates of in-stent restenosis associated with bare-metal stents seen in patients with CAD. To this day, DES remain the gold-standard treatment option for the majority of CAD cases. Their success has relied heavily on the evolution of drug-polymer platforms that control not only how much drug is released but also when, and for how long. The biocompatibility of the polymer, type of drug being eluted, the drug elution profile, and the push to “leave nothing behind” are critical factors which have impacted DES evolution over time (Figure 4.1).

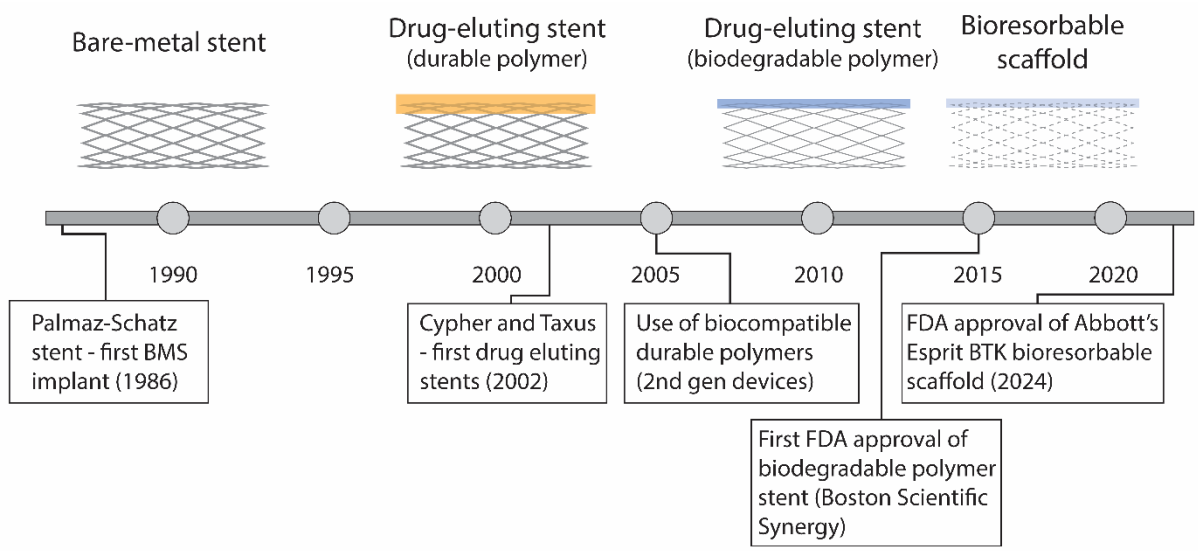

Figure 4.1: Drug-eluting stent timeline

Schematic showing the evolution of drug-eluting stents, from traditional bare-metal stents (BMS) to drug-eluting bioresorbable scaffolds.

First generation DES

First-generation DES used durable polymer coatings that combined anti-proliferative drugs with relatively thick polymer layers. The Cypher stent (Cordis) released sirolimus from a polyethylene–co-vinyl acetate (PEVA) and poly n-butyl methacrylate (PBMA) coating [161], while the Taxus stent (Boston Scientific) released paclitaxel from a poly(styrene–isobutylene–styrene) (SIBS) matrix [162]. These devices shared similar drug elution profiles, releasing their drugs rapidly in the first 10 days, before slower sustained elution out to 2-3 months. For patients with CAD, this technology greatly improved vascular outcomes. In the pivotal RAVEL trial (A Randomised Comparison of a Sirolimus-Eluting Stent With a Standard Stent for Coronary Revascularisation), the 1-, 3-, and 5-year rates of survival free from target lesion revascularization were 99.2%, 93.8%, and 89.7%, respectively, in CAD patients randomly treated with sirolimus-eluting stents versus 75.9%, 75.0%, and 74.0% for patients assigned bare-metal stents, respectively [163]. Furthermore, 0% of patients in sirolimus-eluting stents, compared to 26.6% in the bare-metal stent group, experienced over 50% luminal occlusion

within 1 year [109]. Similarly, the TAXUS-IV trial demonstrated that the Taxus stent reduced 1-year rates of target-lesion and target-vessel revascularisation for de novo coronary lesions by 73% and 62%, respectively, compared to bare-metal stenting [164]. This benefit was maintained through 5 years [165]. In both cases, the polymer coatings used were permanent, meaning the polymers remained even after complete drug release. Despite allowing for sustained drug release, long-term follow-up studies revealed that these durable polymers provoked local inflammation and prevented endothelialisation contributing to late and very late-stage thrombosis [166, 167]. Non-uniform coatings and inconsistent drug distribution further compounded these issues, limiting reproducibility. Thus, while first-generation DES established proof that polymer-based drug release could dramatically reduce restenosis for patients with CAD, their shortcomings underscored the need for safer polymer strategies and set the stage for the development of second-generation platforms.

Second generation DES

Second-generation DES were designed to overcome the safety limitations of their predecessors by introducing thinner stent struts, more biocompatible polymers, newer limus drugs, and more tailored drug eluting kinetics. The everolimus-eluting stent Xience (Abbott Cardiovascular) used a fluoropolymer coating that was significantly less thrombotic and inflammatory compared with the durable polymers of first-generation devices. Its release kinetics were carefully tuned, with ~80% of everolimus released within 30 days and complete elution by 120 days, ensuring therapeutic exposure during the critical window of neointimal proliferation while allowing drug levels to fall as endothelial repair advanced [168]. Similarly, the Resolute stent (Medtronic) employed the proprietary BioLinx polymer system which was a polymer blend of hydrophilic C19 polymer, water-soluble polyvinyl pyrrolidinone, and hydrophobic

C10 polymer designed to extend zotarolimus release for up to 180 days, maintaining suppression of neointimal growth in higher-risk patients [169]. These material refinements translated into tangible clinical improvements for patients with CAD. In the SPIRIT III (Clinical Evaluation of the XIENCE V Everolimus Eluting Coronary Stent System in the Treatment of Patients with De Novo Native Coronary Artery Lesions) trial, the pivotal trial for XIENCE V approval in the United States, patients receiving the XIENCE V everolimus eluting stent demonstrated a 21.2% decrease in coronary target lesion failure and 36.2% reduction in major adverse cardiac events compared to TAXUS paclitaxel eluting stent at 5-year follow up [170]. Similarly, results from the RESOLUTE trial comparing the two primary second generation DES (Resolute zotarolimus eluting stent and XIENCE V everolimus eluting stent) in patients with CAD showed the two systems were non-inferior to each other, with both devices demonstrating very low rates of late stent thrombosis (0.3%) [171]. The 5-year cumulative follow up reported definite or probable stent thrombosis of only 1.2% [172]. Together, these findings confirmed that second-generation DES not only optimised polymer-mediated drug delivery but also markedly improved safety over their predecessors, firmly establishing them as the new clinical standard for treatment of CAD.

Biodegradable polymer DES sought to further improve safety while eliminating the long-term risks of a permanent polymer. In these designs, the polymer coating degrades after drug release, leaving behind a bare-metal scaffold. Examples include the Biomatrix stent (Biosensors) with a polylactic acid coating releasing biolimus [173], and the Synergy stent (Boston Scientific) with a polylactide–glycolide (PLGA) coating releasing everolimus [174]. In these devices, drug delivery was front-loaded into the first 30-90 days before the polymer was fully degraded. Tissue retention of drugs like biolimus remained strong in the first weeks but declined as the polymer resorbed. These designs aimed to reduce very late stent thrombosis by removing

residual polymer once its purpose was fulfilled. Clinically, biodegradable-polymer DES demonstrated clear long-term safety benefits over first-generation durable-polymer stents, while head-to-head trials against second-generation durable-polymer everolimus stents generally showed non-inferiority [173, 175]. Following this, in an attempt to remove the need for polymer coatings all together, polymer-free DES attempted to deliver drugs without any polymer matrix, relying instead on microporous or nanoporous metal surfaces, reservoirs, or carrier layers such as titanium oxide. These stents generally provided rapid drug release within the first few days to weeks, but struggled to maintain prolonged therapeutic levels [176]. Drug doses delivered and retained in the arterial wall was therefore reduced in the long-term compared with polymer-based systems. While these designs avoided polymer-related inflammation, the shorter drug exposure often proved insufficient to suppress neointimal growth over the long-term [177].

Current generation DES

Current-generation DES are dominated by everolimus- and zotarolimus-eluting stents with ultra-thin struts and highly biocompatible polymers. Devices such as the Xience Skypoint (Abbott) and Resolute Onyx (Medtronic) remain widely regarded as clinical gold standards for treatment of CAD, owing to their excellent safety profiles, predictable elution over 1-3 months, and consistent endothelialisation [178, 179]. Alongside these, biodegradable-polymer sirolimus stents such as the Orsiro (Biotronik) have shown superiority in some head-to-head trials, particularly in acute coronary syndromes, and are increasingly recognised as front-line options [180]. However, the transformational benefits of DES in the coronary arteries have largely failed to translate to the peripheral arteries. This discrepancy reflects the unique challenges of treating PAD, where long, calcified lesions and constant vessel motion can

fracture stents and impair polymer coatings. As a result, conventional permanent DES have seen limited adoption in PAD, prompting a shift toward more adaptable solutions. Consistent with the broader push to “leave nothing behind”, resorbable DES have recently emerged as promising stent-based options for patients with PAD. For example, the Esprit BTK system (Abbott), which is currently the only FDA approved resorbable DES for chronic limb-threatening ischemia (CLTI) [181]. This resorbable scaffold is comprised of poly(L-lactide) (PLLA) which provides radial strength similar to a metallic stent within the first six months of implantation to avoid vessel recoil. An everolimus coating is additionally applied to the polymer scaffold, sustaining elution for up to 3 months. Over time, hydrolysis continuously degrades the scaffold, with full resorption occurring after approximately 3 years, ultimately leaving no implant behind [182]. One randomized trial with 261 patients with CLTI compared the Esprit BTK balloon with standard angioplasty for infrapopliteal artery disease (specific form of PAD) and revealed that the incidence of freedom from amputation above the ankle of the target limb, occlusion of the target vessel, and clinically driven revascularization of the target lesion at 1 year was higher in patients who received the Esprit BTK balloon compared to those who received angioplasty [181]. Despite the success in CLTI, the use of resorbable DES in the coronaries has not translated as well, largely failing in head-to-head comparisons with permanent DES [183].

In summary, DES have evolved into the gold-standard treatment for CAD, and new bioresorbable designs that leave no permanent implant behind are emerging as promising options for patients with PAD. However, PAD clinical studies have yet to confirm the efficacy of resorbable DES in the long-term. Instead, the PAD market has largely been dominated by DCB, although long-term efficacy and safety is still a major concern.

4.1.2.2 Drug-coated balloons

When first introduced, balloon angioplasty revolutionised the treatment of occlusive cardiovascular disease. However, elastic recoil and restenosis limited long-term patency, leading to the invention of the stent [184]. While stents reduced elastic recoil, stent thrombosis and in-stent restenosis emerged as significant complications. DES were subsequently developed to mitigate in-stent restenosis, but these too carried drawbacks, including late stent thrombosis and persistent restenosis, particularly in patients with PAD. In the late 2000s, DCB emerged as a promising way to restore vessel patency by delivering anti-restenotic drugs without leaving a permanent implant [107]. This is known in the field as the “leave nothing behind” initiative. DCB have since become an established treatment in settings where stenting is undesirable, such as in peripheral arteries with small vessel diameters or in patients with diffuse lesions. However, their utility heavily depends on the efficiency at which they can deliver drugs to the arterial wall and how well the drug is retained/taken up by the tissue. Since their introduction, DCB have progressed from early proof-of-concept paclitaxel coatings to second-generation platforms with refined excipients to improve drug transfer, and now to sirolimus-based balloons capable of sustained release (Figure 4.2).

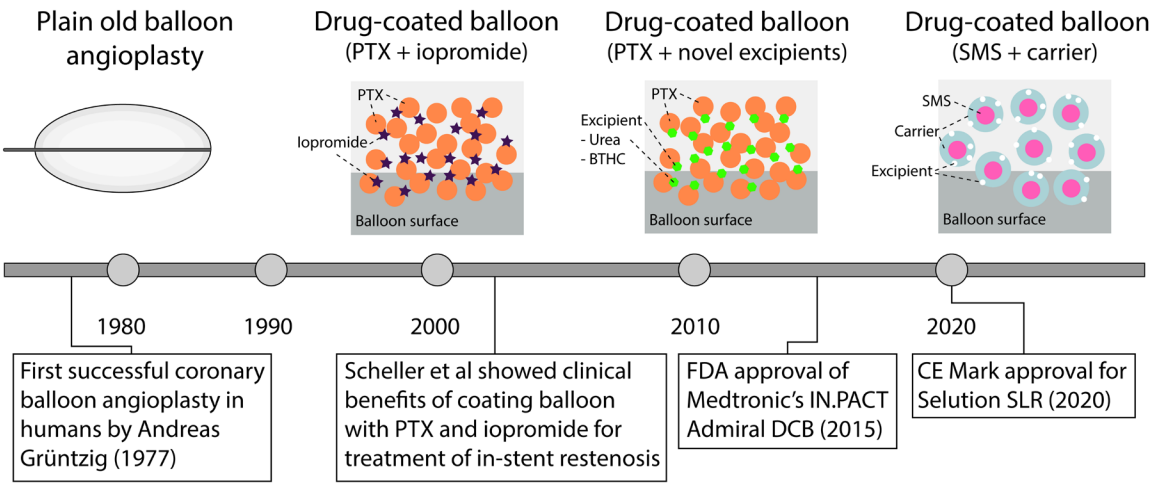

Figure 4.2: Drug-coated balloon timeline

Schematic showing the evolution of drug-coated balloons, from traditional plain old balloon angioplasty to drug-coated balloons incorporating nanocarriers and excipients.

First generation DCB

Paclitaxel was identified early as the most promising drug for balloon-based delivery because of its high lipophilicity and rapid arterial uptake which had been exemplified previously in DES. However, these same physicochemical traits created challenges for local delivery by balloon. Paclitaxel is poorly soluble in blood and prone to competitive binding with plasma proteins, meaning much of the drug is lost to wash-off during balloon advancement and inflation rather than being deposited in the vessel wall [185]. To overcome this, the drug must be paired with an excipient, an inactive additive that improves the stability and solubility of the drug coating, limits premature wash-out, and facilitates more efficient transfer of paclitaxel into arterial tissue. The introduction of such excipients represented a critical turning point in DCB development, transforming paclitaxel from a theoretically attractive option into a clinically viable therapy [186].

Scheller et al were the first to demonstrate the need for an excipient for DCB. They investigated the use of paclitaxel mixed with the highly hydrophilic contrast medium iopromide, an excipient-based matrix later developed by Bayer Schering Pharma termed Paccocath technology [187]. Iopromide was theorised to increase paclitaxel solubility, reduce drug wash-off during the advancement and inflation stage, and lead to a greater dose transfer into arterial tissue. In the first-of-its-kind study investigating the potential for paclitaxel-coated balloons utilising iopromide to reduce in-stent restenosis in pig coronary arteries, Sheller et al demonstrated a 63% reduction in neointimal area at 35-days follow up with the paclitaxel balloon compared to traditional uncoated angioplasty and stent placement [107]. However, despite confirming 92% of initial paclitaxel dose had been eluted from the balloon during inflation, the percentage of initial paclitaxel dose in the vessel wall 40-60 mins after angioplasty was only 9%. This suggested a significant amount of paclitaxel had not actually reached the vessel wall, posing questions around long-term efficacy of this platform. Despite this concern, clinical trials such as the Treatment of In-Stent Restenosis by Paclitaxel-Coated Balloon Catheters (PACCOCATH ISR) trial and the Femoral Paclitaxel (FemPac) trial, showed marked reductions in-stent restenosis and restenosis following angioplasty in femoropopliteal arteries, respectively [188, 189]. In both cases, the authors suggested that these results were seen despite approximately 80-90% of initial paclitaxel dose being lost in the bloodstream, and therefore not having any therapeutic benefits at the site of injury in the arterial wall. This ushered in the next generation of DCBs which trialled different excipients and designs in an attempt to maximise drug-delivery to the vascular wall.

Second generation DCB

Second generation DCB sought to improve paclitaxel delivery by coupling paclitaxel with alternative excipients or carriers. Modern excipients including butyrl-tri-hexyl citrate and urea showed superior paclitaxel delivery capabilities compared to traditional iopromide. Butyrl-tri-hexyl citrate showed to stabilise paclitaxel in a micro-crystalline structure, enhancing its tissue absorption properties, achieving close to 50% of initial dose taken up by the vascular wall after coronary angioplasty in pigs [186]. Importantly, detectable concentrations of paclitaxel were found up to 7 days post intervention, highlighting significant drug retention was achieved. Urea was additionally tested as an excipient for paclitaxel, forming the proprietry FreePac^{TM} coating which was applied to the IN.PACT Admiral balloon (Medtronic vascular, Galway, Ireland) designed for treatment of PAD [190]. Similar to traditional excipients, urea is hydrophilic and soluble in blood, allowing it to act as a release agent for paclitaxel to promote transfer from the balloon to the vessel wall. Unique to urea, it additionally demonstrated a slow rate of paclitaxel dissolution, enabling paclitaxel to last and remain functional in the tissue for longer than any other available DCB at that time [190]. In fact, paclitaxel was observed for over 180 days at therapeutic levels in the vessel wall post-angioplasty with the IN.PACT Admiral balloon. As evident in the IN.PACT SFA Trial, which compared IN.PACT Admiral DCB relative to traditional angioplasty in subjects with femoropopliteal artery disease, this improved retention led to a 54% increase in vessel patency rates for at 3-year follow-up [191]. Notably, IN.PACT Admiral was given FDA approval in 2014 for the treatment of femoropopliteal artery disease, marking only the second FDA approval for DCB at that time [192].

Another key innovation was the development of shielding techniques which protected paclitaxel from early wash-off during insertion, such as the shellac coating used on the second-generation DIOR balloon (DIOR-II). Shellac is a natural hydrophilic coating originally FDA approved as a coating for food. Using shellac, DIOR-II achieved up to a 20-fold higher tissue

paclitaxel concentration compared with first generation paclitaxel coated balloons [193], which translated to significant suppression of neointimal hyperplasia [194]. Despite significant improvements in paclitaxel delivery and retention, high blood concentrations of paclitaxel were still being observed and the long-term safety of paclitaxel was beginning to be questioned [111]. As a result, the field began to look beyond paclitaxel toward sirolimus, mirroring the transition already seen in stent technology and paving the way for a new generation of DCB.

Current generation DCB

Third generation DCB marked a transition from paclitaxel to sirolimus, motivated by its proven efficacy in DES and a broader movement away from paclitaxel due to issues with toxicity. However, sirolimus is far less lipophilic compared to paclitaxel, has lower tissue permeability, and exhibits rapid clearance from the vascular wall, making its delivery via a short balloon inflation technically challenging [195]. To overcome these limitations, several innovative delivery technologies have been developed. For example, the Selution SLR^{TM} balloon (MedAlliance, Nyon, Switzerland), encapsulates sirolimus in PLGA micro-reservoirs that adhere to the vessel wall upon balloon inflation, where they then begin to release sirolimus in a controlled fashion for up to 90 days [196]. The micro-reservoirs are a mix of 4-micron sirolimus-PLGA particles and three phospholipid-based excipients which blend together to reduce paclitaxel wash-off during the procedure, optimise drug transfer, and help increase adherence to the surrounding tissue. The first-in-human trial was performed with the Selution SLR^{TM} for treatment of femoropopliteal lesions and demonstrated 91.2% freedom of restenosis after 6 months, highlighting its ability to sustain tissue drug levels well beyond the inflation period [197].

Similarly, the MagicTouch balloon (Concept Medical, India) employs a phospholipid-based nanocarrier system, known as Nanolute, that coats sirolimus onto the balloon in sub-micron particles. This nanocarrier system incorporates two excipients, the first being a lipid-based component that forms a phospholipid bilayer encapsulating sirolimus, and the second being a calcium phosphorus-based component employed to release sirolimus during changes in pH [198]. Pre-clinical testing demonstrated detectable sirolimus levels in the tissue 14 days after initial procedure, as well as highlighting drug migration from the lumen surface to deeper structures of the vessel wall even when exposed to blood flow [198]. Despite showing promising first-in-human patency after 6 months, a head-to-head study comparing MagicTouch to 2nd generation paclitaxel coated balloons concluded that MagicTouch failed to demonstrate noninferiority compared to paclitaxel coated balloon in patients with de novo small vessel disease [199]. Therefore, despite promising technology, future long-term trials are still needed to evaluate sirolimus coated balloons against prior generations. As a result, paclitaxel-coated balloons continue to dominate the current PAD market. Nevertheless, the increased desire to shift away from paclitaxel, at least in the research and development stages, has prompted the field to explore new drug delivery strategies that can improve drug retention and localisation, thereby creating the next generation of DCB that can effectively deliver a broad range of therapeutics.

4.1.3 Nanoparticles as effective drug carriers

While DES and DEB have established the clinical value of local drug delivery, both approaches carry inherent limitations. Stents leave behind permanent scaffolds, while balloons may not ensure sufficient or sustained drug retention. Nanoparticles have emerged as promising solutions offering the potential for targeted, controlled drug release while minimising systemic

exposure and device-related complications. Their small size and high surface area allow efficient drug loading, while tunable surface chemistry enables controlled release and the potential for selective targeting of injured vascular tissue [200]. Unlike balloons or stents, which provide a single burst or surface-limited release, nanoparticles can circulate or embed within the vessel wall to achieve sustained exposure [201]. They also expand the range of deliverable therapeutics, from small hydrophobic drugs to biologics such as cytokines or nucleic acids, which are difficult to retain with conventional coatings. However, their effectiveness of current platforms depends on toxicity, retention at the injury site, and ability to conjugate cargo without changing functionality, challenges that continue to drive innovation in nanoparticle design.

4.1.3.1 Current nanocarrier platforms for drug delivery

Nanoparticles are increasingly being explored as drug carriers post-endovascular intervention, either systemically or incorporated with DCB or DES. By encapsulating therapeutic agents and improving their pharmacokinetics, nanoparticles can improve local retention and broaden the range of drugs that can be delivered to injured vessels. Current platforms are generally categorised as either organic or inorganic nanoparticles.

Organic nanoparticles

Organic nanoparticles are composed of organic compounds including lipids and polymers [202]. Among the most widely studied platforms are lipid-based nanoparticles which have been popularised by their recent use in COVID-19 vaccines [203]. They are spherical self-assembled vesicles, composed of a lipid bilayer encapsulating an aqueous core. For drug-delivery applications, they are an ideal platform due to their ability to encapsulate therapeutic cargo,

carry it across the cell membrane, and deliver it into the cytosol [203]. Lipid-based nanoparticles have been tested for the use in vascular applications. Lemos et al developed a phospholipid encapsulated sirolimus nanocarrier which, when delivered from a balloon, was successfully delivered to the vessel wall and retained there for days after inflation [198]. In a 28-day preclinical porcine model, this formulation significantly suppressed neointimal proliferation compared to plain old balloon angioplasty control [198]. Liposome nanocarriers have also been trialed for the delivery of other therapeutic agents including gene delivery in the context of restenosis. Yin et al demonstrated successful delivery of tissue factor pathway inhibitor gene using a HVJ-AVE (Hemagglutinating Virus Japan – Artificial Viral Envelope) liposome vector to treat restenosis after balloon angioplasty [204]. This novel gene therapeutic strategy significantly reduced neointimal hyperplasia in rabbits, but failed to reach clinical trials due inconsistent efficacy across pre-clinical models. These examples highlight the promise of liposomes as biocompatible carriers of therapies that don't possess the features that makes paclitaxel an ideal drug for local delivery. However, their modest retention in the vascular environment and absence of promising long-term data remain limitations.

Polymeric nanoparticles have also been utilised for vascular applications such as those made from poly(lactic-co-glycolic acid) (PLGA). For example, Westedt et al developed a paclitaxel-loaded modified poly(vinyl alcohol)-graft-PLGA (PVA-g-PLGA) nanoparticles which, when delivered locally after balloon injury in a rabbit iliac artery model, showed a 50% reduction in neointimal area compared to control [205]. Despite lacking a free paclitaxel control, this study confirmed the ability for polymeric nanoparticles to effectively deliver drugs to the vascular region and result in neointimal suppression. Perhaps even more exciting is the potential of polymeric nanoparticles to open the door to the delivery of new drugs after endovascular intervention. For instance, dexamethasone-loaded PLGA nanoparticles demonstrated high

encapsulation efficiencies of 99.2% and sustained release for up to 30 days *in vitro* [206]. Similarly, a novel PLGA nanoparticle loaded with quercetin showed to be have potent anti-proliferative effects on vascular smooth muscle cells and were highly resistant to wash out *in vitro* [207]. These studies show the promise of polymeric nanoparticles in expanding drug delivery options. However, none have yet made it past pre-clinical testing, citing concerns over complex synthesis, requiring multi step protocols that result in batch-to-batch inconsistency, and issues with drug retention at site of injury.

Inorganic nanoparticles

Inorganic nanoparticles are composed of non-organic materials such as metals, metal oxides, and silica. Their unique physicochemical properties, including high surface area-to-volume ratio, tuneable surface chemistry, and mechanical robustness, have made them attractive candidates for drug delivery in many applications [208]. Although, their use in vascular applications is not as established as organic platforms, most likely due to issues with toxicity in systemic circulation. In saying this, a few groups have explored their potential in vascular settings, primarily studying gold, silica and iron oxide nanoparticles.

Gold nanoparticles are attractive due to their stability in biological environment and relative biocompatibility. Meyers et al. developed a gold nanoparticle functionalised with a collagen targeting peptide that were systemically administered in rats following carotid balloon injury [209]. These nanoparticles selectively bound to exposed collagen at sites of vascular injury and were retained for at least 24 hours, with minimal off-target accumulation. Importantly, no endothelial apoptosis, systemic toxicity, or hepatic/renal dysfunction were observed, highlighting a favourable safety profile [209]. This study demonstrates how gold nanoparticles

can be tailored for lesion-specific vascular targeting, offering a potential use in DCB or DES. Despite promising localisation, no therapeutic benefit was investigated due to complexities related to therapeutic cargo functionalisation intrinsic to gold nanoparticle platforms.

Iron oxide nanoparticles have also been explored both as drug carriers and imaging agents in vascular applications. Kim et al. compared cRGD-targeted and collagen-targeted iron oxide nanoparticles in ApoE−/− mice with early atherosclerotic plaques [210]. Using near-infra-red fluorescence and MRI, they showed that cRGD-targeted iron oxide nanoparticles accumulated more efficiently within plaques than collagen-targeted ones, corresponding to the high angiogenic activity of early lesions. Prussian blue staining confirmed nanoparticle retention within the vascular wall [210]. However, studies demonstrating therapeutic benefits of iron oxide nanoparticles for vascular lesions are not available, highlighting that despite their ability to localise in vascular regions, complexities are limiting their potential.

Mesoporous silica nanoparticles (MSNPs) on the other hand have shown therapeutic benefits in vascular settings. MSNPs allow high drug loading and controlled release of their cargo. Wei et al. investigated honokiol-loaded MSNPs (HNK-MSNPs) for restenosis prevention [211]. In a rat carotid balloon injury model, periadventitial application of HNK-MSNPs markedly reduced neointimal formation at 14 days, with a ~72% decrease in intimal area and ~65% reduction in intima-to-media ratio compared to free honokiol. However, this study lacked a comprehensive toxicity screen of MSNP nanoparticles in key vascular cells such as endothelial cells [211]. Regardless, this work underscores the potential of silica-based carriers to enhance efficacy of otherwise poorly retained drugs.

Together, these examples demonstrate the promise of inorganic nanoparticles in vascular drug delivery, enabling targeted retention and possible therapeutic benefits. However, concerns remain around long-term toxicity and the complexity of manufacturing reproducible formulations [212, 213]. These limitations have thus far hindered translation into clinical vascular applications.

4.1.3.2 Limitations of current platforms

While nanoparticle platforms show promise, their clinical translation is limited by concerns over toxicity and the complexity of manufacturing.

Toxicity

Toxicity remains a major obstacle for nanoparticle translation, with both organic and inorganic platforms demonstrating adverse effects in clinical and preclinical studies. Some liposomal formulations such as cationic liposomes used for drug encapsulation have been consistently associated with toxicity when systemically delivered, limiting their widespread clinical use [214, 215]. Similarly, polymeric platforms, while generally regarded as safe, have been reported to exacerbate vascular inflammation under certain conditions. Xiong et al. demonstrated PLGA nanoparticles increased the release of TNF-α when tested on macrophages *in vitro*, exhibiting up to a 3-fold increase compared to untreated cells [216]. Furthermore, PLGA nanoparticles have been shown to induce acute brain ischemia after intravenous injection in rats [146]. Among inorganic systems, intravenous administration of mesoporous silica nanoparticles has been shown to induce vascular endothelial damage as measured by reductions in endothelial nitric oxide production and increase release of inducible nitric oxide synthase, an enzyme produced under inflammatory stress [217]. A similar study highlighted

that intravenous injection of silica nanoparticles in mice could increase blood platelet aggregation, leading to a thrombogenic environment [218]. These findings underscore even widely studied platforms can provoke significant toxicity or vascular inflammation that limit their clinical potential, especially for vascular applications where these platforms are exposed to systemic blood flow.

Equally concerning are biodistribution patterns that reveal substantial off-target accumulation of nanoparticles in sensitive organs. Nanoparticles are commonly cleared by the liver and spleen after intravenous injection due to the presence of mononuclear phagocytic system (MPS) cells in these organs [219]. However, some platforms have been shown to undergo systemic distribution and accumulate in vital organs which are unable to properly clear the particles, leading to off-target effects. In *in vivo* biodistribution studies, PLGA nanoparticles have been reported to accumulate in the brain. Semete et al reported approximately 13% of PLGA nanoparticles localised in the brain after 7 days post-oral administration in mice [220]. Such high concentrations of PLGA nanoparticles in the brain can lead to acute damage to neuronal tissue as observed by Poulios et al [146]. Inorganic nanoparticles such as gold nanoparticles also show undesirable biodistribution for vascular applications. One study performed tail vein injections of gold nanoparticles in rats and showed distribution not only to liver and spleen, but also to the heart and brain within 24 hours, raising concerns about unintended cardiac and neurological exposure [221]. These findings emphasise that both organic and inorganic platforms suffer from poor toxicity and biodistribution profiles, which directly limits their progression into clinical settings.

Complex manufacturing

Another major limitation of current nanoparticle platforms is the complexity of their manufacturing processes. Many platforms require multi-step wet chemistry protocols to achieve reproducible drug loading and surface functionalisation. For instance, polymeric nanoparticles such as PLGA often demand emulsification-solvent evaporation followed by multiple purification steps, thereby requiring approximately 2-3 days to successfully functionalise the nanoparticle surface with therapeutic cargo [207]. Similarly, inorganic nanoparticles are mostly chemically inert and/or hydrophobic and therefore require chemical linker molecules to immobilise drugs [222, 223]. This often translates to a time-consuming and expensive functionalisation process ultimately unsuitable for scalable production.

Furthermore, in order for drug conjugation to occur with a nanoparticle platform, some sort of chemical conformational change must take place. As a result, it is imperative that drug functionality is not impaired post-conjugation, a phenomenon seen across some current platforms. For instance, van der Valk et al. successfully developed a liposomal based nanoparticle encapsulating the corticosteroid prednisone which demonstrated targeted accumulation to sites of atherosclerotic plaques in patients with iliofemoral atherosclerosis [224]. However, there was no observed reduction in arterial inflammation, a response expected to be seen due to prednisone's potent anti-inflammatory properties. Although there could be several reasons for this, it is believed that encapsulation of prednisone with the liposome impaired drug function, resulting in poor efficacy [224]. Similarly, in a separate study, gold nanoparticles reported a 50% and 89% loss of bioactivity for L218C and D453C enzymes respectively post-functionalisation [225]. Together, these findings underscore that nanoparticle translation is constrained not only by the technical demands of complex drug functionalisation, but also by the potential loss of drug activity following conjugation or encapsulation.

Overcoming these barriers will be critical for developing clinically viable platforms for vascular applications.

4.1.3.3 Plasma polymerised nanoparticles

Plasma polymerised nanoparticles (PPN) represent a new class of drug carriers designed to overcome the limitations of conventional nanoparticle platforms in cardiovascular applications [226]. They are synthesised through plasma polymerisation, a process in which a monomer gas is introduced into a vacuum chamber and exposed to an energetic plasma source, inducing polymerisation and the formation of functional plasma. While this technique has traditionally been used to deposit thin polymer films for industrial processes including plasma etching, lithography, and semiconductor manufacturing [227], it can also give rise to so-called "dusty plasmas," where charged nanoclusters aggregate into particulates within the plasma volume [228]. Once considered contaminants, these particulates share many of the same chemical functionalities as plasma coatings and can be harnessed as stable, functional nanoparticles for biomedical use. In practice, PPN are generated via radiofrequency plasma polymerisation using carbon-based precursors, during which reactive nanoclusters aggregate into charged nanoparticles that diffuse out of the plasma and deposit onto exposed surfaces including tissue culture well plates (Figure 4.3) [226, 229]. The result is a carbon-based nanoparticle with a highly reactive surface chemistry.

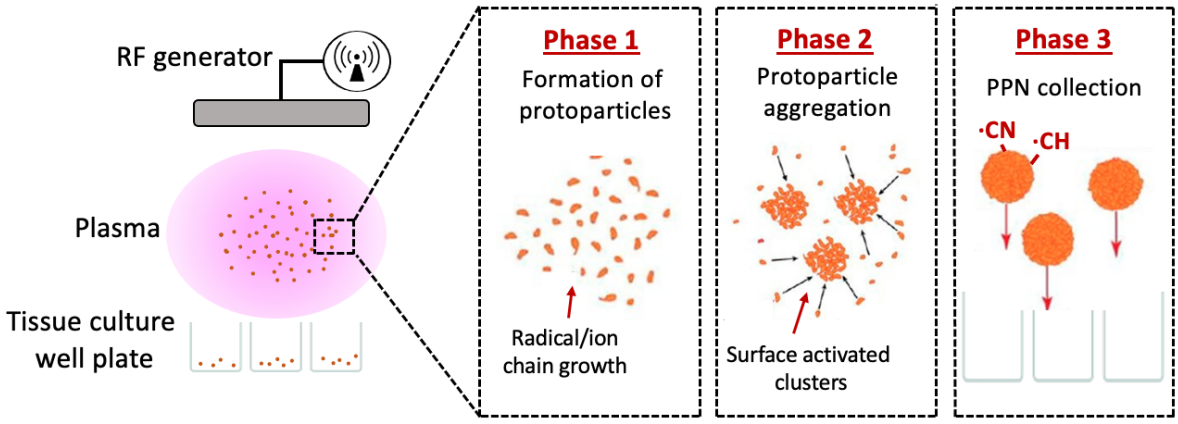

Figure 4.3: Formation and collection of PPN
Schematic showing how the formation of protoparticles in the plasma volume (phase 1) results from reactive plasma polymerisation of carbon-based precursors. Protoparticles (nanoclusters) rapidly aggregate to form spherical PPN with reactive surfaces (phase 2). PPN are dragged out of the plasma once they reach a critical size by iron drag and thermophoretic forces, and can be collected using a tissue culture well plate (phase 3). RF = radiofrequency; ·CN = cyano-radical; ·CH = methylidyne-radical

The physical and chemical properties of PPN can be tailored by altering plasma conditions during synthesis, enabling the generation of nanoparticles with unique surface reactivity and stability. Using a reactive mixture of acetylene, nitrogen and argon in the plasma polymerisation process creates a functional PPN surface characterised by free radical species such as cyano-radical and methylidyne-radical [226]. When removed from the vacuum chamber, atmospheric oxygen reacts with these radicals, restructuring the PPN surface and producing amine and carboxyl functional moieties. These surface functional groups facilitate the rapid attachment of multiple molecules of various sizes in a simple one-step incubation process, bypassing the need for chemical linkers or complex wet chemistry procedures which have stymied the clinical use of other nanoparticle platforms [230]. Whilst doing so, PPN also maintains cargo bioactivity post-conjugation. In aqueous solution, PPN acquire a positive net charge at neutral pH due to the protonation of functional groups. Surface charge and stability of PPN can be fine-tuned by changing the pH of the suspension solution, improving surface hydrophilicity and increasing surface reactivity depending on the type of molecular cargo

[226]. Post-synthesis, PPN can be stored at room temperature for at least 16 months without losing functionality, demonstrating a long shelf-life [229]. As such, PPN reduces the complexity, time and cost of manufacturing and functionalisation compared to other nanoparticle platforms, making it more suitable for up scaled commercial production.

In addition, PPN have shown significant promise for functional therapeutic applications. Delivery of PPNs with siRNA against the vascular endothelial growth factor (siVEGF) were successfully transfected in primary endothelial cells (hCAECs), a cell line notoriously difficult to transfect, and proved to significantly decrease VEGF expression compared with commercial lipid-based nanoparticle platforms carrying 150-fold higher siVEGF concentrations [230]. In a different *in vitro* setting, PPN effectively delivered the anti-proliferative drug paclitaxel resulting in an increase in apoptotic cells [230]. This demonstrated that PPN could conjugate and deliver multiple types of cargo whilst improving their biological function when compared to other nanoparticle platforms. Similar results were seen *in vivo*, with PPN carrying a combination of siVEGF and paclitaxel effectively reducing orthotopic breast tumours in mice [230]. Furthermore, PPN have undergone extensive toxicity studies *in vitro* and *in vivo*, and have demonstrated extremely low toxicity profiles [231]. These studies have highlighted PPN as a safe, easy to use nanoparticle platform which can effectively deliver therapeutic cargo. This makes PPN a promising nanoparticle platform that could potentially overcome issues with current drug delivering vascular devices. However, the biodistribution and retention capabilities of PPN still need to be examined before pre-clinical evaluation can take place.

4.1.4 Therapeutic rationale for MCC950 and IL-10

As highlighted in section 2.2.3 of this thesis, selective anti-inflammatories have emerged as promising drug candidates for treatment of vascular injury post-endovascular intervention. MCC950 and IL-10 represent two leading candidates that have demonstrated potent anti-inflammatory effects combined with pro-healing capabilities.

4.1.4.1 MCC950

MCC950 is a small-molecule drug that has generated considerable interest for its ability to selectively block the NLRP3 inflammasome, a cytosolic multiprotein complex strongly implicated in vascular inflammation and restenosis [232]. MCC950 was first identified through high-throughput screening efforts at The University of Queensland and Trinity College Dublin as a potent, selective inhibitor of the NLRP3 inflammasome [233]. Originally characterised in the context of inflammatory diseases such as rheumatoid arthritis, it quickly gained attention for its potential in other applications. Its specificity and potency made it a valuable tool for inhibiting sterile inflammatory pathways and has increasingly emerged as a promising cardiovascular therapy. A study investigating atherosclerotic lesion development in apolipoprotein E–deficient mice showed MCC950 treatment significantly reduced the development of atherosclerotic lesions as determined by average plaque size and plaque volume [234]. This was the first study to highlight MCC950's potential in vascular settings. Importantly, additional studies suggest that MCC950 targeting of the NLRP3 inflammasome does not compromise activation of other inflammasomes critical to pathogenic inflammation [235]. For instance, MCC950 does not inhibit the NLRC4 inflammasome, a key component of the pathogenic immune response which secretes low levels of IL-1β and TNF-α in the presence of pathogens such as Gram-negative bacteria [233]. These studies point to MCC950 as a specific inhibitor of NLRP3-mediated sterile inflammation common to vascular injury, while

still allowing other nontargeted inflammatory pathways to perform basic immune pathogenic functions such as fighting infection. MCC950 selectively prevents NLRP3 inflammasome assembly by inhibiting ASC oligomerisation, distinguishing it from broader anti-inflammatory agents which act on upstream pathways or cytokine products and broadly suppress immune function [232]. This selectivity makes MCC950 particularly attractive for addressing sterile vascular inflammation associated with restenosis, without compromising host defence.

The rationale for using MCC950 after vascular injury stems from the central role the NLRP3 inflammasome plays in sterile inflammation leading to vascular inflammation [236]. Endothelial denudation and medial injury during angioplasty or stent deployment release damage-associated molecular patterns (DAMPs) that trigger NLRP3 activation [237]. In a two-step priming and activation model, NLRP3 assembles with ASC and caspase-1, cleaving pro-IL-1β and pro-IL-18 into their mature forms [238]. These cytokines amplify inflammation, recruit inflammatory cells and stimulate smooth muscle cell proliferation leading to restenosis [87]. Concurrently, caspase-1-mediated cleavage of gasdermin D induces pyroptosis, an inflammatory form of programmed cell death [239]. Pyroptotic cells release further cytokines and DAMPs, fuelling a self-perpetuating cycle of vascular inflammation and remodelling.

By targeting NLRP3 directly, MCC950 has the ability to inhibit this inflammatory cascade. Chapter 3 in this thesis highlighted the selectivity of MCC950, reducing neointimal hyperplasia and promoting endothelialisation in a murine vascular grafting model. This study confirmed that selectively inhibiting NLRP3 inflammasome formation was an effective strategy for preventing restenosis. However, a more optimised delivery strategy for MCC950 needs to be developed in order to see its efficacy in other endovascular device settings.

In summary, MCC950 offers a highly targeted approach to disrupt the inflammatory processes that drive restenosis after endovascular intervention. By halting both cytokine-mediated inflammation and pyroptotic cell death, it directly addresses the key mechanisms of neointimal hyperplasia. These characteristics make MCC950 an excellent candidate for localised delivery, especially when paired with platforms like plasma polymerised nanoparticles that can enhance retention at the injury site.

4.1.4.2 IL-10

Interleukin-10 (IL-10) is an anti-inflammatory cytokine originally described as a cytokine synthesis inhibitory factor due to its ability to suppress pro-inflammatory responses in T-helper cells [240]. Since then, IL-10 has been recognised as a key regulator of immune balance, limiting damaging inflammation while promoting resolution and repair [241, 242]. This dual role has positioned IL-10 as an attractive therapeutic candidate in a range of inflammatory diseases, and increasingly as a potential intervention for vascular injury and restenosis.

The therapeutic rationale for IL-10 lies in its ability to shape the macrophage response following vascular injury. After angioplasty or stent implantation, endothelial denudation and vessel wall trauma trigger rapid recruitment of circulating monocytes, which differentiate into macrophages at the injury site [87]. In the presence of inflammatory signals, these macrophages adopt a pro-inflammatory M1 phenotype, secreting high levels of TNF-α, IL-1β, and reactive oxygen species. This M1-driven environment promotes smooth muscle cell proliferation and extracellular matrix deposition, driving the development of neointimal hyperplasia [243]. IL-10 acts through its receptor and downstream JAK-STAT3 signalling to inhibit NF-κB-mediated transcription of these pro-inflammatory mediators, while simultaneously inducing a shift

toward the anti-inflammatory M2 phenotype [244, 245]. M2 macrophages are characterised by secretion of IL-10 and TGF-β, upregulation of scavenger and mannose receptors, and production of pro-healing factors that support angiogenesis, matrix remodelling, and endothelial repair [246]. This M1-to-M2 transition reprograms the local immune environment from one that perpetuates inflammation to one that promotes resolution and vascular healing.

Evidence from preclinical studies supports this immunomodulatory role in the setting of vascular injury. In a hypercholesterolemic mouse model of restenosis, knocking-out IL-10 resulted in a significant 1.9-fold increase in neointima hyperplasia compared to non-IL-10 knock-out controls [247]. Conversely, IL-10 overexpression in the same mouse model led to a 45% reduction in neointima formation, with a significant reduction in pro-inflammatory cytokine secretion. Furthermore, Li et al developed a platelet membrane coated PLGA nanoparticle for encapsulation of IL10 and evaluated the platform in a rat model of angioplasty-induced vascular injury [124]. *In vitro*, the IL-10 nanoparticle formulation effectively drove macrophage polarisation towards the ant-inflammatory M2 phenotype and promoted endothelial function, translating to decreased neointima areas at 14 days *in vivo*. Taken together, these studies highlight IL-10 as a uniquely suited therapeutic candidate for post-angioplasty vascular injury. By actively shifting macrophage populations towards a pro-healing phenotype while supporting endothelial recovery, IL-10 offers an immunomodulatory mechanism that directly addresses the inflammatory drivers of restenosis.

As shown in Li et al's study, freely delivering IL-10 inside the vasculature results in poor efficacy, most likely due to poor drug retention because of wash out [124]. The authors here

highlight the need for a drug carrying vessel to improve such properties, concluding that nanoparticles show promise. In this chapter, we evaluate PPN as a platform to improve IL-10 delivery, expanding it's potential as a therapy in endovascular interventions.

4.-2 Methods

4.-2.1 Plasma polymerised nanoparticles (PPN) synthesis

The PPN were synthesized in reactive dusty plasmas via plasma polymerization from acetylene, nitrogen, and argon using low pressure (200 mTorr), radiofrequency discharges (13.52 MHz), as previously described [226]. Nanoparticle formulations were synthesized in this study to assess the biodistribution and toxicity/biosafety profiles of the PPN, as well as their ability to delivery biological cargo. The plasma parameters, including the input power, gas flow rates, and discharge pressure, were chosen based on previous studies [226]. The PPN were collected from the plasma discharge using 24-well polystyrene plates (CLS3524, Merck, Darmstadt, Germany), as previously described [229]. This method allowed for the controlled collection and post-synthesis handling of high yields of PPN with well-defined physical and chemical properties and without inducing nanoparticle aggregation. The nanoparticles were then resuspended directly from wells under sterile conditions with RT-PCR-grade water (4387936, Life Technology, Carlsbad, CA, USA).

4.-2.2 Physical characterisation of PPN

The hydrodynamic size and zeta potential of the PPN were measured using a dynamic light-scattering Zetasizer Nano ZS system (Malvern Panalytical, Almelo, The Netherlands). PPN were dispersed in RT-PCR-grade water and transferred to disposable folded capillary cells

(DTS1070, Malvern Panalytical, Almelo, The Netherlands). The hydrosizes and zeta potentials were then measured for each sample.

4.-2.3 Preparation of ^{89}Zr radiolabelling

The following methods (section 4.2.3 – 4.2.6) were performed by the Centre for Advanced imaging at the University of Queensland. Final report with data was prepared by Dr Karine Mardon, Dr Nick Fletcher and James Humphries, and figures were reconfigured for the purpose of this thesis. Zirconium-89 (^{89}Zr) was provided by Austin Health in 0.05 M Oxalic acid. Prior to labelling, the ^{89}Zr was neutralised to pH = 8-9 with 10% v/v 1M Na_2CO_3. An equal volume of HEPES (4-(2-hydroxyethyl)-1-piperazineethanesulfonic acid) buffer (0.5 M, pH 7) was added. Specific activity (Megabecquerels/mL, MBq/mL) was calculated with a Capintec CRC-25 dose calibrator.

PPN was conjugated with a hexadentate chelator, desferrioxamine (DFO), and suspended in HEPES buffer (0.5 M, pH 7). PPN-DFO was then mixed with ^{89}Zr from the working solution at a ratio of 1 MBq per 10^6 PPN. The reaction was incubated at room temperature without shaking for 30 minutes prior to assessment of radiolabelling efficiency and radiochemical purity.

4.-2.4 *In vitro* serum stability of ^{89}Zr-PPN

Serum stability measurements were also evaluated for the potential degradation and transmetalation behaviour of the labelled compounds. An aliquot of ^{89}Zr-DFO-PPN (10 MBq, simplified as PPN-^{89}Zr in subsequent text) was transferred to an Eppendorf tube containing an equal volume of human serum (H4522, Sigma). The resultant mixture was maintained at 37 °C

in a humidified incubator for 8 days and periodically assessed with diethylenetriaminepentaacetic acid (DTPA) to determine ^{89}Zr transchelation using the radio-instant thin-layer chromatography (radio-iTLC). Briefly, a 2 μL aliquot of radiolabelling reaction mixture was spotted on silica-impregnated TLC paper. A further 2 μL aliquot was taken and mixed with DTPA (5 μL, 5 mM) for 5 minutes. The DTPA-containing conjugate radiolabelled sample was spotted on TLC paper and subsequently run with 50:50 v/v H2O: Ethanol mobile phase. TLC plates were then visualised on an Eckert & Ziegler Mini-Scan and Flow-Count iTLC Reader. The area-under-curve (AUC) was calculated for all peaks. In this solvent system, ^{89}Zr bounding to the DFO-PPN conjugates and free ^{89}Zr (if present) would have an Rf~0, while ^{89}Zr chelated by DTPA (^{89}Zr-DTPA) and ^{89}Zr-DFO (if present) would have an Rf~1.The sample was vigorously mixed prior to sampling each time to account for settling of labelled particles.

4.-2.5 *In vivo* imaging and biodistribution

All the animal procedures were approved by The University of Queensland Animal Ethics Committee (AEC Approval Number: 2022/AE000841). All protocols confirm to the NHMRC animal welfare guidelines. Healthy male Sprague Dawley rats (291 ± 62.9 g) from 10-12 weeks old were obtained from The University of Queensland Biological Resources. ^{89}Zr-radiolabelled carbon-based nanoparticles (^{89}Zr-PPN) were administered intravenously to rats. For PET/CT (Positron emission tomography/Computed tomography) imaging, a total of 18 healthy male Sprague Dawley rats were anaesthetised using an anaesthetic chamber (3% isoflurane in oxygen at a flow of 2L/min, IsoFlo, Abbott Laboratories), a catheter was inserted into the lateral tail vein before the animal being placed in the Si78 PET/CT scanner (Bruker, Germany). Rats were maintained under 1 to 2% isoflurane in air-oxygen mixture at a flow rate of 1L/min for

the duration of the imaging session and monitored by a breathing pillow (SA Instrument, USA). A single intravenous injection of ^{89}Zr-PPN was performed with a total injected volume 300 µL/animal, containing no greater than 15 MBq of radioactive compound in a solution of 1M of Phosphate buffer saline (PBS)(pH 7.4). ^{89}Zr-PPN was infused slowly over one minute period. A 60 min dynamic PET scan was started simultaneously with the radiotracer injection and was followed by a 5 min CT attenuation scan for 1 hour. Rats were also imaged with static scans, at 24 hrs, 48 hrs, 72 hrs, and 8 days after radiotracer injection.

For PPN biodistribution, rats received ^{89}Zr-PPN via intravenous injection and were sacrificed at different time points (n=3 per time point; 1 hr, 4 hrs, 24 hrs, 48 hrs, 5 days and 8 days). Organs were removed, weighed and conducted *ex vivo* gamma-counting analysis using a gamma counter (Wizard 2480, Perkin Elmer, USA). Data were decay corrected to the time of the radiotracer injection and results expressed as percentage of injected dose per gram of tissue (%ID/g).

4.-2.6 Biodistribution data processing and analysis

The CT images were acquired through an X-ray source with the voltage set to 60 kV and the current set to 600 µA with an isotropic resolution of 200 µm. The total CT scanning process took approximately 5 minutes. The CT images were reconstructed using a Feldkamp cone beam back-projection algorithm using Paravision 360 (version 3.4) (Bruker, Germany).

For the dynamic PET data acquisition, the emission data were normalized and corrected for decay. The list-mode data were sorted into 41 frames (10 x 30 sec, 25 x 60 sec, 6 x 300 sec time frames). The resulting sinograms were reconstructed with Paravision 360 (v3.4) using a 0.5mm 3D-maximum likelihood expectation-maximization iterative image reconstruction algorithm. Fusion of CT and PET images and definition of region of interest (ROIs) were performed using PMOD version 4.4 (Bruker, Germany). For each PET image, 3D region of

interest (VOI) was drawn over organs of interest guided by the CT. Activity per voxel was converted to nCi/cc using a conversion factor obtained by scanning a cylindrical phantom filled with a known activity of ^{89}Zr to account for PET scanner efficiency. Activity concentrations were then expressed as percent of the decay-corrected injected activity per cm^3 of tissue that can be approximated as percentage injected dose per gram of tissue (%ID/g). All data were decay corrected to the time of injection of the radiotracer. The mean value in each VOI was used to generate regional time activity curves (TACs). Individual TACs were normalised by the injected dose and results were expressed as % ID/g.

4.-2.7 *In vitro* stimulation assay

PPN (5 x 10^9 PPN/mL) were conjugated to IL-10 (1.65 µg/mL) or MCC950 (3.65 µg/mL) in RT-PCR Grade nuclease free (NFW) water for 30 mins at room temperature. For IL-10 functionality test, J774a.1 murine macrophages were seeded into 96-well plates (2 x 10^4 cells/well) followed by treatment with liposaccharide (LPS) (1 µg/mL). Cells were left for 30 mins, followed by treatment with either PPN (5 x 10^7 PPN/100µL), free IL-10 (16.5 ng/100µL) or PPN-IL10 (corresponding doses for both PPN and IL-10 taken from PPN-IL10 conjugation) and left to incubate for 24 hours. Supernatant was taken to perform TNF-α ELISA (ab208348) and the cells were fixed and stained for F-actin using Phalloidin and nuclei was stained using propidium iodide. For MCC950 functionality, J774a.1 murine macrophages were again seeded into 96-well plates (2 x 10^4 cells/well) followed by treatment with LPS (1 µg/mL). Cells were left for 90 mins, treated with either PPN (5 x 10^7 PPN/well), free MCC950 (36.5 ng/100µL) or PPN-MCC950 (corresponding doses for both PPN and MCC950 taken from PPN-MCC950 conjugation), and left for another 90 mins before being treated with adenosine triphosphate (ATP) (1.25 mM), followed by a 24-hour incubation period. Supernatants were then collected

and analysed using ELISA for IL-1β (ab197741) and TNF-α (ab208348) according to manufacturer's instructions. As done for the IL-10 functionality test, cells were fixed and stained for F-actin using Phalloidin and nuclei was stained using propidium iodide. Cells were imaged using IncuCyte® Live-Cell Analysis microscope.

4.-2.8 Transmission and scanning electron microscopy

Carotid artery samples designated for scanning electron microscopy (SEM) were initially cut open and fixed in 2.5% glutaraldehyde in 0.1 M phosphate buffer (PB) for 1 h. Samples then underwent secondary fixation in 2% osmium tetraoxide (ProSciTech) with 0.1 M PB for 1 h. After washing in 0.1 M PB 3 times, samples were dehydrated in increasing concentrations of ethanol and dehydrated in hexamethyldisilane (Sigma Aldrich, MO, USA), and dried in a desiccator overnight. Samples were mounted on SEM stubs (ProSciTech) with the lumen side facing up, and coated with a 10 nm layer of sputtered gold (Emitech K550X). Samples were imaged on the Zeiss Sigma VP HD Scanning Electron Microscope.

IL-10 (1.65 µg/mL) was conjugated to 10nm gold nanoparticles (ab269933) as per manufactures instructions. IL10-gold conjugates were then conjugated to PPN (5 x 10^9 PPN/mL) and prepared for transmission electron microscopy (TEM). For TEM imaging, PPN-IL10-gold conjugates were collected on a 300-mesh grid with an ultrathin carbon film supported by a lacey carbon film (ProSciTech). Imaging was performed with a FEI Tecnai T12 Transmission Electron Microscope (TEM) at an acceleration tension of 120 kV.

4.-2.9 Rat carotid injury model

Study was approved by the University of Sydney Animal Ethics Committee (protocol number 2022/AE002093). Experiments were conducted in accordance with the Australian Code of Practice for the Care and Use of Animals for Scientific Purpose. Sprague Dawley rats (male, 10-11 weeks) were obtained from Animal Resources Centre (Perth, WA, Australia). PPN (1 x 10^9 PPN/mL) were conjugated to IL-10 (0.33 μg) or MCC950 (0.73 μg) in RT-PCR Grade NFW for 30 mins at room temperature. Samples, including a PPN only group (1 x 10^9 PPN/mL) were spun down in a microcentrifuge for 5 mins at 21 000 g, supernatant was removed and PPN pellet was resuspended in saline. Free IL-10 (0.33 μg/mL) and MCC950 (0.73 μg/mL) in saline were also prepared. Injury was performed to the left carotid artery and treatments were performed as previously described [248]. Briefly, the right carotid artery was isolated and clamps were placed approximately 1.5 cm apart on the exposed artery. A small incision was then made on the proximal side of the artery and blood was washed out using heparinised saline. Microforceps (World Precision Instruments 500373-T) were inserted through the small incision and expanded inside the artery five times. A 22g catheter was then inserted in and out of the artery a further five times for denudation. The artery was then flushed using heparinised saline, and 50 μL of respective samples was injected slowly into the artery through the proximal incision using a separate 22g catheter and syringe. Treatment catheter remained inserted inside the artery for 2 mins to allow proper drug retention. The incision was then closed using 9-0 silk sutures and blood flow was restored. After 14 days, the injured section of the carotid was explanted and animal was euthanised. One artery per rat underwent surgery.

4.-2.10 Retention study

PPN (5 x 10^9 PPN/mL) was conjugated with CF750 (830 ng/mL, Sigma-Aldrich, MX750S100) fluorescent tag following the same protocol outlined above. Rat carotid injury was performed, and either PPN-750 or free 750 was delivered into the artery. After 1 and 5 days, the injured section of artery was explanted and immediately taken for fluorescence imaging using an *in vivo* imaging system (IVIS). Excitation and emission wavelengths were set at 755 nm and 777 nm, respectively.

4.-2.11 Histology and immunohistochemistry

Explanted samples were fixed in paraformaldehyde (4%) overnight at room temperature before being dehydrated through an ascending ethanol gradient and embedded in paraffin wax. Samples were then sectioned transversely at 5 μm using a microtome. For histology staining, five slides from equidistant points along the artery were deparafinized, rehydrated, and stained with haematoxylin and eosin (H&E) stain. The same procedure was conducted for immunohistochemistry staining using the primary antibody against von willebrand factor (vWF, 1:100, ab287962) and a secondary antibody against rabbit (1:250, ab6564). Sections were mounted and cover slipped with DAPI-containing mounting media (Sigma Fluoroshield with DAPI, F6057).

4.-2.12 Quantitative analysis

Analysis of histology and immunohistochemistry slides was done using ImageJ. For H&E staining, neointimal hyperplasia area was calculated and presented as a percentage of total lumen area to give percentage of vessel occlusion. vWF positive lumen coverage was quantified by first measuring the lumen circumference, followed by measuring the length of

endothelium showing positive vWF staining. Lumen coverage was then calculated as length of vWF positive staining divided by lumen circumference.

4.-2.13 Statistical analysis

Data are expressed as mean ± standard error of the mean. Analysis was performed in GraphPad Prism 9 (Graphpad Software, San Diego, California) and statistically significant differences were determined by t-test or one-way analysis of variance followed by Dunnett's multiple comparisons test. $P < 0.05$ was considered statistically significant. *, **, *** and **** display $P < 0.05$, $P < 0.01$, $P < 0.001$, and $P < 0.0001$ respectively.

4.3 Results

4.3.1 Radiolabelling PPN for biodistribution study

To assess PPN biodistribution, PPN was radiolabelled with Zirconium-89 (PPN-^{89}Zr). The synthesis of PPN-^{89}Zr consisted of 2 steps (Figure 4.4A). First, PPN was complexed with siderophore-derived, acyclic chelator desferrioxamine (DFO), bearing the hydroxamate groups, and then PPN-DFO was complexed with ^{89}Zr. In preparation for animal injection, serum stability of PPN-^{89}Zr was examined. PPN exhibited good retention of the ^{89}Zr radionuclide at day 0 (Figure 4.4B), 1 (Figure 4.4C) and 8 (Figure 4.4D), with minimal activity appearing in a second peak (highlighted in yellow) representing ^{89}Zr coordination to the added competitive DTPA chelator. Over the 8 days, only 8.01% transchelation or degradation was apparent during incubation with human serum (Table A1). These results indicated that PPN-^{89}Zr was stable over the time course required for subsequent animal *in vivo* imaging studies.

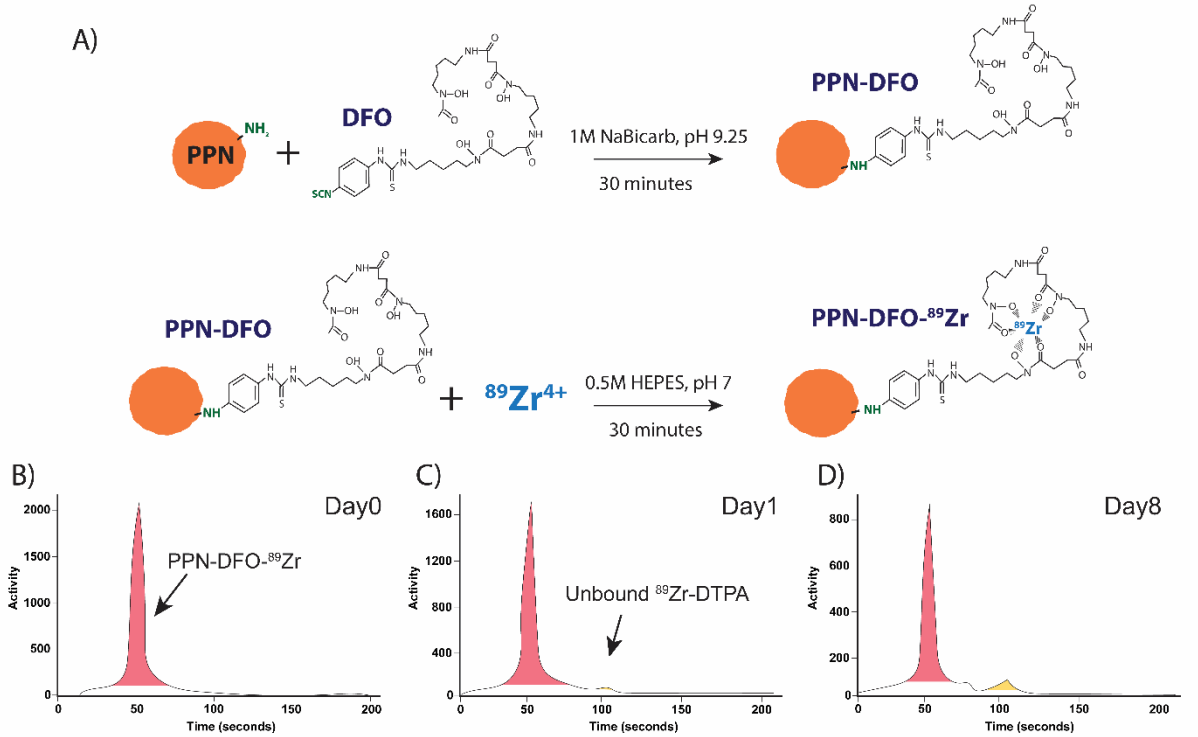

Figure 4.4: Stability of PPN-^{89}Zr *in vitro*
A) Schematic illustration of the conjugation process for PPN and ^{89}Zr. B-D) Stability of PPN-^{89}Zr in human serum at day 0 (B), 1 (C) and 8 (D).

4.3.2 PET/CT scan biodistribution

Following the quality and stability assessments of PPN-^{89}Zr, radiolabelled PPN-^{89}Zr were administered to healthy male Sprague Dawley rats via an intravenous bolus injection for biodistribution studies using PET/CT scanning. A 60-minute dynamic PET/CT scan using a Bruker Si78 scanner was initiated at the time of injection, followed by a static CT scan at allocated time-points (Figure 4.5A). Using PET/CT image quantification, there was a significant increase in PPN-^{89}Zr accumulation in organs, particularly the liver and spleen, within minutes after injection and gradually decreased or stabilised within the first 1 h. Within the first 5 min, 13.26 ± 2.47 %ID/g and 11.79 ± 2.94 %ID/g PPN-^{89}Zr was found in the liver and spleen, respectively. Relatively smaller amounts were found in the kidney (0.24 ± 0.04 %ID/g), stomach (0.22 ± 0.137 %ID/g), lung (1.11 ± 0.122 %ID/g), and heart (1.124 ± 0.144 %ID/g) (Figure 4.5B). Notably, no detectable PPN-^{89}Zr was observed in the brain.

Representative images of the organs between 60 seconds and 210 seconds support this rapid accumulation in the spleen and lungs, with very little signal being visible in any other organs (Figure 4.5C).

Following PPN clearance from the blood circulation, subsequent static CT scans at 1, 2, 3, and 8 days post-injection were performed. Across all time points, the liver and spleen showed the highest PPN accumulation (Figure 4.5D). In liver, PPN-^{89}Zr levels were relatively stable post-injection with a decreasing trend by day 8 (day 1: 7.80 ± 0.73 %ID/g, day 2: 9.71 ± 0.83 %ID/g, day 3: 5.46 ± 0.60 %ID/g, and day 8: 6.96 ± 1.21 %ID/g). Meanwhile, on days 2 and 3, there was a significant increase in PPN-^{89}Zr accumulation in the spleen (day 2: 11.8 ± 0.37 %ID/g, day 3: 15.59 ± 0.59 %ID/g), which decreased to 8.99 ± 0.70 %ID/g by day 8. Less accumulation was observed in the kidney (1.0±0.33 %ID/g) and stomach (0.74±0.48 %ID/g) at 8 days post-injection. Throughout the scanning period, signal activity in the heart, lung, brain, and bone remained low (<0.5 %ID/g), with no significant changes up to 8 days post-injection. Representative images highlight PPN localisation in the liver and spleen across all time points (Figure 4.5E).

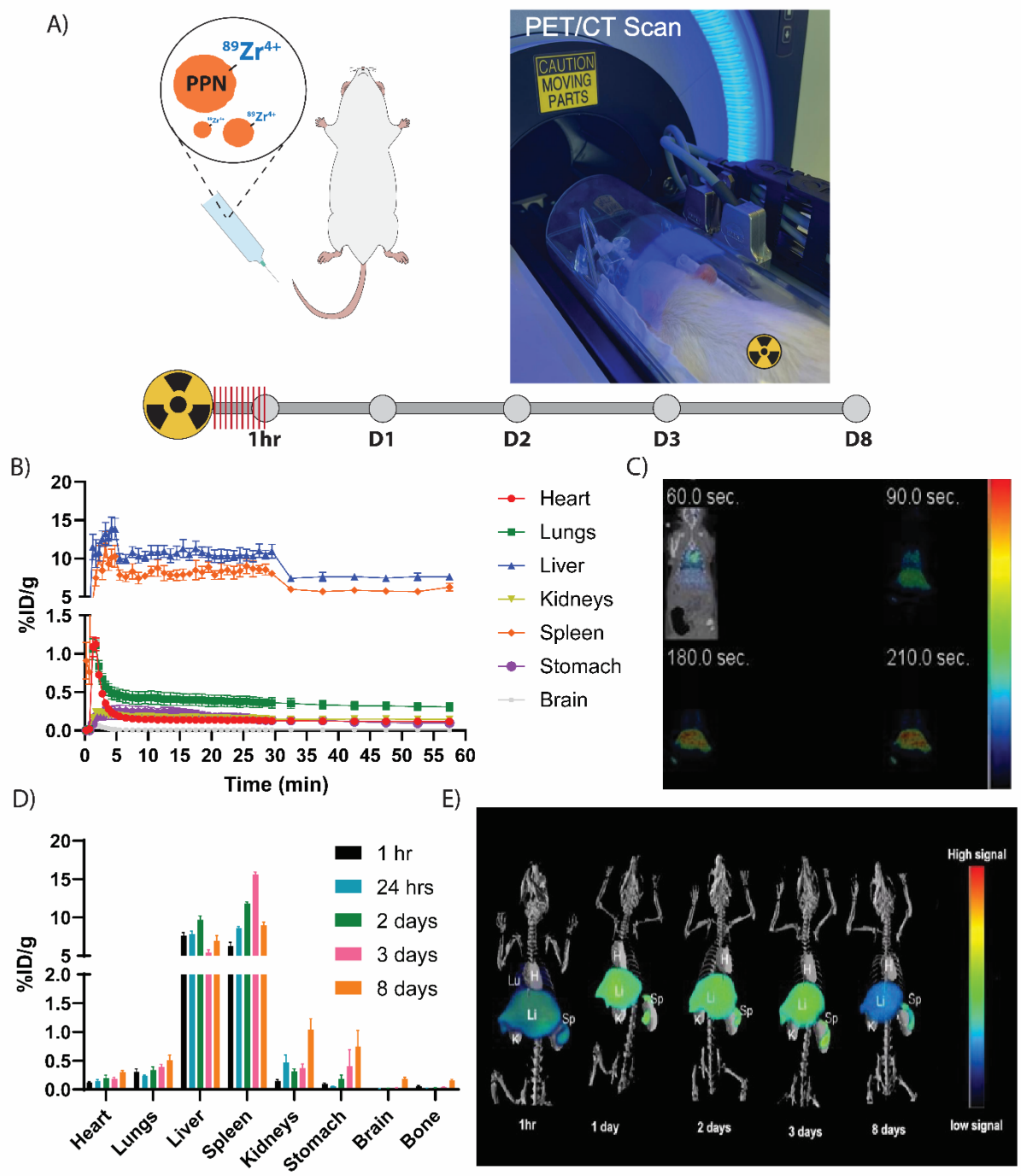

Figure 4.5: PET/CT biodistribution of PPN
A) Schematic design of biodistribution studies using PET/CT scanning in rats. B) Dynamic PET scan showing tracer distribution up to 1-hour period. %ID/g: Percentage of injected dose per gram of tissue. C) Representative PET/CT images at 60 seconds, 90 seconds, 180 seconds and 210 seconds. D) PET/CT image analysis showing PPN-^{89}Zr biodistribution at 1 hour, and 1-, 2-, 3, and 8-days post-injection. E) Representative images highlighting nanoparticle localisation at each time point. Data represents mean ± SEM (n = 3).

4.3.3 *Ex-vivo* gamma-counting clearance analysis

To further support the safety of PPN for clinical applications, PPN-^{89}Zr biodistribution and clearance was determined by dissection and gamma counting. Upon sacrifice, *ex vivo* gamma-counting was performed in the blood and major organs at 1 hour, 4 hours, 1 day, 2 days, 5 days, and 8 days post-injection (Figure 4.6A). The relative percentage of PPN-^{89}Zr remaining in the body throughout the 8-day time course was investigated to determine the propensity for PPN to clear from the body. There was a steady decrease of PPN-^{89}Zr retention in the liver over time, from the initial 73±5.7% at 1 h down to approximately 29.3±5.4% by day 8 (Figure 4.6B). The spleen showed a more stable retention profile, approximately 6.1±1.0% remained on day 8. There were minimal levels of PPN persisting in the blood, heart and lungs, indicating an efficient systemic clearance and minimal long-term retention of PPN. Collectively, these results demonstrated that both the liver and spleen are the primary sites of PPN uptake.

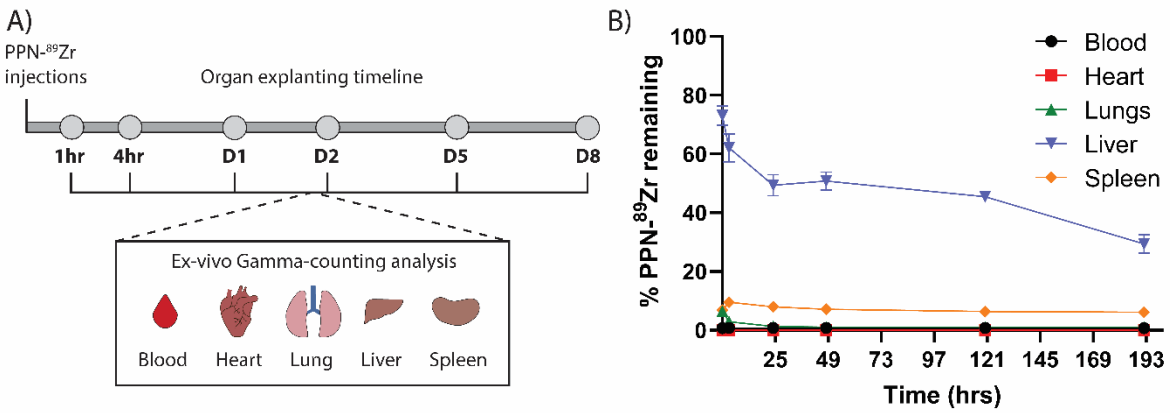

Figure 4.6: PPN *in vivo* clearance
A) Schematic design of ex-vivo gamma-counting analysis for PPN clearance. B) Clearance of PPN-^{89}Zr after intravenous injection. Results show percentage of PPN-^{89}Zr remaining in organs at different time points during the study. Data represents mean ± SEM (n = 3).

4.3.4 PPN-immunotherapy conjugation and characterisation

PPN was conjugated to either IL-10 or MCC950 using a simple one-step incubation process (Figure 4.7A). The binding characteristics of PPN to either IL-10 or MCC950 was first evaluated using dynamic light scattering to determine the hydrodynamic size, size distribution and surface charge of the resulting conjugates. PPN-IL10 conjugates resulted in a significant increase in hydrodynamic size, increasing from 160.3 ± 1.55 nm for PPN only to 442.2 ± 9.96 nm for PPN-IL10 ($p < 0.0001$)(Figure 4.7B). No significant change in hydrodynamic size was observed for PPN-MCC950 conjugates. Similarly, only PPN-IL10 showed a significant increase in polydispersity index (0.038 ± 0.02 vs 0.2 ± 0.01, $p < 0.0005$) (Figure 4.7C), while both PPN-IL10 and PPN-MCC showed a drop in Zeta potential highlighting a change to PPN surface chemistry occurred as a result of conjugation (Figure 4.7D). Together, these results highlighted IL-10 and MCC950 were successfully conjugated to PPN using a one-step incubation process performed at room temperature.

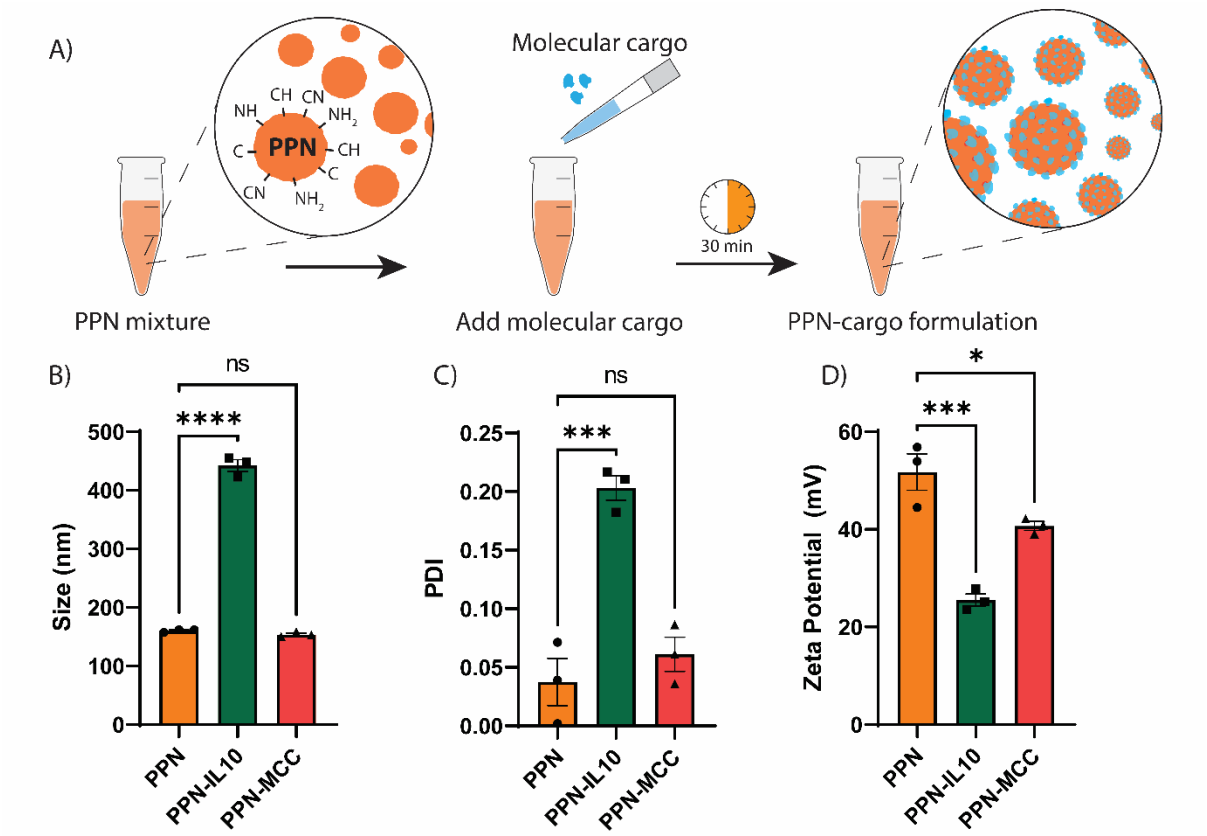

Figure 4.7: Characterisation of PPN conjugated with therapeutic cargo
A) Schematic demonstrating one-step incubation protocol for conjugating molecular cargo with PPN surface. B) Hydrodynamic size of PPN and conjugates. C) Polydispersity index (PDI) of PPN and conjugates. D) Zeta potential of PPN and conjugates. Data represents mean ± SEM (n = 3). Statistical significance is indicated by *p < 0.05, ***p < 0.001, ****p < 0.0001.

4.3.5 PPN-immunotherapy *in vitro* functional assessment

PPN-immunotherapy conjugates were then subject to functional tests specific to their drug type and mechanism of action (Figure 4.8A,E). IL-10 was initially visualised bound to PPN using transmission electron microscopy (TEM), highlighting that conjugation had occurred (Figure 4.8B). Validation of IL-10 function was conducted using an established *in vitro* model of macrophage stimulation using liposaccharide (LPS) which resulted in cell swelling (Figure 4.8C) and TNF-α secretion (Figure 4.8D) in stimulated controls. Treatment of stimulated macrophages with PPN-IL10 prevented cell swelling, with morphology more closely resembling un-stimulated macrophages, and had no observable reduction in cell number

compared to control. ELISA results indicated that PPN-IL10 significantly reduced TNF-α secretion by 82% compared to stimulated control ($p < 0.0001$)(Figure 4.8D). This reduction was a similar magnitude to that seen for free IL-10 at 81% compared to stimulated control ($p < 0.0001$), highlighting IL-10 functionality was not impaired post conjugation with PPN. Interestingly, PPN also significantly reduced TNF-α secretion by 46.9% compared to stimulated control ($p < 0.0001$), although this was not to the same degree as IL-10 or PPN-IL10.

MCC950 functionality was additionally validated using a modified macrophage stimulation protocol in order to activate the NLRP3 inflammasome (Figure 4.8E). Adenosine triphosphate (ATP) was used as a secondary priming agent post LPS-stimulation, resulting in cell death for stimulated cells due to pyroptosis (Figure 4.8F). Treatment of stimulated cells with either PPN-MCC950 or free MCC950 resulted in an increase in cell number compared to stimulated only group, indicating these groups rescued cells from pyroptosis. IL-1β production occurs specifically as a result of NLRP3 activation while TNF-α represents more broad inflammatory activation. Therefore, secretion of IL-1β and TNF-α secretion was used as an indicator of MCC950's functional selectivity post conjugation with PPN. PPN-MCC950 demonstrated a marked 82.9% suppression of IL-1β secretion compared to stimulated control ($p = 0.0003$), which was comparable to free MCC950 (82.2% reduction, $p = 0.0003$)(Figure 4.8G), but had no effect on TNF-α levels (Figure 4.8H), highlighting MCC950's selective mechanism of action was retained post-conjugation to PPN. As above, PPN showed a slight 16.3% reduction in TNF-α secretion ($p = 0.0329$), but did not show any significant decrease in IL-1β levels or an ability to rescue cells from pyroptosis.

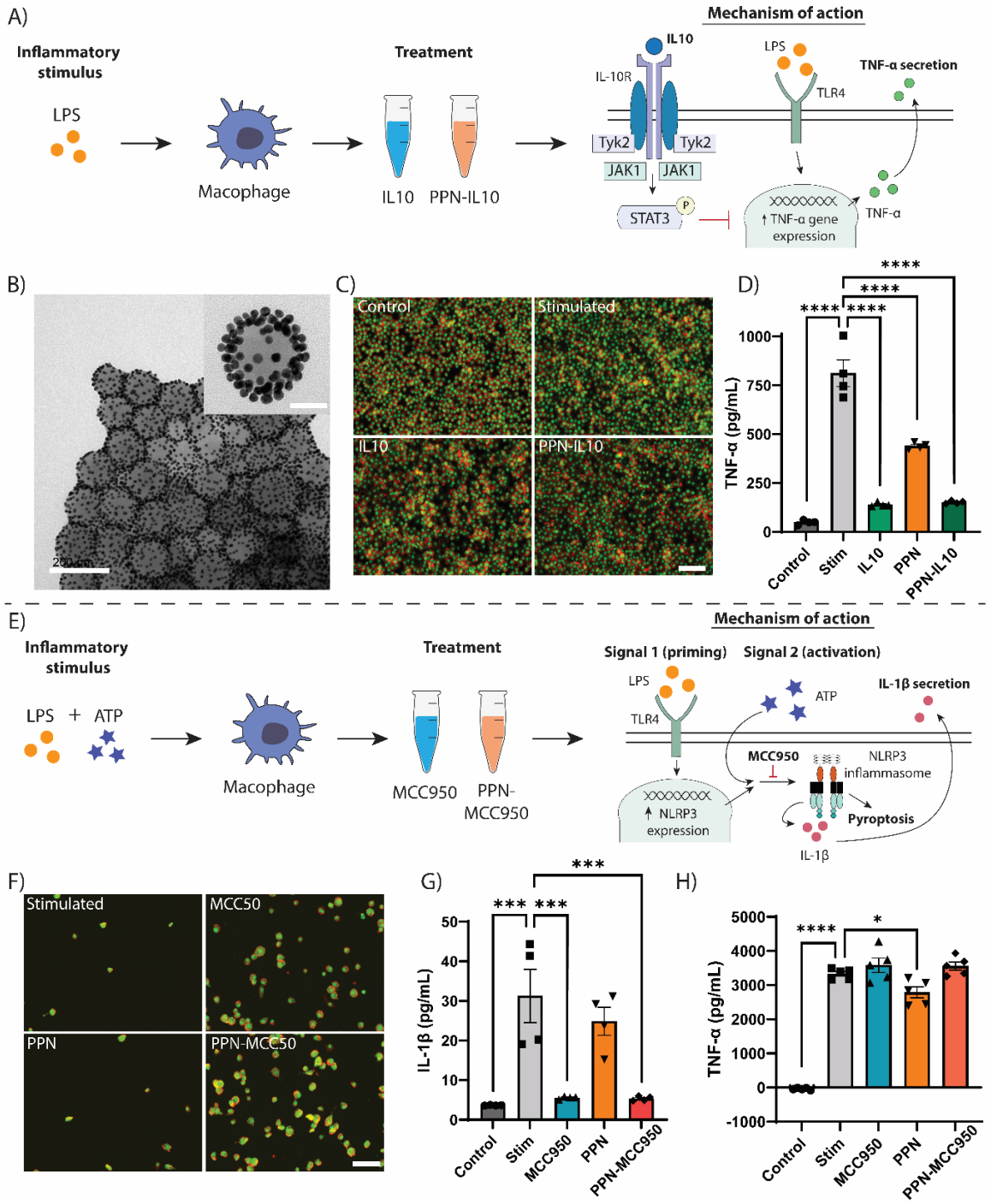

Figure 4.8: *In vitro* functionality of anti-inflammatories post-conjugation with PPN
A) Schematic showing *in vitro* model used to validate PPN-IL10 functionality. B) TEM image of PPN-IL10 (gold-tagged). Scale bars represent 200 nm and 100 nm for back image and insert, respectively. C) Representative images of macrophages after stimulation protocol. Nucleus is visible in green and actin visible in red. Scale bar represents 100 µm. D) Tumour necrosis factor (TNF)-α secretion by non-stimulated (control) and stimulated (stim) macrophages. All treatment groups, as well as stim group, underwent stimulation with LPS (n = 4). E) Schematic showing *in vitro* model used to validate PPN-IL10 functionality. F) Representative images of macrophages after NLRP3 inflammasome stimulation protocol with LPS and ATP. Nucleus is visible in green and actin visible in red. Scale bar represents 100 µm. F, G) Interleukin (IL)-1β (F) and TNF-α (G) secretion by non-stimulated (control) and stimulated (stim) macrophages. All treatment groups, as well as stim group, underwent stimulation with LPS and ATP. All data represents mean ± SEM (G: n = 4, H: n = 5). Statistical significance is indicated by *p < 0.05, ***p < 0.001, ****p < 0.0001.

4.3.6 PPN retention in *in vivo* rat carotid injury model

The ability of PPN to improve retention of cargo was evaluated by conjugating PPN with a near-infrared fluorescent tag (PPN-750) and delivering the conjugate *in vivo* in a rat carotid injury model. Initially, the carotid artery of a rat was injured using forceps and either free fluorescent tag (free 750) or PPN-750 was delivered into the injured area at equal doses (Figure 4.9A)**.** After 1 and 5 days, the treated section of the artery was explanted and imaged under IVIS (Figure 4.9B). At day 1, there was 48.8-fold greater fluorescence signal coming from the artery treated with PPN-750 compared to free 750 (Figure 4.9C). Despite a decrease in signal at day 5, PPN-750 still demonstrated a 3.7-fold greater signal compared to free 750, suggesting that 750 was still present after 5 days only when conjugated to PPN. Scanning electron microscopy (SEM) was used to visualise the extent of vascular injury and determine where PPN was localising to. Injury using forceps and denudation ruptured the endothelium and internal elastic lamina, exposing sub-endothelial collagen which PPN preferentially bound to (Figure 4.9D). PPN was also observed covering un-ruptured endothelium, although to a lesser extent.

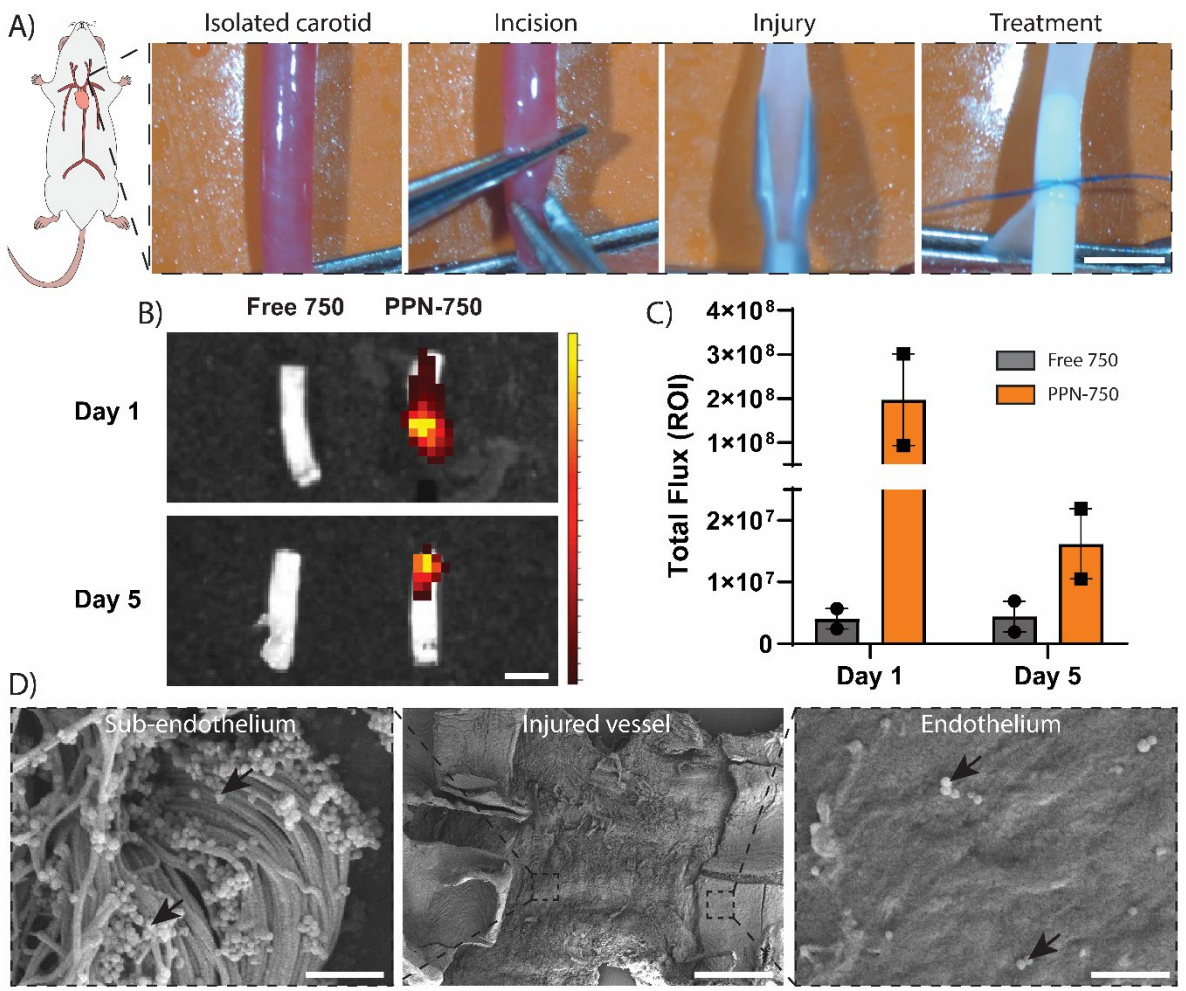

Figure 4.9: Retention of PPN-fluorescent tag *in vivo*
A) Surgical procedure of the forceps injury model in rat carotid arteries. Scale bar represents 2 mm. B) Representative fluorescent images of explanted arteries produced by *in vivo* imaging on days 1 and 5. Free 750 represents freely delivered near-infra red fluorescent tag and PPN-750 represents the same tag conjugated to PPN. The colour gradient indicates relative fluorescence (yellow corresponds to high fluorescence and dark red to low fluorescence. Scale bar represents 2 mm. C) Graph showing total fluorescent intensity within respective arterial sections. Data represents mean ± SEM (n = 2). D) SEM image of injured artery showing PPN binding to sub-endothelium space and endothelium. PPN are seen as spherical balls indicated by black arrows. Scale bar represents 1 µm for the sub-endothelium and endothelium images and 500 µm for injured vessel image.

4.3.7 PPN-immunotherapy conjugates *in vivo* functionality

To evaluate the effectiveness of PPN-IL10 and PPN-MCC950 conjugates at reducing neointimal hyperplasia *in vivo*, these groups were used as treatments during the carotid injury model outlined above. In order to compare efficacy, an injury control without treatment, a PPN only group and freely delivered IL-10 or MCC950 groups were also performed. In this model, vascular injury resulted in considerable neointimal hyperplasia within the vessel lumen after

14-days, contributing to vessel occlusion (Figure 4.10A). The percentage of vessel occlusion was therefore quantified based on the neointimal hyperplasia area and the total lumen area. Neither freely delivered MCC950 nor IL-10 were able to reduce neointimal hyperplasia after carotid injury (Figure 4.10B). In contrast, PPN-MCC950 and PPN-IL10 treatment significantly reduced vessel occlusion percentage by 61% and 63%, respectively, compared to control (p = 0.0304 and p = 0.0168, respectively).

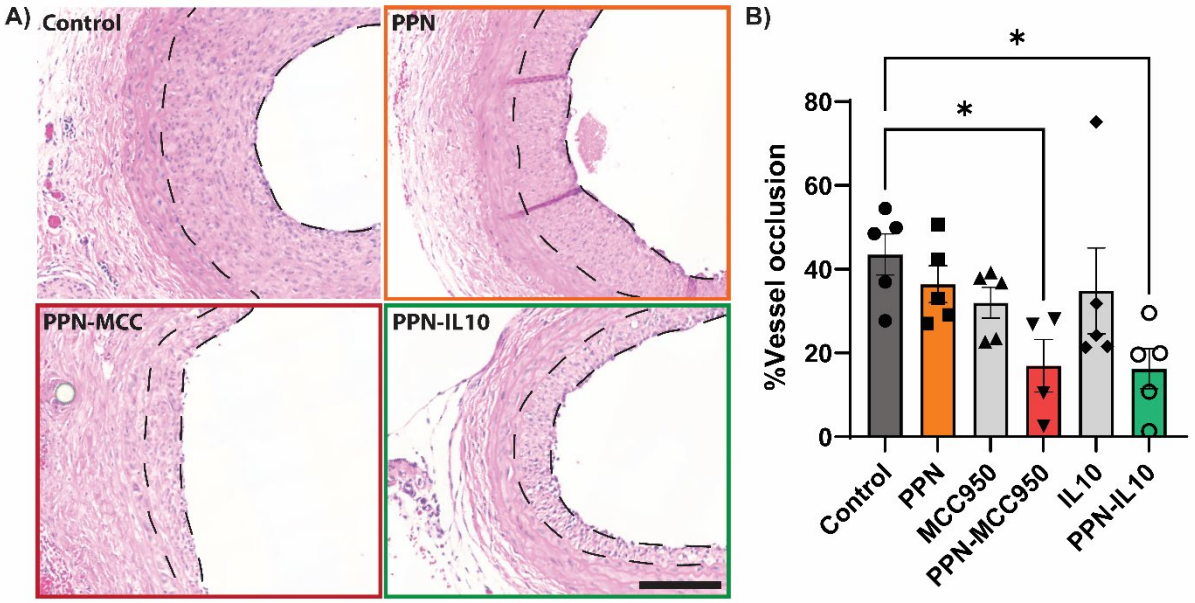

Figure 4.10: *In vivo* neointimal hyperplasia reduction by PPN-anti-inflammatory conjugates
A) Representative images of hematoxylin and eosin-stained sections after 14-day injury model showing neointimal hyperplasia. Black dotted lines outline the neointima. Scale bar represents 100 µm. B) Quantification of neointimal area expressed as a percentage of total lumen area and presented as percentage of vessel occlusion. Data represents mean ± SEM (n = 4-5). Statistical significance is indicated by *p < 0.05.

The re-endothelialisation outcomes of each treatment group were additionally assessed by measuring the percentage of endothelial coverage, indicated by vWF^{+} staining present after 14-days (Figure 4.11A). Arteries that underwent the injury procedure but did not obtain any treatment (control) showed poor, incomplete endothelial coverage at 19% ± 1.2% of the total artery lumen (Figure 4.11B). Treatment with either PPN-MCC950, IL10 or PPN-IL10 showed marked increases in endothelial coverage compared to control, correlating to 2.9-fold, 2.4-fold,

and 2.7-fold improvements, respectively (p = 0.0001, p = 0.0013, p = 0.0003, respectively). Collectively, these results indicate MCC950 and IL-10 have therapeutic benefits when delivered with PPN in an *in vivo* carotid injury model.

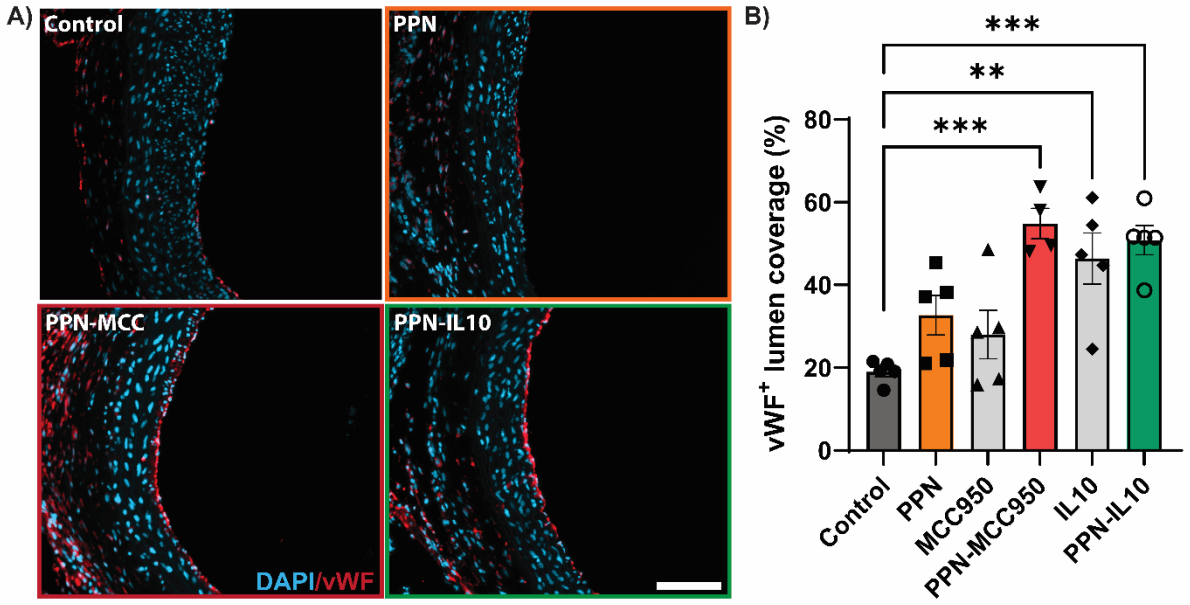

Figure 4.11: *In vivo* endothelialisation promotion by PPN-anti-inflammatory conjugates
A) Representative images of von Willebrand Factor (vWF) stained sections after 14-day injury model. DAPI stained in blue, vWF stained in red. Scale bar represents 100 µm. B) Quantification of vWF positive staining within the lumen of the artery. Data represents mean ± SEM (n = 4-5). Statistical significance is indicated by **p < 0.01, ***p < 0.001.

4.4 Discussion

Endovascular intervention causes vascular injury that initiates an inflammatory cascade leading to device failure. Current strategies using DCBs or DESs rely on non-specific anti-proliferatives, which reduce neointimal hyperplasia in the short term but delay vessel healing and fail to provide durable outcomes [157]. Selective targeting of relevant inflammatory pathways while promoting endothelial repair is increasingly recognised as essential for long-term device success, particularly as the field moves toward temporary implants that demand rapid restoration of vessel integrity. Nanoparticle-based delivery systems offer a potential solution, but their translation has been limited by poor biodistribution, efficacy and complex

functionalisation protocols [213]. PPN present favourable surface properties that overcome several of these barriers. This chapter aimed to evaluate PPN as a local delivery platform for the selective anti-inflammatory agents MCC950 and IL-10 to improve vascular outcomes following arterial injury.

Radiolabelling is an established method for investigating nanoparticle biodistribution *in vivo*. In this chapter, PPN was radiolabelled with ^{89}Zr, an ideal radioisotope for PET imaging due to its long half-life of 78.4 hours and proven compatibility with *in vivo* pharmacokinetics [249]. To do so, PPN was first complexed with DFO, currently the only chelator used in clinical settings [250], and then ^{89}Zr was added, forming a PPN-DFO-^{89}Zr (PPN-^{89}Zr) complex which was used for biodistribution experiments. Serum stability of PPN-^{89}Zr was evaluated prior to animal injection and showed excellent stability with minimal degradation in human serum. PPN-^{89}Zr is notably more stable than ^{89}Zr-DFO-liposome, where the radiolabel retention was reduced to 83% after 48 hours storage *in vitro* [251]. This confirmed the stability of the PPN-^{89}Zr complex and justified progressing with intravenous injections into rats to visualise biodistribution.

Within the first hour post-intravenous injection, PPN-^{89}Zr primarily localised to the liver and spleen. Biodistribution of nanoparticles is strongly influenced by their physicochemical properties [252, 253]. Interestingly, the observed clearance of PPN into the liver and spleen aligned well with its size (~150 nm), spherical shape and surface charge [226]. Typically, nanocarriers larger than 100 nm are eliminated through the liver, while nanoparticles smaller than 5 nm are mainly eliminated through the kidney [254, 255]. Blood flow velocity of nanomaterials between 100-500 nm have shown to reduce up to 1000-fold as they enter and

traverse the liver, leading to significantly higher level of cellular interactions, correlating with increased cellular uptake [256]. Larger particles are likely to be taken in by phagocytes, such as macrophages and/or neutrophils, and activate the mononuclear phagocyte system (MPS) [257]. Both the liver and spleen are key sites of the MPS. The liver in particular contains a high abundance of phagocytic Kupffer cells which are known to sequester nanosized foreign substances including nanoparticles. The spherical shape of PPN also facilitated its accumulation in the phagocyte rich liver and spleen as phagocytes preferentially up-take and internalise spherical substances [258]. Furthermore, nanoparticles with positive surface charges such as PPN are known to interact more readily with phagocytic cells, and undergo clearing mainly by Kupffer cells and splenic macrophages. Collectively, these results highlighted that PPN is efficiently cleared out of the blood stream and begin to accumulate in organs with specialised processing capabilities. Importantly, this feature is attributed to the synergistic effects of PPN's physicochemical properties which favour the MPS.

Extended biodistribution out to 8 days showed similar trends with PET/CT imaging, revealing the liver and spleen as the two main organs for PPN accumulation. PPN accumulation in the liver generally declined throughout the 8 days, suggesting effective clearing by the biliary system and probable eventual removal in feces. Conversely, PPN levels in the spleen and kidneys largely increased over time. This trend suggested that after the initial PPN uptake in the first 24 hours, other organs could potentially re-distribute PPN to be sequestrated in the spleen. The increase PPN accumulation in the kidneys could also be attributed to re-distribution of partially broken down PPN which are taken to the kidney for urinary excretion [255]. Similarly, these results could be explained by ^{89}Zr radiometal being released from PPN when undergoing clearance over time, re-circulating into other organs. Importantly, negligible levels of PPN were found in the brain and heart across the 8 days. The blood-brain barrier prevents

the entry of pathogens and/or foreign substances from the brain vasculature to the brain. It is well established that the majority of nanoparticle platforms are unable to cross this barrier, making nanoparticle accumulation in the brain rare. As this study is not related to diseases within the brain, accumulation here would be undesirable and therefore the inability to cross the blood brain barrier (BBB) is a positive feature of PPN, reducing the risk of off-target effects. The same is true for the heart as it is not specifically designed for clearing and breaking down molecular substances, accumulation here can induce off-target toxicity issues. For instance, silica nanoparticles are known to accumulate within the heart following intraperitoneal injection in rats, leading to excessive ROS production and tissue damage [147].

Gamma-counting analysis showed the percentage of radiotracer remaining in organs from the time of injection to 8 days, highlighting PPN-^{89}Zr was efficiently cleared from the liver over time. It is important to note that PPN injections in this biodistribution study were systemically delivered rather than locally delivered. In the context of systemic administration of nanoparticles, retention in organs is an undesirable outcome as this can lead to organ toxicity and off-target effects [259, 260]. Therefore, taken together, these biodistribution results indicate that intravenous administration of PPN is rapidly cleared from the bloodstream via the MPS with minimal accumulation in vital organs, supporting its therapeutic potential as a drug carrier.

Complex nanoparticle-drug functionalisation protocols are a key barrier to commercialisation. The reactive surface of PPN enables direct conjugation of bioactive cargo through a simple one step incubation process [230]. This functionalisation protocol was tested in this chapter for the separate binding of two different anti-inflammatory molecules, the large inflammatory regulating cytokine IL-10 and the small molecular drug MCC950. IL-10 consists of two 18.5

kDa monomers, forming a 37 kDa dimer complex [261]. Owing to its large size, successful conjugation of IL-10 was confirmed by an increase in hydrodynamic size and PDI. However, the molecular weight of MCC950 is only 404.5 Da, requiring conjugation to be validated using zeta potential whereby a subsequent drop in surface charge of PPN post-functionalisation was observed. Although successful cargo conjugation is a common feature of nanoparticles, the majority of current platforms rely heavily on wet-chemistry protocols and the use of chemical linkers to attach desired cargo, adding considerable complexity and cost to manufacturing greatly limiting their feasibility for large scale clinical use [262]. Previous approaches for conjugating a targeting peptide to a polymer-based nanoparticle for DCB delivery required pre-functionalisation with poly-l-lysine to produce amine and carboxylic acid functional groups on the otherwise bare surface, as well as to stabilize the particles and prevent aggregation [263]. Similarly, liposomal nanoparticles rely on drug encapsulation methods such as thin-film hydration which require a time-consuming solvent removal step, often taking over 24-hours [264, 265]. Comparing these multi-step conjugation protocols common to current nanoparticle platforms to the simple one-step incubation required to conjugate cargo to PPN demonstrates the added utility of PPN over competing platforms.

Consistent with previous PPN studies, functionality of MCC950 and IL-10 was retained post-conjugation in *in vitro* macrophage inflammatory stimulation models [230]. This is a feature that inorganic nanoparticles struggle to overcome, with one study reporting a 50% and 89% loss of bioactivity for L218C and D453C enzymes, respectively, following conjugation with gold nanoparticles [225]. By implementing more advanced surface modification techniques, inorganic nanoparticle platforms are beginning to overcome this functional hurdle, although efficacy issues are still common with certain types of cargo [266]. Interestingly, unconjugated PPN suppressed TNF-α secretion but did not exhibit the selective anti-inflammatory effects

characteristic of MCC950 in the NLRP3 inflammasome stimulation assay, including no rescue from pyroptosis or suppression of IL-1β release. This broader immunosuppressive effect is likely related to the highly reactive PPN surface, which readily adsorbs proteins from the culture medium including albumin. Albumin has been shown to bind to plasma polymer coatings with similar surface chemistries to PPN [267], and albumin itself has been reported to attenuate TLR4 signalling in leukocytes, leading to reduced NF-κB activation and downstream cytokine production [268]. It is therefore possible PPN is conjugating albumin when added into the cell culture media and, when interacting with macrophages, causing alterations to receptor-ligand interactions resulting in modest anti-inflammatory effects. Regardless, this is the first time the functionality of two selective anti-inflammatories of different forms has been confirmed post-conjugation with PPN, validating the platforms therapeutic potential *in vitro*.

PPN markedly improved vascular retention of conjugated cargo *in vivo* following local delivery to injured arteries. Compared to the free fluorescent dye, PPN-750 exhibited nearly 50-fold greater signal at day 1 and remained detectable at significantly higher levels after 5 days. These findings indicate that unlike freely delivered 750, PPN-750 were able to stick to the damaged arterial wall and were resistant to wash-off from blood flow. This property of PPN overcomes the limitations of conventional drug-coated balloon and stent platforms, where poor tissue uptake and rapid washout of hydrophilic drugs remain major barriers to efficacy [269]. To address this, most clinical devices have relied on lipophilic drugs such as paclitaxel, whose favourable tissue binding properties underlies its dominance despite concerns about safety. Alternative nanoparticle carriers, including liposomes and polymeric nanoparticles, have been investigated to improve arterial retention and potentially open the door for delivery of therapies other than paclitaxel. Yin et al developed a PLGA nanoparticle platform that could stick to the vascular wall by hydrogen and covalent bonding, resulting in a 525% increase in sirolimus

retention *in vivo* [270]. However, to achieve this, an adhesive coating had to be applied on the PLGA particles using in-situ UV-triggered polymerisation. Contrastingly, PPN underwent no extra coating modification in order to achieve arterial binding, further emphasising its usability and commercial promise. SEM imaging highlighted PPN preferentially bound to the fibrous collagen in the subendothelial layer, indicating that PPN uptake could favour more seriously injured arteries with ruptured internal elastic layer. Together, these results highlighted for the first time the ability of PPN to directly adhere to injured arterial surfaces and retain cargo for several days, positioning PPN as a unique and potentially transformative approach to local drug delivery.

In vivo functionality of PPN-anti-inflammatory conjugates was tested in the same carotid injury model as done for the retention study, but extended out to 14 days in order to achieve relevant neointimal hyperplasia levels. In this model, neither freely delivered MCC950 nor IL-10 significantly reduced neointimal hyperplasia, despite both agents show promising anti-inflammatory effects *in vitro*. Despite the promise of MCC950 and IL-10 as anti-inflammatory agents, they share common limitations experienced with other vascular drug delivery candidates regarding poor intrinsic tissue retention. Compared to paclitaxel, MCC950 has shown to have relatively poor bioavailability and half-life of only 3.27 hours, emphasising the need for rapid and local retention of MCC950 at a desired site [233]. Similarly, as a protein cytokine, IL-10 is inherently unstable in circulation, prone to proteolysis and rapid clearing [271]. These features are potentially the reason for the inability of these freely delivered drugs to reduce neointimal hyperplasia. In contrast, when conjugated to PPN, both MCC950 and IL-10 significantly reduced neointimal lesion burden by ~60% relative to controls, translating into marked improvements in luminal patency. This is most likely due to PPN improving the retention and localisation of its cargo as seen for PPN-750 previously. By increasing drug

retention through the use of carriers, many studies have demonstrated how this can translate to superior biological function and outcomes. Most notably, Li et al evaluated platelet membrane-coated PLGA nanoparticles carrying IL-10 against freely delivered IL-10 in a balloon-induced carotid artery injury model in rats and demonstrated only IL-10 loaded nanoparticles showed neointimal hyperplasia suppression, the authors attributing this to the improved localisation of IL-10 at the injury site [124].

Parallel assessment of vWF positive staining within the lumen demonstrated that conjugation of MCC950 or IL-10 to PPN led to enhanced endothelialisation. Notably, free IL-10 delivery also enhanced endothelial coverage to a similar extent as PPN-IL10. This likely reflects the temporal nature of the processes being targeted. Endothelial regeneration occurs relatively early after vascular injury, and even transient local exposure to IL-10 at the delivered dose may be sufficient to stimulate pro-tissue regeneration signalling required for endothelial cell proliferation and migration [272]. In contrast, suppression of neointimal hyperplasia requires sustained modulation of inflammatory and proliferative pathways over a longer period [273]. Because free IL-10 was likely rapidly cleared from the injury site, it lacked the prolonged presence necessary to influence these chronic remodelling processes. Thus, while free IL-10 promoted acute endothelialisation, effective suppression of neointimal hyperplasia required a delivery system such as PPN that ensured extended local drug retention. MCC950 on the other hand only promoted endothelialisation when delivered conjugated to PPN, highlighting the benefits of PPN for improving therapeutic capabilities of drugs when performing local drug delivery in the vasculature. As such, these results position PPN as a promising nanoparticle platform that can effectively deliver selective anti-inflammatories including IL-10 and MCC950 to an injured arterial wall. These nanoparticle-drug conjugates demonstrated both suppressed neointimal hyperplasia and improved endothelialisation after 14-days. While other

nanoparticle platforms have shown similar therapeutic benefits, the off-the-shelf nature of PPN makes it a significantly more commercially viable option, justifying evaluation of PPN-IL10 and PPN-MCC950 in future pre-clinical/large animal studies.

Despite the promise of PPN-IL10 and PPN-MCC950 highlighted throughout this chapter, several limitations of this study should be acknowledged. PPN-^{89}Zr demonstrated strong *in vitro* serum stability with minimal evidence of degradation, meeting a requirement established in the literature as a necessary step in biodistribution studies [251]. However, this study did not include radiolabelled control particles or orthogonal analytical methods to assess PPN-^{89}Zr stability throughout the *in vivo* biodistribution model. Although generally not performed due to technical constrains, future studies incorporating dual-labelling strategies, *ex vivo* nanoparticle recovery, or complementary imaging modalities would help validate whether PET signals represented intact PPN or free ^{89}Zr released following particle degradation or label dissociation. In addition, while *in vitro* assays confirmed retention of IL-10 bioactivity post-conjugation, the long-term physicochemical stability and functional persistence of PPN-IL10 conjugates under physiological conditions remain incompletely characterised. Given the susceptibility of protein therapeutics to undergo proteolytic degradation, further investigation of cargo stability, release kinetics, and biological activity over extended timeframes will be required before clinical testing [274]. The *in vivo* functional model performed in this chapter somewhat confirms short-term stability of PPN-IL10 and PPN-MCC950, but long-term stability still needs to be validated in an *in vivo* setting. This could be achieved by doing an additional 30-day and 90-day timepoint for the arterial injury model instead of only the acute 14-day study.

Furthermore, although histological assessment demonstrated reduced neointimal hyperplasia and improved endothelialisation following treatment with PPN-conjugated MCC950 and IL-10 *in vivo*, the study did not include detailed molecular or cellular characterisation of vascular inflammation. Additional assessment of inflammatory and vascular biomarkers, such as immune cell infiltration, endothelial activation markers (e.g. eNOS, VCAM-1 and ICAM-1), and macrophage phenotype profiling using CD206 and MHC class II stains, would provide deeper mechanistic insight into how these therapies modulate vascular healing [125]. Similarly, the *in vivo* model relied on histological endpoints to evaluate functional outcomes, providing limited insight into broader immune regulation. Future work incorporating transcriptomic, proteomic, and metabolomic profiling would enable a more holistic assessment of immune and vascular signalling pathways, allowing detection of prolonged or unintended immune suppression that may not be apparent from histology alone [275]. Importantly, such approaches could distinguish adaptive, local immune modulation from global immunosuppression and reveal how therapeutic responses vary across different injury severities and timepoints. Given the highly context-dependent nature of cardiovascular biology, integrating multi-omics profiling across acute and chronic injury models would be particularly valuable. In this context, while IL-10 is a potent anti-inflammatory cytokine, excessive or sustained suppression of immune surveillance could theoretically impair host defence or delay appropriate tissue remodelling. Future studies should therefore combine molecular profiling with functional immune assessments, including evaluation of immune competence, infection susceptibility, and long-term vascular remodelling following PPN-IL10 delivery. Despite these limitations, the findings presented in this chapter establish proof-of-concept for PPN as a local delivery platform for selective anti-inflammatory therapies and provide a strong foundation for further translational and preclinical development.

4.5 Conclusion

Taken together, these findings further demonstrate the commercial promise of PPN, including the first detailed study into its use as a delivery platform for two selective anti-inflammatory agents including IL-10 and MCC950 in the context of vascular injury. When injected systemically in rats, PPN showed preferential accumulation in the liver and spleen, followed by gradual elimination over an 8-day period. Anti-inflammatory therapies IL-10 and MCC950 successfully conjugated to PPN using a simple one-step incubation protocol at room temperature while retaining their function *in vitro. In vivo*, PPN improved the retention of a fluorescent tag out to 5 days when exposed to blood flow. PPN's ability to increase cargo retention translated to improved therapeutic effects for PPN-IL10 and PPN-MCC950 conjugates which both reduced neointimal hyperplasia and promoted endothelialisation. These promising outcomes highlight the commercial viability of PPN-IL10 and PPN-MCC950, justifying further work evaluating these therapies in pre-clinical models.

Chapter 5

Plasma polymerised nanoparticles as a platform for surface biofunctionalisation of bioprosthetic heart valves

5. Chapter 5 – Plasma polymerised nanoparticles as a platform for surface biofunctionalisation of bioprosthetic heart valves

5.1 Introduction

Bioprosthetic tissue is increasingly recognised as the preferred biomaterial solution for surgical and transcatheter aortic valve replacements [276]. While mechanical heart valves are made from highly durable materials including stainless steel, titanium and/or pyrolytic carbon, patients require life-long anticoagulation drug therapy to prevent valve thrombosis, placing them at an ongoing long-term risk of clinically significant bleeding [277]. Introduced in the 1960s, bioprosthetic valves are made from glutaraldehyde-fixed bovine or porcine pericardial tissue and were designed to improve blood compatibility while reducing the need for lifelong anticoagulation [278]. In the early 2000s, bioprosthetic tissue also proved compatible with transcatheter delivery systems, enabling valve deployment using minimally invasive endovascular procedures [53]. For aortic valve replacement, this procedure is known as transcatheter aortic valve replacement (TAVR), and has been proven to provide patients with additional clinical benefits of reduced peri-procedural complications and faster post-operative recovery compared to more traditional surgical aortic valve replacement (SAVR) [76]. These combined advantages have led to the widespread adoption of bioprosthetic valves over mechanical valves, despite several known limitations including structural valve degeneration (SVD).

5.1.1 Biological drivers of structural valve degeneration

As outlined in section 1.4.2 of this thesis, SVD is the leading cause of bioprosthetic valve failure and arises from a series of interconnected biological processes that progressively

compromise valve leaflet integrity and function. The three principal drivers include thrombosis, inflammation, and calcification. Together, these mechanisms act synergistically to accelerate valve deterioration and ultimately lead to failure (Figure 5.1).

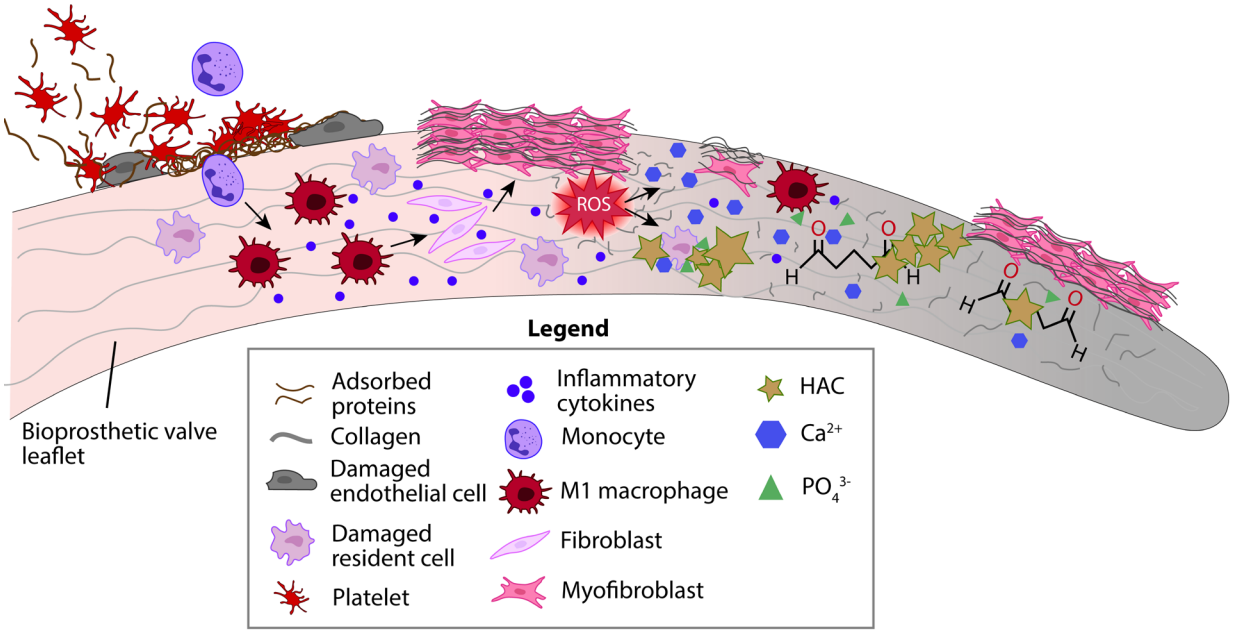

Figure 5.1: Biological modes of structural valve degeneration
Schematic showing the biological modes of structural valve degeneration, a primary cause of bioprosthetic valve failure. HAC refers to hydroxyapatite crystals, Ca^{2+} refers to calcium ions, PO_4^{3-} refers to phosphate ions, ROS refers to reactive oxygen species.

5.1.1.1 Thrombosis

Thrombosis is the pathological formation of a blood clot on the surface of bioprosthetic valve leaflets that can impair motion and increase transvalvular gradients. In recent years, advances in cardiac four-dimensional computed tomography (4D-CT) have revealed that leaflet thrombosis occurs not only as a clinical obstruction, but also in a subclinical form characterised by hypo-attenuated leaflet thickening (HALT) and, in some cases, reduced leaflet motion (RLM) [279]. While often asymptomatic, these phenomena are increasingly recognised as contributors to SVD.

At the cellular level, dysfunctional endothelialisation and platelet activation are early drivers of thrombus formation on leaflet surfaces. The altered surface chemistry of glutaraldehyde-fixed tissue, combined with non-physiological shear stresses and areas of stagnant flow in the native sinus and neosinus, causes dysfunctional endothelial cells to populate the leaflet surface within the first day following TAVR [95]. This dysfunction promotes platelet activation, leading to increased thrombin levels and platelet adhesion [280]. As the platelets become more aggravated, they begin to secrete platelet factor 4 (PF4) which amplifies platelet recruitment and promotes aggregation. Simultaneously, activation of the coagulation cascade leads to more thrombin generation and fibrin deposition, stabilising platelet-rich blood clots [280].

Clinical thrombosis is a rare event, occurring in 0.6-2.8% of patients within the first year following TAVR [281, 282]. On the other hand, subclinical thrombosis (SLT) is very common post-TAVR, occurring in 10-15% of patients at 1 month and up to 30% by 1 year [283]. SLT is only identifiable through 4D-CT imaging, where it appears as HALT. Importantly, SLT and downstream conditions such as HALT and RLM are often asymptomatic, meaning many cases have gone undiagnosed and unreported. As such, the clinical significance of SLT is largely unknown. However, platelets and fibrin, the major components of SLT, have been shown to serve as scaffolds for monocyte adhesion and macrophage differentiation, leading to local inflammation and leaflet fibrosis, key drivers of SVD. These converging processes position SLT as a central initiating event associated with a 2.5-fold increase in the risk of SVD [284].

Oral anticoagulant agents have been shown to reduce SLT risk following TAVR. The GALILEO-4D and ATLANTIS substudies showed that oral anticoagulants significantly reduced the incidence of SLT [285, 286]. However, these studies also demonstrated that routine

use of oral anticoagulants after TAVR increases risk of bleeding, thromboembolic complications and all-cause mortality, leading to the consensus that anticoagulation should be reserved for patients with clear, clinical indications.

Within the field, SLT has shifted from being viewed as a benign imaging finding to a potential early driver of inflammation and long-term SVD, with ongoing work examining whether targeted prevention or early treatment could improve valve durability [287].

5.1.1.2 Inflammation

Inflammation is a central driver of structural valve degeneration, arising from the chronic immune response to glutaraldehyde-fixed tissue. Although fixation reduces immunogenicity, residual aldehyde groups, xenograft tissue, and the absence of viable endothelium create a persistent inflammatory stimulus [94]. This chronic inflammatory response gradually remodels the valve leaflets and accelerates SVD.

Macrophages are the dominant effector cells in this process. Following implantation, circulating monocytes are recruited into the valve and differentiate into macrophages, where they adopt predominantly pro-inflammatory M1 phenotypes [96]. These cells release pro-inflammatory cytokines such as IL-1β, TNF-α and IL-6, which amplify leukocyte recruitment, promote reactive oxygen species release, and drive fibrotic remodelling. Cytokine signalling stimulates fibroblast proliferation and differentiation into myofibroblasts, which deposit excess collagen and extracellular matrix proteins on the surface of leaflets [94]. This maladaptive tissue deposition thickens the leaflet, reducing flexibility and contributing to increased

transvalvular gradients. Histological analyses of 23 explanted transcatheter hearxt valves demonstrated that all patients with valves implanted for over 60 days had high levels of fibrosis in combination with thrombus [95]. In this study, progressive remodelling and maturing of fibrosis was observed over time and strongly correlated with calcification in the long-term.

5.1.1.3 Calcification

Calcification represents the final stage of SVD and is strongly linked to the surface chemistry of glutaraldehyde-fixed pericardial leaflets [288]. After fixation, residual free aldehyde groups remain within the extracellular matrix and on the leaflet surface. These reactive carbonyl groups act as nucleation sites, binding circulating calcium ions through electrostatic interactions and forming stable complexes that initiate mineral deposition. Over time, these calcium-aldehyde complexes provide the template for phosphate binding, which subsequently mature into hydroxyapatite crystals. [289] Hydroxyapatite crystals are the principal mineral deposits seen in failed explanted bioprosthetic valves. Once initial hydroxyapatite deposits form, they act as further nucleation sites for calcium and phosphate, creating a vicious cycle of calcification [94].

In addition to residual free aldehydes, devitalized resident cells within the pericardial leaflets also contribute to calcification. These cells lose the ability to regulate intracellular calcium due to dysfunctional calcium-dependent ATPases, resulting in calcium build up within the cell [290]. In turn, these high calcium concentration areas act as foci for hydroxyapatite crystal formation. Over time, these events culminate in widespread leaflet stiffening and loss of physiological function.

Notably, calcification has been observed exclusively in valves that also exhibited both fibrosis and thrombosis, suggesting that these processes are not independent but rather sequential and interdependent [95]. The chronic inflammatory environment established by persistent thrombus and excessive fibrosis provides the biochemical conditions, including high oxidative stress and ECM degradation, that promote calcium release and hydroxyapatite crystal formation [94]. Ultimately, these processes lead to SVD, characterised by leaflet stiffening and loss of valve function.

5.1.2 Overview of existing tissue treatment technologies

Several tissue treatment technologies have been developed to improve the durability of bioprosthetic valves and reduce the risk of structural valve degeneration (SVD). The most widely explored approaches include decellularization, alternative crosslinking methods, and anti-calcification treatments, each representing distinct strategies to enhance long-term valve performance

5.1.2.1 Decellularization

Residual cells and cellular debris present within bioprosthetic leaflets is known to accelerate SVD [94, 290]. As such, decellularization of bioprosthetic heart valves is common strategy to improve valve longevity. Decellularization is most commonly achieved by combining physical and chemical treatments. However, it is imperative that the decellularization process does not impair the native ECM architecture as this is essential for providing the leaflets with mechanical strength and flexibility.

Physical decellularization techniques can include sonication and agitation, and are predominantly performed along side chemical treatment. The most commonly used chemical treatments include amphiphilic detergents capable of solubilising cell membranes and separating DNA from proteins [291]. Ionic detergents, such as sodium dodecyl sulfate (SDS), combined with sonication, has been shown to effectively remove residual DNA from tissue. Sonication allowed SDS to penetrate sample depths of up to 500 μm within 24 hours, achieving 98% removal of DNA from aortic tissue ECM [292]. SDS treated glutaraldehyde-fixed bovine pericardium showed a significant reduction in calcification compared to control glutaraldehyde-fixed only samples in a 90-day rat subcutaneous model, highlighting its potential to reduce SVD [293].

Similarly, decellurization techniques can also help to eliminate xenogeneic antigens which are known to activate immune responses post-bioprosthetic valve implantation. Li et al investigated combining multiple freeze-thaw cycles with Triton X-100 treatment as an efficient decellularization protocol for bovine pericardium [294]. Freeze-thaw cycles disrupt and lyse residual cells by forming intracellular ice crystal. This combination protocol achieved a significant reduction in α-Gal antigen and DNA components compared to non-treated bovine pericardium, translating to reduced immune response and calcification *in vivo* [294]. While experimental studies demonstrate reduced DNA content, antigen removal, and calcification, translation into commercial products has proven more complex.

Despite apparent advantages, decellularization protocols have not been introduced in the manufacturing of current, commercially available bioprosthetic valves, most likely due to the lack of long-term data surrounding mechanical integrity and time-consuming protocols. In

order to achieve complete decellularization, defined as samples with less than 50ng double stranded DNA/mg of dry ECM, protocols take between 3-7 days, making it very challenging for companies to incorporate this into already existing manufacturing pipelines [295]. In saying this, Anteris Technologies developed a proprietary tissue treatment process for their DurAVR® transcatheter heart valve called ADAPT® which, among other properties, removes remnant DNA, phospholipids and α-Gal epitopes, achieving what they claim to be completely acellular tissue [296]. Although 1-year data from their first-in-human trials suggests promising absence of SVD and favourable hemodynamic performance, long-term follow-ups are still needed to validate the treatment process [297].

5.1.2.2 Alternative cross-linking methods

Conventional glutaraldehyde crosslinking has long been the standard for stabilising bioprosthetic heart valve tissue, providing durability and mechanical strength by forming stable chemical bonds between collagen molecules. Glutaraldehyde contains two aldehyde groups. One of these groups interacts with a collagen amino group, resulting in crosslinking. However, the remaining aldehyde group remains free to other chemical interactions. These residual aldehydes can act as sites for calcium binding and have shown to promote inflammatory responses [94]. These limitations have motivated the development of alternative crosslinking chemistries designed to retain mechanical stability while reducing calcification, immunogenicity and long-term degeneration.

Several alternative crosslinking methods have been trialled to address the shortcomings of glutaraldehyde. For instance, polyepoxy compounds such as polyethylene glycol diglycidyl ether (PGDE) have shown promise as they contain multiple reactive epoxy groups which can

form stable covalent bonds with amino, hydroxyl and carboxyl groups of collagen, achieving strong cross-linking without residual aldehydes. In a rabbit subcutaneous model, polyepoxy-crosslinked bovine pericardium showed a 1.5-fold reduction in calcification compared to samples that underwent standard glutaraldehyde fixation [298]. Similarly, Yu et al used a bicyclic oxazolidine (OX-Et) as a cross-linking agent for porcine pericardium [299]. Compared to glutaraldehyde-crosslinked pericardium, OX-Et showed similar thermodynamic and biochemical stability with superior anti-thrombotic and endothelisation properties. When implanted subcutaneously in rats, OX-Et demonstrated significantly less CD68 positive macrophage accumulation and reduced calcification at 30 and 60 days [299].

Dual and hybrid crosslinking strategies for bioprosthetic heart valve tissue have also been investigating using natural compounds with intrinsic anti-oxidant and anti-inflammatory properties. Utilising dialdehyde xanthan gum as the primary crosslinking agent providing structural stability and curcumin, a natural occurring anti-inflammatory compound found in turmeric, as a secondary crosslinker, Hu et al., developed a dual crosslinking strategy for bovine pericardium that was able to promote endothelial cell proliferation and dampen the inflammatory response *in vivo* [300]. A hybrid crosslinking method utilising neomycin trisulfate, PGDE and Tannic acid showed similar biomechanical properties and 90-day collagen stability compared to glutaraldehyde fixed bovine pericardium, but significantly reduced inflammation and calcification after 90 days of subcutaneous implantation in a rat [301]. With this method, PGDE crosslinked collagen, neomycin crosslinked glycosaminoglycans, and the plant polyphenol Tannic acid stabilised elastin, the latter two of which are not stabilised with glutaraldehyde fixation alone.

Despite the promise of these novel strategies, none have yet achieved commercial viability. The majority of alternative crosslinking methods remain confined to preclinical or early feasibility studies, with limited long-term data on durability. Challenges include reproducibility of protocols, scalability for commercial production, and ensuring that modified chemistries do not compromise leaflet mechanics or hemodynamic performance over decades of use. As a result, glutaraldehyde fixation remains the only clinically approved crosslinking method in commercially available bioprosthetic heart valves, underscoring both its robustness and the significant translational barriers that novel tissue treatments must overcome.

5.1.2.3 Anti-calcification treatment

Calcification remains the predominant cause of late bioprosthetic valve failure and represents the terminal stage of SVD. Anti-calcification treatments have therefore become a critical focus for commercial valve companies. Currently, two anti-calcification tissue treatments dominate the market including RESILIA™ tissue (Edwards Lifesciences) and 2-amino oleic acid (AOA™, Medtronic). These treatment protocols chemically modify the tissue to resist calcium binding and hydroxyapatite crystal formation.

RESILIA™ tissue uses a proprietary tissue treatment process that combines aldehyde capping, glycerolisation and ethylene oxide sterilisation [302]. Capping of aldehyde groups present in glutaraldehyde fixed bovine pericardium prevents calcium binding and reduces risk of tissue oxidation, while glycerolisation replaces water in the tissue with glycerol, allowing the valves to be packaged and stored dry without glutaraldehyde [303]. Data on the performance of RESILIA™ tissue in transcatheter heart valves is scarce, but has shown success in surgical valves. In a preclinical juvenile sheep model study, bioprosthetic mitral valves containing

RESILIA™ tissue showed 72% less calcium content after 8 months compared to the same valves without RESILIA™ treatment [304]. In Edwards' pivotal COMMENCE trials, RESILIA™ surgical valves revealed 99.3% freedom from SVD at 7 years in patients with a mean age of 67, generating significant clinical and commercial interest [305]. However, a closer look at early data reveals signs of increasing transvalvular gradients and declining effective orifice areas, suggesting that subtle valve dysfunction may already be emerging. Long-term data (>10 years) is still required to fully assess RESILIA™ durability as well as studies that apply the treatment technology within transcatheter valves to determine if these benefits are maintained/applicable to TAVR.

Medtronic has developed a complementary anti-calcification technology based on treatment of porcine bioprosthetic tissue with AOA™, a long-chain fatty acid derivative. Studies have shown AOA to covalently bind free aldehyde groups of glutaraldehyde fixed tissue, leading to reduced calcium ion diffusion compared to non-AOA pretreated bioprosthetic tissue [306]. Furthermore, AOA has been shown to act as a surfactant, removing residual phospholipids which can otherwise function as nucleation sites of calcium ions. Anti-calcification efficacy of AOA treatment was evaluated using left ventricle-to-descending thoracic aorta conduit implantation in juvenile sheep. Quantitative calcium content analyses revealed AOA-treated conduits experienced 93% less calcification of valve cusps compared to control [307]. Clinical performance of AOA-treated surgical valves also shows promise, demonstrating 98% freedom from reintervention after 7 years [308]. However, it should be noted that 'freedom of reintervention' does not necessarily correlate with absence of SVD, as patients may still have SVD but not undergo reintervention. As such, similar to RESILIA, AOA exhibits improved chemical properties of bioprosthetic tissue leading to reduced calcification potential, but long-

term data is still required and studies investigating the tissue treatment on transcatheter valves still need to be performed.

Anti-calcification tissue treatments have emerged as the most commercially successful strategy to date for mitigating SVD and extending bioprosthetic valve durability. Unlike decellularization or alternative crosslinking methods, these approaches can be directly integrated into existing valve designs without altering device design or manufacturing workflows. This compatibility has made them particularly attractive commercially, offering a practical, off-the-shelf upgrade within established regulatory and clinical pathways. As a result, anti-calcification treatments such as RESILIA™ and AOA™ now dominate the commercial landscape, reflecting their unique balance of biological efficacy and translational feasibility. However, these technologies remain inherently passive, masking free aldehydes or removing residual cellular debris in order to reduce calcium binding. As such, they fail to intervene with the underlying biological cascades that drive SVD including thrombosis, inflammation and calcification. An alternative approach that actively modulates these mechanisms represents the next frontier in valve design, with the potential to dramatically improve long-term bioprosthetic durability.

5.1.3 Promise of drug functionalisation/delivery

Modulating biological modes of failure through drug delivery has revolutionised transcatheter interventions for atherosclerosis. DCBs and DESs locally release therapeutic agents that modulate multiple aspects of their surrounding vascular biology, reducing restenosis and extending durability. The benefits of these technologies have been highlighted in sections 2.2.1 and 4.1.2 of this thesis. To summarise, the introduction of drug-eluting technology for stents

and balloons reduced failure rates by approximately 40-70%, making drug elution/coatings standard clinical practice for improving device longevity [106, 108]. As such, introducing drug delivery strategies into bioprosthetic heart valves could be a promising approach to improving their performance and durability (Figure 5.2). However, applying this technology to bioprosthetic valves has remained largely elusive due to technical challenges encountered at the leaflet surface, including complex drug-crosslinking strategies for glutaraldehyde fixed tissue and the difficulty of incorporating thick polymer drug-elution coatings onto the leaflet surface without compromising leaflet motion.

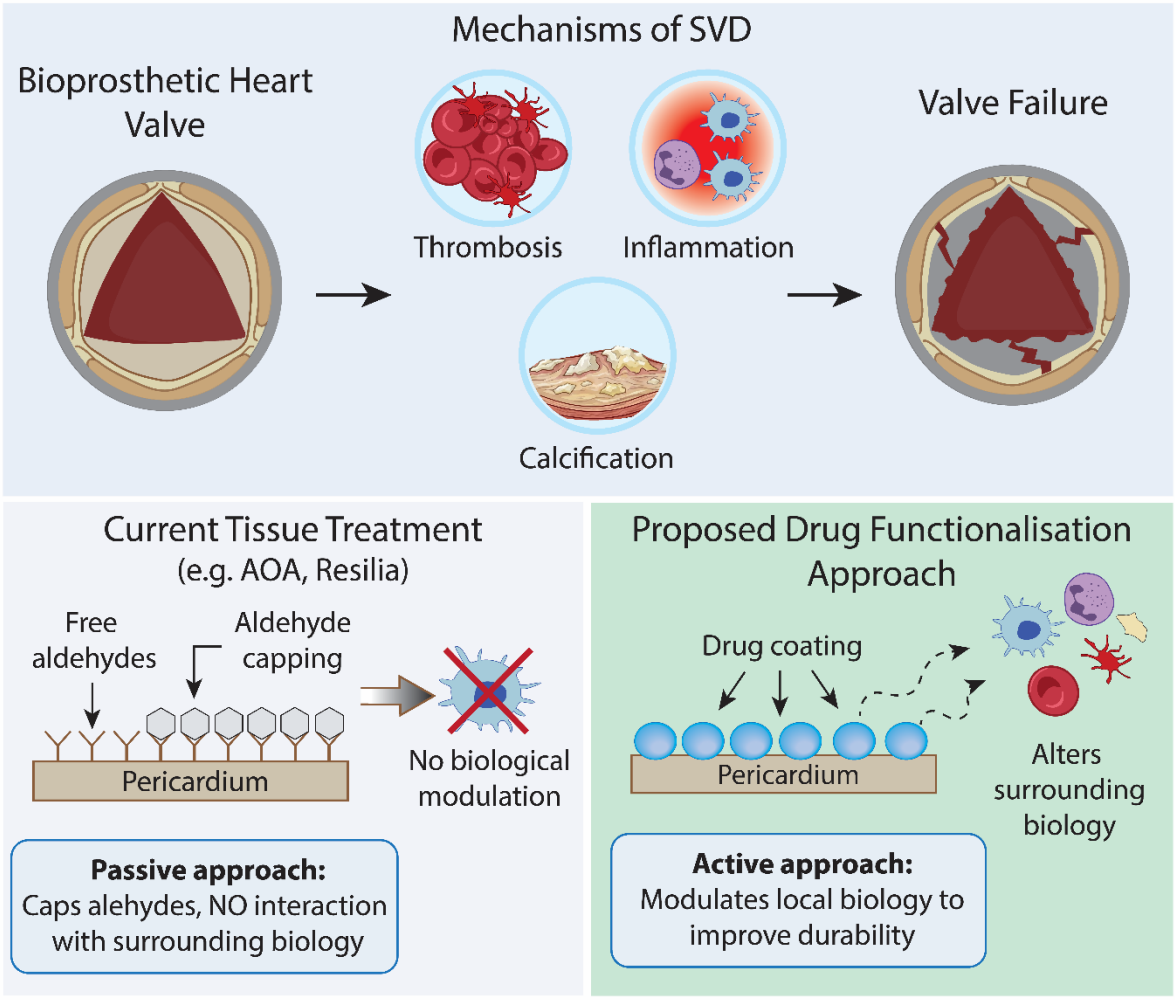

Figure 5.2: The promise of active biological modulation for bioprosthetic heart valves

Summary schematic highlighting the proposed drug functionalisation approach to improving bioprosthetic heart valve durability. SVD refers to structural valve degeneration.

5.1.4 Mechanical and hemodynamic factors

The aortic valve is situated in an extremely dynamic environment, opening and closing up to 40 million times per year [309]. During each cycle, the valve is exposed to transvalvular pressures, pulsatile and oscillatory shear stresses, and bending and axial stresses. Patients undergoing TAVR usually present with co-morbidities, hypertension being the most common . In one TAVR trial in the US, 50% of patients undergoing TAVR had hypertension [310]. Furthermore, these patients have diseased vasculature. In turn, they experience even harsher valve environments, with blood peak flow velocity through the aortic valve reaching 7.0 m/s, compared to 1.2 m/s for healthy individual, and tensile strain and stress increasing by more than 25% [311]. Furthermore, valves undergo bending stress and axial stretching during the cardiac cycle, both of which are vital for sufficient leaflet opening and closing.

In addition to these mechanical forces, valve function is critically determined by hemodynamic performance metrics. The three most important metrics related to valve function (both native valves and bioprosthetic valves) include the effective orifice area (EOA), regurgitation fraction (RF) and pulse pressure differential (PPD) [312]. EOA reflects the actual cross-sectional area available for blood flow through a valve. RF quantifies retrograde blood flow during valve closure, capturing how effectively the leaflets close together to prevent backflow. PPD reflects the magnitude of the pressure difference across the valve during a cardiac cycle, providing a measure for how well the valve can accommodate and transmit pulsatile blood flow.

For this reason, any tissue treatment technology or drug-functionalisation strategy must be designed not only to resist the biological drivers of SVD but also to withstand the extreme mechanical environment of the aortic root. Just as importantly, these modifications must

preserve valve hemodynamics. A treatment that thickens the leaflets, narrows the EOA, increases regurgitation, or alters the pressure differential would compromise performance and accelerate degeneration, regardless of its biological advantages. Ultimately, the success of next-generation valve technologies will depend on achieving this delicate balance between biological protection and uncompromised hemodynamic function.

5.2 Methods

5.2.1 Plasma polymerised nanoparticle synthesis

PPN were produced in a capacitively coupled radiofrequency (rf) plasma reactor as previously described in section 4.2.1 of this thesis. Briefly, an rf-driven (13.52 MHz) plasma discharge was generated at a pressure of 200 mTorr by ionization of a gaseous mixture comprising of argon, nitrogen, and acetylene. The total gas flow rate was set constant at 19 sccm and monitored by mass flow controllers (Alicat Scientific, USA) throughout the process. The rf power was delivered by a rf power supply (Seren, USA) and coupled to the plasma via an automatic matching box (Seren, USA) to maximize power delivery. The plasma radiative emission fingerprint was monitored in situ via optical emission spectroscopy (OES) using an Ocean Optics HR4000 (Oceans Optics). The OES process was used for quality control purposes by tracking the emission dynamics of selected molecular species, including molecular nitrogen excited states and ions, as well as CN molecular radicals.

5.2.2 PPN collection

The nanoparticles produced within the plasma bulk were collected in 24-well polystyrene plates (Corning) directly from the active plasma volume as previously described [229].

Following synthesis, the plates were brought to atmospheric pressure by venting the chamber with nitrogen and removed from the vacuum chamber for storage at room temperature and in ambient air for at least 48 h before resuspension in aqueous solution. As PPN are produced in a dry plasma state, they can be stored in their native dry state and only be resuspended in solution as needed before functionalization with molecular cargo. Here, PPN were dispersed in ultra-pure nuclease-free water (NFW) directly from the well plates, into 1.5 mL Eppendorf tubes. The concentration of PPN in solution was determined by UV/VIS spectroscopy as previously described, [226] by measuring the optical density of PPN in solution at 500 nm.

5.2.3 Immobilisation of PPN onto pericardium

Sheets of glutaraldehyde (0.625%) fixed pericardium (Maverick Biosciences) were either biopsy punched into 6mm diameter circular discs or cut to desired size with a scalpel. Samples were then washed twice in saline (2 x 5 mins) and treated with 4% L-Cysteine (pH: 1.8) for 6 hours on a plate shaker at room temperature. PPN resuspended in nuclease free water was then added to the pericardium at concentrations ranging from $5x10^9$ – $5x10^{11}$ PPN/mL overnight on a shaker at 4˚C. PPN concentration was $5x10^{10}$ PPN/mL unless otherwise specified. Samples were then washed once in NFW to remove unbound PPN, followed by treatment with either apixaban (20 μM), the small molecule anti-inflammatory MCC950 (20 μM), or naturally occurring antioxidant phytic acid (20 μM) for 30 minutes, again on a shaker at 4˚C. Samples were washed twice in PBS (2 x 5 mins) to remove un-bound cargo. All treatments were done in 96-well plate for 6mm biopsy punches or 24 well plate for larger pericardium patches.

5.2.4 Scanning and transmission electron microscopy (SEM/TEM)

Pericardium samples designated for SEM analysis were fixed in 2.5% glutaraldehyde in 0.1 M phosphate buffer (PB) for 1 h followed by 2% osmium tetraoxide (ProSciTech) in 0.1 M PB for 1 h. After thorough washing in 0.1M PB, samples were dehydrated in increasing concentrations of ethanol and dehydrated in hexamethyldisilane (Sigma Aldrich, MO, USA), and dried in a desiccator overnight. Samples were mounted on SEM stubs (ProSciTech) and coated with a 10 nm layer of sputtered gold (Emitech K550X). Samples were imaged on the Zeiss Sigma VP HD Scanning Electron Microscope. Quantification of PPN coverage was done through manual false colouring of PPN on pericardium surface using Adobe Photoshop, and analysing area of colour coverage using ImageJ. SEM-energy dispersive X-ray spectroscopy (EDS) was done using the Thermo Scientific Phenom XL Desktop SEM.

For SEM imaging of PPN-Apixaban (gold tagged) functionalised pericardium, Apixaban (20 μM) was first conjugated to 10nm gold nanoparticles (ab269933) as per manufactures instructions. Apixaban-gold conjugates were then conjugated to PPN coated pericardium and prepared for SEM as above. Imaging was performed using backscattered electrons on the Zeiss Sigma VP HD SEM in order to visualise the gold nanoparticles.

For transmission electron microscopy (TEM), PPN were collected on a 300-mesh grid with an ultrathin carbon film supported by a lacey carbon film (ProSciTech). Imaging was performed with a FEI Tecnai T12 Transmission Electron Microscope (TEM) at an acceleration tension of 120 kV.

5.2.5 Retention of PPN under peristaltic flow

Six pericardium patches (1.2cm x 0.5cm) were treated with 4% L-Cysteine followed by PPN. Three of the samples were prepared for SEM imaging (control group). Remaining samples were sutured into a peristaltic pump loop system and washed with PBS for 28 days at 110 rpm.

PBS was removed twice a week and replaced with fresh, sterile PBS. After 28 days, these 'washed' samples were then prepared for SEM imaging. PPN coverage was then quantified using false colouring technique described earlier in this section. For retention under flow analysis, one image for each replicate was quantified.

5.2.6 Free aldehyde visualisation

1cm x 1.2cm pericardium rectangles were prepared according to their designated treatment group and were incubated in 1mL Schiff base reagent stain for 20 minutes. Shiffs reagent reacts with aldehyde groups to form a purple colour. Samples were therefore imaged and amount of purple on each sample was quantified using ImageJ.

5.2.7 Endothelial cell viability and attachment

Human coronary artery endothelial cells (HCAECs) were seeded onto 6mm pericardium samples which were prepared according to their respective treatment group. For cell viability assay, HCAECs were seeded (8000 cells/pericardium) onto samples. After 24 hours, cell-seeded samples were incubated with Alamar Blue reagent (1:10 with cell culture media) for 3 h and viability was quantified using a microplate reader (Infinite M1000 PRO) for fluorescence analysis. Excitation and emission wavelengths were set at 560 and 590 nm, respectively. For cell attachment, HCAECs were seeded (25000 cells/pericardium) onto pericardium samples and left for one hour. Samples were then gently rinsed 3 times with PBS, fixed with 4% paraformaldehyde for 30 min and washed with PBS (3 × 5 min) followed by fluorescent staining of F-actin with actinRed™ 555 ReadyProbes® (Thermo Fisher Scientific, USA). Cells on the pericardium were visualized and imaged using Zen inverted fluorescent microscope.

5.2.8 Biaxial testing

The mechanical properties of the samples were tested using an ElectroForce 200N 2 Motor Plan (one motor per axis). Briefly, pericardium samples (1.6 cm x 1.6 cm) were hooked and connected to the four arms of the biaxial tester. Four hooks for each side of the sample were used to guarantee an equal distribution of the load. Before testing, the samples were pre-stressed to achieve a 1.0 N load. The samples were then stretched up to 3.5 mm in both directions (axial and transversal) with a strain rate of 0.1 mm/s. The maximum load (achieved at 3.5 mm displacement) and the stiffness (calculated as the ratio between the load and the displacement) of each samples were recorded. Cyclic tests were also carried out, with the samples subjected to ten cycles of a 3.5 mm displacement at 0.01 mm/s.

5.2.9 Water contact angle

Pericardium tissue samples were cut into 1 cm x 1 cm squares and treated according to their respective treatment groups. Material surface wettability was measured via contact angle goniometry (Flex, Attension, Biolin Scientific, Stockholm, Sweden). Samples were initially dabbed dry with paper towel and a 5µL droplet of Milli-Q water was placed on the pericardium surface. The water contact angle between the water droplet and the pericardium surface was measured using the systems inbuilt analysis software OneAttension.

5.2.10 Whole blood clotting assay

Wells in a 24 well plate were coated with 3% bovine serum albumin in PBS for 1 hour at room temperature. Plates were then washed 3× with PBS and left to dry overnight. Pericardium

samples were cut into 0.8 × 1.2 cm patches, prepared according to their treatment group, pre-weighed and placed into individual wells. Fresh human blood was obtained from donors (male or female, 18-60 years old) with informed consent, in accordance with guidelines of The University of Sydney Office for Research Integrity, Human Ethics Committee (Project 2014/244) and the Declaration of Helsinki. Blood was drawn via standard venepuncture into polypropylene syringes (Terumo, Tokyo, Japan) with heparin (0.3 U/mL, Pfizer, NY, USA) and 10% w/v saline. Whole blood (750 µL/well) was added onto samples and left for 1.5 hours on an orbital shaking incubator (IntelliStack, Thermo Fisher Scientific, USA) at 70 rpm and 37 °C. Blood was removed and samples were washed 3× with PBS before being weighed. Clot weight was calculated by subtracting the weight of the samples post-blood incubation by initial weight. Photographic images were taken for representative purposes. An enzyme-linked immunosorbent assay (ELISA) kit for platelet factor 4 (PF4, Abcam, ab100628) was used to quantify PF4 secretion after whole blood clotting according to manufacturer's instructions. Platelet-poor plasma was obtained by first centrifuging blood solution at 200 g for 14 minutes, and secondly centrifuging the resulting plasma at 2000 g for 10 minutes at 22 °C.

5.2.11 Platelet rich plasma assay

Heparinized whole blood (0.3 U/ml) was centrifuged for 15 min at 1000 rpm in swinging rotors. The supernatant, platelet rich plasma (PRP) was removed and incubated with each sample for 60 minutes while rocking on an orbital shaking incubator (IntelliStack, Thermo Fisher Scientific, USA) at 70 rpm and 37 °C. Samples were fixed in 2.5% glutaraldehyde in 0.1 M phosphate buffer and imaged by SEM as previously described.

5.2.12 *In vitro* inflammation assay

Pericardium samples (6mm diameter circular biopsy punches) were prepared according to their respective treatment groups. THP-1s (70k/pericardium) were seeded onto the pericardium samples and immediately treated with PMA (100 ng/mL) for 24 h. Cells were then stimulated with lipopolysaccharide (1 µg/mL) for 3 h at 37 °C, followed by ATP (1.25 mM), and left at 37 °C, inside the humidified incubator (5% CO2) overnight. Enzyme-linked immunosorbent assay (ELISA) kits for TNFα (Abcam, ab181421) and IL-1ß (Abcam, ab214025) were used to quantify cytokine levels in supernatants according to manufacturer's instructions.

5.2.13 *In vitro* calcification assay on tissue culture plastic

Human dermal fibroblasts (hFB, ThermoFisher Scientific, Waltham, MA, USA) were seeded into a 12-well plate (30000 cells/well) and left to grow until 90% confluency. Cells were then starved using starving media (DMEM with 0.5% FBS and 1% P/S) overnight and replaced with standard complete DMEM media along with treatment groups including 50µM Phytic Acid. The next day, media was replaced with calcification media (3mM CaCl in complete DMEM) and fresh 50µM Phytic Acid. Calcification media and treatment was changed every other day. After 14 days, cells were washed in PBS (2 x 5 mins) and fixed in 4% paraformaldehyde overnight. Cells were washed again in PBS (2 x 5 mins) and stained with 2% Alizarin red for 20 mins with gentle rocking on plate shaker. Stain was then removed and cells were washed with miliQ water (5 x 1 mins) before being left to dry overnight at room temperature. 10% Acetic acid (v/v) was added to wells for 30 mins and the contents was then transferred to individual 1.5mL Eppendorf tubes. Eppendorf tubes were vortexed for 30 seconds and placed under heat at 85˚C for 10 mins. After heating, samples were placed on ice for 5 mins before 500 µL of contents were transferred to new Eppendorf tubes. 500 µL of 10% Ammonium

hydroxide (v/v) was then added to tubes and mixed. 200µL of contents was then added to 96 well plate and absorbance at 405nm was measured using a Tecan M-1000 plate reader.

5.2.14 Calcification solution

Pericardium tissue samples (6mm diameter circular biopsy punches) were prepared according to their respective treatment groups. Samples were placed in Eppendorf tubes containing 1 mL of calcium phosphate solution comprised of 3.87 mM calcium chloride and 2.32 mM dipotassium phosphate in Tris buffer (pH 7.4). Samples were incubated on a plate shaker set to 120 rpm at 37°C for 1 month. Calcium phosphate solution within each test tube was replaced every other day. Samples were then prepared for SEM imaging.

5.2.15 *In vivo* rat subcutaneous model

Study was approved by the University of Sydney Animal Ehtics Committee (protocol number 2024/AE002532). Experiments were conducted in accordance with the Australian Code of Practice for the Care and Use of Animals for Scientific Purpose. 10 mm diameter circular discs were created by biopsy hole punching pericardium tissue samples and prepared according to their respective treatment groups. Pericardium samples were washed in saline (2 x 5 minutes) prior to subcutaneous implantation into separate regions of 8-week-old Sprague Dawley male rats. Rats were anesthetized with 3% isoflurane in oxygen and maintained under aseptic conditions on a heated surgical platform. The dorsal surface was shaved and sterilized sequentially with 70% ethanol. Four 1-1.5 cm dorsal incisions were made to create subcutaneous pockets separated by ~2 cm. Pericardial tissue samples (untreated, PPN-coated, PPN-drug functionalised or drug only treated) were inserted into each pocket, and incisions were closed with 4-0 PDS interrupted sutures. Animals were monitored daily for wound

healing, behaviour, and general health throughout the 28-day implantation period before euthanasia and tissue collection for histological analysis. After 28 days, scaffolds were explanted and fixed in 4% paraformaldehyde overnight at room temperature. Scaffolds were then dehydrated through an ascending ethanol gradient, embedded in paraffin and sectioned at 5 μm (Thermo Fisher HM340 semi-automated microtome). Histopathology staining included Mason's trichrome for collagen to visualize fibrous capsule formation and Alizarin red S to visualize calcification.

5.2.16 Pulse duplicator valve testing

An EvolutTM 22.0 mm diameter TAVI valve (Medtronic) was tested, both before and after PPN coating, in a pulse duplicator (HDTi-6000, BDC Laboratories) for hydrodynamic performance under standard aortic conditions: 70 bpm, 5 L/min cardiac output, 35% systolic duration, 120 mmHg systolic pressure, 80 mmHg diastolic pressure, isotonic saline solution of 0.9% sodium chloride as the test fluid, and 37 °C fluid temperature. Output metrics included the effective orifice area (EOA; a measure of how well the valve opens), regurgitant fraction (RF; a measure of how well the valve coapts during closing), and positive pressure difference (PPD; a measure of the transvalvular pressure gradient across the valve). These parameters were compared between the uncoated and PPN-coated valve, and against the ISO 5840-2 standards to demonstrate proper and clinically relevant functionality. Valve opening and closing was also qualitatively analysed through the resulting images processed by the Statys software (BDC Laboratories). For the coating, the valve was pretreated with 4% L-Cysteine and incubated in a 30 mL falcon tube containing $5x10^{10}$ PPN/mL suspended in nuclease free water and left on a shaker overnight at 4 ˚C.

5.2.17 Statistical analysis

Data are expressed as mean ± standard error of the mean (SEM). Analysis was performed in GraphPad Prism 9 (Graphpad Software, San Diego, California) and statistically significant differences were determined by t-test or using one- or two-way analysis of variance followed by Dunnett's multiple comparisons test. Accepted statistical difference was at $p < 0.05$ and indicated in the figures as $* p < 0.05$, $** p < 0.01$, $*** p < 0.001$, and $**** p < 0.0001$.

5.3 Results

5.3.1 Immobilisation of PPN on pericardium

Glutaraldehyde-fixed bovine pericardium sheets (Figure A2.1) were used as a model substrate to develop and optimise PPN coatings prior to application on a bioprosthetic valve. Circular samples of 6 mm diameter were biopsy punched from sheets, providing size-controlled samples for high-throughput evaluation of functionalisation efficiency and bioactivity (Figure 5.3A). Samples were pre-treated with Cysteine (Cys) to enhance PPN coverage during subsequent dip coating. This pre-treatment resulted in more homogenous PPN attachment, with increasingly greater PPN coverage across the pericardium surface as concentration increased (Figure 5.3B,C). Photomicrographs of PPN-treated pericardium appeared dark brown, serving as a visual indicator of PPN coverage and further highlighted the need for Cys pre-treatment to enable efficient PPN binding. Collectively, this validated dip coating as the foundational application for binding PPN to bioprosthetic tissue.

Given the constant motion and dynamic forces that bioprosthetic leaflets are subject to *in vivo*, we performed retention studies to determine the durability of PPN coatings under simulated physiological conditions. A custom-built closed loop system driven by a peristaltic pump was used to replicate pulsatile flow using PBS (Figure 5.3D). Pericardium samples were subjected to flow for 28 days at an accelerated RPM equating to approximately 12 weeks of cardiac cycles at average heart rate of 70 beats per minute. SEM images taken before (pre-wash) and after (post-wash) 28 days flow period showed that PPN coverage was uniformly reduced across the pericardium surface, without evidence of uneven/localised reductions (Figure 5.3E). Quantification of PPN coverage after flow showed that there was retention of 74% ± 3% of pre-wash PPN coverage ($p = 0.0015$) (Figure 5.3F). This indicated a level of stability that may

be sufficient to support early to intermediate post-implantation therapeutic activity for valves *in vivo*.

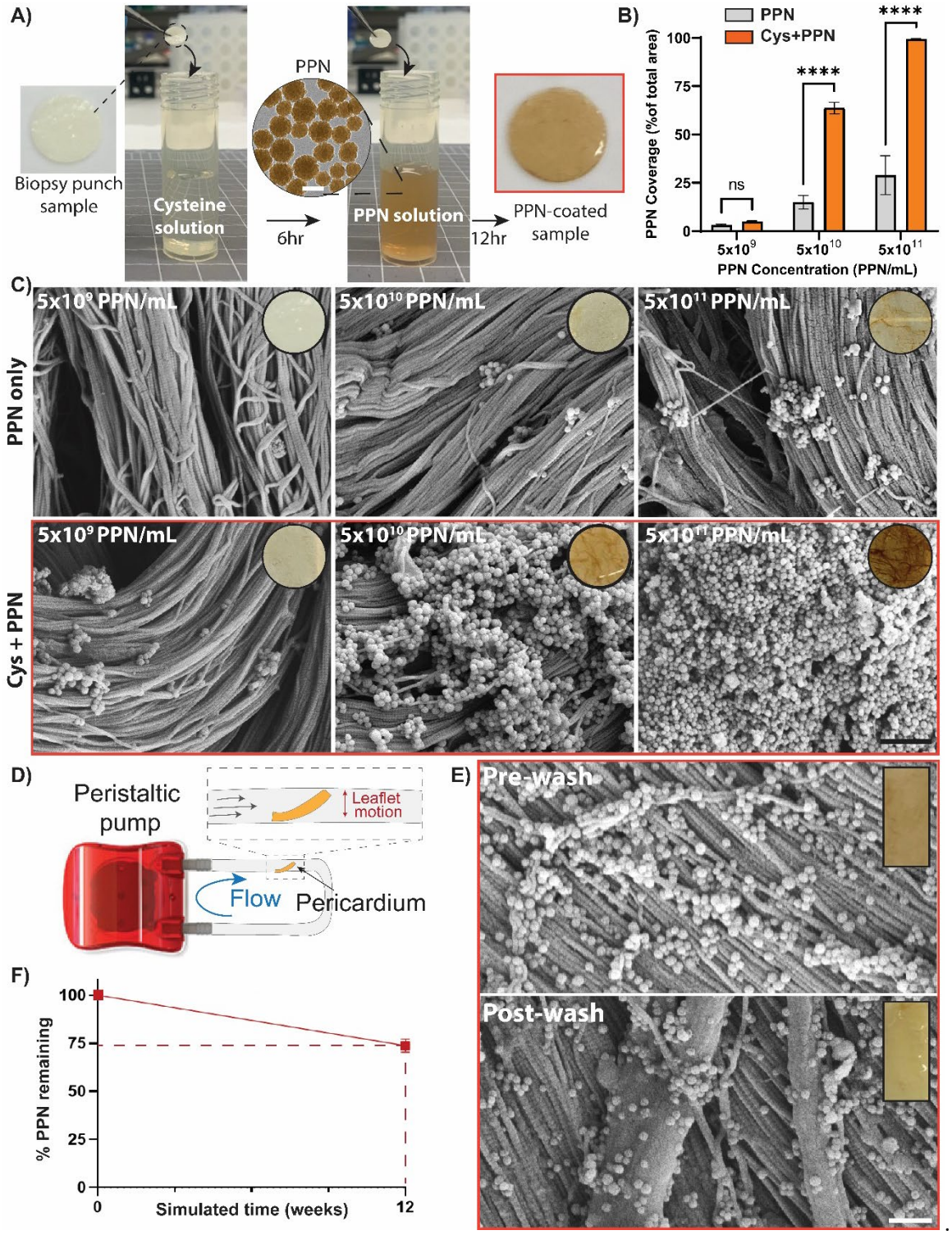

Figure 5.3: Immobilisation of PPN on pericardium
A) Schematic of plasma polymerised nanoparticle (PPN) coating process (scale bar represents 100 nm). B) Quantification of percentage area of pericardium surface covered after PPN conjugation, with and without pre-treatment with Cysteine (Cys). C) Scanning electron microscopy (SEM) and photographs of pericardium after coating with PPN with and without Cys pre-treatment (scale bar represents 1µm). D) Schematic representation of experimental set-up to test PPN retention under flow. E) SEM images and photographs of PPN coated pericardium (5x10^{10} PPN/mL) before washing (pre-wash) and after (post-wash) (scale bar represents 500nm). F) Quantification of the surface coverage of post-wash

pericardium samples as a percentage of pre-wash samples. Simulated time was calculated as per the methods. (n=3 per group). Statistical significance is indicated by ****p < 0.0001.

5.3.2 Reduction of residual free aldehydes on glutaraldehyde-fixed pericardium

Glutaraldehyde fixation leaves residual free aldehyde groups which have been linked to cytotoxicity and leaflet calcification. Cys treatment can facilitate a nucleophilic addition reaction between its thiol (-SH) or amine ($-NH_2$) groups and the free aldehyde (-CHO) functional groups, resulting in a stable thiazolidine derivative that effectively neutralises the free aldehyde group (Figure 5.4A). This reaction was validated in Cys pre-treatment of pericardium tissue using a Schiff-base reagent stain. Control untreated pericardium samples showed strong purple staining indicating high residual levels of free aldehyde groups. In contrast, no positive staining was observed on pericardium samples pre-treated with Cys only nor Cys+PPN (Figure 5.4B**)**. This suggested that Cys treatment was the main driver of free aldehyde reduction and that PPN attachment did not inhibit this reaction.

Endothelial cell attachment and viability was assessed next to determine cell compatibility of PPN coatings. (Figure 5.4C). Endothelial cells attached to Cys only and Cys+PPN treated samples appeared larger and more abundant compared to untreated controls (Figure 5.4D). Quantification of endothelial cell number and spreading after acute attachment showed a 5.8-fold increase in cell number and 7.9-fold increase in cell spreading on Cys+PPN treated samples compared to untreated controls (p = 0.0204 and p = 0.0359, respectively) (Figure 5.4E,F). This was consistent with AlamarBlue measurements which showed a 13.1-fold increase in cell viability (p = 0.0005) (Figure 5.4G). Notably, cell compatibility observed in Cys+PPN groups were not significantly different from Cys treatment only, indicating that the observed improvements were largely a result of Cys treatment rather than PPN.

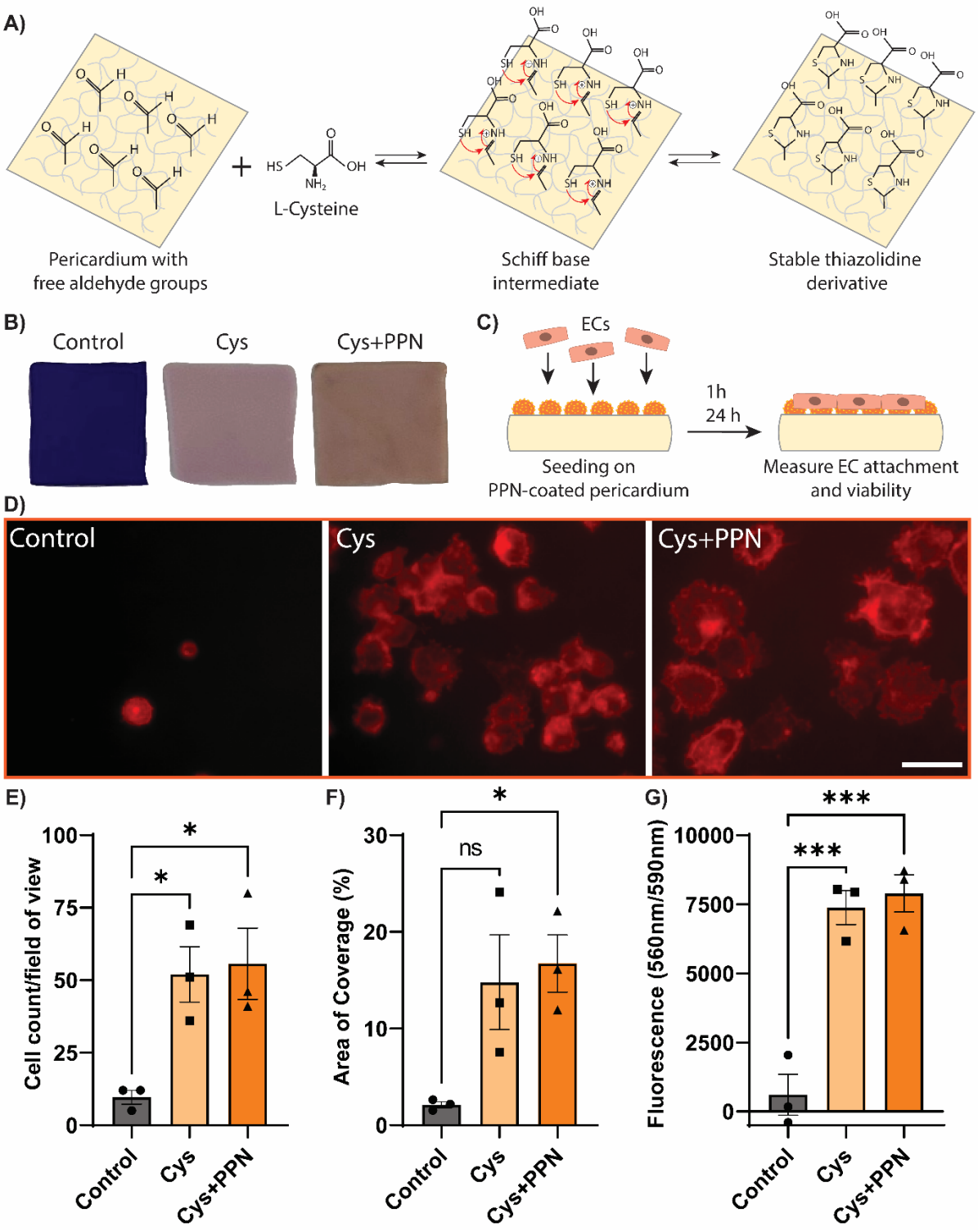

Figure 5.4: Reduction of residual aldehyde groups and its effect on biocompatibility
A) Chemistry schematic showing the aldehyde reduction using Cysteine (Cys). B) Photograph images of control, Cys or Cys+PPN treated pericardium stained with Schiff reagent which stains aldehyde groups purple. C) Representative schematic showing endothelial cell (EC) seeding methodology. D) Representative images of EC attachment after 1h (scale bar represents 20 µm). F-actin shown in red. E) Quantification of EC number 1h after seeding. F) Quantification of EC F-actin staining after 1h attachment. G) Quantification of EC viability after 24h. (n=3 per group).). Statistical significance is indicated by *p < 0.05, ***p < 0.001.

5.3.3 Mechanical and surface properties of PPN coated pericardium

Distinct mechanical properties are required for pericardium tissue to function effectively as a valve leaflet [313]. Biaxial mechanical testing was performed to assess whether Cys or PPN treatment altered these properties (Figure 5.5A). Control pericardium tissue exhibited anisotropic properties where in the axial direction, samples exhibited higher stiffness and a larger maximum load at maximum deformation compared to in the transversal direction (Figure 5.5B,C). Importantly, Cys only and PPN treatment showed no significant differences compared to control in either stiffness or maximum load (Figure 5.5B,C) in either direction. A cyclic deformation test was also performed to evaluate changes in mechanical performance under repeated loading, specifically assessing any reduction in max loading capacity. PPN treatment showed no significant difference in degradation compared to control, indicating that PPN coating does not compromise mechanical durability over repeated deformation cycles (Figure 5.5D). In contrast, Cys-only treated pericardium exhibited a significant relative decline in maximum load, reaching 76% of its initial value after 10 cycles. However, this higher rate of degradation is largely attributable to the elevated initial maximum load observed in Cys-treated tissue (Figure A2.2). Across all cycles, Cys-treated samples retained a higher absolute maximum load than control, suggesting that the relative decline does not reflect inferior mechanical performance.

To further characterise the surface level effects of PPN treatment, water contact angle measurements were performed to assess changes in tissue wettability (Figure 5.5E). Cys treatment resulted in a 1.6-fold increase in water contact angle compared to untreated pericardium (11˚ ± 2˚ vs 29˚ ± 4˚, $p = 0.0071$) (Figure 5.5F). PPN treatment partially reversed this effect, reducing the angle to 22˚ ± 0.6˚, though it remained significantly higher than that of untreated pericardium ($p = 0.0463$).

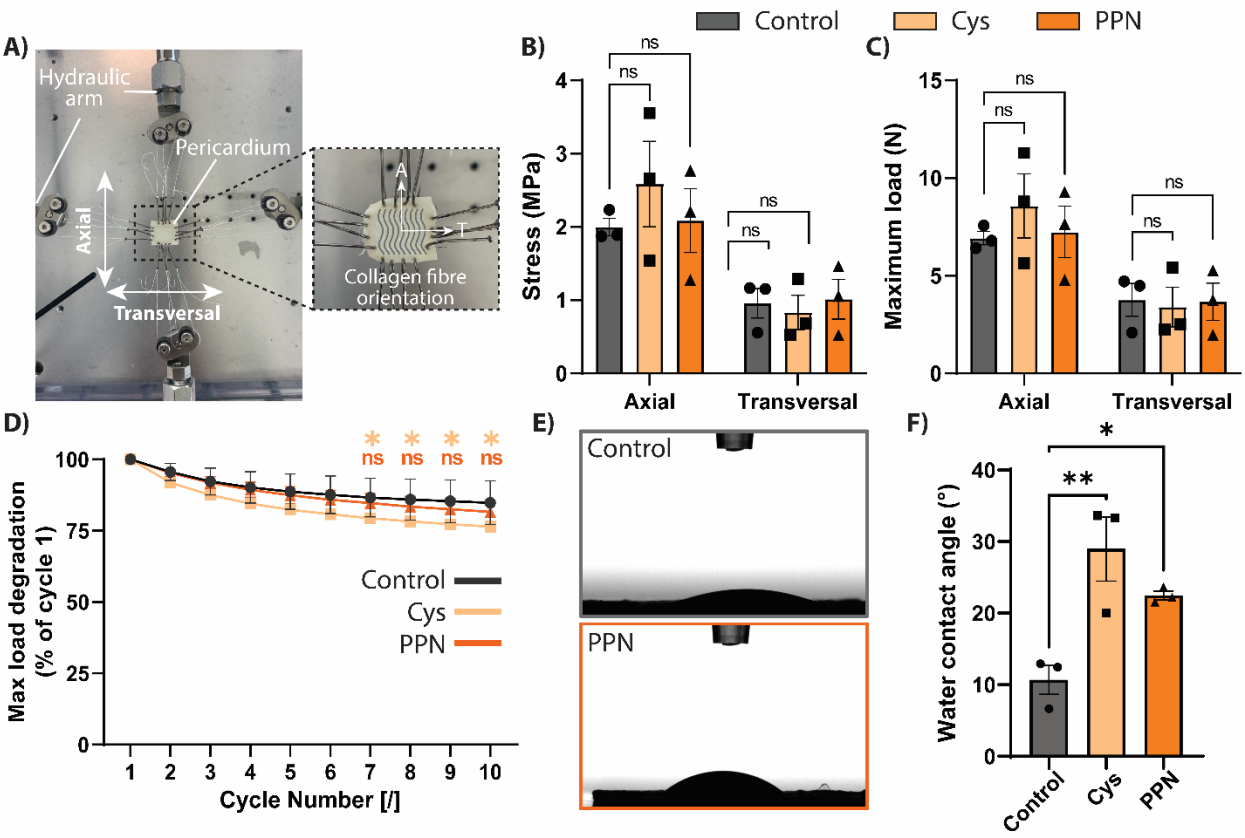

Figure 5.5: Mechanical and surface properties of PPN coated pericardium
A) Photograph of biaxial testing set up. A refers to axial and T refers to transversal direction in insert. B) Results for stress test and maximum load (C) for control, Cysteine (Cys) treated and PPN treated pericardium in both the axial and transversal directions. D) Quantification of max load degradation over 10 cycles. Values are given as a percentage of initial maximum load test. E) Representative images of water contact angle testing. F) Quantification of water contact angle testing across control, Cysteine (Cys) treated and PPN treated pericardium. (n=3 per group). Statistical significance is indicated by *p < 0.05, **p < 0.01.

5.3.4 Functionalisation of pericardium with apixaban to reduce thrombosis

When coated onto pericardium tissue, the remaining exposed surfaces of PPN coated onto pericardium tissue serve as functional sites for drug loading/functionalisation. Aligning this feature with the biological challenges of SVD, we chose the anti-coagulant Apixaban (APX), a clinically approved drug used to prevent valve thrombosis, as a model compound for initial PPN drug functionalisation (Figure 5.6A). PPN-coated pericardium samples were initially incubated in solutions of APX tagged with gold nanoparticles for visualisation under SEM. Gold nanoparticle-tagged APX was observed uniformly decorating the exposed surfaces of

individual PPN nanoparticles (Figure 5.6B). Importantly, APX/gold nanoparticles were not observed by themselves on the underlying pericardium fibers, highlighting the necessity of PPN for immobilising APX on the pericardium surface.

Whole blood clotting assays were then used to evaluate APX functionality *in vitro*. Fresh human blood was incubated with pericardium samples and blood clot weight measured after 1.5 hours. Untreated control pericardium showed large areas of thrombus formation on their surface (Figure 5.6C). Only PPN-coated pericardium samples functionalised with APX (PPN-APX) showed reduced thrombus formation, indicated by an 8.4-fold reduction in clot weight compared to untreated controls ($p = 0.0013$) (Figure 5.6D). Interestingly, PPN only treatments showed slight reductions in clot weight, however these were not significant ($p = 0.1527$). Passively absorbed APX (Free APX) did not show any reductions in clotting weight, further supporting the need for PPN to facilitate drug functionalisation.

Inhibition of platelet activation, determined through platelet aggregation and levels of PF4 secretion, is an indirect downstream anticoagulation mechanism of APX and was used to further evaluate drug function. To test this, platelet rich plasma (PRP) was incubated with pericardium samples for 1 hour. After incubation, PRP supernatant was removed for analysis using PF4 ELISA and pericardium samples were imaged using SEM. Platelet attachment and aggregation was observed to be significantly reduced on PPN-APX samples compared to control (Figure 5.6E). This was consistent with PF4 secretion levels which showed a 4-fold reduction only in PPN-APX groups when compared to control ($p = 0.0236$) (Figure 5.6F). Notably, both PPN only and Free-APX controls showed no reductions in PF4 expression.

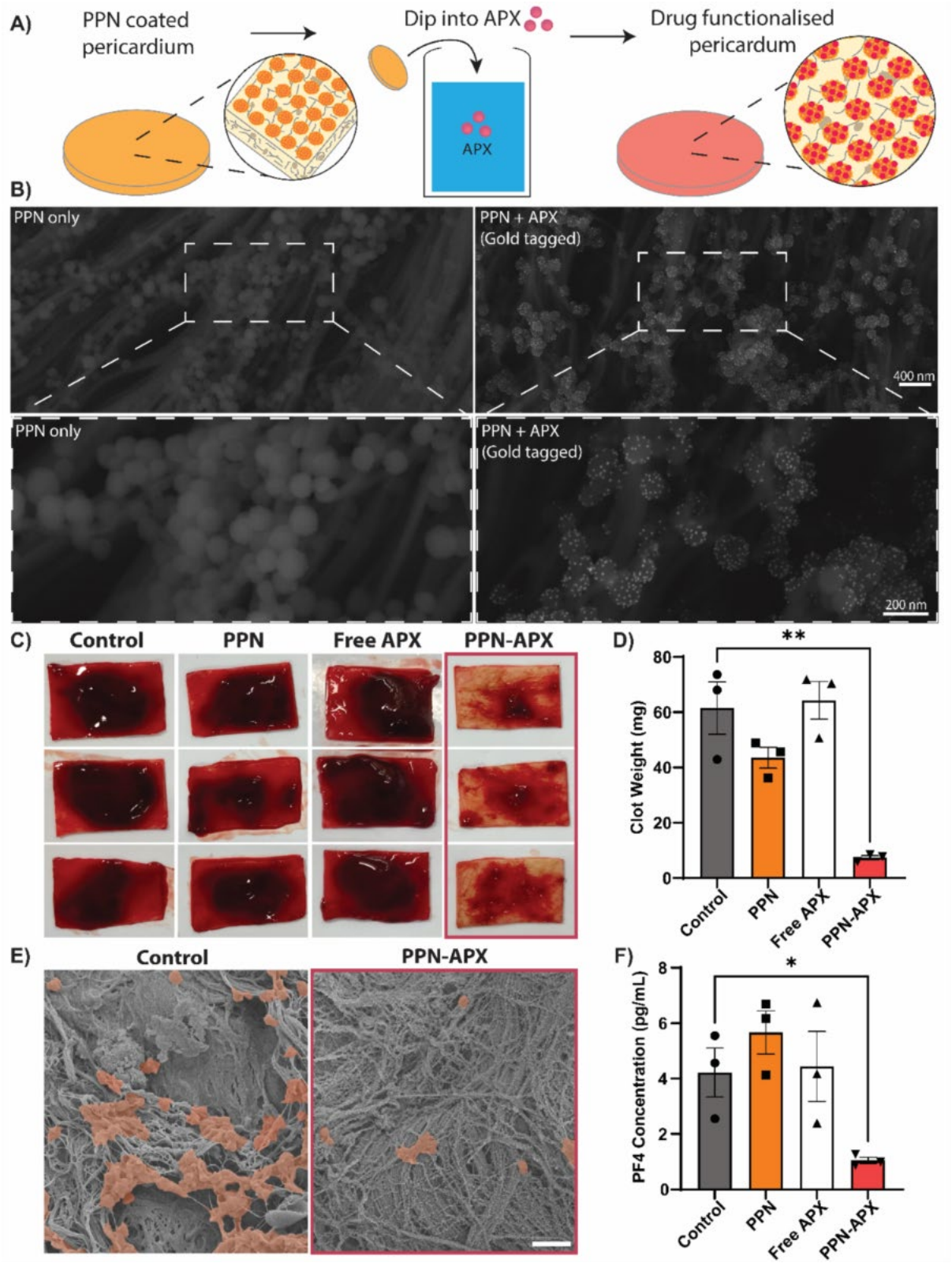

Figure 5.6: Functionalisation of pericardium with apixaban to reduce thrombosis
A) Schematic representation of molecular cargo dip-coating functionalisation step. B) SEM images using back-scattered electron detector of gold-tagged apixaban (APX) functionalised onto PPN-coated pericardium. C) Representative images of whole blood clotting assay. D) Quantification of blood clot weight. E) SEM images of platelet attachment and aggregation on pericardium after 1h incubation. Platelets are false coloured in orange (scale bar represents 4μm). F) PF4 ELISA results following whole blood clotting assay. (n=3 per group). Statistical significance is indicated by *$p < 0.05$, **$p < 0.01$.

5.3.5 Functionalisation of pericardium with MCC950 to inhibit inflammation

PPN was next evaluated for functional presentation of the anti-inflammatory drug MCC950 to address pathological inflammation underlying SVD. PPN-coated pericardium tissue was functionalised with MCC950 using the same incubation dip-coating process. Macrophages were seeded onto pericardium samples and stimulated using LPS and ATP (Stim), to model NLRP3 inflammasome–specific immune activation. Pericardium samples that were not pre-treated with Cys showed no macrophages present after seeding, due to poor cell compatibility, and therefore stimulation was not possible for these groups (Figure A2.3 A-C). All samples were therefore treated with Cys before cell seeding to allow for cell attachment and stimulation (Figure 5.7A). ELISAs were used to quantify the amount of IL-1β and TNF-α secreted from the macrophages. Stimulation resulted in significantly increased secretion of both cytokines compared to control (Figure 5.7B,C). PPN-MCC treated pericardium showed a significant 2.3-fold decrease in IL-1β levels compared to stimulated control ($p = 0.0316$, Figure 5.6B), while TNF-α levels remained unchanged (Figure 5.7C). No significant differences in either cytokine were observed between stimulated control groups and pericardium groups treated with either PPN only or passively absorbed MCC (Free MCC).

Functionality of MCC950 bound to PPN coatings was further examined using an *in vivo* rat subcutaneous implant model over 28 days (Figure 5.7D). The thickness of the fibrotic capsule around pericardium samples was measured using a mason's trichrome stain as an indicator of the degree of immunomodulation (Figure 5.7E). PPN-MCC treated pericardium significantly reduced fibrotic capsule thickness by 42 ± 12% ($p = 0.0400$) compared to control after 28 days, with no significant differences seen for PPN and free MCC treated samples (Figure 5.7F). These findings demonstrate that MCC950 retains its functional bioactivity when coated onto pericardium by PPN.

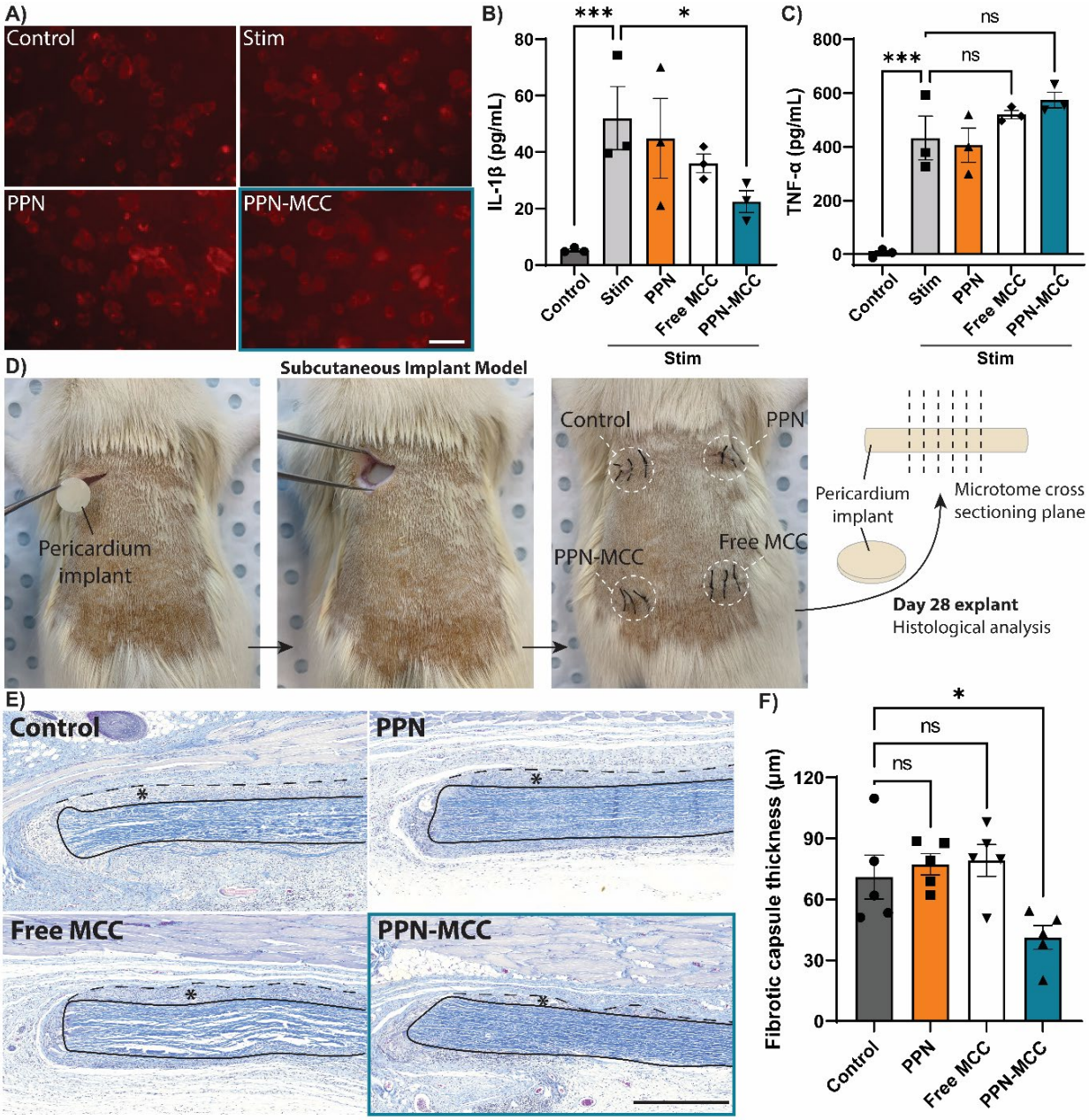

Figure 5.7: Functionalisation of pericardium with MCC950 to inhibit inflammatory response
A) Representative images of control, stimulated only (stim), stimulated and PPN coated, and stimulated and PPN-MCC950 coated (PPN-MCC) pericardium with macrophages seeded on the surface. All groups were pre-treated with Cysteine to allow for macrophage adhesion and stimulation (scale bar represents 50µm). B) IL-1β and TNF-α (C) ELISA quantification from macrophages seeded on differently coated pericardium samples post-stimulation. D) Schematic showing rat subcutaneous implant model. E) Representative images of Masson's Trichrom staining with the pericardium implant outlined in black and fibrotic capsule denoted by a star (scale bar represents 500µm). E) Quantification of fibrotic capsule thickness surrounding the implant. (n=5 per group). Statistical significance is indicated by *$p < 0.05$, ***$p < 0.001$.

5.3.6 Functionalisation of pericardium with phytic acid to prevent calcification

Using an *in vitro* model of fibroblast calcification, we first showed that phytic acid (PA) significantly inhibited calcium crystal formation indicated by reduced alizarin red staining (Figure 5.8A,B). PPN was then evaluated for its ability to functionally present PA, as a strategy to mitigate pathological calcification associated with SVD (Figure 5.8C). An established *in vitro* bench-top model of accelerated hydroxyapatite crystal formation was used to assess PPN coated pericardium functionalised with PA (PPN-PA) for 1 month. SEM imaging analysis showed that the surface of untreated control pericardium was obscured due to extensive calcification (Figure 5.8D, yellow). However, in both the PPN and PPN-PA coated groups, the pericardium surface was clearly visible, indicating significantly reduced hydroxyapatite crystal formation. No significant reduction in calcification was observed in samples treated with passively absorbed PA alone (Free PA) (Figure 5.8E). Further evaluation using elemental mapping analysis highlighted that all groups treated with Cys showed some level of reduction in calcium content compared to control (Figure A2.4). These findings point to Cys as the primary cause for the observed calcification reduction, confirming its aldehyde reducing capabilities and validating the link between calcification and residual aldehydes.

Appreciating that *in vivo* calcification is a multifaceted biological process [314], we then evaluated PPN-PA functionalised pericardium samples using an established 28-day rat subcutaneous implantation model. After 28 days, Alizarin red staining of implanted pericardium cross-sections showed large and dense areas of calcification in untreated control samples. This appeared to be reduced in PPN treated controls and even further in PPN-PA functionalised samples (Figure 5.8F). Percentages of positive alizarin red staining showed that PPN-PA functionalisation led to a 4.5-fold reduction in calcification compared to untreated control ($p = 0.0033$) (Figure 5.8G). PPN also showed a 2-fold reduction in alizarin staining compared to control, although this was not statistically significant ($p = 0.0644$). Similar to

previous findings of passively absorbed drugs, positive staining in Free PA groups was not significantly different to untreated control. These findings demonstrate that PPN can functionalise PA to reduce calcification on bioprosthetic tissue.

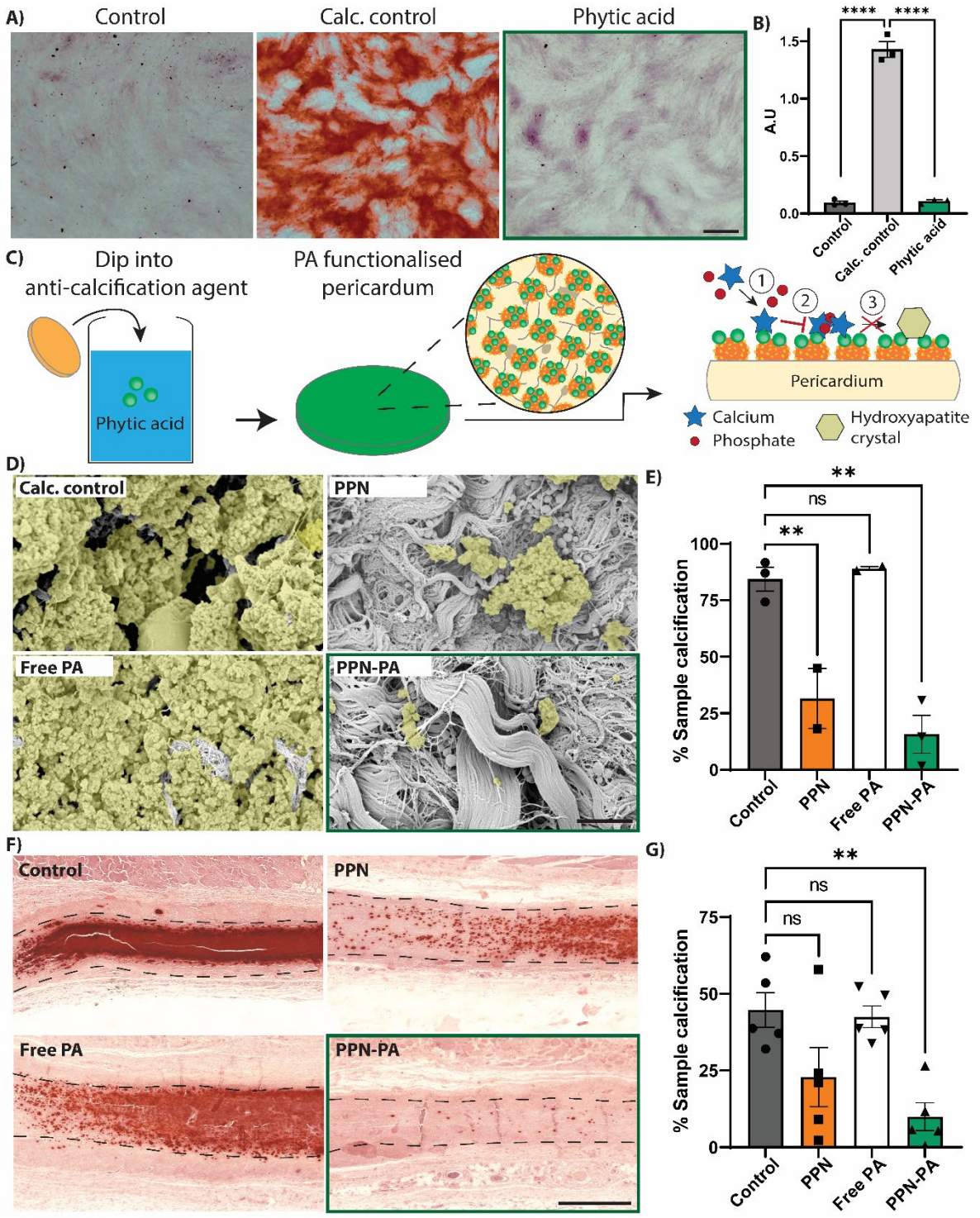

Figure 5.8: Functionalisation of pericardium with phytic acid to prevent calcification
A) Representative images of human fibroblasts which underwent treatment with calcification media. Alizarin red staining was performed (scale bar represents 1 mm). B) Quantification of Alizarin red staining. C) Schematic representation showing phytic acid (PA) functionalisation and mechanism of action. Free calcium and phosphate ions (1) traditionally bind together to form hydroxyapatite crystals on pericardium surface. Phytic acid functionalised on PPN coated pericardium preferentially binds calcium ions, inhibiting phosphate ion interactions (2), and preventing hydroxyapatite crystal formation (3). D) SEM images of differently treated pericardium samples incubated with a calcium phosphate solution showing hydroxyapatite crystal formation false coloured in yellow (scale bar represents 10µm). E) Quantification of hydroxyapatite crystal coverage across samples. (n=2-3). F) Representative images of Alizarin red staining in the pericardium implant outlined in black (scale bar represents 500µm). G)

Quantification of percentage of implant stained positively by Alizarin red. (n=5 per group). Statistical significance is indicated by **p < 0.01, ****p < 0.0001.

5.3.7 Hydrodynamic performance of PPN coated bioprosthetic valve leaflets

The challenge of translating drug functionalisation strategies to bioprosthetic valves is to ensure the coatings do not interfere with the complex mechanics of leaflet motion. Modifications to the leaflet surface must preserve key hydrodynamic metrics commonly used to evaluate valve performance including regurgitation fraction (RF), effective orifice area (EOA), and pulse pressure differential (PPD). PPN coatings were applied to a self-expanding transcatheter porcine bioprosthetic aortic valve (Evolut R 26mm valve, Medtronic, Minnesota, USA) using a scaled-up dip coating procedure to accommodate the large valve size and complex leaflet geometry. Visual inspections of dark brown coloured pericardium leaflets combined with SEM imaging verified successful PPN coating of the transcatheter valve (Figure 5.9A). Valves were then deployed in an industry-standard BDC pulse duplicator system to subject valves to physiologically relevant flow and pressure (Figure 5.9B). Aortic views of the deployed valve within the pulse duplicator showed uninterrupted motion of the valve leaflets when coated with PPN in either an open or closed state (Figure 5.9C). This was verified through readouts from the pulse duplicator showing no significant differences in RF, EOA, and mean PPD when comparing PPN-coated valve to untreated valve (Figure 5.9D-F). Importantly, all hydrodynamic measurements from the PPN-coated valve were well within compliance for ISO 5840 standards for heart valve substitutes.

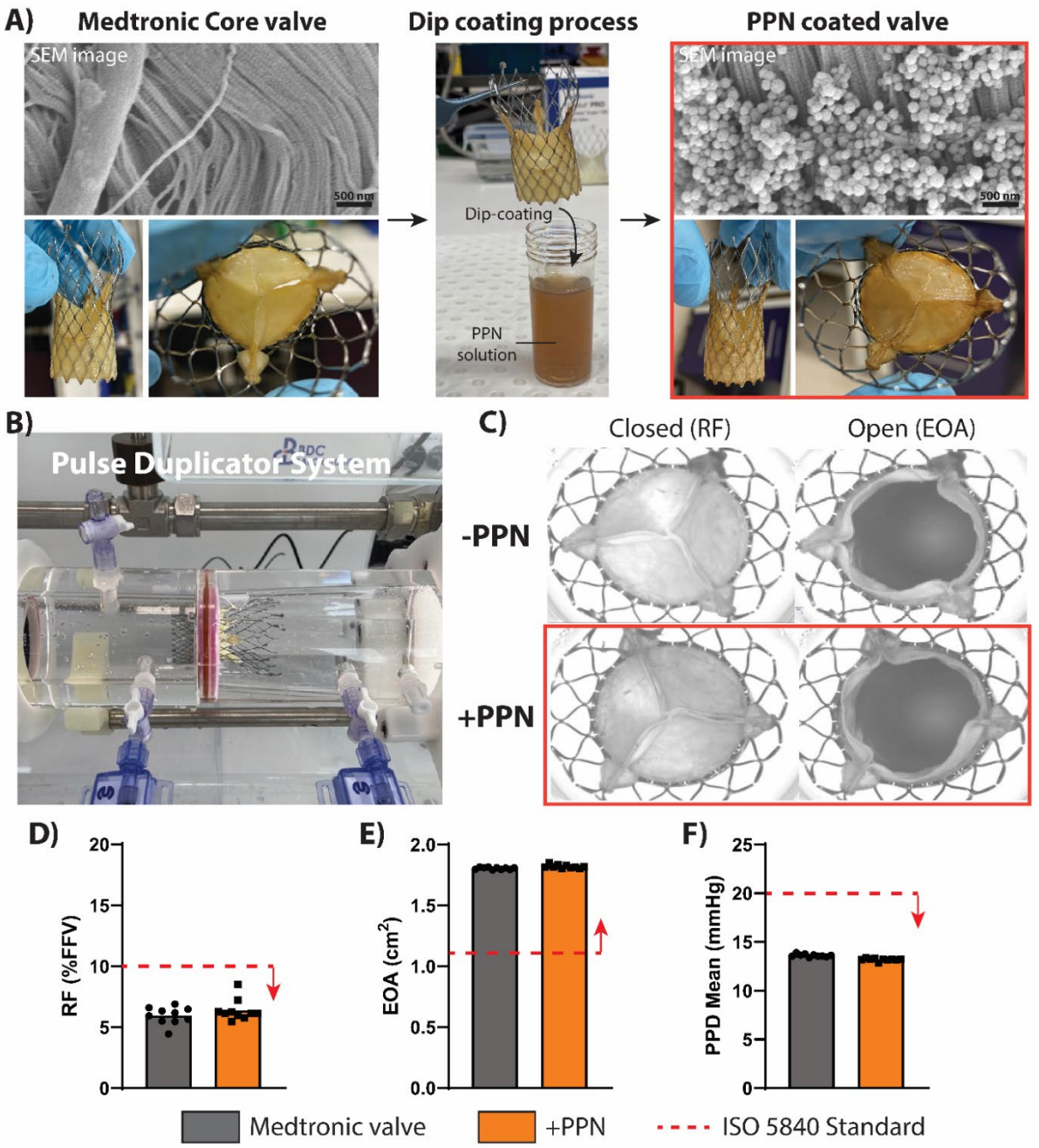

Figure 5.9: Translatability of PPN coating on commercial TAVR valve
A) Photograph images showing the dip-coating process used to conjugate PPN to a Medtronic transcatheter valve. SEM images show the surface of the pericardium leaflets before and after PPN-coating. (Scale bar represents 500nm). B) Photograph of pulse duplicator system. C) Photograph images of Medtronic valve inside pulse duplicator system with and without PPN coating. RF refers to regurgitation fraction and EOA refers to effective orifice area. D,E,F) Quantification of RF (D), EOA (E), and mean pressure gradient (F). PPD refers to pulse pressure differential.

5.4 Discussion

The durability of current bioprosthetic heart valves is limited by SVD, a pathological combination of interconnected biological processes including thrombosis, inflammation and calcification [94]. Current strategies to reduce SVD primarily comprise of chemically treating the glutaraldehyde pericardial tissue to mask calcium binding sites. However, the long-term effectiveness of these technologies is yet to be confirmed and their application to transcatheter heart valves has only recently been introduced. Furthermore, these treatments offer only a passive approach to reducing SVD and its underlying biological processes. An alternative approach that actively modulates the biology at the leaflet interface could potentially enhance bioprosthetic valve resilience to SVD. Here, we investigate the potential of a novel nanoparticle platform PPN to allow active drug functionalisation on bioprosthetic valve tissue. By applying the platform across three distinct drugs, we exemplify how it can separately target each of the three underlying biological modes of SVD in thrombosis, inflammation and calcification.

First, a strategy for achieving efficient PPN coating on glutaraldehyde fixed bovine pericardium was established. Pre-treating the pericardium samples with 4% L-Cysteine (Cys) for 6 hours before applying PPN led to significant PPN coverage across the sample. Hence, successful PPN coating was achieved with two dip coating steps, totalling an 18-hour protocol. Coating was also macroscopically confirmed by qualitatively measuring pericardium brownness. Previously reported coating strategies for bioprosthetic tissue, such as layer-by-layer (LbL) assembly [315, 316] and covalent grafting [317], rely on multi-step chemical protocols that present significant challenges for scalability and routine validation. LbL techniques involve the sequential deposition of oppositely charged, drug-laden layers and require multiple immersion and rinsing steps, making the process time-consuming and poorly

suited for large-scale application. Similarly, covalent grafting of nitric oxide-releasing compounds requires surface pre-functionalisation via EDC/NHS chemistry and additional coupling reactions [318]. Both approaches further depend on complex analytical techniques, including XPS, elemental mapping, ATR-FTIR, and/or SEM to verify coating integrity and uniformity. These requirements add labour and instrumentation burdens, limiting their practical utility in high-throughput or manufacturing contexts. PPN coatings offer significant practical advantages in comparison. PPN application is achieved using a simple dip-coating method, while also offering ready visual confirmation of coating success, streamlining optimisation and early-stage screening without the need for complex validation analytics. Importantly, PPN coatings demonstrated good short to medium term retention capabilities under flow, remaining present on pericardium surface after being exposed to the equivalent of approximately 12 weeks of pulsatile flow. Given the distinct temporal profiles of SVD mechanisms, with thrombosis and inflammation typically manifesting acutely and calcification progressing over time [94], the platform supports temporally targeted therapeutic intervention. In instances when prolonged PPN surface retention is required, optimised coating protocols may enhance long-term stability and extend therapeutic potential to chronic degenerative processes such as late-stage calcification.

Next, the ability of Cys to reduce residual aldehyde groups was examined using a Schiff-base reagent stain. Pre-treating glutaraldehyde-fixed pericardium with Cys successfully reduced free aldehyde groups, the reaction of which was not interfered with by subsequent application of PPN. This is expected as the Cys and free aldehyde groups have already formed stable thiazolidine rings before PPN addition. The amine and carboxyl groups present on the PPN surface are not strong enough nucleophiles to outcompete the thiol group of the cysteine, making reversal of this reaction highly unlikely [226]. Furthermore, while potential side

reactions such as Cys-Cys disulfide bridging or thiol oxidation could theoretically occur, the significant reduction in Shiff-base staining indicates that the condensation reaction with tissue aldehydes remains the dominant pathway. Despite prior mention of Cys as a potential aldehyde-reducing agent for pericardium, its use for targeted aldehyde-capping has not been systematically explored [319]. Our results demonstrate for the first time the ability of Cys to effectively reduce residual aldehydes on pericardium with a single 6-hour incubation step, comparable with the current gold-standard aldehyde capping technology Resilia™ (Edwards Lifesciences) which takes between 4-6 hours to achieve complete free-aldehyde removal [320], and far more efficient compared to Medtronic's AOA™ treatment which takes 48-120 hours for optimal performance [321]. Given that many commercially treated bioprosthetic tissues already incorporate aldehyde-capping steps, this suggests that PPN coatings could be applied directly to these valve leaflets without the need for additional pre-treatment. This positions PPN as a compatible add-on that does not require alteration of existing leaflet chemistry or design.

Furthermore, improving the cell compatibility of fixed pericardium is essential for promoting beneficial cell remodelling that can positively impact valve durability [94]. For example, re-establishment of an intact leaflet endothelium is critical for long-term maintenance of a non-thrombogenic leaflet surface, regulating inflammatory responses and preserving tissue homeostasis, all of which can contribute to enhanced resilience against SVD [322]. The effect of the PPN coating protocol on endothelial cell attachment and viability was therefore investigated. Both attachment and viability of endothelial cells improved when seeded onto pericardium treated with either Cys only or Cys and PPN, with no observable difference between the two treated groups. In this way, Cys was the primary cause of these improvements. These effects were largely unsurprising, given previous studies showing similar amino acid

pre-treatment, using L-glutamic acid, improved endothelialization and reduced long-term thrombosis over 3 months in pericardium grafts used in sheep carotid arteries [323]. More importantly, PPN attachment following Cys pre-treatment did not compromise this improved cell compatibility, both supporting previous findings of low cytotoxicity of PPN [324] and highlighting that surface modification can be achieved without sacrificing the biological performance of the underlying tissue.

Distinct mechanical properties are required for pericardium tissue to function effectively as a valve leaflet [313]. Biaxial mechanical testing was used to assess if any changes to these properties occurs after Cys or PPN treatment. Firstly, pericardium exhibited anisotropic mechanical properties, consistent with the directionally aligned orientation of collagen fibres which make up the pericardium. Importantly, neither Cys or PPN negatively impacted pericardium stiffness or maximum load capabilities in either the axial or transversal direction. Cys has previously been shown to preserve tensile properties, likely because it does not disrupt the macro-architecture of the pericardium collagen fibers [319]. Our findings demonstrated that PPN coatings have no impact on mechanical performance, even after repeat loading stress, supporting that they function as exclusively surface-level modifications that do not affect the bulk properties of the tissue. This preservation of mechanical integrity reinforces the potential for integrating PPN into existing bioprosthetic valve designs without compromising leaflet function.

Water contact angle is a common measure of tissue wettability often used for assessing how coatings alter surfaces of materials. Treated pericardium presented as more hydrophobic compared to untreated pericardium. This decrease in wettability was largely due to Cys reacting with aldehyde groups on the pericardium, which are known to form stable and

hydrophobic thioether bonds which drive increased water contact angles [325]. PPN has previously shown to enhance substrate hydrophilicity which was also observed here when comparing PPN treated samples to Cys only [326]. However, the final contact angle still remained markedly higher than that of untreated tissue. This increase in hydrophobicity may be beneficial in the context of valve leaflet performance as hydrophobic surfaces can reduce excessive water uptake and swelling, helping to preserve mechanical integrity [327], and may limit undesired interactions with plasma proteins that trigger immune or thrombogenic responses [328]. These findings suggest that PPN treatment not only enables surface functionalisation but also contributes to tuning surface wettability to a level potentially favourable for long-term leaflet durability and biocompatibility.

After characterisation and evaluation of the PPN coating, functionalisation of this coating with therapeutic cargo was performed. PPN have been previously demonstrated as a versatile nanocarrier platform for therapeutic molecules, enabling simple drug attachment by binding biomolecules directly from solution without the need for additional linker chemistry [230, 326]. The direct factor Xa inhibitor apixaban (APX) was selected as a therapeutic agent to be functionalised on PPN coated pericardium due to its anticoagulation properties. APX functionalised PPN-coated pericardium reduced thrombus weight and platelet activation compared to control, highlighting that APX remained functional post-functionalisation. This represents a significant advance over previous work demonstrating that PPN can bind bioactive cargo when applied on synthetic polymers [326]. These findings show PPN are still an effective functionalisation platform on glutaraldehyde-fixed bioprosthetic tissue. Relevant to the anti-thrombotic function of APX, similar effects on bioprosthetic tissue have been achieved using anticoagulant-laden nanogel coatings [329]. However, this coating required preloading of drug into nanogels, covalent grafting of PEG, and incorporation of enzymatic triggers, steps that add chemical and logistical complexity which may pose translational challenges. In contrast, the

PPN platform enables a simple, dip-coating process, followed by linker-free drug attachment achieved within 30 minutes, offering greater flexibility and clinical feasibility. From a clinical perspective, this strategy also addresses a critical limitation in the use of systemic anticoagulation following valve replacement procedures. Oral drugs like APX have been shown to reduce the incidence of SLT, however their systemic use has been associated with increased bleeding and thromboembolic events [285]. Localised drug presentation at the leaflet surface where SLT originates, may offer a safer alternative with reduced off-target effects. The successful findings with APX supported broader investigation into versatility of the platform to present other drugs targeting the remaining major modes of bioprosthetic valve failure.

MCC950 is a selective inhibitor of the NLRP3 inflammasome, blocking downstream IL-1β secretion without affecting broader immune signalling pathways such as TNF-α secretion [233]. Maintaining this selectively presented a stringent test for drug functionalisation of the PPN platform. This selective functionality was preserved post-functionalisation, evidenced by the reduction in IL-1β but not TNF-α following macrophage stimulation. In addition, our previous work has shown MCC950 to significantly reduce foreign body fibrosis and inflammation of implanted materials [330], providing an additional metric for evaluating its functional activity. As such, the observed *in vivo* reduction of fibrotic capsule thickness of MCC950 functionalised PPN-coated pericardium further validated the functional presentation of MCC950. This effect was not observed in groups treated with free, passively adsorbed MCC950, underscoring the importance of PPN in enabling therapeutically meaningful drug presentation *in vivo*. This marks the first demonstration of PPN functioning as an effective *in vivo* biomaterial coating capable of sustaining localised drug activity. This has important clinical implications for bioprosthetic heart valves which inherently trigger foreign body responses, leading to leaflet fibrosis and excessive extracellular matrix (ECM) deposition.

Notably, leaflet fibrosis has been observed as early as 60 days post-implantation, restricting mobility and impairing valve function, ultimately leading to SVD [95]. Leaflet fibrosis is increasingly recognised as a key intermediate stage in the progression of structural valve deterioration (SVD), bridging early thrombotic events and later calcific degeneration [331, 332]. Developing leaflets that can locally inhibit inflammation and promote better integration with the vasculature is crucial for long-term valve performance and would represent a significant advance in valve durability.

Enhancing pericardium resistance to calcification has arguably been the largest industry focus to improve long-term valve durability, representing another key target for drug functionalisation. Bioprosthetic valve calcification is a chronic process believed to be driven by passive calcium phosphate deposition on collagen and elastin fibers within pericardium ECM, leading to hydroxyapatite crystal formation [94]. Phytic acid (PA), a calcium-chelating drug, has been shown to inhibit calcification by blocking calcium crystal nucleation and growth in vascular applications such as decellularized grafts and arterial tissues [333]. These findings support its potential utility in bioprosthetic valve leaflets, where similar ECM-driven calcification mechanisms are known to occur. In our *in vitro* accelerated calcification model, reduced hydroxyapatite formation was observed in all PPN-coated groups, consistent with the well known anti-calcification effects of aldehyde capping pretreatments like Cys [329, 334-336]. This validates the current industry strategy to employ tissue technologies that target residual aldehydes to prevent calcification. However, it was in the *in vivo* setting where the added value of PPN-PA functionalisation became evident. While Cys pretreatment alone contributed to a trend toward reduced calcification, significant reductions were only achieved in PPN-PA functionalised groups. This highlights the potential of combining passive anti-calcification strategies (e.g. tissue technologies) with active drug functionalisation for

enhanced clinical outcomes. However, it is important to note that the models used in this study reflect accelerated calcification, whereas bioprosthetic valve calcification is a chronic process that spans decades. Further studies are needed to assess the long-term durability of PPN-PA, including both the PPN coating itself and the sustained activity of PA over time. Future work may focus on optimising stability and drug binding to ensure prolonged anti-calcification performance of PPN-PA coatings over the lifespan of a bioprosthetic valve.

Leaflet mechanics can be significantly altered by changing leaflet thickness even on a micron scale. One study evaluated valves with varying leaflet thickness using a pulse duplicator system and concluded that increasing leaflet thickness from 0.24 mm to 0.46 mm resulted in a reduction in EOA (reduced from 2.5 cm^2 to 1.1 cm^2) and an increase in mean pressure gradient from 8 mmHg to 25 mmHg [337]. It also demonstrated that even changing leaflet thickness by 25 μm can markedly affect hydrodynamic performance. PPN are approximately 100-200 nm in size [226] and therefore translated to no observable changes in leaflet mechanics when coated onto bioprosthetic valve leaflets. However, polymer coatings currently range between 5-15 μm and therefore are believed to directly impact leaflet mechanics, making them not suitable for valve applications [338]. This highlights the translatability of PPN with regard to commercial transcatheter aortic valves.

5.5 Conclusion

In this study, we present a novel approach for the biofunctionalisation of bioprosthetic valves using PPN. PPN coatings can potentially enhance the long-term durability of bioprosthetic valves by enabling a diverse range of targeting strategies to actively address key biological mechanisms driving SVD. Our platform employs a simple two-step process completed within

24 hours, eliminating the need for complex chemistries and lengthy production workflows. Aligned more with an active approach to preventing SVD, the main advantage of PPN is its role as a drug-functionalisation platform. Using Apixaban, MCC950 and Phytic acid, we demonstrate the capability of PPN to immobilise therapeutic agents while preserving their bioactivity in direct relevance to major SVD pathways. PPN successfully functionalised Apixaban to provide enhanced resistance to clotting and platelet activation. Similarly, PPN-MCC950 functionalised pericardium showed a reduction in inflammation in both in vitro and in vivo inflammatory models. Lastly, PPN coatings of Phytic acid inhibited hydroxyapatite crystal formation in vitro and reduced accelerated calcification in vivo. These findings establish PPN as powerful platform for enhancing drug efficacy by immobilising therapeutics directly at the leaflet surface. This approach is scalable and functionally compatible with transcatheter self-expanding bioprosthetic valves. Collectively, this study showcases PPN as a fundamentally new advance in leaflet innovation, offering new opportunities to enhance bioprosthetic valve longevity and ultimately transform valve replacement therapy.

Chapter 6

Concluding remarks

6. Chapter 6 – Concluding remarks

Cardiovascular disease (CVD) remains the leading cause of death globally [99]. With an ageing population, CVD incidence is expected to increase dramatically into the future. In advanced cases, cardiovascular devices and implants are playing an increasingly prominent treatment role, often complementing and/or taking precedence over drug therapies. Cardiovascular devices such as balloons, stents, and bioprosthetic heart valves have ushered in a new approach to surgery, taking advantage of minimally invasive procedures which have accelerated their use across broader patient populations [100]. However, current devices are not appropriately designed to last for ever, and often don't outlast the patient's lifespan, resulting in repeat surgical intervention. Reintervention carries an increased risk of procedural complication, compromised device performance and significant burden on patients and their families [50, 51]. Recent innovation in the cardiovascular device space has aimed to extend device longevity by coupling implants with anti-proliferative drugs which kill off tissue growth around the implant which otherwise causes device failure. However, despite the introduction of drug eluting technology, balloon angioplasty and stenting still routinely require reintervention within 3-5 years [110], and bioprosthetic heart valves rarely last longer than 10-12 years [92]. As such, there is an urgent clinical need to improve durability of current cardiovascular devices. Increasing evidence suggests targeting inflammation, the underlying cause and/or driver of implant failure, could be a promising approach.

The results of this thesis contribute to the novel understanding that targeting inflammation could be a better alternative for drug-eluting cardiovascular devices, and proposed innovative solutions to incorporate this knowledge to existing devices.

Chapter 3 of this thesis evaluated a selective anti-inflammatory drug-elution strategy for cardiovascular materials against the current clinical anti-proliferative approach. Anti-proliferative drugs paclitaxel and sirolimus have been the dominant drug-eluting agents for cardiovascular devices since drug-elution technology was introduced in the early 2000's [105-108]. Despite considerable improvements in the understanding of the pathophysiology of restenosis and the drivers of cardiovascular device failure since then, anti-proliferatives have remained the clinical standard. As a result, there is significant lag between what is known regarding the fundamental scientific understanding of device failure and the engineering solutions which aim to improve device performance and longevity. What is known in the literature is that both prevention of restenosis and vessel healing are necessary outcomes for sustained vessel patency [339]. While sirolimus and paclitaxel are able to reduce restenosis in the short term, they predominately fail to promote vessel healing characterised by rapid endothelialisation, leading to failure in the long term. This chapter therefore investigated the potential of the selective anti-inflammatory MCC950 to both inhibit restenosis and promote vascular healing.

MCC950 is a specific inhibitor of the NLRP3 inflammasome pathway which is implicated in vascular inflammation and restenosis [236, 237]. *In vitro* studies in Chapter 3 highlighted that MCC950 was functioning through a completely distinct mechanism of action compared to paclitaxel and sirolimus, being able to reduce pro-inflammatory cytokine secretion without demonstrating anti-proliferative/cytotoxic effects. While this anti-inflammatory effect of MCC950 has been established in the literature, this was the first time it has been investigated in a vascular context. Notably, the ability of MCC950 to reduce clot weight and fibrin deposition highlighted the importance of NLRP3 inflammasome driven inflammation in platelets and the blood clotting cascade more broadly, a pathway that had never previously been

targeted by the drug. This further suggested MCC950 could be a more favourable drug-elution agent compared to paclitaxel and sirolimus.

MCC950 was then evaluated *in vivo* using an established mouse carotid interposition grafting model for neointimal hyperplasia. While both paclitaxel and sirolimus showed no improvement in endothelialisation at 7 or 28 days, MCC950 promoted more rapid and functional endothelialisation, highlighting for the first time a vascular reparative effect. MCC950 treatment similarly enhanced long-term reduction of neointimal hyperplasia, firstly suggesting that suppressing underlying inflammation is sufficient in reducing risk of restenosis, and secondly, by selecting the right pathway, selective inhibition of inflammation can both decrease pathological inflammation while not only preserving healing, but actively enhancing it.

These findings represent the first time a selective NLRP3 inflammasome inhibitor has been evaluated both *in vitro* and *in vivo* against current commercial drug eluting agents in the context of vascular materials, providing a basis for further investigation of selective anti-inflammatories as a drug elution strategy.

Chapter 4 of this thesis aimed to evaluate the potential of plasma polymerised nanoparticles (PPN) as a localised drug delivery platform for selective anti-inflammatory therapies in the context of vascular injury. Nanoparticle-based carriers have long been proposed as a means to improve tissue uptake and extend local drug retention for cardiovascular applications, but translation has been limited by poor biodistribution, complex functionalisation protocols, and loss of drug functionality upon conjugation [146, 207, 220, 225]. In this chapter, PPN were investigated as an alternative nanocarrier platform to overcome these limitations and enhance the therapeutic potential of the selective anti-inflammatories MCC950 and IL-10.

The first part of this chapter focused on biodistribution and clearance of systemically delivered PPN, using radiolabelling with zirconium-89 and PET/CT imaging. PPN accumulated

primarily in the liver and spleen shortly after administration, consistent with their physicochemical properties which suggest clearance through the mononuclear phagocyte system [257]. Accumulation in the heart and brain was negligible, reducing the risk of off-target toxicity often observed for other nanoparticle systems such as silica or gold nanoparticles [147, 259, 260]. Over time, PPN were cleared from the liver via the biliary system, reflecting normal processing pathways for nanosized materials. These findings demonstrated that PPN follow predictable biodistribution and clearance routes, with no evidence of prolonged accumulation in vital organs, supporting their safety profile as a drug carrier.

The simplicity of conjugating therapeutic cargo to PPN and the retention of drug functionality was additionally tested in this chapter. Unlike other nanoparticle systems that rely on multi-step wet-chemistry protocols or require additional coatings to stabilise drug loading [262], PPN enable one-step surface conjugation of bioactive cargo. Both a large protein cytokine (IL-10) and a small molecule (MCC950) were successfully conjugated, confirmed by shifts in hydrodynamic size, PDI, and zeta potential. Importantly, both retained their bioactivity *in vitro*, suppressing inflammatory cytokine secretion in macrophage stimulation assays. This outcome contrasts with inorganic platforms such as gold nanoparticles, where conjugation has frequently impaired drug activity [225]. Thus, this study highlighted PPN as a practical, scalable, and function-preserving platform for conjugation of two classes of selective anti-inflammatory agents.

In vivo studies revealed the therapeutic advantages of PPN as a drug delivery platform for vascular applications. Fluorescently labelled PPN showed markedly improved arterial retention compared to free dye following arterial injury, adhering directly to the damaged vessel wall and resisting washout under blood flow for up to 5 days. Building on this, PPN-MCC950 and

PPN-IL10 conjugates significantly reduced neointimal hyperplasia and enhanced endothelialisation after 14 days, whereas freely delivered drugs were unable to achieve both outcomes simultaneously. These findings underscore the importance of drug retention. Endothelialisation is an acute repair response that can be supported even by transient IL-10 exposure, but suppression of neointimal hyperplasia requires sustained drug presence, which was only achieved when conjugated with PPN. By combining retention with functional preservation, PPN enabled these selective anti-inflammatories to demonstrate favourable vascular outcomes *in vivo* for the first time when delivered locally following arterial injury.

Together, these results identify PPN as a promising nanoparticle platform that addresses key barriers to nanoparticle translation including predictable biodistribution and clearance without accumulation in vital organs, simple drug-functionalisation protocol, preservation of drug function, and robust *in vivo* efficacy through enhanced retention. This chapter therefore provides proof-of-concept that PPN can effectively deliver selective anti-inflammatory agents such as MCC950 and IL10 to sites of vascular injury, reducing neointimal hyperplasia while promoting endothelial repair. These findings support further evaluation of PPN-MCC950 and PPN-IL10 therapies in pre-clinical models and position the platform as a commercially viable solution for next-generation cardiovascular drug delivery.

Finally, a novel approach for the biofunctionalisation of bioprosthetic valves using PPN was developed in chapter 5 of this thesis. Here, a customised dip-coating protocol utilising L-Cysteine (Cys) pre-treatment was developed which not only allowed PPN to effectively bind to the glutaraldehyde-fixed bovine pericardium in less than 24 hours, but also chemically reduced residual free aldehyde functional groups on the tissue surface, a common feature current commercial bioprosthetic valves have adopted in order to reduce calcification [304,

320, 321]. PPN coatings resulted in a dark brown colouration of pericardial tissue providing an immediate visual validation for coating success, simplifying quality control and potential clinical translation. Importantly, Cys pre-treatment drove enhanced cell compatability, with implications for positive cell remodelling and host integration. This is particularly relevant for re-establishing the leaflet endothelium, a critical component in maintaining a long-term non-thrombogenic surface and mitigating early-stage complications such as SLT and HALT [94].

The mechanical and surface properties of pericardial tissue coated with PPN was then evaluated to ensure the coating protocol did not cause any adverse effects. Using a biaxial mechanical tester, no change in mechanical properties including stiffness, degradation or cyclic deformation were observed when comparing PPN coated pericardium to control, highlighting the potential of PPN to be incorporated into existing bioprosthetic valves without compromising leaflet integrity. Interestingly, water contact angle testing indicated PPN coating enhanced the hydrophobicity of the pericardium surface, potentially having favourable anti-thrombogenicity implications by mitigating plasma protein adsorption and minimising blood-surface contact.

Aligned more with an active approach to preventing SVD, the main advantage of PPN is its role as a drug-functionalisation platform. Using apixaban, MCC950 and phytic acid, this chapter additionally demonstrated the capability of PPN to immobilise therapeutic agents while preserving their bioactivity in direct relevance to major SVD pathways. PPN successfully functionalised apixaban to provide enhanced resistance to clotting and platelet activation. Similarly, the selective inflammation inhibitory mechanism of action of MCC950 was retained *in vitro* when functionalised onto PPN coated pericardium, which translated to reduced fibrotic encapsulation of the material *in vivo*. Furthermore, PPN coatings of phytic acid inhibited hydroxyapatite crystal formation in both *in vitro* and *in vivo* models of accelerated calcification. These findings establish PPN as powerful platform for enhancing drug efficacy by

immobilising therapeutics directly at the leaflet surface. This is the first demonstration of a bioprosthetic valve coating platform that can functionalise a diverse range of therapeutics which actively address key biological mechanisms driving SVD, without altering the coating protocol.

Importantly, this approach is scalable and functionally compatible with transcatheter self-expanding bioprosthetic valves. PPN coatings did not impair key hydrodynamic parameters during pulse duplicator testing including regurgitation fraction, effective orifice area, and pulse pressure gradients across the valve, all of which remained well within ISO standards for heart valve substitutes. These findings validate that PPN coatings seamlessly integrate into current bioprosthetic valve designs, reinforcing their clinical feasibility. Collectively, this chapter showcased PPN as a fundamentally new advance in leaflet innovation, offering new opportunities to enhance bioprosthetic valve longevity and ultimately transform valve replacement therapy.

Overall, this thesis demonstrated a new strategy to improve cardiovascular device durability through selective immunomodulation and active engagement with local biology. Evaluation of MCC950, a novel NLRP3 inhibitor, in the context of vascular materials showed that targeted anti-inflammatory drug-elution can suppress inflammation while promoting healing, offering clear advantages over current commercially used anti-proliferatives. Building on this, PPN were established as a localised delivery platform that enhanced drug retention and produced favourable vascular outcomes, potentially extending the benefits of selective immunomodulation to other vascular settings. Finally, a PPN-based, commercially viable coating was developed for bioprosthetic heart valves, creating functional surfaces that mitigated key failure modes without impairing performance. Collectively, these findings highlight the potential of selective anti-inflammatories and PPN-based solutions to underpin the next generation of cardiovascular devices with improved longevity.

References

1. Herman, I.P., *Physics of the human body*. 2007: Springer.
2. Camasão, D.B. and D. Mantovani, *The mechanical characterization of blood vessels and their substitutes in the continuous quest for physiological-relevant performances. A critical review.* Materials Today Bio, 2021. **10**: p. 100106.
3. Galley, H.F. and N.R. Webster, *Physiology of the endothelium.* British Journal of Anaesthesia, 2004. **93**(1): p. 105-113.
4. Yau, J.W., H. Teoh, and S. Verma, *Endothelial cell control of thrombosis.* BMC Cardiovascular Disorders, 2015. **15**(1): p. 130.
5. Reitsma, S., et al., *The endothelial glycocalyx: composition, functions, and visualization.* Pflugers Arch - European Journal of Physiology, 2007. **454**(3): p. 345-59.
6. van Thiel, B.S., et al., *Structure and cell biology of the vessel wall*, in *The ESC Textbook of Vascular Biology*, R. Krams and M. Bäck, Editors. 2017, Oxford University Press. p. 0.
7. Majesky, M.W., et al., *The Adventitia.* Arteriosclerosis, Thrombosis, and Vascular Biology, 2011. **31**(7): p. 1530-1539.
8. Maiellaro, K. and W.R. Taylor, *The role of the adventitia in vascular inflammation.* Cardiovasc Res, 2007. **75**(4): p. 640-8.
9. Shah, S., et al., *The Heart: Anatomy, Physiology and Exercise Physiology*, in *Integrating Cardiology for Nuclear Medicine Physicians: A Guide to Nuclear Medicine Physicians*, A. Movahed, et al., Editors. 2009, Springer Berlin Heidelberg: Berlin, Heidelberg. p. 3-22.
10. Reyaldeen, R., et al., *Pericardial Anatomy, Interventions and Therapeutics: A Contemporary Review.* Structural Heart, 2021. **5**(6): p. 556-569.
11. Shereen, R., et al., *A comprehensive review of the anatomical variations in the right atrium and their clinical significance.* Translational Research in Anatomy, 2019. **17**: p. 100046.
12. Lansakara, M. and S. Unai, *An overview of aortic valve anatomy: the current understanding.* Indian J Thorac Cardiovasc Surg, 2023. **39**(Suppl 2): p. 246-252.
13. Gumpangseth, T., S. Lekawanvijit, and P. Mahakkanukrauh, *Histological assessment of the human heart valves and its relationship with age.* Anat Cell Biol, 2020. **53**(3): p. 261-271.
14. Mongkoldhumrongkul, N., M.H. Yacoub, and A.H. Chester, *Valve Endothelial Cells - Not Just Any Old Endothelial Cells.* Curr Vasc Pharmacol, 2016. **14**(2): p. 146-54.
15. Horne, T.E., et al., *Dynamic Heterogeneity of the Heart Valve Interstitial Cell Population in Mitral Valve Health and Disease.* Journal of Cardiovascular Development and Disease, 2015. **2**(3): p. 214-232.
16. Yoganathan, A.P., *Fluid mechanics of aortic stenosis.* Eur Heart J, 1988. **9 Suppl E**: p. 13-7.
17. Balachandran, K., P. Sucosky, and A.P. Yoganathan, *Hemodynamics and mechanobiology of aortic valve inflammation and calcification.* Int J Inflam, 2011. **2011**: p. 263870.
18. Lindstrom, M., et al., *Global Burden of Cardiovascular Diseases and Risks Collaboration, 1990-2021.* J Am Coll Cardiol, 2022. **80**(25): p. 2372-2425.
19. Frostegård, J., *Immunity, atherosclerosis and cardiovascular disease.* BMC Medicine, 2013. **11**(1): p. 117.
20. Lusis, A.J., *Atherosclerosis.* Nature, 2000. **407**(6801): p. 233-241.

21. Stark, B., C. Johnson, and G.A. Roth, *GLOBAL PREVALENCE OF CORONARY ARTERY DISEASE: AN UPDATE FROM THE GLOBAL BURDEN OF DISEASE STUDY.* JACC, 2024. **83**(13_Supplement): p. 2320-2320.
22. Health, A.I.o. and Welfare, *Heart, stroke and vascular disease: Australian facts*. 2024, AIHW: Canberra.
23. Olin, J.W. and B.A. Sealove, *Peripheral artery disease: current insight into the disease and its diagnosis and management.* Mayo Clin Proc, 2010. **85**(7): p. 678-92.
24. Armstrong, E.J. and D.G. Armstrong, *Critical limb ischemia.* 2021. **26**(2): p. 228-231.
25. Tuttolomondo, A., et al., *Atherosclerosis as an inflammatory disease.* Curr Pharm Des, 2012. **18**(28): p. 4266-88.
26. Ridker, P.M., et al., *Inflammation, Aspirin, and the Risk of Cardiovascular Disease in Apparently Healthy Men.* New England Journal of Medicine, 1997. **336**(14): p. 973-979.
27. Ross, R., *Atherosclerosis — An Inflammatory Disease.* New England Journal of Medicine. **340**(2): p. 115-126.
28. Spagnoli, L.G., et al., *Role of Inflammation in Atherosclerosis.* Journal of Nuclear Medicine, 2007. **48**(11): p. 1800.
29. Andreotti, F., et al., *Inflammatory gene polymorphisms and ischaemic heart disease: review of population association studies.* Heart, 2002. **87**(2): p. 107.
30. Libby, P., *Interleukin-1 Beta as a Target for Atherosclerosis Therapy: Biological Basis of CANTOS and Beyond.* Journal of the American College of Cardiology, 2017. **70**(18): p. 2278-2289.
31. Bevilacqua, M.P., et al., *Interleukin-1 activation of vascular endothelium. Effects on procoagulant activity and leukocyte adhesion.* Am J Pathol, 1985. **121**(3): p. 394-403.
32. Osiecki, H., *The role of chronic inflammation in cardiovascular disease and its regulation by nutrients.* Altern Med Rev, 2004. **9**(1): p. 32-53.
33. Bobryshev, Y.V., et al., *Macrophages and Their Role in Atherosclerosis: Pathophysiology and Transcriptome Analysis.* BioMed Research International, 2016. **2016**(1): p. 9582430.
34. Hu, D., et al., *Vascular Smooth Muscle Cells Contribute to Atherosclerosis Immunity.* Frontiers in Immunology, 2019. **Volume 10 - 2019**.
35. Bentzon, J.F., et al., *Mechanisms of plaque formation and rupture.* Circ Res, 2014. **114**(12): p. 1852-66.
36. Carabello, B.A., *Introduction to Aortic Stenosis.* Circulation Research, 2013. **113**(2): p. 179-185.
37. Strange, G., et al., *Uncovering the treatable burden of severe aortic stenosis in Australia: current and future projections within an ageing population.* BMC Health Services Research, 2021. **21**(1): p. 790.
38. T, M., et al., *Our Hidden Ageing: Time to Listen to the Heart.* The Baker Heart and Diabetes Institute, 2021.
39. Adams, H.S.L., et al., *Contemporary review of severe aortic stenosis.* Intern Med J, 2019. **49**(3): p. 297-305.
40. Helske, S., et al., *Aortic valve stenosis: an active atheroinflammatory process.* Curr Opin Lipidol, 2007. **18**(5): p. 483-91.
41. Raddatz, M.A., et al., *Macrophages Promote Aortic Valve Cell Calcification and Alter STAT3 Splicing.* Arteriosclerosis, Thrombosis, and Vascular Biology, 2020. **40**(6): p. e153-e165.
42. Erkhem-Ochir, B., et al., *Inflammatory and immune checkpoint markers are associated with the severity of aortic stenosis.* JTCVS Open, 2021. **5**: p. 1-12.

43. Shu, L., et al., *Oxidative stress and valvular endothelial cells in aortic valve calcification.* Biomedicine & Pharmacotherapy, 2023. **163**: p. 114775.
44. Trimaille, A., et al., *Aortic stenosis and the haemostatic system.* Cardiovascular Research, 2022. **119**(6): p. 1310-1323.
45. Otto, C.M., et al., *Characterization of the early lesion of 'degenerative' valvular aortic stenosis. Histological and immunohistochemical studies.* 1994. **90**(2): p. 844-853.
46. Lim, M.S., et al., *Characteristics of Bicuspid Aortic Valve Disease and Stenosis: The National Echo Database of Australia.* Journal of the American Heart Association, 2021. **10**(17): p. e020785.
47. Olsson, M., J. Thyberg, and J. Nilsson, *Presence of Oxidized Low Density Lipoprotein in Nonrheumatic Stenotic Aortic Valves.* Arteriosclerosis, Thrombosis, and Vascular Biology, 1999. **19**(5): p. 1218-1222.
48. Aikawa, E., et al., *Dynamic and reversible changes of interstitial cell phenotype during remodeling of cardiac valves.* The Journal of heart valve disease, 2004. **13**: p. 841-7.
49. Leopold, J.A., *Cellular Mechanisms of Aortic Valve Calcification.* Circulation: Cardiovascular Interventions, 2012. **5**(4): p. 605-614.
50. Labib, H.s.A., et al., *Effect of minimally invasive cardiac surgery compared with conventional surgery on post-operative physical activity and rehabilitation in patients with valvular heart disease.* Egyptian Rheumatology and Rehabilitation, 2023. **50**(1): p. 5.
51. Di Bacco, L., A. Miceli, and M.J.J.o.T.D. Glauber, *Minimally invasive aortic valve surgery.* Journal of Thoracic Disease, 2021. **13**(3): p. 1945-1959.
52. Grüntzig, A., *TRANSLUMINAL DILATATION OF CORONARY-ARTERY STENOSIS.* The Lancet, 1978. **311**(8058): p. 263.
53. Cribier, A., et al., *Percutaneous Transcatheter Implantation of an Aortic Valve Prosthesis for Calcific Aortic Stenosis.* Circulation, 2002. **106**(24): p. 3006-3008.
54. *Endovascular versus surgical treatment in patients with carotid stenosis in the Carotid and Vertebral Artery Transluminal Angioplasty Study (CAVATAS): a randomised trial.* The Lancet, 2001. **357**(9270): p. 1729-1737.
55. Nichols, A.B., et al., *Importance of balloon size in coronary angioplasty.* Journal of the American College of Cardiology, 1989. **13**(5): p. 1094-1100.
56. Muramatsu, T., et al., *Clinical expert consensus document on drug-coated balloon for coronary artery disease from the Japanese Association of Cardiovascular Intervention and Therapeutics.* Cardiovascular Intervention and Therapeutics, 2023. **38**(2): p. 166-176.
57. Rockley, M., et al., *Prolonged versus brief balloon inflation during arterial angioplasty for de novo atherosclerotic disease: a systematic review and meta-analysis.* CVIR Endovascular, 2019. **2**(1): p. 29.
58. Yetgin, T., et al., *Impact of multiple balloon inflations during primary percutaneous coronary intervention on infarct size and long-term clinical outcomes in ST-segment elevation myocardial infarction: real-world postconditioning.* Basic Research in Cardiology, 2014. **109**(2): p. 403.
59. Brandt, M.C., et al., *Same-day discharge after percutaneous coronary procedures—Consensus statement of the working group of interventional cardiology (AGIK) of the Austrian Society of Cardiology.* Wiener klinische Wochenschrift, 2024. **136**(3): p. 61-74.
60. Wolfe, M.W., et al., *Length of Hospital Stay and Complications After Percutaneous Transluminal Coronary Angioplasty.* Circulation, 1995. **92**(3): p. 311-319.
61. Mendes, M., *Is There a Role for Cardiac Rehabilitation After Coronary Artery Bypass Grafting?* Circulation, 2016. **133**(24): p. 2538-2543.

62. Rensing, B.J., et al., *Quantitative angiographic assessment of elastic recoil after percutaneous transluminal coronary angioplasty.* The American Journal of Cardiology, 1990. **66**(15): p. 1039-1044.
63. Sigwart, U., et al., *Intravascular Stents to Prevent Occlusion and Re-Stenosis after Transluminal Angioplasty.* The New England Journal of Medicine, 1987. **316**(12): p. 701-706.
64. Schatz, R.A., et al., *Clinical experience with the Palmaz-Schatz coronary stent. Initial results of a multicenter study.* Circulation, 1991. **83**(1): p. 148-161.
65. Dyet, J.F., et al., *Mechanical properties of metallic stents: How do these properties influence the choice of stent for specific lesions?* CardioVascular and Interventional Radiology, 2000. **23**(1): p. 47-54.
66. Schmidt, T. and J.D. Abbott *Coronary Stents: History, Design, and Construction*. Journal of Clinical Medicine, 2018. **7**, DOI: 10.3390/jcm7060126.
67. Duerig, T.W. and M. Wholey, *A comparison of balloon- and self-expanding stents.* Minimally Invasive Therapy & Allied Technologies, 2002. **11**(4): p. 173-178.
68. *Stenting for peripheral artery disease of the lower extremities: an evidence-based analysis.* Ont Health Technol Assess Ser, 2010. **10**(18): p. 1-88.
69. Boskovski, M.T. and T.G. Gleason, *Current Therapeutic Options in Aortic Stenosis.* Circulation Research, 2021. **128**(9): p. 1398-1417.
70. Thourani, V.H., et al., *Outcomes of Surgical Aortic Valve Replacement in High-Risk Patients: A Multiinstitutional Study.* The Annals of Thoracic Surgery, 2011. **91**(1): p. 49-56.
71. Cribier, A., et al., *PERCUTANEOUS TRANSLUMINAL VALVULOPLASTY OF ACQUIRED AORTIC STENOSIS IN ELDERLY PATIENTS: AN ALTERNATIVE TO VALVE REPLACEMENT?* The Lancet, 1986. **327**(8472): p. 63-67.
72. Andersen, H.R., L.L. Knudsen, and J.M. Hasenkam, *Transluminal implantation of artificial heart valves. Description of a new expandable aortic valve and initial results with implantation by catheter technique in closed chest pigs.* European Heart Journal, 1992. **13**(5): p. 704-708.
73. Rana, M., *Aortic Valve Stenosis: Diagnostic Approaches and Recommendations of the 2021 ESC/EACTS Guidelines for the Management of Valvular Heart Disease -A Review of the Literature.* Cardiol Cardiovasc Med, 2022. **6**(3): p. 315-324.
74. Wang, G., et al., *Comparison of rehabilitation outcomes for transcatheter versus surgical aortic valve replacement as redo procedure in patients with previous cardiac surgery: Evidence based on 11 observational studies.* Medicine (Baltimore), 2021. **100**(45): p. e27657.
75. Koren, O., et al., *The safety of early discharge following transfemoral transcatheter aortic valve replacement under general anesthesia.* Frontiers in Cardiovascular Medicine, 2022. **9**.
76. Adams, D.H., et al., *Transcatheter Aortic-Valve Replacement with a Self-Expanding Prosthesis.* The New England Journal of Medicine, 2014. **370**(19): p. 1790-1798.
77. Smith Craig, R., et al., *Transcatheter versus Surgical Aortic-Valve Replacement in High-Risk Patients.* New England Journal of Medicine. **364**(23): p. 2187-2198.
78. Nishimura, R.A., et al., *2017 AHA/ACC Focused Update of the 2014 AHA/ACC Guideline for the Management of Patients With Valvular Heart Disease: A Report of the American College of Cardiology/American Heart Association Task Force on Clinical Practice Guidelines.* Circulation, 2017. **135**(25): p. e1159-e1195.
79. Makkar Raj, R., et al., *Five-Year Outcomes of Transcatheter or Surgical Aortic-Valve Replacement.* New England Journal of Medicine, 2020. **382**(9): p. 799-809.

80. Van Mieghem, N.M., et al., *Self-expanding Transcatheter vs Surgical Aortic Valve Replacement in Intermediate-Risk Patients: 5-Year Outcomes of the SURTAVI Randomized Clinical Trial.* JAMA Cardiology, 2022. **7**(10): p. 1000-1008.
81. Baumgartner, H., et al., *2017 ESC/EACTS Guidelines for the management of valvular heart disease.* Eur Heart J, 2017. **38**(36): p. 2739-2791.
82. Forrest John, K., et al., *5-Year Outcomes After Transcatheter or Surgical Aortic Valve Replacement in Low-Risk Patients With Aortic Stenosis.* JACC, 2025. **85**(15): p. 1523-1532.
83. Mack Michael, J., et al., *Transcatheter Aortic-Valve Replacement in Low-Risk Patients at Five Years.* New England Journal of Medicine, 2023. **389**(21): p. 1949-1960.
84. Otto, C.M., et al., *2020 ACC/AHA Guideline for the Management of Patients With Valvular Heart Disease: A Report of the American College of Cardiology/American Heart Association Joint Committee on Clinical Practice Guidelines.* Circulation, 2021. **143**(5): p. e72-e227.
85. Shlofmitz, E., M. Iantorno, and R. Waksman, *Restenosis of Drug-Eluting Stents.* Circulation: Cardiovascular Interventions. **12**(8): p. e007023.
86. Kornowski, R., et al., *In-Stent Restenosis: Contributions of Inflammatory Responses and Arterial Injury to Neointimal Hyperplasia.* Journal of the American College of Cardiology, 1998. **31**(1): p. 224-230.
87. Welt, F.G.P. and C. Rogers, *Inflammation and Restenosis in the Stent Era.* Arteriosclerosis, Thrombosis, and Vascular Biology, 2002. **22**(11): p. 1769-1776.
88. Strauss, B.H., et al., *In Vivo Collagen Turnover Following Experimental Balloon Angioplasty Injury and the Role of Matrix Metalloproteinases.* Circulation Research, 1996. **79**(3): p. 541-550.
89. Scott, N.A., et al., *Identification of a Potential Role for the Adventitia in Vascular Lesion Formation After Balloon Overstretch Injury of Porcine Coronary Arteries.* Circulation, 1996. **93**(12): p. 2178-2187.
90. Sartore, S., et al., *Contribution of Adventitial Fibroblasts to Neointima Formation and Vascular Remodeling.* Circulation Research, 2001. **89**(12): p. 1111-1121.
91. Siow, R.C.M., C.M. Mallawaarachchi, and P.L. Weissberg, *Migration of adventitial myofibroblasts following vascular balloon injury: insights from in vivo gene transfer to rat carotid arteries.* Cardiovascular Research, 2003. **59**(1): p. 212-221.
92. Thyregod, H.G.H., et al., *Transcatheter or surgical aortic valve implantation: 10-year outcomes of the NOTION trial.* European Heart Journal, 2024. **45**(13): p. 1116-1124.
93. Capodanno, D., et al., *Standardized definitions of structural deterioration and valve failure in assessing long-term durability of transcatheter and surgical aortic bioprosthetic valves: a consensus statement from the European Association of Percutaneous Cardiovascular Interventions (EAPCI) endorsed by the European Society of Cardiology (ESC) and the European Association for Cardio-Thoracic Surgery (EACTS).* European Heart Journal, 2017. **38**(45): p. 3382-3390.
94. Kostyunin, A.E., et al., *Degeneration of Bioprosthetic Heart Valves: Update 2020.* Journal of the American Heart Association, 2020. **9**(19): p. e018506.
95. Sellers, S.L., et al., *Transcatheter Aortic Heart Valves: Histological Analysis Providing Insight to Leaflet Thickening and Structural Valve Degeneration.* JACC: Cardiovascular Imaging, 2019. **12**(1): p. 135-145.
96. Teshima, H., et al., *Obstruction of st jude medical valves in the aortic position: histology and immunohistochemistry of pannus.* The Journal of Thoracic and Cardiovascular Surgery, 2003. **126**(2): p. 401-407.
97. Simionescu, D.T., *Prevention of calcification in bioprosthetic heart valves: challenges and perspectives.* Expert Opinion on Biological Therapy, 2004. **4**(12): p. 1971-1985.

98. Nair, V., et al., *Characterizing the inflammatory reaction in explanted Medtronic Freestyle stentless porcine aortic bioprosthesis over a 6-year period.* Cardiovascular Pathology, 2012. **21**(3): p. 158-168.
99. Chong, B., et al., *Global burden of cardiovascular diseases: projections from 2025 to 2050.* European Journal of Preventive Cardiology, 2024. **32**(11): p. 1001-1015.
100. Karangelis, D., et al., *Minimally invasive cardiac surgery: in the pursuit to treat more and hurt less.* Journal of Thoracic Disease, 2021. **13**(11): p. 6209-6213.
101. Williams, D.F., *On the mechanisms of biocompatibility.* Biomaterials, 2008. **29**(20): p. 2941-2953.
102. Adhami, M., et al., *Drug loaded implantable devices to treat cardiovascular disease.* Expert Opinion on Drug Delivery, 2023. **20**(4): p. 507-522.
103. van Beusekom, H.M.M., et al., *Drug-eluting stents show delayed healing: paclitaxel more pronounced than sirolimus.* European Heart Journal, 2007. **28**(8): p. 974-979.
104. Miura, K., H. Nakaya, and Y. Kobayashi, *Experimental assessment of effects of antiproliferative drugs of drug-eluting stents on endothelial cells.* Cardiovascular Revascularization Medicine, 2015. **16**(6): p. 344-347.
105. Gallo, R., et al., *Inhibition of Intimal Thickening After Balloon Angioplasty in Porcine Coronary Arteries by Targeting Regulators of the Cell Cycle.* Circulation, 1999. **99**(16): p. 2164-2170.
106. Sousa, J.E., et al., *Sustained Suppression of Neointimal Proliferation by Sirolimus-Eluting Stents.* Circulation, 2001. **104**(17): p. 2007-2011.
107. Scheller, B., et al., *Paclitaxel Balloon Coating, a Novel Method for Prevention and Therapy of Restenosis.* Circulation, 2004. **110**(7): p. 810-814.
108. Grube, E., et al., *TAXUS I.* Circulation, 2003. **107**(1): p. 38-42.
109. Morice, M.-C., et al., *A Randomized Comparison of a Sirolimus-Eluting Stent with a Standard Stent for Coronary Revascularization.* New England Journal of Medicine, 2002. **346**(23): p. 1773-1780.
110. Tepe, G., et al., *5-Year Outcomes of Drug-Coated Balloons for Peripheral Artery In-Stent Restenosis, Long Lesions, and CTOs.* JACC: Cardiovascular Interventions, 2023. **16**(9): p. 1065-1078.
111. Katsanos, K., et al., *Risk of Death Following Application of Paclitaxel-Coated Balloons and Stents in the Femoropopliteal Artery of the Leg: A Systematic Review and Meta-Analysis of Randomized Controlled Trials.* Journal of the American Heart Association, 2018. **7**(24): p. e011245.
112. Katsanos, K., et al., *Editor's Choice - Risk of Major Amputation Following Application of Paclitaxel Coated Balloons in the Lower Limb Arteries: A Systematic Review and Meta-Analysis of Randomised Controlled Trials.* Eur J Vasc Endovasc Surg, 2022. **63**(1): p. 60-71.
113. Nordanstig, J., et al., *Paclitaxel-coated versus uncoated devices for infrainguinal endovascular revascularisation in patients with intermittent claudication (SWEDEPAD 2): a multicentre, participant-masked, registry-based, randomised controlled trial.* The Lancet, 2025. **406**(10508): p. 1115-1127.
114. Coutinho, A.E. and K.E. Chapman, *The anti-inflammatory and immunosuppressive effects of glucocorticoids, recent developments and mechanistic insights.* Molecular and Cellular Endocrinology, 2011. **335**(1): p. 2-13.
115. Hoffmann, R., et al., *Evaluation of a high-dose dexamethasone-eluting stent.* The American Journal of Cardiology, 2004. **94**(2): p. 193-195.
116. Pires, N.M.M., et al., *Histopathologic alterations following local delivery of dexamethasone to inhibit restenosis in murine arteries.* Cardiovascular Research, 2005. **68**(3): p. 415-424.

117. Yu, T., et al., *A versatile drug-controlled release polymer brush hybrid non-glutaraldehyde bioprosthetic heart valves with enhanced anti-inflammatory, anticoagulant and anti-calcification properties, and superior mechanical performance.* Biomaterials, 2023. **296**: p. 122070.
118. Kamann, S., et al. *Bare Metal Stents on Resveratrol-Coated Balloons in Porcine Coronary and Peripheral Arteries*. International Journal of Molecular Sciences, 2021. **22**, DOI: 10.3390/ijms222313099.
119. Hu, S., et al., *Exosome-eluting stents for vascular healing after ischaemic injury.* Nature Biomedical Engineering, 2021. **5**(10): p. 1174-1188.
120. Tu, Q., et al., *Spatiotemporal dual-delivery of therapeutic gas and growth factor for prevention of vascular stent thrombosis and restenosis.* Applied Materials Today, 2020. **19**: p. 100546.
121. Li, P., et al., *Bilayer vascular grafts with on-demand NO and H2S release capabilities.* Bioactive Materials, 2024. **31**: p. 38-52.
122. Gao, Y., et al., *Anti-inflammatory itaconate-loaded, cell-adhesive peptide-conjugated artificial small diameter vascular grafts for blood vessel regeneration.* Acta Biomaterialia, 2025.
123. Grant, A.J., et al., *Selective NLRP3 Inflammasome Inhibitor MCC950 Suppresses Inflammation and Facilitates Healing in Vascular Materials.* Advanced Science, 2023. **10**(20): p. 2300521.
124. Li, F., et al., *Vascular restenosis reduction with platelet membrane coated nanoparticle directed M2 macrophage polarization.* iScience, 2022. **25**(10): p. 105147.
125. Tan Richard, P., et al., *Bioactive Materials Facilitating Targeted Local Modulation of Inflammation.* JACC: Basic to Translational Science, 2019. **4**(1): p. 56-71.
126. Gray, W.A., et al., *A polymer-coated, paclitaxel-eluting stent (Eluvia) versus a polymer-free, paclitaxel-coated stent (Zilver PTX) for endovascular femoropopliteal intervention (IMPERIAL): a randomised, non-inferiority trial.* The Lancet, 2018. **392**(10157): p. 1541-1551.
127. Ding, K., et al., *Small diameter expanded polytetrafluoroethylene vascular graft with differentiated inner and outer biomacromolecules for collaborative endothelialization, anti-thrombogenicity and anti-inflammation.* Colloids and Surfaces B: Biointerfaces, 2023. **229**: p. 113449.
128. Gao, F., et al., *Layer-by-layer deposition of bioactive layers on magnesium alloy stent materials to improve corrosion resistance and biocompatibility.* Bioactive Materials, 2020. **5**(3): p. 611-623.
129. Wen, L., et al., *Vascular stent with immobilized anti-inflammatory chemerin 15 peptides mitigates neointimal hyperplasia and accelerates vascular healing.* Acta Biomaterialia, 2024. **179**: p. 371-384.
130. Wu, H., et al., *A drug-free cardiovascular stent functionalized with tailored collagen supports in-situ healing of vascular tissues.* Nature Communications, 2024. **15**(1): p. 735.
131. Phillips, B., et al., *The preparation of PLGA coating on nitinol wire for vascular stent applications.* Journal of Coatings Technology and Research, 2025. **22**(4): p. 1451-1459.
132. Udrițe, A.S., et al. *Coatings for Cardiovascular Stents—An Up-to-Date Review*. International Journal of Molecular Sciences, 2024. **25**, DOI: 10.3390/ijms25021078.
133. Tang, K., et al., *Flexible coatings based on hydrogel to enhance the biointerface of biomedical implants.* Advances in Colloid and Interface Science, 2025. **335**: p. 103358.
134. Huang, K., et al., *Integrated hydrogel of fucoidan and rhCol III for bioprosthetic heart valves to promote the antithrombosis, anti-inflammatory, and anti-calcification properties.* Composites Part B: Engineering, 2025. **298**: p. 112396.

135. Yang, F., G. Guo, and Y. Wang, *Inflammation-triggered dual release of nitroxide radical and growth factor from heparin mimicking hydrogel-tissue composite as cardiovascular implants for anti-coagulation, endothelialization, anti-inflammation, and anti-calcification.* Biomaterials, 2022. **289**: p. 121761.
136. Zhou, M., et al., *Passivated hydrogel interface: Armor against foreign body response and inflammation in small-diameter vascular grafts.* Biomaterials, 2025. **317**: p. 123010.
137. Peng, P., et al., *A self-sacrificing anti-inflammatory coating promotes simultaneous cardiovascular repair and reendothelialization of implanted devices.* Bioactive Materials, 2025. **47**: p. 502-512.
138. Moura, D., et al., *Long-term in vivo degradation and biocompatibility of degradable pHEMA hydrogels containing graphene oxide.* Acta Biomaterialia, 2024. **173**: p. 351-364.
139. Chen, Y., et al., *A tough nitric oxide-eluting hydrogel coating suppresses neointimal hyperplasia on vascular stent.* Nature Communications, 2021. **12**(1): p. 7079.
140. Li, J., et al., *Facile engineering of interactive double network hydrogels for heart valve regeneration.* Nature Communications, 2024. **15**(1): p. 7462.
141. Ahmad Wan Azman, W., et al., *Treatment of Coronary De Novo Lesions by a Sirolimus- or Paclitaxel-Coated Balloon.* JACC: Cardiovascular Interventions, 2022. **15**(7): p. 770-779.
142. Kawai, K., et al., *Efficacy and Safety of Dual Paclitaxel and Sirolimus Nanoparticle-Coated Balloon.* JACC: Basic to Translational Science, 2024. **9**(6): p. 774-789.
143. Zhang, X., et al., *Robust genome editing in adult vascular endothelium by nanoparticle delivery of CRISPR-Cas9 plasmid DNA.* Cell Reports, 2022. **38**(1).
144. Zhu, Q., et al., *Microenvironment-responsive coating for vascular stents to regulate coagulation-inflammation interaction and promote vascular recovery.* Bioactive Materials, 2025. **48**: p. 443-457.
145. Hu, C., R. Luo, and Y. Wang, *Heart Valves Cross-Linked with Erythrocyte Membrane Drug-Loaded Nanoparticles as a Biomimetic Strategy for Anti-coagulation, Anti-inflammation, Anti-calcification, and Endothelialization.* ACS Applied Materials & Interfaces, 2020. **12**(37): p. 41113-41126.
146. Poulios, C., et al., *Bringing pathology to nanomedicine: a comparison of in vivo toxicity of polymeric nanoparticle carriers with and without chitosan coating.* Virchows Archiv, 2023. **483**(6): p. 775-786.
147. Hozayen, W.G., et al., *Cardiac and pulmonary toxicity of mesoporous silica nanoparticles is associated with excessive ROS production and redox imbalance in Wistar rats.* Biomedicine & Pharmacotherapy, 2019. **109**: p. 2527-2538.
148. Bamezai, S., et al., *Pro-efferocytic nanotherapies reduce vascular inflammation without inducing anemia in a large animal model of atherosclerosis.* Nature Communications, 2024. **15**(1): p. 8034.
149. Lawton, J.S., et al., *2021 ACC/AHA/SCAI Guideline for Coronary Artery Revascularization: A Report of the American College of Cardiology/American Heart Association Joint Committee on Clinical Practice Guidelines.* Circulation, 2022. **145**(3): p. e18-e114.
150. Vizgan, G., et al., *Integrating medicine, engineering and business to educate early-stage researchers in cardiovascular device development.* Nature Biotechnology, 2022. **40**(10): p. 1528-1529.
151. Salthouse, D., et al., *Interplay between biomaterials and the immune system: Challenges and opportunities in regenerative medicine.* Acta Biomaterialia, 2023. **155**: p. 1-18.

152. Kahn, J.K., et al., *Inflation pressure requirements during coronary angioplasty.* Catheterization and Cardiovascular Diagnosis, 1990. **21**(3): p. 144-147.
153. Trerotola, S.O., et al., *Prospective Study of Balloon Inflation Pressures and Other Technical Aspects of Hemodialysis Access Angioplasty.* Journal of Vascular and Interventional Radiology, 2005. **16**(12): p. 1613-1618.
154. Xia, T., et al., *Vascular endothelial cell injury: causes, molecular mechanisms, and treatments.* MedComm, 2025. **6**(2): p. e70057.
155. Chaabane, C., et al., *Biological responses in stented arteries.* Cardiovascular Research, 2013. **99**(2): p. 353-363.
156. Won, H., et al., *Optical coherence tomography derived cut-off value of uncovered stent struts to predict adverse clinical outcomes after drug-eluting stent implantation.* The International Journal of Cardiovascular Imaging, 2013. **29**(6): p. 1255-1263.
157. Aihara, K., et al., *Pathological evaluation of predictors for delayed endothelial coverage after currently available drug-eluting stent implantation in coronary arteries: Impact of lesions with acute and chronic coronary syndromes.* American Heart Journal, 2024. **277**: p. 114-124.
158. Ridker Paul, M., et al., *Antiinflammatory Therapy with Canakinumab for Atherosclerotic Disease.* New England Journal of Medicine. **377**(12): p. 1119-1131.
159. Nidorf Stefan, M., et al., *Colchicine in Patients with Chronic Coronary Disease.* New England Journal of Medicine, 2020. **383**(19): p. 1838-1847.
160. Philpott, A.C., et al., *Long-term outcomes of patients receiving drug-eluting stents.* Canadian Medical Association Journal, 2009. **180**(2): p. 167.
161. Busch, R., et al., *New stent surface materials: The impact of polymer-dependent interactions of human endothelial cells, smooth muscle cells, and platelets.* Acta Biomaterialia, 2014. **10**(2): p. 688-700.
162. Kamath, K.R., J.J. Barry, and K.M. Miller, *The Taxus™ drug-eluting stent: A new paradigm in controlled drug delivery.* Advanced Drug Delivery Reviews, 2006. **58**(3): p. 412-436.
163. Morice, M.-C., et al., *Long-Term Clinical Outcomes With Sirolimus-Eluting Coronary Stents.* JACC, 2007. **50**(14): p. 1299-1304.
164. Stone, G.W., et al., *One-Year Clinical Results With the Slow-Release, Polymer-Based, Paclitaxel-Eluting TAXUS Stent.* Circulation, 2004. **109**(16): p. 1942-1947.
165. Ellis, S.G., et al., *Long-Term Safety and Efficacy With Paclitaxel-Eluting Stents: 5-Year Final Results of the TAXUS IV Clinical Trial (TAXUS IV-SR: Treatment of De Novo Coronary Disease Using a Single Paclitaxel-Eluting Stent).* JACC: Cardiovascular Interventions, 2009. **2**(12): p. 1248-1259.
166. Roukoz, H., et al., *Comprehensive Meta-Analysis on Drug-Eluting Stents versus Bare-Metal Stents during Extended Follow-up.* The American Journal of Medicine, 2009. **122**(6): p. 581.e1-581.e10.
167. Wenaweser, P., et al., *Incidence and Correlates of Drug-Eluting Stent Thrombosis in Routine Clinical Practice: 4-Year Results From a Large 2-Institutional Cohort Study.* Journal of the American College of Cardiology, 2008. **52**(14): p. 1134-1140.
168. Perkins, L.E.L., et al., *XIENCE V™ Everolimus-Eluting Coronary Stent System: A Preclinical Assessment.* Journal of Interventional Cardiology, 2009. **22**(s1): p. S28-S40.
169. Udipi, K., et al., *The next generation Endeavor Resolute Stent: role of the BioLinx™ Polymer System.* EuroIntervention, 2007. **3**(1): p. 137-139.
170. Gada, H., et al., *5-Year Results of a Randomized Comparison of XIENCE V Everolimus-Eluting and TAXUS Paclitaxel-Eluting Stents.* JACC: Cardiovascular Interventions, 2013. **6**(12): p. 1263-1266.

171. Silber, S., et al., *Unrestricted randomised use of two new generation drug-eluting coronary stents: 2-year patient-related versus stent-related outcomes from the RESOLUTE All Comers trial.* The Lancet, 2011. **377**(9773): p. 1241-1247.
172. Yeh Robert, W., et al., *5-Year Safety and Efficacy of Resolute Zotarolimus-Eluting Stent.* JACC: Cardiovascular Interventions, 2017. **10**(3): p. 247-254.
173. Windecker, S., et al., *Biolimus-eluting stent with biodegradable polymer versus sirolimus-eluting stent with durable polymer for coronary revascularisation (LEADERS): a randomised non-inferiority trial.* The Lancet, 2008. **372**(9644): p. 1163-1173.
174. Kereiakes, D.J., et al., *Efficacy and Safety of a Novel Bioabsorbable Polymer-Coated, Everolimus-Eluting Coronary Stent.* Circulation: Cardiovascular Interventions, 2015. **8**(4): p. e002372.
175. Kim, H.-S., et al., *Durable Polymer Versus Biodegradable Polymer Drug-Eluting Stents After Percutaneous Coronary Intervention in Patients with Acute Coronary Syndrome.* Circulation, 2021. **143**(11): p. 1081-1091.
176. Khatri, M., et al., *Clinical Outcomes of Polymer-Free Versus Polymer-Coated Drug-Eluting Stents in Patients With Coronary Artery Disease: A Systematic Review and Meta-Analysis.* Cureus, 2023. **15**(4): p. e38215.
177. Kufner, S., et al., *10-Year Outcomes From a Randomized Trial of Polymer-Free Versus Durable Polymer Drug-Eluting Coronary Stents.* Journal of the American College of Cardiology, 2020. **76**(2): p. 146-158.
178. Park, K.E., et al., *One-year Outcomes of XIENCE Skypoint 48-mm Drug-Eluting Stents in Long Coronary Lesions: The SPIRIT 48 Trial.* Journal of the Society for Cardiovascular Angiography & Interventions, 2023. **2**(4): p. 101001.
179. Price, M.J., et al., *Safety and efficacy of the next generation Resolute Onyx zotarolimus-eluting stent: Primary outcome of the RESOLUTE ONYX core trial.* Catheterization and Cardiovascular Interventions, 2018. **92**(2): p. 253-259.
180. Yoon, C.-H., et al., *BioMatrix Versus Orsiro Stents for Coronary Artery Disease: A Multicenter, Randomized, Open-Label Study.* Circulation: Cardiovascular Interventions, 2023. **16**(1): p. e012307.
181. Varcoe Ramon, L., et al., *Drug-Eluting Resorbable Scaffold versus Angioplasty for Infrapopliteal Artery Disease.* New England Journal of Medicine, 2024. **390**(1): p. 9-19.
182. Varcoe, R.L., et al., *Evaluation of an Infrapopliteal Drug-Eluting Resorbable Scaffold: Design Methodology for the LIFE-BTK Randomized Controlled Trial.* Journal of the Society for Cardiovascular Angiography & Interventions, 2023. **2**(4): p. 100964.
183. Stone Gregg, W., et al., *5-Year Outcomes After Bioresorbable Coronary Scaffolds Implanted With Improved Technique.* JACC, 2023. **82**(3): p. 183-195.
184. Haude, M., et al., *Quantitative analysis of elastic recoil after balloon angioplasty and after intracoronary implantation of balloon-expandable Palmaz-Schatz stents.* JACC, 1993. **21**(1): p. 26-34.
185. Sadeghi-Oroumiyeh, A., H. Valizadeh, and P. Zakeri-Milani, *Determination of Paclitaxel Solubility and Stability in the Presence of Injectable Excipients.* Pharmaceutical Chemistry Journal, 2021. **55**(9): p. 983-987.
186. Radke, P., et al., *Vascular effects of paclitaxel following drug-eluting balloon angioplasty in a porcine coronary model: the importance of excipient.* EuroIntervention, 2011. **7**(6): p. 730-737.
187. Scheller, B., et al., *Addition of paclitaxel to contrast media prevents restenosis after coronary stent implantation.* JACC, 2003. **42**(8): p. 1415-1420.

188. Scheller, B., et al., *Treatment of Coronary In-Stent Restenosis with a Paclitaxel-Coated Balloon Catheter.* New England Journal of Medicine. **355**(20): p. 2113-2124.
189. Werk, M., et al., *Inhibition of Restenosis in Femoropopliteal Arteries.* Circulation, 2008. **118**(13): p. 1358-1365.
190. Peterson, S., et al., *IN.PACT™ Admiral™ drug-coated balloon: Durable, consistent and safe treatment for femoropopliteal peripheral artery disease.* Advanced Drug Delivery Reviews, 2017. **112**: p. 69-77.
191. Schneider, P.A., et al., *Treatment Effect of Drug-Coated Balloons Is Durable to 3 Years in the Femoropopliteal Arteries.* Circulation: Cardiovascular Interventions, 2018. **11**(1): p. e005891.
192. Torii, S., et al., *IN.PACT™ Admiral™ drug-coated balloons in peripheral artery disease: current perspectives.* Medical Devices: Evidence and Research, 2019. **12**: p. 53-64.
193. Belkacemi, A., et al., *Drug-eluting Balloons in Coronary Artery Disease - Current and Future Perspectives.* Interventional Cardiology, 2011.
194. Pósa, A., et al., *Optimization of drug-eluting balloon use for safety and efficacy: Evaluation of the 2nd generation paclitaxel-eluting DIOR-balloon in porcine coronary arteries.* Catheterization and Cardiovascular Interventions, 2010. **76**(3): p. 395-403.
195. Kawai, K., et al., *Vascular Response, Downstream Effect, and Pharmacokinetics After Sirolimus- and Paclitaxel-Coated Balloons in Porcine Coronary Arteries.* Catheterization and Cardiovascular Interventions, 2025. **105**(6): p. 1434-1444.
196. Böhme, T., et al., *The Selution SLR™ drug-eluting Balloon System for the Treatment of Symptomatic Femoropopliteal Lesions.* Future Cardiology, 2021. **17**(2): p. 257-267.
197. Zeller, T., et al., *Six-Month Outcomes From the First-in-Human, Single-Arm SELUTION Sustained-Limus-Release Drug-Eluting Balloon Trial in Femoropopliteal Lesions.* Journal of Endovascular Therapy, 2020. **27**(5): p. 683-690.
198. Lemos, P.A., et al., *Emerging technologies: polymer-free phospholipid encapsulated sirolimus nanocarriers for the controlled release of drug from a stent-plus-balloon or a stand-alone balloon catheter.* EuroIntervention, 2013. **9**(1): p. 148-156.
199. Ninomiya, K., et al., *A Prospective Randomized Trial Comparing Sirolimus-Coated Balloon With Paclitaxel-Coated Balloon in De Novo Small Vessels.* JACC: Cardiovascular Interventions, 2023. **16**(23): p. 2884-2896.
200. Islam, S., et al., *Advances in nanoparticles in targeted drug delivery–A review.* Results in Surfaces and Interfaces, 2025. **19**: p. 100529.
201. Thompson, A.J. and O. Eniola-Adefeso, *Dense nanoparticles exhibit enhanced vascular wall targeting over neutrally buoyant nanoparticles in human blood flow.* Acta Biomaterialia, 2015. **21**: p. 99-108.
202. Hussein Kamareddine, M., et al., *Organic Nanoparticles as Drug Delivery Systems and Their Potential Role in the Treatment of Chronic Myeloid Leukemia.* Technology in Cancer Research & Treatment, 2019. **18**: p. 1533033819879902.
203. Tenchov, R., et al., *Lipid Nanoparticles─From Liposomes to mRNA Vaccine Delivery, a Landscape of Research Diversity and Advancement.* ACS Nano, 2021. **15**(11): p. 16982-17015.
204. Yin, X., et al., *Tissue factor pathway inhibitor gene delivery using HVJ-AVE liposomes markedly reduces restenosis in atherosclerotic arteries.* Cardiovascular Research, 2002. **56**(3): p. 454-463.
205. Westedt, U., et al., *Poly(vinyl alcohol)-graft-poly(lactide-co-glycolide) nanoparticles for local delivery of paclitaxel for restenosis treatment.* Journal of Controlled Release, 2007. **119**(1): p. 41-51.

206. Ji, K., Y. Zhang, and D. Huang, *The Intervention of Nano-targeted Drugs & Angioplastryin Treatment and Prevention of Vascular Restenosis and its Influence on Monocyte Chemotactic Protein-1 in Lower Extremity Angiopathy.* Cellular and Molecular Biology, 2022. **68**(3): p. 347-355.
207. Craciun, I., et al., *Nanoparticle coatings for controlled release of quercetin from an angioplasty balloon.* PLOS ONE, 2022. **17**(8): p. e0268307.
208. Arias, L.S., et al. *Iron Oxide Nanoparticles for Biomedical Applications: A Perspective on Synthesis, Drugs, Antimicrobial Activity, and Toxicity*. Antibiotics, 2018. **7**, DOI: 10.3390/antibiotics7020046.
209. Meyers, M.W., et al., *Systemically administered collagen-targeted gold nanoparticles bind to arterial injury following vascular interventions.* Physiological Reports, 2017. **5**(4): p. e13128.
210. Kim, M., et al., *Comparison of in vivo targeting ability between cRGD and collagen-targeting peptide conjugated nano-carriers for atherosclerosis.* Journal of Controlled Release, 2018. **269**: p. 337-346.
211. Wei, X., et al., *Honokiol-mesoporous Silica Nanoparticles Inhibit Vascular Restenosis via the Suppression of TGF-β Signaling Pathway.* International Journal of Nanomedicine, 2020. **15**: p. 5239-5252.
212. Zhu, M.-T., et al., *Comparative study of pulmonary responses to nano- and submicron-sized ferric oxide in rats.* Toxicology, 2008. **247**(2): p. 102-111.
213. Bao, G., S. Mitragotri, and S. Tong, *Multifunctional Nanoparticles for Drug Delivery and Molecular Imaging.* Annual Review of Biomedical Engineering, 2013. **15**(Volume 15, 2013): p. 253-282.
214. Dokka, S., et al., *Oxygen Radical-Mediated Pulmonary Toxicity Induced by Some Cationic Liposomes.* Pharmaceutical Research, 2000. **17**(5): p. 521-525.
215. Lv, H., et al., *Toxicity of cationic lipids and cationic polymers in gene delivery.* Journal of Controlled Release, 2006. **114**(1): p. 100-109.
216. Xiong, S., et al., *Size influences the cytotoxicity of poly (lactic-co-glycolic acid) (PLGA) and titanium dioxide (TiO2) nanoparticles.* Archives of Toxicology, 2013. **87**(6): p. 1075-1086.
217. Feng, L., et al., *Silica nanoparticles trigger the vascular endothelial dysfunction and prethrombotic state via miR-451 directly regulating the IL6R signaling pathway.* Particle and Fibre Toxicology, 2019. **16**(1): p. 16.
218. Nemmar, A., et al., *Amorphous silica nanoparticles impair vascular homeostasis and induce systemic inflammation.* International Journal of Nanomedicine, 2014. **9**: p. 2779-89.
219. Ngo, W., et al., *Why nanoparticles prefer liver macrophage cell uptake in vivo.* Advanced Drug Delivery Reviews, 2022. **185**: p. 114238.
220. Semete, B., et al., *In vivo evaluation of the biodistribution and safety of PLGA nanoparticles as drug delivery systems.* Nanomedicine: Nanotechnology, Biology and Medicine, 2010. **6**(5): p. 662-671.
221. De Jong, W.H., et al., *Particle size-dependent organ distribution of gold nanoparticles after intravenous administration.* Biomaterials, 2008. **29**(12): p. 1912-1919.
222. Lin, X., et al., *Multifunctional theranostic nanosystems enabling photothermal-chemo combination therapy of triple-stimuli-responsive drug release with magnetic resonance imaging.* Biomaterials Science, 2020. **8**(7): p. 1875-1884.
223. Wang, J., et al., *A novel nanocomposite based on fluorescent turn-on gold nanostars for near-infrared photothermal therapy and self-theranostic caspase-3 imaging of glioblastoma tumor cell.* Colloids and Surfaces B: Biointerfaces, 2018. **170**: p. 303-311.

224. van der Valk, F.M., et al., *Prednisolone-containing liposomes accumulate in human atherosclerotic macrophages upon intravenous administration.* Nanomedicine: Nanotechnology, Biology and Medicine, 2015. **11**(5): p. 1039-1046.
225. Liu, F., et al., *Modulating the Activity of Protein Conjugated to Gold Nanoparticles by Site-Directed Orientation and Surface Density of Bound Protein.* ACS Applied Materials & Interfaces, 2015. **7**(6): p. 3717-3724.
226. Santos, M., et al., *Plasma Synthesis of Carbon-Based Nanocarriers for Linker-Free Immobilization of Bioactive Cargo.* ACS Applied Nano Materials, 2018. **1**(2): p. 580-594.
227. Janůšová, M., et al., *Insight into plasma polymerization with a significant contribution of etching to the deposition process.* Surface and Coatings Technology, 2025. **503**: p. 131962.
228. Rubel, M., et al., *Dust particles in controlled fusion devices: morphology, observations in the plasma and influence on the plasma performance.* Nuclear Fusion, 2001. **41**(8): p. 1087.
229. Santos, M., et al., *Substrate geometry modulates self-assembly and collection of plasma polymerized nanoparticles.* Communications Physics, 2019. **2**(1): p. 52.
230. Michael, P., et al., *Plasma polymerized nanoparticles effectively deliver dual siRNA and drug therapy in vivo.* Scientific Reports, 2020. **10**(1): p. 12836.
231. Michael, P.L., et al. *Comprehensive Evaluation of the Toxicity and Biosafety of Plasma Polymerized Nanoparticles*. Nanomaterials, 2021. **11**, DOI: 10.3390/nano11051176.
232. Coll, R.C., et al., *MCC950 directly targets the NLRP3 ATP-hydrolysis motif for inflammasome inhibition.* Nature Chemical Biology, 2019. **15**(6): p. 556-559.
233. Coll, R.C., et al., *A small-molecule inhibitor of the NLRP3 inflammasome for the treatment of inflammatory diseases.* Nature Medicine, 2015. **21**(3): p. 248-255.
234. van der Heijden, T., et al., *NLRP3 Inflammasome Inhibition by MCC950 Reduces Atherosclerotic Lesion Development in Apolipoprotein E–Deficient Mice—Brief Report.* Arteriosclerosis, Thrombosis, and Vascular Biology, 2017. **37**(8): p. 1457-1461.
235. Vande Walle, L., et al., *MCC950/CRID3 potently targets the NACHT domain of wild-type NLRP3 but not disease-associated mutants for inflammasome inhibition.* PLOS Biology, 2019. **17**(9): p. e3000354.
236. Grebe, A., F. Hoss, and E. Latz, *NLRP3 Inflammasome and the IL-1 Pathway in Atherosclerosis.* Circulation Research, 2018. **122**(12): p. 1722-1740.
237. Bai, B., et al., *NLRP3 inflammasome in endothelial dysfunction.* Cell Death & Disease, 2020. **11**(9): p. 776.
238. Kelley, N., et al. *The NLRP3 Inflammasome: An Overview of Mechanisms of Activation and Regulation*. International Journal of Molecular Sciences, 2019. **20**, DOI: 10.3390/ijms20133328.
239. Shi, J., et al., *Cleavage of GSDMD by inflammatory caspases determines pyroptotic cell death.* Nature, 2015. **526**(7575): p. 660-665.
240. Opp, M.R., E.M. Smith, and T.K. Hughes, *Interleukin-10 (cytokine synthesis inhibitory factor) acts in the central nervous system of rats to reduce sleep.* Journal of Neuroimmunology, 1995. **60**(1): p. 165-168.
241. Carlini, V., et al., *The multifaceted nature of IL-10: regulation, role in immunological homeostasis and its relevance to cancer, COVID-19 and post-COVID conditions.* Frontiers in Immunology, 2023. **14**: p. 1161067.
242. Branchett, W.J., M. Saraiva, and A. O'Garra, *Regulation of inflammation by Interleukin-10 in the intestinal and respiratory mucosa.* Current Opinion in Immunology, 2024. **91**: p. 102495.

243. Tan Richard, P., et al., *Macrophage Polarization as a Novel Therapeutic Target for Endovascular Intervention in Peripheral Artery Disease.* JACC: Basic to Translational Science, 2021. **6**(8): p. 693-704.
244. Riley, J.K., et al., *Interleukin-10 Receptor Signaling through the JAK-STAT Pathway: REQUIREMENT FOR TWO DISTINCT RECEPTOR-DERIVED SIGNALS FOR ANTI-INFLAMMATORY ACTION**. Journal of Biological Chemistry, 1999. **274**(23): p. 16513-16521.
245. Hutchins, A.P., D. Diez, and D. Miranda-Saavedra, *The IL-10/STAT3-mediated anti-inflammatory response: recent developments and future challenges.* Briefings in Functional Genomics, 2013. **12**(6): p. 489-498.
246. Strizova, Z., et al., *M1/M2 macrophages and their overlaps – myth or reality?* Clinical Science, 2023. **137**(15): p. 1067-1093.
247. Eefting, D., et al., *The effect of interleukin-10 knock-out and overexpression on neointima formation in hypercholesterolemic APOE*3-Leiden mice.* Atherosclerosis, 2007. **193**(2): p. 335-342.
248. Tan, R.P., et al., *Highly reproducible rat arterial injury model of neointimal hyperplasia.* PLOS ONE, 2023. **18**(8): p. e0290342.
249. Vázquez, S.M., et al., *Translational Development of a Zr-89-Labeled Inhibitor of Prostate-specific Membrane Antigen for PET Imaging in Prostate Cancer.* Molecular Imaging and Biology, 2022. **24**(1): p. 115-125.
250. Brandt, M., et al., *Radiolabelling of the octadentate chelators DFO* and oxoDFO* with zirconium-89 and gallium-68.* Journal of Biological Inorganic Chemistry, 2020. **25**(5): p. 789-796.
251. Li, N., et al., *A generic (89)Zr labeling method to quantify the in vivo pharmacokinetics of liposomal nanoparticles with positron emission tomography.* International Journal of Nanomedicine, 2017. **12**: p. 3281-3294.
252. Hoshyar, N., et al., *The Effect of Nanoparticle Size on In Vivo Pharmacokinetics and Cellular Interaction.* Nanomedicine, 2016. **11**(6): p. 673-692.
253. Wang, Y., et al., *Effect of physicochemical properties on in vivo fate of nanoparticle-based cancer immunotherapies.* Acta Pharmaceutica Sinica B, 2021. **11**(4): p. 886-902.
254. Jasinski, D.L., H. Li, and P. Guo, *The Effect of Size and Shape of RNA Nanoparticles on Biodistribution.* Molecular Therapy, 2018. **26**(3): p. 784-792.
255. Longmire, M., P.L. Choyke, and H. Kobayashi, *Clearance Properties of Nano-Sized Particles and Molecules as Imaging Agents: Considerations and Caveats.* Nanomedicine, 2008. **3**(5): p. 703-717.
256. Tsoi, K.M., et al., *Mechanism of hard-nanomaterial clearance by the liver.* Nature Materials, 2016. **15**(11): p. 1212-1221.
257. Zelepukin, I.V., K.G. Shevchenko, and S.M. Deyev, *Rediscovery of mononuclear phagocyte system blockade for nanoparticle drug delivery.* Nature Communications, 2024. **15**(1): p. 4366.
258. Gustafson, H.H., et al., *Nanoparticle uptake: The phagocyte problem.* Nano Today, 2015. **10**(4): p. 487-510.
259. Nishimori, H., et al., *Histological analysis of 70-nm silica particles-induced chronic toxicity in mice.* European Journal of Pharmaceutics and Biopharmaceutics, 2009. **72**(3): p. 626-629.
260. Missaoui, W.N., R.D. Arnold, and B.S. Cummings, *Toxicological status of nanoparticles: What we know and what we don't know.* Chemico-Biological Interactions, 2018. **295**: p. 1-12.
261. Syto, R., et al., *Structural and Biological Stability of the Human Interleukin 10 Homodimer.* Biochemistry, 1998. **37**(48): p. 16943-16951.

262. Nam, N.H. and N.H. Luong, *Chapter 7 - Nanoparticles: synthesis and applications*, in *Materials for Biomedical Engineering*, V. Grumezescu and A.M. Grumezescu, Editors. 2019, Elsevier. p. 211-240.
263. Trepanier, C.M., et al., *Synthesis, characterization, and surface modification of degradable polar hydrophobic ionic polyurethane nanoparticles for the delivery of therapeutics to vascular tissue.* Acta Biomaterialia, 2024. **188**: p. 184-196.
264. Lee, H.-I., et al. *A Multilayer Functionalized Drug-Eluting Balloon for Treatment of Coronary Artery Disease*. Pharmaceutics, 2021. **13**, DOI: 10.3390/pharmaceutics13050614.
265. Lombardo, D. and M.A. Kiselev *Methods of Liposomes Preparation: Formation and Control Factors of Versatile Nanocarriers for Biomedical and Nanomedicine Application*. Pharmaceutics, 2022. **14**, DOI: 10.3390/pharmaceutics14030543.
266. Amina, S.J. and B. Guo, *A Review on the Synthesis and Functionalization of Gold Nanoparticles as a Drug Delivery Vehicle.* International Journal of Nanomedicine, 2020. **15**: p. 9823-9857.
267. Siow, K.S., et al., *QCM-D and XPS study of protein adsorption on plasma polymers with sulfonate and phosphonate surface groups.* Colloids and Surfaces B: Biointerfaces, 2019. **173**: p. 447-453.
268. Casulleras, M., et al., *Albumin internalizes and inhibits endosomal TLR signaling in leukocytes from patients with decompensated cirrhosis.* Science Translational Medicine, 2020. **12**(566): p. eaax5135.
269. Anbalakan, K., et al., *Assessing the influence of atherosclerosis on drug coated balloon therapy using computational modelling.* European Journal of Pharmaceutics and Biopharmaceutics, 2021. **158**: p. 72-82.
270. Yin, Y.-j., et al., *Adhesive polyelectrolyte coating on PLGA particles prolongs drug retention to vessel lesion.* Journal of Controlled Release, 2025. **378**: p. 949-960.
271. Minshawi, F., et al., *The Generation of an Engineered Interleukin-10 Protein With Improved Stability and Biological Function.* Frontiers in Immunology, 2020. **11**: p. 1794.
272. Evans, C.E., M.L. Iruela-Arispe, and Y.-Y. Zhao, *Mechanisms of Endothelial Regeneration and Vascular Repair and Their Application to Regenerative Medicine.* The American Journal of Pathology, 2021. **191**(1): p. 52-65.
273. Matic, L., *Transcriptomic profiling of experimental arterial injury reveals new mechanisms and temporal dynamics in vascular healing response.* Atherosclerosis, 2020. **315**: p. e14.
274. Sarvepalli, S., et al. *A Review on the Stability Challenges of Advanced Biologic Therapeutics*. Pharmaceutics, 2025. **17**, 550 DOI: 10.3390/pharmaceutics17050550.
275. Kaarbø, M., et al., *Transcriptomic and proteomic profiling reveal immune and metabolic dysregulation in the colonic mucosa of people living with HIV with incomplete immune recovery.* Frontiers in Immunology, 2025. **16**.
276. Brown, J.M., et al., *Isolated aortic valve replacement in North America comprising 108,687 patients in 10 years: Changes in risks, valve types, and outcomes in the Society of Thoracic Surgeons National Database.* The Journal of Thoracic and Cardiovascular Surgery, 2009. **137**(1): p. 82-90.
277. Taghizadeh, B., et al., *Biomaterials in Valvular Heart Diseases.* Frontiers in Bioengineering and Biotechnology, 2020. **8**.
278. David, T., *How to Decide Between a Bioprosthetic and Mechanical Valve.* Canadian Journal of Cardiology, 2021. **37**(7): p. 1121-1123.
279. Jilaihawi, H., et al., *Systematic CT Methodology for the Evaluation of Subclinical Leaflet Thrombosis.* JACC: Cardiovascular Imaging, 2017. **10**(4): p. 461-470.

280. Morris, A.H., D.K. Stamer, and T.R. Kyriakides, *The host response to naturally-derived extracellular matrix biomaterials.* Seminars in Immunology, 2017. **29**: p. 72-91.
281. Latib, A., et al., *Treatment and Clinical Outcomes of Transcatheter Heart Valve Thrombosis.* Circulation: Cardiovascular Interventions, 2015. **8**(4): p. e001779.
282. Jose, J., et al., *Clinical Bioprosthetic Heart Valve Thrombosis After Transcatheter Aortic Valve Replacement: Incidence, Characteristics, and Treatment Outcomes.* JACC: Cardiovascular Interventions, 2017. **10**(7): p. 686-697.
283. Marchandot, B., et al., *Subclinical Leaflet Thrombosis and Subclinical Aortic Valve Complex Thrombosis in TAVR.* JACC: Advances, 2025. **4**(9): p. 102085.
284. Makki, N., et al., *A meta-analysis of reduced leaflet motion for surgical and transcatheter aortic valves: Relationship to cerebrovascular events and valve degeneration.* Cardiovascular Revascularization Medicine, 2018. **19**(7, Part B): p. 868-873.
285. De Backer, O., et al., *Reduced Leaflet Motion after Transcatheter Aortic-Valve Replacement.* New England Journal of Medicine, 2020. **382**(2): p. 130-139.
286. Collet, J.P., et al., *Apixaban vs. standard of care after transcatheter aortic valve implantation: the ATLANTIS trial.* European Heart Journal, 2022. **43**(29): p. 2783-2797.
287. Makkar, R. and T. Chakravarty, *Missing Pieces of the Transcatheter Aortic Valve Replacement Subclinical Leaflet Thrombosis Puzzle.* Circulation, 2022. **146**(6): p. 494-497.
288. Schoen, F.J. and R.J. Levy, *Tissue heart valves: Current challenges and future research perspectives.* Journal of Biomedical Materials Research, 1999. **47**(4): p. 439-465.
289. Siddiqui, R.F., J.R. Abraham, and J. Butany, *Bioprosthetic heart valves: modes of failure.* Histopathology, 2009. **55**(2): p. 135-144.
290. Kim, K.M., G.A. Herrera, and H.D. Battarbee, *Role of Glutaraldehyde in Calcification of Porcine Aortic Valve Fibroblasts.* The American Journal of Pathology, 1999. **154**(3): p. 843-852.
291. Snyder, Y. and S. Jana, *Strategies for development of decellularized heart valve scaffolds for tissue engineering.* Biomaterials, 2022. **288**: p. 121675.
292. Azhim, A., et al. *The use of sonication treatment to completely decellularize blood arteries: A pilot study*. in *2011 Annual International Conference of the IEEE Engineering in Medicine and Biology Society*. 2011.
293. Collatusso, C., et al., *Effect of SDS-based decelullarization in the prevention of calcification in glutaraldehyde-preserved bovine pericardium: study in rats.* Brazilian Journal of Cardiovascular Surgery, 2012. **27**(1): p. 88-96.
294. Li, N., et al., *Efficient decellularization for bovine pericardium with extracellular matrix preservation and good biocompatibility.* Interactive CardioVascular and Thoracic Surgery, 2018. **26**(5): p. 768-776.
295. Crapo, P.M., T.W. Gilbert, and S.F. Badylak, *An overview of tissue and whole organ decellularization processes.* Biomaterials, 2011. **32**(12): p. 3233-3243.
296. Strange, G., et al., *An evaluation of Admedus' tissue engineering process-treated (ADAPT) bovine pericardium patch (CardioCel) for the repair of cardiac and vascular defects.* Expert Review of Medical Devices, 2015. **12**(2): p. 135-141.
297. Kodali, S.K., et al., *Early safety and feasibility of a first-in-class biomimetic transcatheter aortic valve - DurAVR.* EuroIntervention, 2023. **19**(4): p. e352-e362.
298. Tingfei, X., et al., *Prevention of tissue calcification on bioprosthetic heart valve by using epoxy compounds: A study of calcification tests in vitro and in vivo.* Journal of Biomedical Materials Research, 1992. **26**(9): p. 1241-1251.

299. Yu, T., et al., *A bioprosthetic heart valve cross-linked by a non-glutaraldehyde reagent with improved biocompatibility, endothelialization, anti-coagulation and anti-calcification properties.* Journal of Materials Chemistry B, 2021. **9**(19): p. 4031-4038.
300. Hu, M., et al., *Dialdehyde xanthan gum and curcumin synergistically crosslinked bioprosthetic valve leaflets with anti-thrombotic, anti-inflammatory and anti-calcification properties.* Carbohydrate Polymers, 2023. **310**: p. 120724.
301. Liu, Y., et al., *The hybrid crosslinking method improved the stability and anti-calcification properties of the bioprosthetic heart valves.* 2022. **Volume 10 - 2022**.
302. Huang, X., et al., *Degeneration mechanisms and advancements in optimization for preparation and crosslinking strategy of pericardium-based bioprosthetic heart valves.* Acta Biomaterialia, 2025. **201**: p. 51-74.
303. Tod, T.J. and J.S. Dove, *The association of bound aldehyde content with bioprosthetic tissue calcification.* Journal of Materials Science: Materials in Medicine, 2015. **27**(1): p. 8.
304. Flameng, W., et al., *A randomized assessment of an advanced tissue preservation technology in the juvenile sheep model.* The Journal of Thoracic and Cardiovascular Surgery, 2015. **149**(1): p. 340-345.
305. Beaver, T., et al., *Seven-year outcomes following aortic valve replacement with a novel tissue bioprosthesis.* The Journal of Thoracic and Cardiovascular Surgery, 2024. **168**(3): p. 781-791.
306. Chen, W., F.J. Schoen, and R.J. Levy, *Mechanism of efficacy of 2-amino oleic acid for inhibition of calcification of glutaraldehyde-pretreated porcine bioprosthetic heart valves.* Circulation, 1994. **90**(1): p. 323-9.
307. Gott, J.P.M.D., et al., *Refinement of the Alpha Aminooleic Acid Bioprosthetic Valve Anticalcification Technique.* The Annals of Thoracic Surgery, 1997. **64**(1): p. 50-58.
308. Sabik, J.F., III, et al., *Seven-year outcomes after surgical aortic valve replacement with a stented bovine pericardial bioprosthesis in over 1100 patients: a prospective multicentre analysis.* European Journal of Cardio-Thoracic Surgery, 2025. **67**(1): p. ezae414.
309. Schoen, F.J., *Evolving Concepts of Cardiac Valve Dynamics.* Circulation, 2008. **118**(18): p. 1864-1880.
310. Butala, N.M., et al., *Applicability of Transcatheter Aortic Valve Replacement Trials to Real-World Clinical Practice: Findings From EXTEND-CoreValve.* JACC: Cardiovascular Interventions, 2021. **14**(19): p. 2112-2123.
311. Jhun, C.-S., et al., *Dynamics of Blood Flows in Aortic Stenosis: Mild, Moderate, and Severe.* ASAIO Journal, 2021. **67**(6).
312. Ashraf, H. and W.K. Freeman, *Echocardiographic Assessment of Prosthetic Valves.* Reviews in Cardiovascular Medicine, 2022. **23**(10).
313. Oveissi, F., et al., *Materials and manufacturing perspectives in engineering heart valves: a review.* Materials Today Bio, 2020. **5**: p. 100038.
314. Wen, S., et al., *Mechanisms and Drug Therapies of Bioprosthetic Heart Valve Calcification.* Frontiers in Pharmacology, 2022. **13**: p. 909801.
315. Wei, Y., et al., *A photo-triggered coating of prosthetic valve leaflet surface to realize antibacterial and thrombolysis on-demand.* Chemical Engineering Journal, 2024. **479**: p. 147438.
316. De Cock, L.J., et al., *Layer-by-Layer Incorporation of Growth Factors in Decellularized Aortic Heart Valve Leaflets.* Biomacromolecules, 2010. **11**(4): p. 1002-1008.

317. Huang, X., et al., *Hyaluronic Acid-Grafted Bioprosthetic Heart Valves Achieved by Copolymerization Exhibited Improved Anticalcification and Antithrombogenicity.* ACS Biomaterials Science & Engineering, 2022. **8**(8): p. 3399-3410.
318. Xu, Y., et al., *Development of transcatheter tissue-engineered heart valves with dual crosslinking and nitric oxide releasing decellularized matrix composites for in-situ regeneration.* Composites Part B: Engineering, 2025. **291**: p. 112048.
319. Mendoza-Novelo, B. and J.V. Cauich-Rodríguez, *The Effect of Surfactants, Crosslinking Agents and L-Cysteine on the Stabilization and Mechanical Properties of Bovine Pericardium.* Journal of Applied Biomaterials and Biomechanics, 2009. **7**(2): p. 123-131.
320. Dove, J., *Capping Bioprosthetic Tissue to Reduce Calcification*. 2011, Edwards Lifesciences Corporation, Irvine, CA (US): United States.
321. Chen, W., F.J. Schoen, and R.J. Levy, *Mechanism of efficacy of 2-amino oleic acid for inhibition of calcification of glutaraldehyde-pretreated porcine bioprosthetic heart valves.* Circulation, 1994. **90**(1): p. 323-329.
322. Jana, S., *Endothelialization of cardiovascular devices.* Acta Biomaterialia, 2019. **99**: p. 53-71.
323. Grimm, M., et al., *Improved Biocompatibility of Bioprosthetic Heart Valves by L-Glutamic Acid Treatment.* Journal of Cardiac Surgery, 1992. **7**(1): p. 58-64.
324. Michael, P.L., et al., *Comprehensive Evaluation of the Toxicity and Biosafety of Plasma Polymerized Nanoparticles.* Nanomaterials (Basel), 2021. **11**(5).
325. Sun, Q., et al., *Thioether-bridged surfactants for interfacial hydrophobic regulation and enhanced mineral flotation recovery.* AIChE Journal, 2025. **n/a**(n/a): p. e18772.
326. Santos, M., et al., *On-Demand Bioactivation of Inert Materials With Plasma-Polymerized Nanoparticles.* Advanced Materials, 2024. **36**(38): p. 2311313.
327. Mudigonda, J., et al., *A Biohybrid Material With Extracellular Matrix Core and Polymeric Coating as a Cell Honing Cardiovascular Tissue Substitute.* Frontiers in Cardiovascular Medicine, 2022. **9**: p. 807255.
328. Li, M., et al., *A hydrophobic antifouling surface coating on bioprosthetic heart valves for enhanced antithrombogenicity.* Journal of Biomedical Materials Research Part B: Applied Biomaterials, 2022. **110**(5): p. 1082-1092.
329. Wang, Y., et al., *A multi-in-one strategy with glucose-triggered long-term antithrombogenicity and sequentially enhanced endothelialization for biological valve leaflets.* Biomaterials, 2021. **275**: p. 120981.
330. Chan, A.H.P., et al., *Selective Immunosuppression Targeting the NLRP3 Inflammasome Mitigates the Foreign Body Response to Implanted Biomaterials While Preserving Angiogenesis.* Advanced Healthcare Materials, 2023. **12**(32): p. 2301571.
331. Sato, Y., et al., *Pathology of Self-Expanding Transcatheter Aortic Bioprostheses and Hypoattenuated Leaflet Thickening.* Circulation: Cardiovascular Interventions, 2025. **18**(2): p. e014523.
332. Cartlidge, T.R.G., et al., *Detection and Prediction of Bioprosthetic Aortic Valve Degeneration.* Journal of the American College of Cardiology, 2019. **73**(10): p. 1107-1119.
333. Donato, M., et al., *The Emerging Role of Nutraceuticals in Cardiovascular Calcification: Evidence from Preclinical and Clinical Studies.* Nutrients, 2021. **13**(8).
334. Liang, X., et al., *Biomimetic-modified bioprosthetic heart valves with Cysteine-Alanine-Glycine peptide for anti-thrombotic, endothelialization and anti-calcification.* International Journal of Biological Macromolecules, 2023. **250**: p. 126244.

335. Jiang, Z., et al., *Improved Cytocompatibility and Reduced Calcification of Glutaraldehyde-Crosslinked Bovine Pericardium by Modification With Glutathione.* Front Bioeng Biotechnol, 2022. **10**: p. 844010.
336. Liu, Y., et al., *Free-aldehyde neutralized and oligohyaluronan loaded bovine pericardium with improved anti-calcification and endothelialization for bioprosthetic heart valves.* Frontiers in Bioengineering and Biotechnology, 2023. **11**: p. 1138972.
337. Stasiak, J.R., et al., *Design, development, testing at ISO standards and in vivo feasibility study of a novel polymeric heart valve prosthesis.* Biomaterials Science, 2020. **8**(16): p. 4467-4480.
338. Hassan, S., M.N. Ali, and B. Ghafoor, *Evolutionary perspective of drug eluting stents: from thick polymer to polymer free approach.* J Cardiothorac Surg, 2022. **17**(1): p. 65.
339. Inoue, T., et al., *Vascular Inflammation and Repair: Implications for Re-Endothelialization, Restenosis, and Stent Thrombosis.* JACC: Cardiovascular Interventions, 2011. **4**(10): p. 1057-1066.

Appendices

Appendix 1

A1.1 Stability of radiolabelled PPN-Zr^{89}

Day	**Identifier**	**Area**	**% Peaks**
0	Peak 1	19996	100
1	Peak 1	15264.5	98.76
	Peak 2	192	1.24
2	Peak 1	13059	99.09
	Peak 2	120	0.91
5	Peak 1	6706	94.21
	Peak 2	412	5.79
8	Peak 1	7668	91.99
	Peak 2	667.5	8.01

Table A1: Serum stability of radiolabelled PPN-Zr^{89}
Area-under-curve data presented and corresponding peak percentages at days 0, 1, 2, 5 and 8.

Appendix 2

A2.1 Bovine pericardium sheet

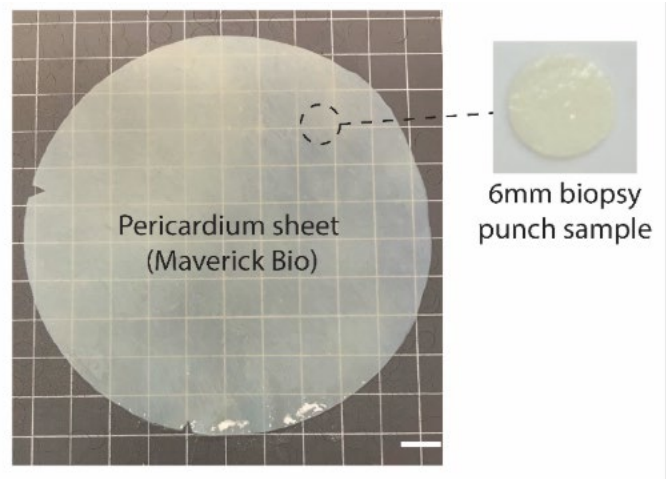

Figure A2.1: Glutaraldehyde-fixed bovine pericardium sheet
6mm biopsy punches were taken from larger pericardium sheets supplied by Maverick Biosciences (scale bar represents 1 cm).

A2.2 Cycle degradation test

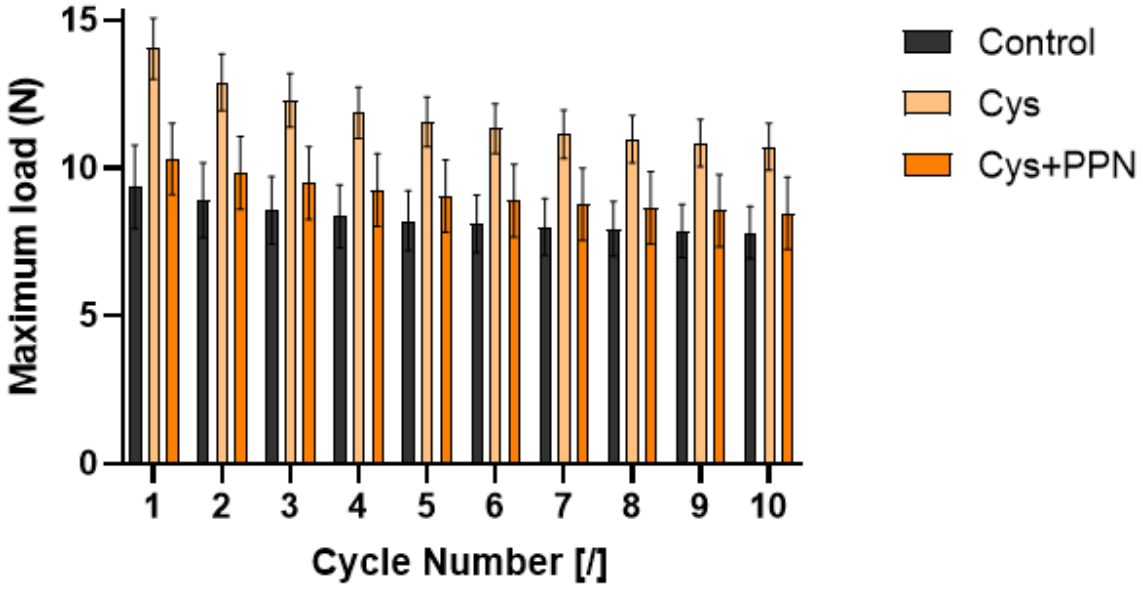

Figure A2.2: Cyclic degradation test
Cyclic maximum load testing of control, Cysteine (Cys) treated and Cysteine plus plasma polymerised nanoparticle (Cys+PPN) treated pericardium across 10 cycles. (n = 3)

A2.3 Cell viability on glutaraldehyde-fixed pericardium

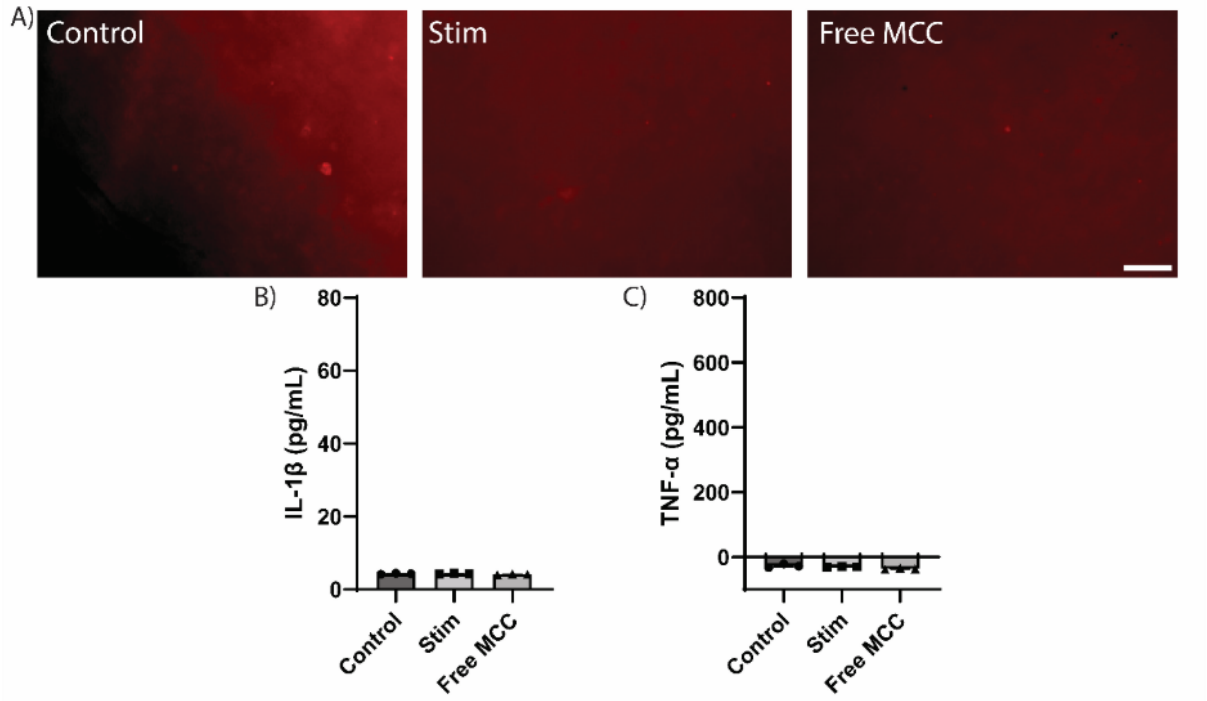

Figure A2.3: Macrophage seeding on pericardium
A) Representative images after THP-1 seeding was performed on non-Cysteine treated glutaraldehyde-fixed pericardium. Actin is stained in red (scale bar represents 50µm). B) Interleukin (IL)-1β and tumour necrosis factor (TNF)-α (C) ELISA quantification from macrophages seeded on non-Cysteine treated pericardium samples post-stimulation.

A2.4 Calcification EDS analysis

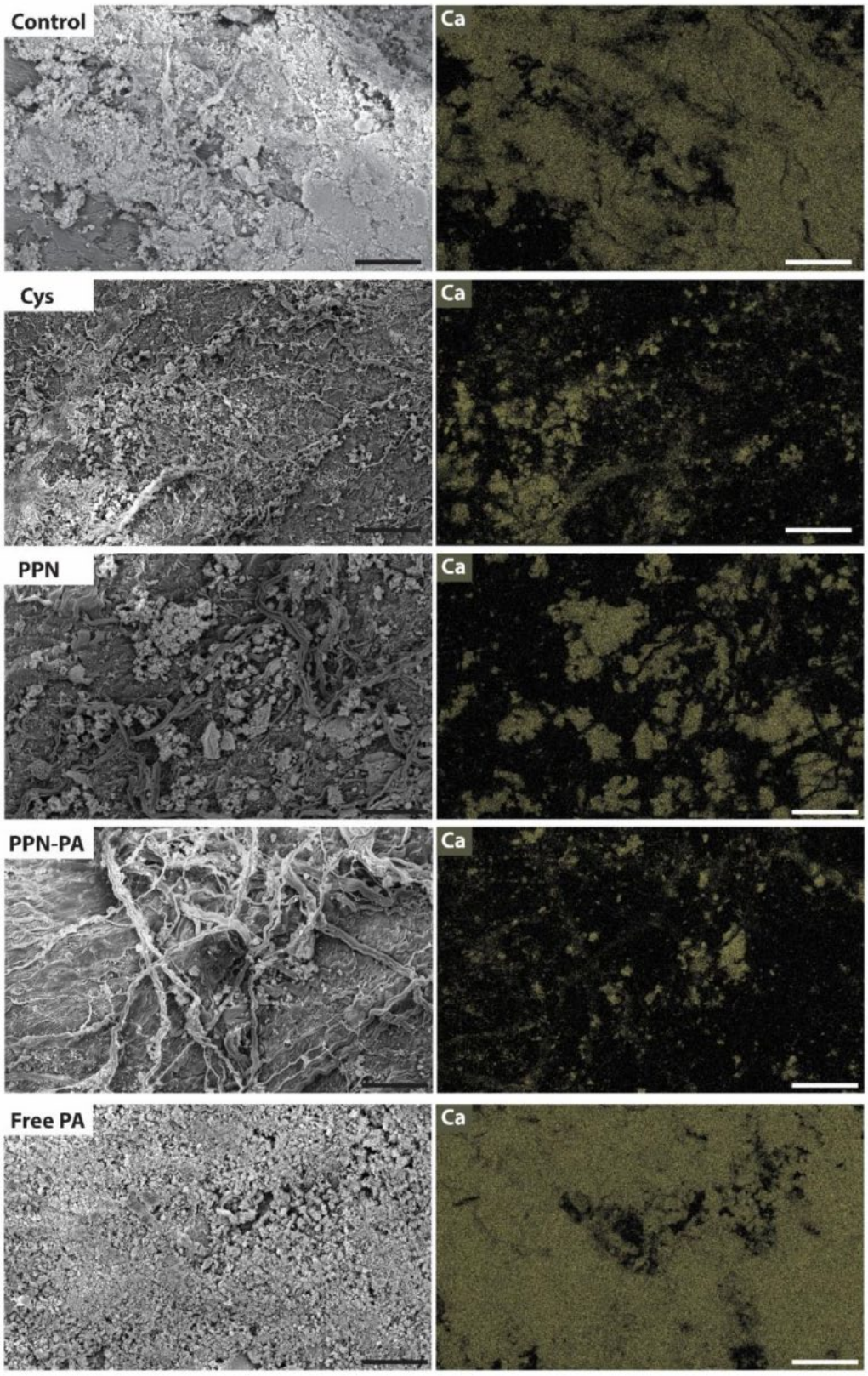

Figure A2.4: Calcification on pericardium surface
Scanning electron microscopy (SEM) images alongside respective SEM-energy dispersive X-ray spectroscopy images of differently coated pericardium surfaces showing calcium (Ca) presence (scale bar represents 100 μm).